MODELLING THE EVOLUTION OF ICE-RICH PERMAFROST LANDSCAPES IN RESPONSE TO A WARMING CLIMATE

Dissertation

zur Erlangung des akademischen Grades

Dr. rer. nat.

im Fach Geographie

eingereicht an der

Mathematisch-Naturwissenschaftlichen Fakultät
der Humboldt-Universität zu Berlin

von

Jan Nitzbon (M. Sc.)

Präsidentin der Humboldt-Universität zu Berlin
Prof. Dr.-Ing. Dr. Sabine Kunst

Dekan der Mathematisch-Naturwissenschaftlichen Fakultät
Prof. Dr. Elmar Kulke

Gutachter:	Prof. Dr. Christoph Schneider Prof. Dr. Guido Grosse Prof. Dr. Sebastian Westermann
Tag der mündlichen Prüfung:	12. November 2020

Zusammenfassung

Jan Nitzbon

Modellierung der Entwicklung von eisreichen Permafrostlandschaften unter Klimaerwärmung

Permafrost ist ein Bestandteil der Kryosphäre der Erde, der für Ökosysteme und Infrastruktur in der Arktis von Bedeutung ist und auch eine Schlüsselrolle im globalen Kohlenstoffkreislauf einnimmt. Die globale Klimaerwärmung, die in den Polarregionen besonders ausgeprägt ist, stellt eine erhebliche Störung der Permafrostregion dar, welche auf ein empfindliches thermisches Gleichgewicht zwischen der Atmosphäre und der Landoberfläche angewiesen ist. Das Auftauen von Permafrost unter Klimaerwärmungsszenarien mittels großskaliger Klimamodelle zu projizieren ist mit sehr großen Unsicherheiten behaftet, da die Modelle entscheidende Komplexitäten von Permafrostlandschaften, wie zum Beispiel kleinskalige Heterogenitäten und Rückkopplungen durch laterale Transportprozesse, nicht berücksichtigen. Insbesondere bleiben in diesen Modellen Auftauprozesse in eisreichem Permafrost unberücksichtigt, welche weitreichende Landschaftsveränderungen – sogenannter Thermokarst – hervorrufen.

Im Rahmen dieser Dissertation habe ich ein numerisches Modell entwickelt, um Auftauprozesse in eisreichen Permafrostlandschaften zu untersuchen, und habe es angewendet, um verbesserte Projektionen darüber zu erhalten, wie viel Permafrost infolge einer Klimaerwärmung auftauen würde. Der Schwerpunkt meiner Forschung lag auf besonders kalten, eis- und kohlenstoffreichen Permafrostablagerungen in der nordostsibirischen Arktis, und dort insbesondere auf Landschaften, die durch Eiskeilpolygone gekennzeichnet sind. In drei eng miteinander verbundenen Forschungsartikeln habe ich gezeigt, dass der neuartige Modellierungsansatz in From von lateral gekoppelten "Kacheln" verwendet werden kann, um die Entwicklung von eisreichen Permafrostlandschaften realistisch zu simulieren. Anhand von numerischen Simulationen habe ich gezeigt, dass der kleinskalige laterale Transport von Wärme, Wasser, Schnee und Sediment die Dynamik von Permafrostlandschaften sowie die Menge des aufgetauten Permafrosts unter Klimaerwärmungsszenarien entscheidend beeinflusst. Weiterhin habe ich gezeigt, dass in numerischen Simulationen, die Thermokarstprozesse berücksichtigen, wesentlich mehr Kohlenstoff vom Auftauen des Permafrosts betroffen ist, als in Simulationen, in denen eisreiche Ablagerungen unberücksichtigt bleiben. Diese Ergebnisse deuten darauf hin, dass konventionelle großskalige Modelle, die für Projektionen des zukünftigen Klimas verwendet werden, das Auftauen von Permafrostböden und die damit verbundenen Rückkopplungen mit dem Kohlenstoffkreislauf erheblich unterschätzen könnten. Insgesamt stellt die in dieser Dissertation dargelegte Forschungsarbeit einen substantiellen Fortschritt bezüglich einer realistischeren Einschätzung der Dynamik eisreicher Permafrostlandschaften mittels numerischer Modelle dar. Insbesondere wurde in der Arbeit das Potenzial von "Kachel"-basierten Modellierungsmethoden demonstriert, um kleinskalige Heterogenität und laterale Prozesse rechentechnisch effizient in großskaligen Klimamodellen zu implementieren.

Abstract

Jan Nitzbon

Modelling the Evolution of Ice-rich Permafrost Landscapes in Response to a Warming Climate

Permafrost is a component of Earth's cryosphere which is of importance for ecosystems and infrastructure in the Arctic, and plays a key role in the global carbon cycle. Global climate warming which is particularly pronounced in polar regions constitutes a major disturbance to permafrost environments which rely on a vulnerable thermal equilibrium between the atmosphere and the land surface. Large-scale climate models reveal high uncertainties in projections of how much permafrost would thaw in response to climate warming scenarios, since they do not represent key complexities of permafrost environments such as small-scale landscape heterogeneities and feedbacks through lateral transport processes. In particular, large-scale models do not take into account thaw processes in ice-rich permafrost which cause widespread landscape change referred to as thermokarst.

For this thesis, I have developed a numerical model to investigate thaw processes in ice-rich permafrost landscapes, and I have used it to obtain improved projections of how much permafrost would thaw in response to climate warming. The focus of my research was on cold, ice- and carbon-rich permafrost deposits in the northeast Siberian Arctic, and on landscapes characterized by ice-wedge polygons. In three closely interrelated research articles I have demonstrated that the novel modelling approach of laterally coupled “tiles” can be used to realistically simulate the evolution of ice-rich permafrost landscapes. The numerical simulations have revealed that small-scale lateral transport of heat, water, snow, and sediment crucially affect the dynamics of permafrost landscapes and how much permafrost would thaw under climate warming scenarios. My research revealed that substantially more permafrost carbon is affected by thaw in numerical simulations which take into account thermokarst processes, than in simulations which lack a representation of excess ice. These results suggest that conventional large-scale models used for future climate projections might considerably underestimate permafrost thaw and associated carbon-cycle feedbacks. Overall, the research presented in this thesis constitutes a major progress towards the realistic assessment of ice-rich permafrost landscape dynamics using numerical models, and demonstrates the high potential of tile-based modelling paradigms for the computationally efficient representation of subgrid-scale heterogeneity and lateral processes in large-scale climate models.

Acknowledgments

The past three and a half years have been a very special time for me, which I would not want to miss. There are so many people which accompanied me on this journey with ups and downs.

First of all, I would like to thank my supervisor Julia Boike, who has placed her complete trust in me from the very beginning and has given me the greatest possible freedom to pursue my own interests in this field of research. Julia, you have an incomparable intuition for knowing what each member of your group needs at any given moment.

Next, my sincere thanks go to Moritz Langer and Sebastian Westermann, whose innovative ideas laid the foundation for my research and with whom I have had enriching discussions about my work and beyond at many times during the past years.

I would like to thank Guido Grosse for supportively accompanying my research as a member of my advisory committee, and for agreeing to examine this dissertation.

At AWI Potsdam, I would like to thank all members of the SPARC team, who cerated an incredibly enjoyable and warmhearted working atmosphere. Special thanks go to Niko, Stephan and Bill, whose unconditional help with the many little problems in everyday life is invaluable. I would also like to thank all members of the PermaRisk team, who gave me a second home at AWI. I also appreciate the support by all members of the Permafrost Research Section in various ways. In particular, I am thankful to my fellow PhDs Mike, Soraya, Simone, and Loeka: It is good to know that you are not alone in the adventures of a PhD.

At HU Berlin, I would like to thank Christoph Schneider for engaging support from a distance, and for agreeing to examine this dissertation. In the Climate Geography group, I especially acknowledge the support of the Cirrus admins, Sebastian Schubert and Anselm Arndt, the hidden heroes who enabled my research.

At Uni Oslo, I am thankful to the Cryosphere Research group who made my research stay in spring 2019 a very enriching experience. I would like to express my deepest thanks Léo – the best CryoGrid comrade I could think of – for climbing with me the rocks around Oslo and for countless laughs while reading his comments on my manuscripts.

A big thanks goes to all participants in the expedition to the Lena River delta in 2017 and to the personnel of the Samoylov Research station. It has been an unforgettable experience and a great privilege to experience the Arctic up close. A winking thanks to Oliver, Katharina, and Stephan for teaching me to play Doppelkopf.

Many institutions and agencies supported my PhD research in various ways. I would like to mention in particular the POLMAR office at AWI, the Geo.X Young Academy, the German Academic Exchange Service, CSDMS at CU Boulder, and the APECS and PYRN networks.

Finally, I would like to thank my friends and family, for always reminding me of what really matters in life. I would like to express my deepest thanks to my parents for their never ending support. At last, I would like to express my deepest gratitude to my dearest Elisa – the best companion in my life.

Selbständigkeitserklärung

Ich erkläre, dass ich die Dissertation selbständig und nur unter Verwendung der von mir gemäß § 7 Abs. 3 der Promotionsordnung der Mathematisch-Naturwissenschaftlichen Fakultät, veröffentlicht im Amtlichen Mitteilungsblatt der Humboldt-Universität zu Berlin Nr. 42/2018 am 11.07.2018 angegebenen Hilfsmittel angefertigt habe.

Potsdam, Mai 2020 Jan Nitzbon

Contents

I Overview 1

1 Introduction and Background 3
- 1.1 Permafrost Uncertainties 3
- 1.2 Permafrost Peculiarities 6
- 1.3 Permafrost Modelling 8
- 1.4 Research Objectives 10

2 Theory and Methodology 13
- 2.1 Concepts from periglacial geomorphology 13
  - 2.1.1 Ground thermal regime 13
  - 2.1.2 Ground ice 15
  - 2.1.3 Ice-wedge polygons and thermokarst landforms 16
- 2.2 Study area and observational data 19
  - 2.2.1 Ice-rich permafrost lowlands in northeast Siberia 19
  - 2.2.2 Long-term permafrost monitoring in the central Lena River delta 20
- 2.3 Landscape tiling 22
- 2.4 The CryoGrid 3 permafrost model 24
  - 2.4.1 Heat conduction 24
  - 2.4.2 Surface energy balance 27
  - 2.4.3 Snow 28
  - 2.4.4 Water balance 29
  - 2.4.5 Excess ice melt 29
  - 2.4.6 Spatial heterogneity and lateral fluxes 29

3 Summary of Research 31
- 3.1 Article 1 32
- 3.2 Article 2 32
- 3.3 Article 3 34

4 Synthesis and Outlook 35
- 4.1 Understanding controls and feedbacks in ice-rich permafrost landscapes 35
- 4.2 Constraining the response of ice-rich permafrost to a warming climate 36

4.3 Employing laterally coupled tiles to represent subgrid-scale processes in land surface models 37
4.4 Outlook 39

II Articles **41**

5 Pathways of ice-wedge degradation in polygonal tundra under different hydrological conditions **43**

6 Fast response of cold ice-rich permafrost in northeast Siberia to a warming climate **81**

7 Effects of multi-scale heterogeneity on the simulated evolution of ice-rich permafrost lowlands under a warming climate **95**

Bibliography **127**

Publications **143**

Appendix **145**

A Supplementary Information for Article 2 **145**

Part I

Overview

CHAPTER 1

Introduction and Background

1.1 Permafrost Uncertainties

The global climate models used for the Fifth Assessment Report (AR5) of the International Panel on Climate Change (IPCC) show little agreement on the simulated extent of permafrost under future warming scenarios (Figure 1.1, Koven et al., (2013) and Stocker et al., (2013)). Under recent climatic conditions, the simulated extent ranges between less than 5 and up to almost 30 million square kilometers. Projected extents for the year 2100 under the Representative Concentration Pathway 8.5 scenario (RCP8.5), which reflects strong global warming, range between complete disappearance of near-surface permafrost and about 15 million square kilometers. Also, the transient evolution of the simulated permafrost extent during the twenty-first century shows very different patterns. To put it boldly, the climate models used for AR5 are not capable of consistently answering the simple but important question:

> How much permafrost will thaw in response to a warming climate?

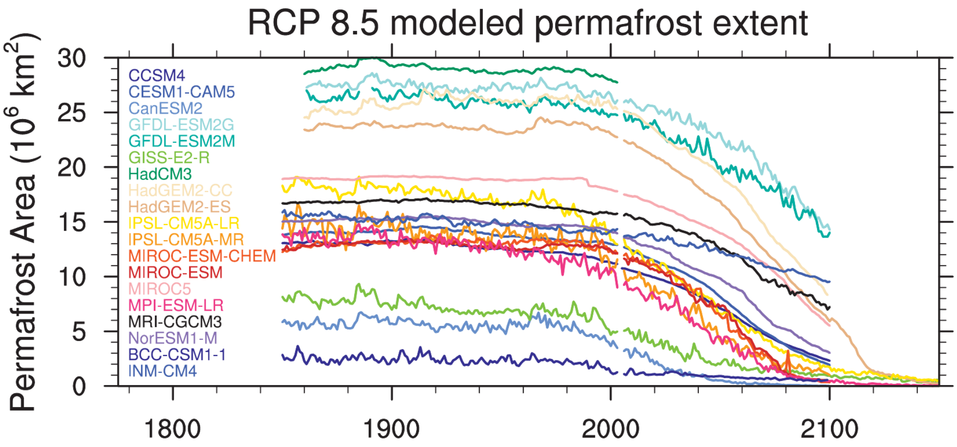

Figure 1.1: Simulated extent of the permafrost area in coupled Earth system models (ESMs). There is a huge variability in the models projections, which can partly be ascribed to shortcomings of how the models represent the land surface processes relevant to permafrost. Adopted from Koven et al., (2013).

Before digging deeper into why these projections produce an inconsistent picture, I would like to begin by discussing why we should concern ourselves with this question in the first place. Permafrost is a component of Earth's cryosphere, defined as ground material which has been at a temperature below 0 °C for at least two consecutive years (EVERDINGEN, 1998). At present, it is estimated – using more suitable tools than the AR5 climate models – that permafrost underlies about 14 million square kilometers, corresponding to about 15 %, of the Northern Hemisphere's exposed land area (Figure 1.2, OBU et al., (2019)). Typically, permafrost contains ground ice, which provides structural stability to the ground. Depending on the spatial scale we are looking at, permafrost has different functions demonstrating its importance. At a global scale, the permafrost region acts as a major storage of carbon. It is estimated that soils in the permafrost region contain about 1300 Gt of carbon (HUGELIUS et al., 2014), which is almost twice the amount contained in the entire atmosphere. About 800 Gt of this carbon pool are contained in perennially frozen deposits. This vast carbon pool makes the permafrost region an important component of the global carbon cycle which in turn plays a crucial role for Earth's climate system (CIAIS et al., 2014). At a regional scale, permafrost affects landscapes' hydrology and geomorphology, and the presence of permafrost has a marked influence on the structure and functioning of Arctic ecosystems (SCHUUR et al., 2018). At a local scale, these permafrost ecosystems provide valuable services to both indigenous and nonnative people (SCHUUR et al., 2018), for example by supporting livelihoods (CRATE et al., 2017), providing natural resources, and promoting stability to built infrastructure (NELSON et al., 2002).

These points demonstrate that the presence of permafrost is of key importance to humans, ecosystems, and the functioning of the climate system. It is important to note that the existence of permafrost is a result of heat exchange between the atmosphere and the land surface, which in turn is primarily controlled by the climate (SHUR et al., 2007). The relatively stable climatic conditions throughout the Holocene epoch brought ecosystems and landscapes in the permafrost region into a sensitive equilibrium state. The recent warming of the Arctic, which is about twice as fast as the global average (HINZMAN et al., 2005), and the expected future warming in the region thus constitute a substantial disturbance to this equilibrium. As a consequence, permafrost across the Arctic is warming (BISKABORN et al., 2019) and thawing (FARQUHARSON et al., 2019; JORGENSON et al., 2006; LILJEDAHL et al., 2016). The degradation of permafrost also means a loss of soil structural stability, with substantial consequences for the functions that permafrost takes over. At a local scale, permafrost degradation puts infrastructure at risk of damage (HJORT et al., 2018), and poses threats to Arctic communities (IRRGANG et al., 2019). Regionally, permafrost landscapes are seeing drastic changes across the Arctic (ROWLAND et al., 2010; TURETSKY et al., 2019; VINCENT et al., 2017), with implications for ecosystems such as loss of wildlife habitats and biodiversity (GILG et al., 2012; WRONA et al., 2016). Of global relevance is the potential change of the permafrost region from a carbon sink to a carbon source (NATALI et al., 2019; SCHUUR et al., 2015). Thawing of permafrost makes previously freeze-locked organic matter accessible to microbial decomposition, facilitating the turnover of organic carbon into the greenhouse gases carbon dioxide (CO_2) and methane (CH_4). If emitted into the atmosphere, these greenhouse gases contribute to global warming. This permafrost

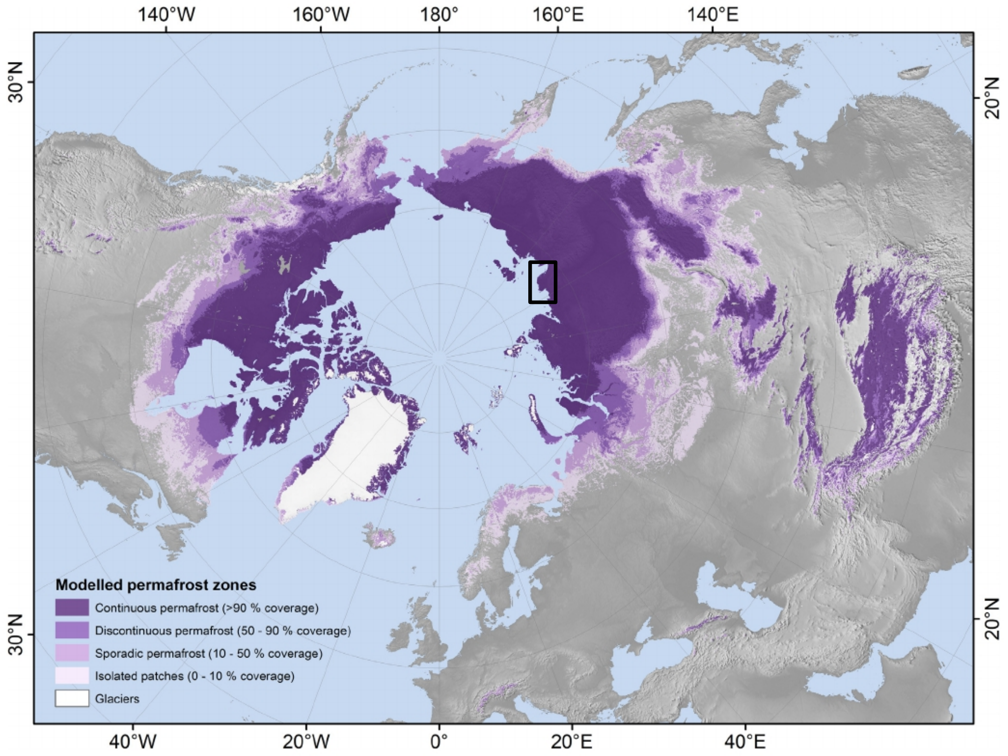
140°W
160°W
180°
160°E
140°E
30°N
20°N
30°N
20°N
40°W
20°W
0°
20°E
40°E
Modelled permafrost zones
Continuous permafrost (>90 % coverage)
Discontinuous permafrost (50 - 90 % coverage)
Sporadic permafrost (10 - 50 % coverage)
Isolated patches (0 - 10 % coverage)
Glaciers

Figure 1.2: Map showing the estimated distribution of permafrost in the Northern Hemisphere, and the partitioning into different zones according to the probability of permafrost occurrence. The map is based on equilibrium simulations of ground temperatures under recent climatic conditions. The black rectangle shows the location of the Lena River delta which is the focus study area in this thesis. Adapted from Obu et al., (2019).

carbon–climate feedback (PCF) is one of several carbon cycle–climate feedbacks which introduce substantial uncertainties into global model projections of future and past climates on Earth (Heimann et al., 2008; Luo, 2007). For example, carbon emissions from permafrost wetlands might have contributed to global climate warming during the last deglaciation (Tesi et al., 2016; Walter et al., 2007, 2006).

Projecting the response of permafrost to a warming climate in the future requires mathematical models which can simulate the relevant physical processes that control the presence and stability of permafrost. As outlined in the beginning of this section, coupled global climate models demonstrate large discrepancies in their projections of permafrost thaw in response to climate warming scenarios. In the subsequent Section 1.2, I explain some of the peculiarities and complexities of permafrost which constitute major challenges for its simulation in large-scale numerical models. After that, in Section 1.3 I give an overview of recent modelling approaches to investigate permafrost thaw dynamics.

1.2 Permafrost Peculiarities

Given the simple temperature-based definition of permafrost, one is inclined to ask: What makes it so difficult to assess the extent of permafrost and its response to climatic change in large-scale models? In fact, there are many answers to this question and many issues to consider. Some of these issues do not only apply to permafrost, but generally to the representation of the land surface in global climate models. But there are also very peculiar problems characteristic to permafrost. If we want to know *how much* permafrost will thaw in response to a warming climate, we need to ask: *How* does permafrost thaw in the first place? One answer to this is: through gradual deepening of the active layer – the upper part of the ground which undergoes freezing and thawing during the annual cycle, situated above perennially frozen ground (Figure 1.3 a; see Section 2.1.1 for details). This gradual "top-down" thawing of permafrost is the typical way of how thawing proceeds in much of the permafrost region, and it is – in principle – also represented in large-scale climate models. However, thawing proceeds differently in terrain which hosts ice-rich permafrost deposits (Figure 1.3 b; see Section 2.1.2 for details). When ice-rich ground thaws or massive ground ice melts, the permafrost loses its stability, and the soild ground material subsides as a consequence. This processes is referred to as thermokarst and it involves the formation of characteristic landforms such as thermokarst lakes or thermokarst mounds (KOKELJ et al., 2013) (see Section 2.1.3 for details). Compared to gradual, top-down thawing, thermokarst can induce positive feedbacks such as water impoundment, which cause much more rapid thawing of the ground. This type of thaw has thus been termed "abrupt" (SCHUUR et al., 2015; TURETSKY et al., 2019), and it is not captured by large-scale climate models, as they do not specifically represent permafrost deposits containing excess ice (KOVEN et al., 2013).

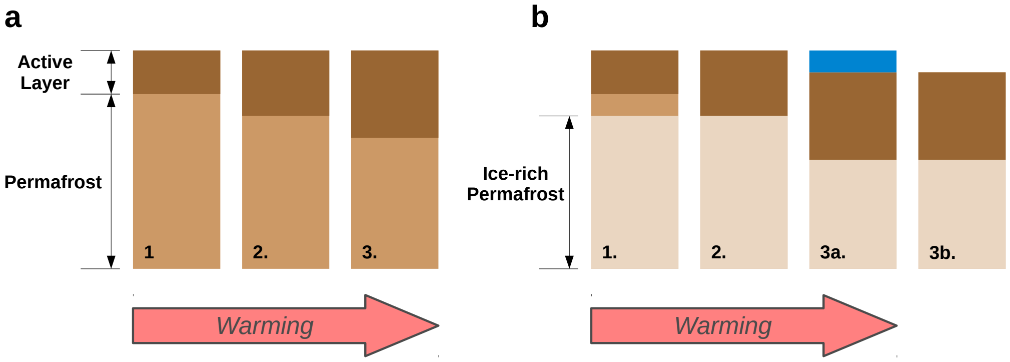

Figure 1.3: Illustration of different types of permafrost thaw in response to warming. a: If the permafrost contains no excess ice, warming leads to a gradual deepening of the active layer over time (1.-3.). b: Once the thaw depth reaches ice-rich permafrost (2.), the ground material settles into the space previously occupied by the ice. The excess water either ponds at the surface (3a.), or drains, causing net subsidence of the surface (3b.). The landscape change due to thawing of ice-rich permafrost is called thermokarst and is not represented in large-scale climate models.

One reason why thermokarst is not represented in large-scale models is that it is a localized process which is initiated at small spatial scales (meters to hundreds of meters). Thermokarst results in spatial heterogeneities which are far below the lateral resolution of large-scale models (tens to hundreds of kilometers; see Figure 1.4). Characteristic thermokarst landforms and other surface patterns in permafrost environments (see Section 2.1.3 for details) are linked to heterogeneities in many surface and subsurface properties such as water cover, vegetation, microtopography, soil moisture, soil texture, carbon contents and ice contents.

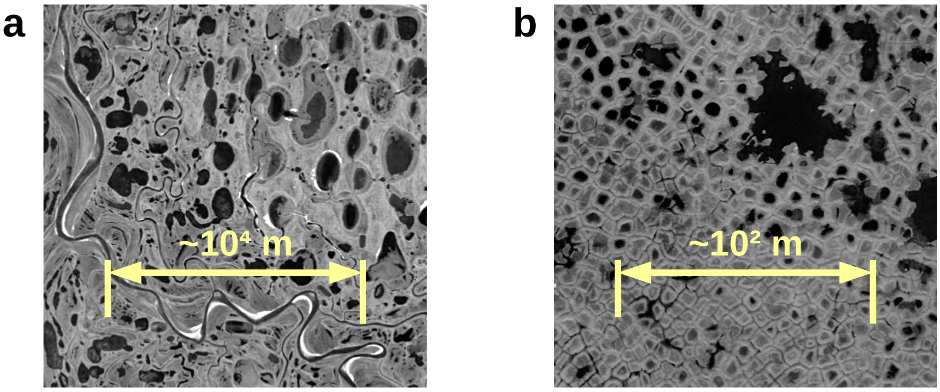

Figure 1.4: Satellite and aerial images showing typical landscape configuration in the Lena River delta during snow-free conditions. Ice-rich permafrost landscapes are characterized by pronounced spatial heterogeneities at different scales which can be ascribed to thermokarst and other periglacial processes. Examples include the formation (and drainage) of thermokarst lakes (a), and the regular patterns associated with ice-wedge polygons (b). Large-scale climate models are not able to capture these small-scale landscape features and dynamics. See Section 2.1 for details on periglacial geomorphology. Image credits: a: Google Earth, b: Adapted from MUSTER et al., (2012b).

To complicate things further, these subgrid-scale heterogeneities give rise to lateral transport processes on small spatial scales, such as snow redistribution and water fluxes in dependence of the terrain's microtopography. These small-scale transport processes involve various feedbacks on the exchange of energy and water within the landscape and also between the land and the atmosphere; consequently, they are also affecting how permafrost thaws under a warming climate. Since the land surface schemes of large-scale climate models only represents vertical transport processes, they cannot take into account the effect of these lateral fluxes on permafrost thaw dynamics.

In summary, I have identified the following complexities which make it difficult to accurately projecting permafrost thaw dynamics in large-scale models: (i) thaw-processes in ice-rich permafrost (thermokarst), (ii) spatial heterogeneities of surface and subsurface properties, and (iii) lateral transport processes on small spatial scales. Having identified these major challenges for permafrost modelling, I pose the following research question which is central to this thesis:

How can subgrid-scale heterogeneity, lateral fluxes, and thaw processes in ice-rich permafrost be efficiently represented in large-scale models?

To address this question further, it is instructive to assess which approaches exist to mathematically model permafrost thaw processes. In the next section, I briefly review existing permafrost modelling approaches, and I identify the need for novel modelling paradigms to overcome current limitations to realistically assess permafrost thaw dynamics across spatial scales.

1.3 Permafrost Modelling

Permafrost models are mathematical tools which serve different purposes. On the one hand, they are used to improve the understanding of processes acting in permafrost environments. On the other hand, they allow to make projections of permafrost in response to external changes such as climate warming. As the definition of permafrost is temperature-based, the key purpose of a permafrost model is to quantify the thermal state of the ground, which is primarily a function of climate (RISEBOROUGH et al., 2008; SHUR et al., 2007).

The most simple models assume the thermal state of the ground to be in equilibrium with the climate, and provide mathematical equations relating the thermal state of the lower atmosphere, expressed in quantities such as thawing- and freezing-degree days of the air temperature, with the thermal regimes at the ground surface and in the subsurface. Typically, these **equilibrium models** make use of empirical parameters which emulate the physical energy transfer processes between the atmosphere, the surface, and the ground. An example for an equilibrium models are n-factors which establish a relation between the ground surface temperature and the air temperature, taking into account the thermal buffering through vegetation in summer and snow in winter (LUNARDINI, 1978). Similarly, the TTOP model can be used to relate ground surface temperatures with subsurface temperatures below the active layer (RISEBOROUGH, 2002; SMITH et al., 1996). There are also equilibrium models such as the Stefan model (STEFAN, 1891) and the Kudryavtsev model (KUDRYAVTSEV et al., 1977) which can be used to calculate the depth of the seasonally thawed (or frozen) layer. While all of these equilibrium models make strong simplifying assumptions and are limited in their capacity to quantify transient changes in the state of permafrost, they have the big advantage of being highly efficient in terms of computational demand. Hence, statistical ensembles of these models can be used to quantify uncertainties, and they can be employed at pan-Artic scales – for example, to generate maps of present-day permafrost probability assuming equilibrium conditions (see Figure 1.2, OBU et al., (2019)).

Besides these “classical” modelling approaches to quantify thermal characteristics of the ground, more recent permafrost models can roughly be divided into two categories, each being associated with different scientific questions driving their development (Figure 1.5). On the one hand, vertical (1D) subsurface heat and water transport schemes have been developed within the framework of **land surface models** (LSMs). Examples for LSMs include the CLM (LAWRENCE

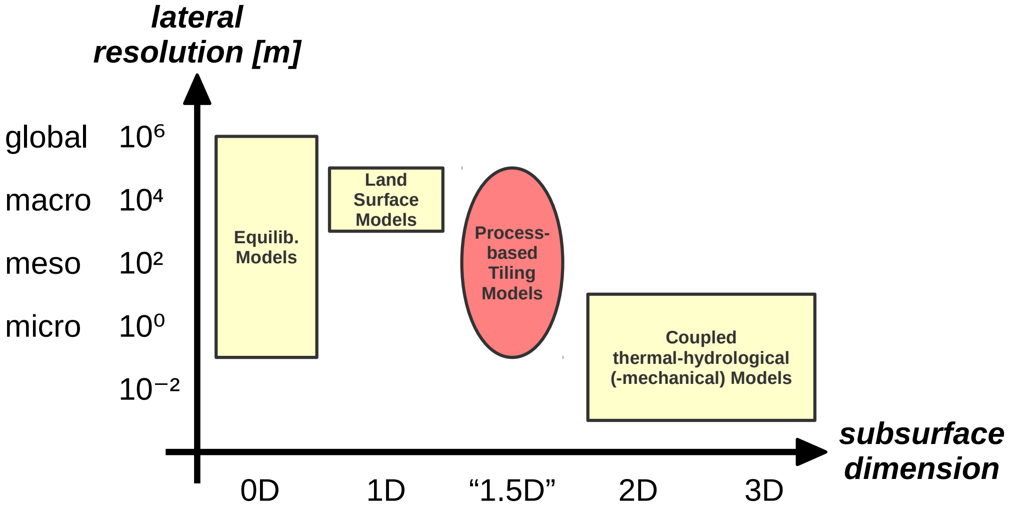

Figure 1.5: "Landscape" of permafrost modelling approaches, partitioned by lateral resolution and subsurface dimension. Simple equilibrium models can be employed at any scale, but lack explicit representation of physical processes. Large-scale land surface models are employed at global scales but lack key complexities. These complexities can partly be addressed by high-resolution, coupled thermal-hydrological models which represent the subsurface in two or three dimensions at the cost of high computational demands. Process-based tiling models aim at "bridging" the gap between those approaches by reflecting key heterogeneities and lateral fluxes within the vertical structure of LSMs.

et al., 2019), JSBACH (Ekici et al., 2014), ORCHIDEE (Krinner et al., 2005), JULES (Best et al., 2011; Clark et al., 2011), Noah-MP (Niu et al., 2011), and SURFEX (Masson et al., 2013). The original purpose of such LSMs is to provide "lower boundary conditions" for the atmospheric models of global Earth system models (ESMs). LSMs are also used as stand-alone tools to investigate subsurface thermal, hydrological, and biogeochemical processes in response to a prescribed meteorological forcing at the surface. While the representation of permafrost dynamics in LSM frameworks has improved significantly in recent years (Andresen et al., 2020; Chadburn et al., 2015; Ekici et al., 2015; McGuire et al., 2016), it is important to keep in mind that their major focus is on quantifying exchanges of heat, water, carbon, and momentum between the land and the lower atmosphere.

In contrast to the "top-down" perspective on permafrost taken by LSMs which see permafrost in a global context, there is a wide range of models dedicated to simulate thermal, hydrological, and mechanical processes in permafrost environments at the site-level, thus taking more of a "bottom-up" perspective. These **coupled thermal-hydrological(-mechanical) models** are often based on catchment-scale hydrology models which were complemented by parameterizations for heat transfer and freeze-thaw processes (Figure 1.5). Examples include SUTRA (Voss, 1984), PFLOTRAN (HAMMOND et al., 2014), Amanzi-ATS (PAINTER et al., 2016), and GEOtop (ENDRIZZI et al., 2014). These models have in common that they represent subsurface heat and water transport also in the lateral direction (2D or 3D), and typically solve the Richard's equations for subsurface water transport (GRENIER et al., 2018). These models have successfully been applied to investigate thermal and hydrological dynamics in permafrost environments at the site-level (e.g., ABOLT et al., (2018), JAFAROV et al., (2018), KUMAR et al., (2016), KURYLYK et al., (2016), and SJÖBERG et al., (2016)). However, the computational demand to solve the underlying coupled partial differential equations in multiple spatial dimensions is very high, such that the simulation periods are limited to few years and an employment at regional or global scales is not feasible.

While it is clear that the various types of models are tailored for different purposes and research questions, none of the discussed models is capable of meeting all challenges for projecting permafrost thaw that are detailed in Section 1.2. While coupled thermal-hydrological models are able to capture micro-scale heterogeneities, they are too computationally expensive to deliver long-term projections at global scales. LSMs in turn are regularly used for such projections, but lack key complexities of permafrost dynamics and insufficiently capture subgrid-scale heterogeneities and lateral fluxes. Finally, and maybe most importantly – with few exceptions (LEE et al., 2014) – none of the above-mentioned permafrost models comprises a representation of thaw processes in ice-rich permafrost landscapes and the associated landscape changes and feedbacks. Given the considerable parts of the permafrost region which are susceptible to thermokarst (OLEFELDT et al., 2016), various authors have thus identified a demand for novel modelling techniques, which take into account abrupt thaw related to thermokarst, and which bridge the scale-gap between existing permafrost modelling paradigms (AMAP, 2017; ROWLAND et al., 2015; SCHUUR et al., 2015; TURETSKY et al., 2019; WESTERMANN et al., 2016).

1.4 Research Objectives

In this thesis, the capacity of a novel modelling approach is explored which is intended to fill a white spot in the "landscape" of permafrost models (Figure 1.5) by bridging the scale-gap between high-resolution, multi-dimensional models on the one hand, and globally-distributed one-dimensional schemes on the other hand. The underlying hypothesis of this novel modelling paradigm is, that key heterogeneities and lateral feedback processes in permafrost environments can be captured by lateral coupling of so-called "landscape tiles". Each of these tiles is associated with a one-dimensional representation of the subsurface, making the model an intermediate case between 1D and 2D subsurface representations ("1.5D"). The computational costs of the tiling approach scale approximately linear with the number of tiles used to represent landscape heterogeneity, while being independent of the lateral resolution of the heterogeneity that is to be represented. This keeps the computational demand at a reasonable level compared to models with a 2D or 3D subsurface representation. The emerging class of process-based tiling models (PTMs) facilitates an improved understanding of processes on the micro- and meso-scale, and allows long-term projections of the transient response of permafrost to climatic change.

In this thesis, I use and enhance the CryoGrid 3 permafrost model, which has been used before to showcase the potential of landscape tiling (LANGER et al., 2016), and which comprises a process-based scheme to simulate thaw-processes acting in ice-rich permafrost (WESTERMANN et al., (2016), see Section 2.4 for details). I employ numerical modelling methods to address substantial gaps in the understanding of processes which control permafrost thaw dynamics, and to explore how technological hurdles which impede a satisfying representation of permafrost in global-scale climate models could be overcome. The overarching goal of this dissertation is to contribute to answering the question of how permafrost responds to a warming climate, by addressing the following three major research objectives:

Research objectives:

1. To improve the understanding of physical processes and feedbacks which are involved in the degradation of ice-rich permafrost landscapes, with a specific focus on ice-wedge thermokarst in continuous permafrost lowlands.
2. To constrain the relevance of ice-wedge thermokarst for permafrost thaw, hydrology, and thaw-affected carbon stocks under a warming climate, with a specific focus on ice- and organic-rich permafrost deposits in northeast Siberia.
3. To develop methods to represent subgrid-scale heterogeneity and lateral processes, which are affecting permafrost thaw dynamics, within global-scale land surface models.

Each of the three research articles that are part of this cumulative thesis, contribute to all of these three research objectives. The full research articles are provided in Part II of this thesis. I summarize the contents of the three articles and how they are connected to each other in Chapter 3. In Chapter 4, I synthesize the major conclusions of my research with respect to the objectives stated above. The following Chapter 2 provides further background information on concepts from periglacial geomorphology, the main study area of my research, and the CryoGrid 3 permafrost model.

CHAPTER 2

Theory and Methodology

In the previous Chapter I have outlined why established permafrost models have various shortcomings to realistically project the fate of permafrost under a warming climate. Based on the models' shortcomings, I have identified three major research objectives, which are addressed in this thesis. Before summarizing and synthesizing my research in Chapters 3 and 4, this Chapter provides an overview of the necessary "ingredients" to address the objectives of my thesis: an established theory, a suitable study area, and an effective methodology. The theoretical foundation for my research lies in various concepts from the field of periglacial geomorphology, which are needed to understand the processes which drive the evolution of permafrost landscapes. These concepts are introduced in Section 2.1. The study area for which I have conducted my research are lowlands in northeast Siberia which are underlain by cold, deep, and ice-rich permafrost which formed during the Late Pleistocene and the Holocene. A special focus lies on ice-rich deposits in the central Lena River delta, which I have personally visited during an expedition in summer 2017 (Section 2.2). In the final two sections of this chapter, I introduce aspects of the methodological approach pursued in this thesis: the concept of landscape tiling (Section 2.3) and the numerical permafrost model CryoGrid 3 (Section 2.4).

2.1 Concepts from periglacial geomorphology

2.1.1 Ground thermal regime

The definition of permafrost is based on the temperature of ground material. From a physical perspective, the existence of permafrost depends on the exchange of heat between the ground and the overlying atmosphere. In thermal equilibrium between the ground and the atmosphere, the temperature profile in the subsurface ($T(z)$) increases linearly with depth due to the geothermal heat flux from the inner Earth (Figure 2.1). If the climate at the surface is sufficiently cold, a certain part of the subsurface has temperatures which are perennially below 0 °C. This part of the subsurface is referred to as **permafrost** (EVERDINGEN, 1998). The annual variability of the climatic conditions at the surface modifies the vertical temperature profile in the upper part of the ground, with the maximum and minimum annual temperature profiles giving rise to the iconic "trumpet"-shape that characterizes the thermal regime of the ground. The upper part of the ground, which undergoes annual freezing and thawing, is referred to as the **active layer**.

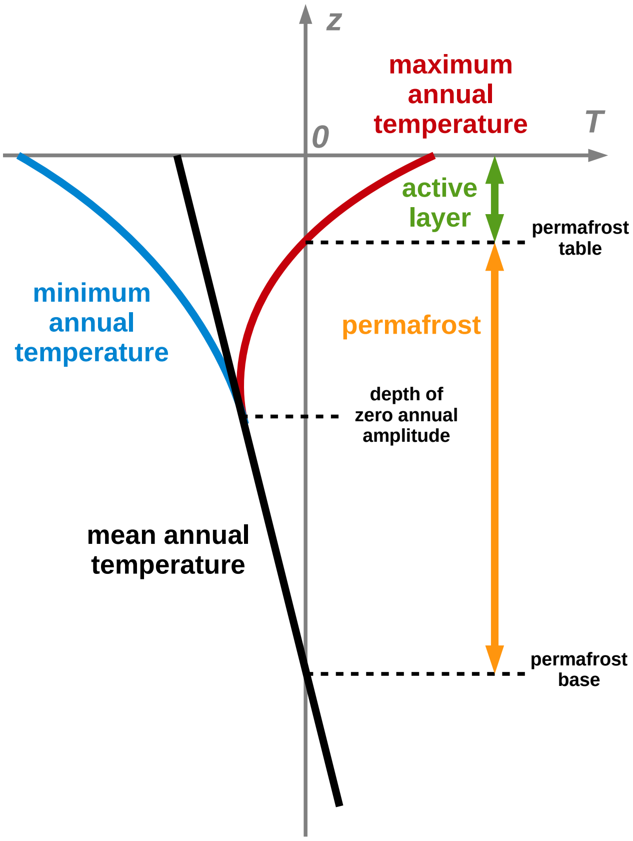
z
maximum
annual
temperature
T
0
active
layer
permafrost
table
minimum
annual
temperature
permafrost
depth of
zero annual
amplitude
mean annual
temperature
permafrost
base

Figure 2.1: Schematic of the ground thermal regime under permafrost conditions which has a “trumpet”-like shape confined by the minimum and maximum annual temperature profiles. The portion of the ground which is perennially below zero degree is defined as permafrost, while the upper part of the ground which undergoes annual freezing and thawing is denoted as active layer.

Various processes can disturb the thermal equilibrium between the ground and the atmosphere. For example, warming of the climate brings the ground thermal regime in a disequilibrium, which causes the permafrost to warm, and the active layer to deepen. The associated lowering of the permafrost table is referred to as **permafrost degradation**. While the dependency of permafrost on the heat exchange between the ground and the atmosphere is intuitive to understand qualitatively, detailed quantification of the temporal evolution of ground temperatures ($T(z,t)$) can be complicated and involves many factors which influence the thermal processes, such as temperature-dependent ground thermal properties, freezing and thawing, and snow cover properties. Hence, numerical models are typically required, to calculate the transient response of the ground thermal regime to different disturbances such as changing conditions at the surface. One factor that makes these calculations particularly difficult is the phase change of pore water in the ground.

2.1.2 Ground ice

If water is present in the ground, the phase change of water occurring below its freezing point gives rise to the presence of **ground ice**. Unlike in pure water, where the phase change occurs at a discrete temperature, freezing of ground that consists of fine-grained sediments occurs over a certain temperature range, in which liquid water and ice coexist. The partitioning into liquid water and ice can be described by the freezing-characteristic curve of the soil, which mainly depends on the soil's constituents and its texture (YERSHOV, 1998). The presence of ice in the subsurface has substantial implications for thermal and hydrological processes in the subsurface, because freezing of the ground drastically changes its capacities to transport heat and water.

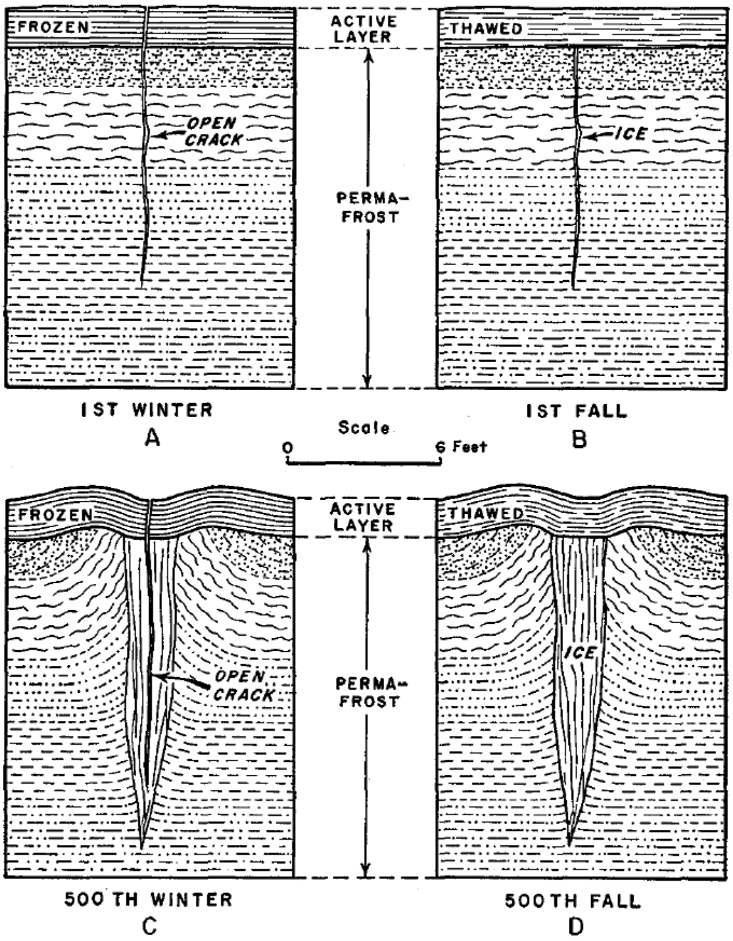
FROZEN
OPEN CRACK
ACTIVE LAYER
PERMA-FROST
THAWED
ICE
1ST WINTER
A
Scale
0
6 Feet
1ST FALL
B
FROZEN
OPEN CRACK
ACTIVE LAYER
PERMA-FROST
THAWED
ICE
500 TH WINTER
C
500 TH FALL
D

Figure 2.2: Schematic illustrating the process of ice-wedge formation. Initially, frost cracks form in cold winters (A). These cracks fill with meltwater in the subsequent summer which refreezes to ice (B). Over several centuries, repeated cracking at the same locations leads to accumulation of massive wedge-shaped ice bodies (c,d). Note the deformation of the surface which gives rise to polygonal patterned ground. Adopted from LACHENBRUCH, (1962).

Ice existing in the pores of frozen soil is denoted as **pore ice**. However, various processes acting under periglacial conditions, allow ground ice formation in different ways than freezing of pore water, and can cause the absolute ice content of the ground to exceed the pore space of the sediment constituents it contains (FRENCH, 2007). These types of ground ice are referred to as **excess ice**, and permafrost containing excess ice is referred to as **ice-rich permafrost** (EVERDINGEN, 1998). For the scope of my thesis, it is important to distinguish between the following two types of excess ice which are also the most abundant ones:

1. **Segregation ice** forms through the preferential migration of liquid water in soil pores towards regions which undergo freezing. This process results in the formation of ice lenses oriented parallel to the ground surface, and causes an overall heaving of the ground above (WALDER et al., 1985). Segregation ice is typically found directly below the active layer (GILBERT et al., 2016).
2. **Wedge ice** forms through the infiltration and refreezing of meltwater in vertical cracks in the ground, which form through the process of thermal contraction under rapid freezing (LACHENBRUCH, 1962; LEFFINGWELL, 1915) (see Figure 2.2 for an illustration). Repeated frost-cracking which occurs preferentially along existing cracks in the terrain, results in ice-wedge growth over decades and centuries, causing the accumulation of massive wedge ice bodies several meters wide and deep.

Ground ice dynamics are an important driver of the geomorphological evolution of landscapes under permafrost conditions. The next section introduces important processes and landforms associated with the accumulation and melting of excess ice. These geomorphological processes are key to understand the spatial heterogeneities in permafrost landscapes and how they can be investigated using numerical models.

2.1.3 Ice-wedge polygons and thermokarst landforms

Periglacial environments feature characteristic landforms which emerge from the cyclic freezing and thawing of ground, and the associated formation and melting of ground ice (FRENCH, 2007). The geomorphological processes which shape periglacial landscapes and landforms interact with hydrological, thermal, and ecological processes, giving rise to unique ecosystems. The most widespread periglacial landform is **polygonal patterned ground** in Arctic tundra lowlands (see Figure 2.3). These patterns form as a result of thermal contraction cracks which tend to form networks of polygons with typical diameters of about 10 to 30 m. The formation of wedge ice described in Section 2.1.2 occurs in such frost cracks, and hence there is an inherent link between the subsurface distribution of excess ice and the polygonal patterns of the surface microtopography (Figure 2.4 a). Across Arctic tundra landscapes, there is a large variability in the size and morphology of **ice-wedge polygons**, which can be related to manifold factors, including the climate, the substrate and the age (CHRISTIANSEN et al., 2016). There are further features forming under periglacial conditions as a result of ground ice accumulation, such as palsas or pingos (FRENCH, 2007), which are, however, not studied in detail within the scope of this thesis.

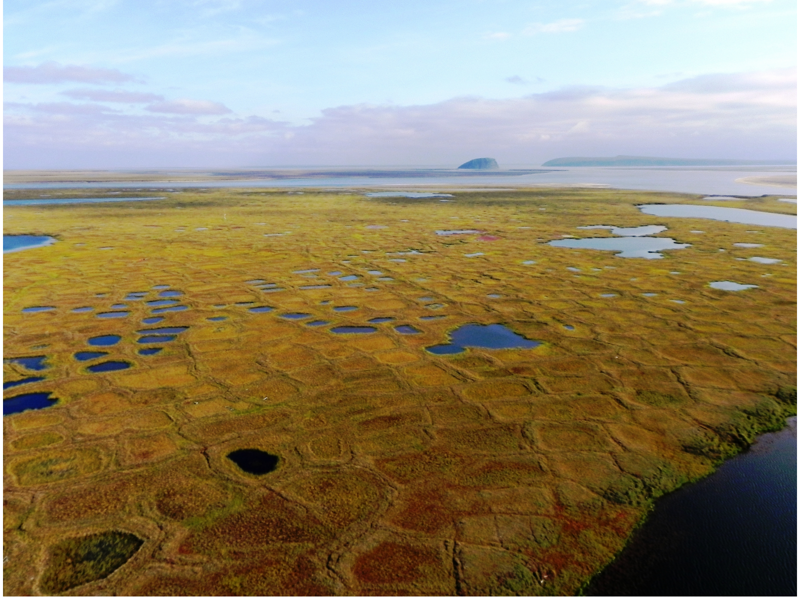

Figure 2.3: Aerial photo of a polygonal tundra landscape in northeast Siberia (Samoylov Island, Lena River delta). The surface microtopography is linked to networks of ice wedges underlying the terrain. The microtopography controls the energy and water balance of the terrain, which can change substantially, when ice wedges melt (see Figure 2.4). Photo credits: S. Zubrzycki.

In contrast to landforms emerging from the accumulation of ground ice, there is a wide range of landscape features associated with thawing and erosion of ice-rich permafrost and the melting of massive ground ice. When excess ice melts, the above-lying ground material is moved downward into the space previously occupied by the ice, while the meltwater ponds at the surface or drains laterally (see Figure 1.3 b; KOKELJ et al., (2013)). At the landscape-scale, this leads to topographic changes entailing the reorganization of the hydrology. These landscape changes are collectively referred to as **thermokarst**. Depending on the type and distribution of the excess ice that is melting, there is a large variety of thermokarst landforms (FRENCH, 2007; KOKELJ et al., 2013).

In polygonal tundra, the melting of ice wedges from the top typically causes the ponding of water in **thermokarst troughs** forming above the ice wedges (see Figure 2.4 b). At the same time, the rims of the low-centred polygons start to subside, improving the hydrological connection between the polygon centers and the troughs. If this process continues over several years, it can cause an inversion of the microtopographic relief, i.e., a transition from low-centred polygons to high-centred polygons (FRENCH, 2007). More recent research has suggested that widespread occurrence of ice-wedge thermokarst could have substantial effects on the landscape hydrology (LILJEDAHL et al., 2016). A high abundance of high-centred polygons would cause the hydrological connectivity of the troughs to increase. Ultimately, this would result in the efficient drainage of the entire landscape (Figure 2.4 c). Such landscape-wide ice-wedge degradation would be associated with substantial changes to the subsurface thermal and hydrological regimes

(Walvoord et al., 2016), and would also have implications for biogeochemical processes and vegetation succession (Lara et al., 2015). As these landscape-scale transitions originate from processes acting at small spatial scales (meters to tens of meters), they are not represented in large-scale models, even though they might have substantial implications for the exchange of energy, water, and carbon between the land and the atmosphere.

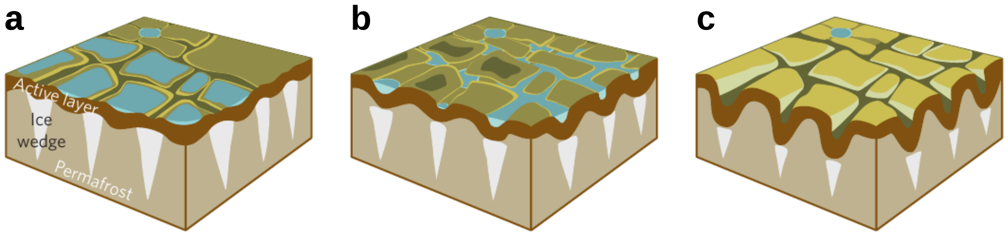

Figure 2.4: Schematic evolution of polygonal tundra from undegraded ice wedges under low-centred polygons (a), over initial ice-wedge degradation and water-filled troughs (b), to advanced ice-wedge degradation and high-centred polygons (c). The drainage efficiency of the landscape improves from the left to the right. Note that ice wedges can also stabilize at different stages and their degradation can be interrupted. Adopted from Liljedahl et al., (2016).

At a larger spatial scale, melting of excess ice can lead to the formation of **thaw lakes** in poorly-drained terrain (Kokelj et al., 2013). These lakes show a large variability in size and depth (Muster et al., 2019) and are abundant in tundra lowlands of Alaska, Canada, and Siberia (Grosse et al., 2013). In uplands and well-drained landscapes in turn, excess ice melt typically results in the formation of efficient drainage channels termed **thermo-erosional gullies** (Fortier et al., 2007; Kokelj et al., 2013). Both, the formation of thaw lakes and of thermo-erosional gullies, typically involves the melting of wedge ice at a micro-scale. There are further thermokarst landforms, such as retrogressive thaw slumps, and thermokarst bogs, which are not further investigated within the scope of this theses, since they occur in different permafrost or vegetation zones, or are associated with types of excess ice that are not abundant in the main study region (see Section 2.2).

The periglacial landforms described above are associated either with the accumulation or with the melting of excess ice. However, on very long timescales (centuries to several millennia) ice-rich permafrost landforms undergo a quasi-cyclic evolution. For example, the degradation of ice wedges is typically succeeded by a stabilization phase, and, eventually, the regrowth of secondary ice wedges (Jorgenson et al., 2006; Kanevskiy et al., 2017). Similarly, it has been hypothesized that thermokarst lakes could undergo cycles of formation, expansion, drainage and regrowth (Billings et al., 1980; Britton, 1957), but it is not clear whether Arctic tundra landscapes underwent such thaw-lake cycles completely during the course of the Holocene (Grosse et al., 2013; Shur et al., 2007). It should be noted, that the concepts of the cyclic evolution of ice-rich permafrost landscapes have mainly been developed in view of past climate variability during the Holocene. Hence, these conceptual models might not hold in view of the strong disturbances brought upon the permafrost region due to anthropogenic climate warming in the near future.

In this section, I have introduced a number of periglacial processes and landforms which are key to understand what drives the spatial heterogeneity of ice-rich permafrost landscapes, and how these are related to the aggradation and degradation of permafrost. It should be noted that, until recently, few numerical modelling studies have investigated the geomorphological evolution of ice-rich permafrost landscapes (KESSLER et al., 2012; PLUG et al., 2009) and how these could respond to climatic changes (LANGER et al., 2016; WESTERMANN et al., 2016). In particular, large-scale climate models do not take into account the complexities associated with the accumulation and melting of ground ice, and the feedbacks of these small-scale processes on the degradation of permafrost.

2.2 Study area and observational data

The study area for this thesis were lowland tundra landscapes in northeast Siberia (Figure 2.5). The region features permafrost deposits with relatively cold mean annual ground temperatures (-8 to $-12\,^{\circ}$C; Figure 1.2; (OBU et al., 2019)), and estimated thicknesses in the order of $400-600$ m depth (YERSHOV et al., 1999), which formed under unglaciated conditions during the last glacial period. Due to the abundance of ice-rich permafrost deposits, the region is highly suitable for the application of numerical models addressing thermokarst processes.

2.2.1 Ice-rich permafrost lowlands in northeast Siberia

The study area lies within the larger Arctic region referred to as Beringia, located roughly between the last glacial maximum extents of the Eurasian ice sheet to the west and the Laurentide and Cordilleran ice sheets to the east, which remained largely unglaciated throughout the Pleistocene glaciations. Today this region features cold and deep permafrost, and particularly ice-rich deposits referred to as Yedoma (SCHIRRMEISTER et al., (2013), Figure 2.5). Yedoma deposits in northeast Siberia contain massive ice wedges, that can reach depth of more than 20 m and can take up 50 % of the ground volume (ULRICH et al., 2014). In addition, Yedoma deposits host well-preserved organic matter constituting a globally significant carbon pool (STRAUSS et al., 2017).

The ice-rich permafrost deposits in northeast Siberia that accumulated during the last glacial period, have been subject to degradation through thermokarst processes throughout the Holocene (SCHIRRMEISTER et al., 2008). The development and growth of thermokarst lakes and thermo-erosional valleys, and the interaction of these features which causes drainage of deep basins (GROSSE et al., 2013), led to a diverse mosaic of landscape types in the lowlands of the study area, including lakes of various sizes (MUSTER et al., 2012a), complex valley systems, and drained lakes basins (also termed **alas**) (MORGENSTERN et al., (2013); see also Figure 1.4 a). As a result of the complex interplay between climatic, geomorphological, hydrological, and ecological processes, the present-day lowlands of northeast Siberia exhibit pronounced

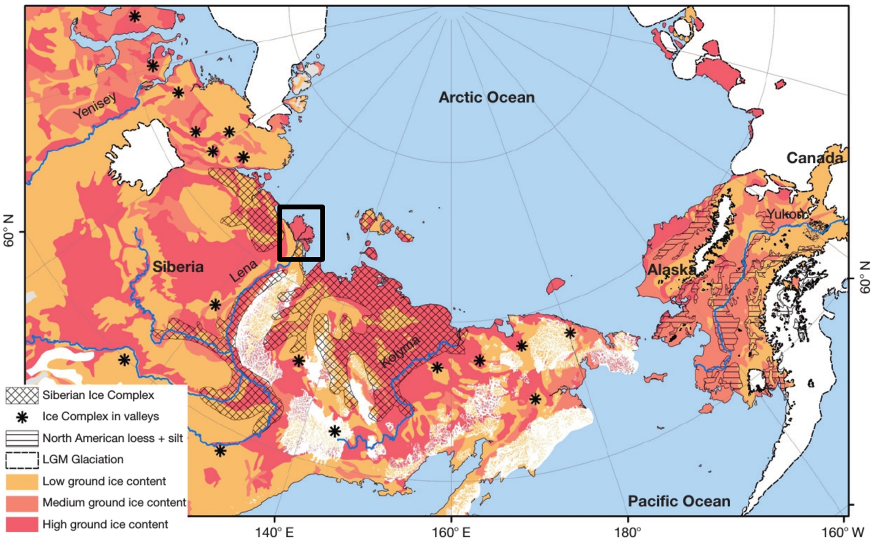
Arctic Ocean
Yenisey
Canada
Yukon
60° N
Siberia
Lena
Alaska
60° N
Kolyma
Siberian Ice Complex
Ice Complex in valleys
North American loess + silt
LGM Glaciation
Low ground ice content
Medium ground ice content
High ground ice content
Pacific Ocean
140° E
160° E
180°
160° W

Figure 2.5: Map showing the present-day extent of the Yedoma domain and estimated ground ice contents in Siberia and Alaska. The landmasses of Eurasia and North America were connected during the last glacial period when global sea levels were substantially lower. The region referred to as Beringia was largely unglaciated and characterized by a cold-arid climate favouring the deposition of ice-rich sediments termed Yedoma. The black rectangle indicates the Lena River delta which was the focus study area in this thesis. Figure adapted from SCHIRRMEISTER et al., (2013) with ground ice contents according to BROWN et al., (1997).

heterogeneities across spatial scales. Abundant excess ice in undegraded deposits of the lowlands make the region prone to thermokarst activity in the future, particularly under warming climatic conditions.

2.2.2 Long-term permafrost monitoring in the central Lena River delta

A special focus of this thesis was put on the ice-rich permafrost lowlands in the central Lena River delta, in particular the islands of Samoylov and Kurungnakh. This focus study area has the advantage that it has been investigated during numerous expeditions in the past two decades, and that there is a long-term record of meteoroglical and ground conditions. In addition, the research I conducted for this thesis benefited from my participation in an expedition to the Lena River delta in summer 2017, which provided me with invaluable insights into the environments to be represented in mathematical models.

The islands of Samoylov and Kurungnakh belong to different geomorphological units (river terraces) of the Lena River delta (Figure 2.6 a,b). Kurungnkah Island belongs to the third, most-elevated (about 30 – 55 m a.s.l.) terrace of the delta, consisting of deposits from a fluvial stage about 88 – 43 ka before present (BP), overlain by ice complex deposits (Yedoma), deposited during the late Pleistocene about 43 – 14 ka BP (SCHWAMBORN et al., 2002). The surface of Kurungnakh has been coined by thermokarst processes during the Holocene, and

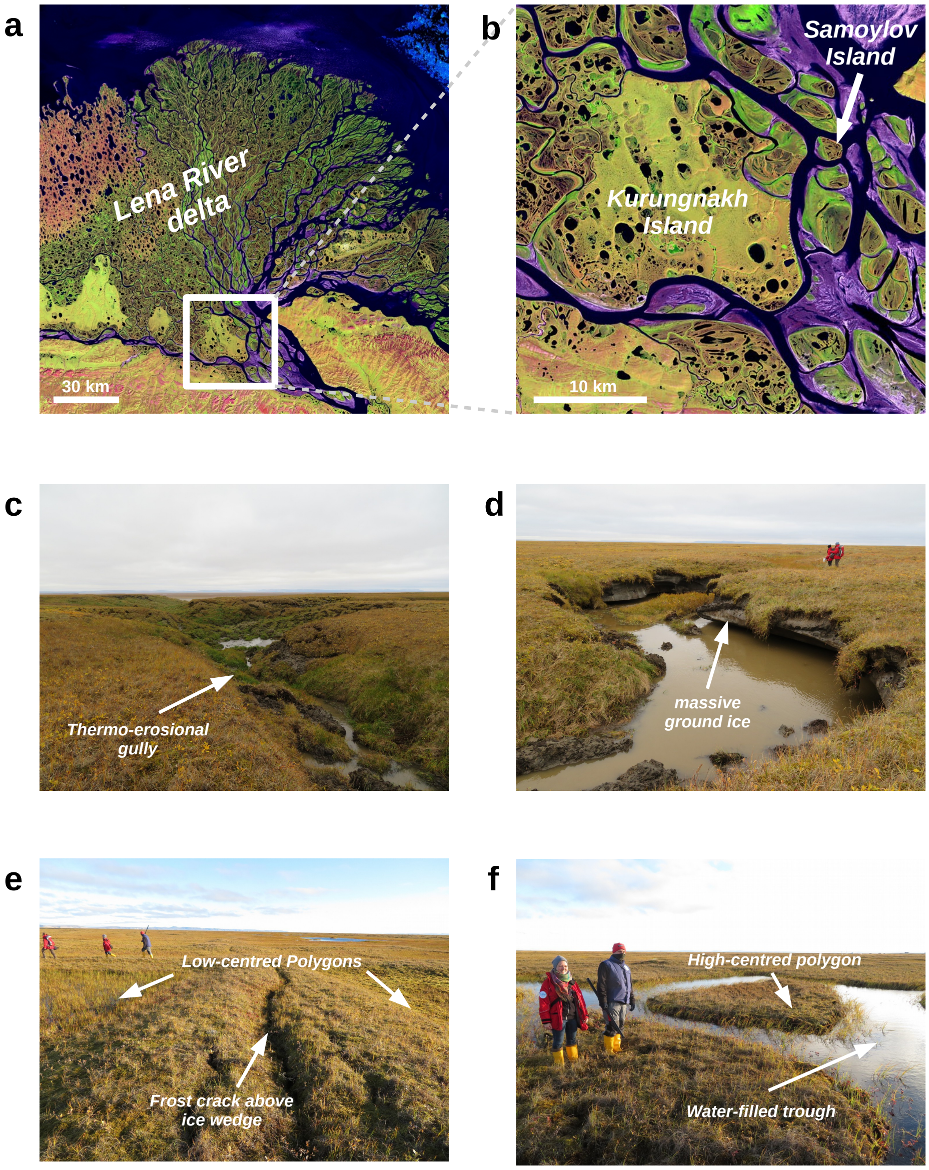
a
Lena River delta
30 km
b
Samoylov Island
Kurungnakh Island
10 km
c
Thermo-erosional gully
d
massive ground ice
e
Low-centred Polygons
Frost crack above ice wedge
f
High-centred polygon
Water-filled trough

Figure 2.6: a,b: Landsat 7 false-color image from July 2000 showing the full extent of the Lena River delta (a) and a detail featuring Kurungnakh and Samoylov Island (b); scales are approximate. c-f: Photos taken on Kurungnakh Island (c,d) and Samoylov Island (e,f) during an expedition in September 2017 showing typical landscape features. On Kurungnakh, thermokarst-induced ground subsidence causes the formation of thermo-erosional gullies (c), and water impoundments (d). On Samoylov, both active ice wedges in low-centred polygon terrain (e), and degraded ice wedges in high-centred polygon terrain (f) coexist. Image credits for a and b: NASA / USGS EROS Data Center.

features manifold landforms characteristic to ice-rich permafrost, including large thermokarst lakes, drained lake basins, thermo-erosional gullies, and thermokarst mounds. Samoylov Island belongs to the lower-elevated (about $1-14$ m a.s.l.) terrace of the delta, formed by fluvial erosion and deposition during the late Holocene (since about 2.7 ka BP) (SCHWAMBORN et al., 2002). The western part of Samoylov consists of a floodplain which is regularly inundated during the spring flood of the Lena River. The eastern part of the island is higher-elevated (about $8-14$ m a.s.l.) and characterized by ice-wedge polygons which partly formed concurrent to the sedimentation (syngenetic) and partly after exposure of unfrozen sediments, e.g., after lake drainage (epigenetic). The volumes and depths of these Holocene ice wedges are substantially lower than those of late Pleistocene ice wedges in Yedoma deposits found on Kurungnakh. Together, the islands of Samoylov and Kurungnakh feature a wide range of periglacial landforms, ground ice conditions, and thermokarst processes (Figure 2.6 c-f), which make them highly suited as a baseline for the development and exploration of numerical modelling techniques for ice-rich permafrost landscapes.

On Samoylov Island, climate, permafrost, and active layer conditions have been monitored continuously since 1998 (BOIKE et al., 2019; BOIKE et al., 2013). The climate can be characterized as Arctic continental with a mean annual air temperature of about −12 °C, and annual summer precipitation of about 145 mm. During most parts of the year, typically from late September until early June) the landscape is continuously covered by a snowpack which reaches depths of 0.3 to 0.5 m by the end of the winter, with large inter-annual as well as spatial variabilities. During the relatively short snow-free period (June to September) the upper part of the soil thaws, with maximum thaw depths ranging between 0.4 and 0.6 m by the end of the summer. Maximum thaw depths which have been systematically monitored on Samoylov Island since 2002, do not show a significant trend over the period of observation. However, permafrost temperatures which have been measured in a borehole since 2006 increased from −9.1 °C (2007) to −7.7 °C (2017) at the depth of zero annual amplitude (about 21 m) during the past decade (BISKABORN et al., 2019). In addition to the long-term monitoring, dedicated field campaigns addressed the spatial heterogeneity of surface characteristics and the water and energy balance of Samoylov Island, in both the summer (LANGER et al., 2011a; MUSTER et al., 2012a) and the winter season (GOUTTEVIN et al., 2018; LANGER et al., 2011b). These studies suggest a strong control exerted by the microtopography associated with the polygonal patterned tundra. The in-situ measurements gathered during many field campaigns to the Lena River delta served as an important baseline for the evaluation and validation of the numerical modelling work of this thesis (BOIKE et al., 2015; BOIKE et al., 2019; BOIKE et al., 2013; GOUTTEVIN et al., 2018; HELBIG et al., 2013; LANGER et al., 2011a,b; MUSTER et al., 2012a). I would like to point out, however, that the developed methods and investigated processes are generally transferable to any study area hosting ice-rich permafrost.

2.3 Landscape tiling

A key objective of thesis was to develop and evaluate novel approaches to represent subgrid-scale heterogeneity associated with thermokarst landforms and processes in numerical models for an improved simulation of permafrost thaw dynamics. These processes occur on spatial scales ranging from meters (e.g., ice-wedge troughs) to kilometers (e.g., thermokarst lakes), and are thus not resolved in the land surface schemes of large-scale climate models, whose lateral resolution is in the order of tens to hundreds of kilometers (e.g., Fisher et al., (2020)). While large-scale models fail in representing subgrid-heterogeneity realistically, fine-scale models that resolve the three-dimensional structure of ice-rich terrain's microtopography are computationally very expensive and thus unsuitable for multi-year assessments (see Section 1.3). For the research of this thesis, I pursued the approach of "landscape tiling" which is intended to capture key heterogeneities of the land surface on different spatial scales, while requiring less computational resources than fine-scaled, multi-dimensional models. The concept of "tiling" has been established since decades to parametrize subgrid-scale heterogeneities of the land surface – mainly different types of vegetation – within atmospheric models (Avissar et al., 1989; Essery et al., 2003; Giorgi et al., 1997; Koster et al., 1992), and more recently it has also been employed to represent the spatial variability related to seasonal snow cover (Aas et al., 2017). Within the context of permafrost landscapes, Langer et al., (2016) have used geometrical relations among different landscape elements to also quantify lateral fluxes of heat on subgrid scales.

Landscape tiling involves the partitioning of heterogeneous landscapes into a low number of distinct units, which are similar with respect to certain properties or features, such as the topographic elevation. The parts of the landscape which belong to the same unit are then collectively described via one "landscape tile". Each of these different landscape tiles is then associated with an individual realization of a one-dimensional permafrost model. It is further possible to incorporate lateral exchange processes amongst the tiles, which take into account the geometrical relations between the landscape units, such as their relative areal proportions. Landscape tiling involves the following main steps which are also visualized in Figure 2.7 for the example of polygonal tundra:

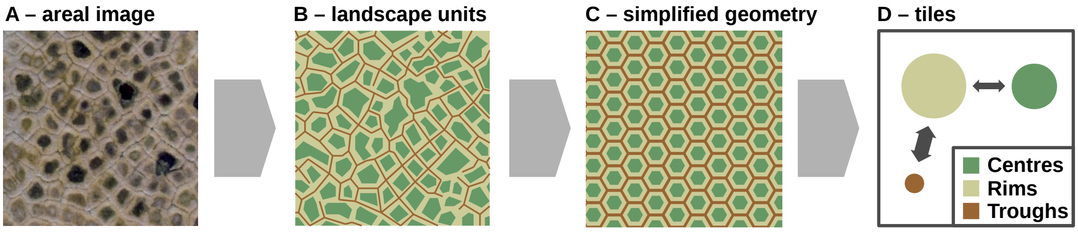

Figure 2.7: The concept of landscape tiling demonstrated for polygonal tundra.

1. **Identification of landscape units.** First, a certain number of distinct landscape units is identified. The choice of the number of distinct units, and the criteria based on which these are differentiated, depend on the type of terrain under consideration, and on the scientific question of interest. For the ice-wedge polygon terrain investigated in this thesis, the surface microtopography constitutes an important heterogeneity, based on which the

landscape can be partitioned into polygon centres, polygon rims, and inter-polygonal troughs (Figure 2.7 a,b).

2. **Simplifying assumptions.** In order to reduce the landscape's complexity further, simplifying assumption are made, exploiting symmetries or periodicity of landscape units. For example, polygonal patterned tundra can be simplified by assuming that all polygons in a region of interest have the same geometric shape and are arranged in a periodic way (Figure 2.7 b,c).
3. **Geometrical relations among the landscape tiles.** Given the simplified landscape units, topological and geometrical relations among them can be quantified. For the lateral processes treated in this thesis, it is further necessary, to quantify the areal proportions (A), the lateral distances between adjacent units (D), and the length of the contact faces (L) between adjacent units. All parts belonging to the same landscape unit, are then effectively described via one tile (Figure 2.7 c,d)
4. **Setting up a process-based model.** Finally, the landscape tiles are used to set up a numerical model that incorporates the landscapes's heterogeneity as reflected by the tiles. Each tile is associated with an individual set of state variables and parameter values of the model. Lateral processes acting between the tiles can be accounted for in the model by making use of the topological and geometric relations among the tiles.

The concept of landscape tiling is a generic approach to reduce the complexity and to represent the spatial heterogeneity of landscapes. For this thesis, I have tailored the concept to applications in ice-rich permafrost landscapes. Specifically, I implemented a landscape tiling scheme in the numerical permafrost model CryoGrid 3 which is explained in further detail in the next Section.

2.4 The CryoGrid 3 permafrost model

The key tool to investigate physical processes in permafrost landscapes within the scope of this thesis was the CryoGrid 3 permafrost model (LANGER et al., 2016; WESTERMANN et al., 2016). Essentially, CryoGrid 3 is a numerical model that simulates the temperature field in the subsurface ($T(z,t)$ [K]) in response to temporally changing boundary conditions prescribed at the surface. CryoGrid 3 is a numerical model dedicated to represent one-dimensional subsurface heat transfer under permafrost conditions, while the full surface energy balance is calculated as upper boundary condition, such that it provides land-atmosphere fluxes of water and energy in the same way as an LSM.

2.4.1 Heat conduction

The fundamental physical law underlying the model is the conservation of energy, which can be expressed in terms of a continuity equation:

$$\frac{\partial u(\vec{x},t)}{\partial t} + \nabla \cdot \vec{q}(\vec{x},t) = 0 \tag{2.1}$$

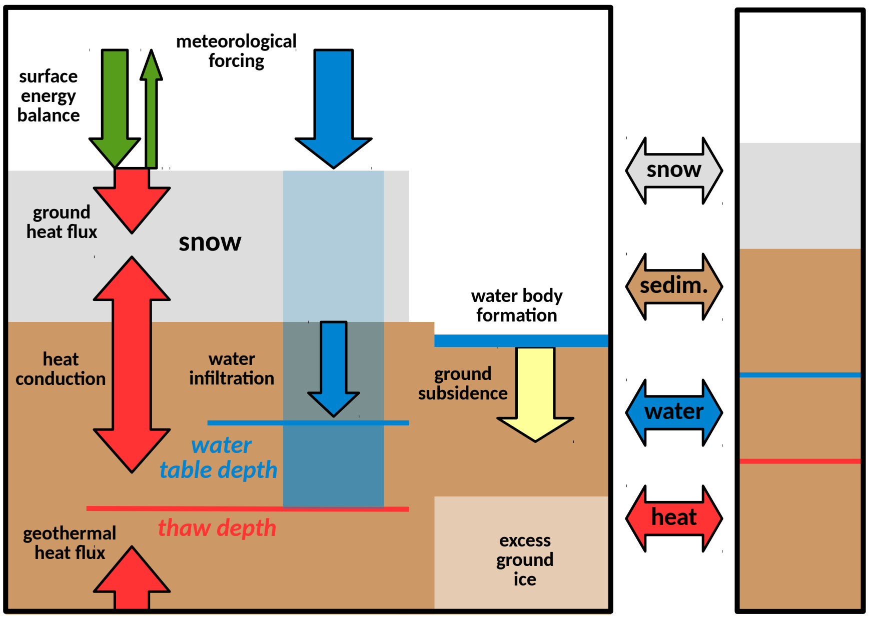
surface
energy
balance
meteorological
forcing
ground
heat flux
snow
heat
conduction
water
infiltration
water body
formation
ground
subsidence
water
table depth
geothermal
heat flux
thaw depth
excess
ground
ice
snow
sedim.
water
heat

Figure 2.8: Overview of the physical processes represented in CryoGrid 3. The processes indicated in the left box correspond to vertical fluxes of mass and energy which are represented in a one-dimensional fashion. The right box represents a second one-dimensional realization ("tile"). Lateral fluxes of mass and energy can be applied between multiple one-dimensional model realizations.

where $u(\vec{x},t)$ $[\mathrm{J\,m^{-3}}]$ denotes the internal energy density field of the ground, and $\vec{q}(\vec{x},t)$ $[\mathrm{W\,m^{-2}}]$ is the local heat flux density. Combining Equation (2.1) with Fourier's law, which states that the heat flux density is proportional to the local temperature gradient ($\vec{q}(\vec{x},t) = -k(\vec{x},t)\nabla T(\vec{x},t)$ with k $[\mathrm{W\,m^{-1}\,K^{-1}}]$ being the thermal conductivity), one obtains the heat conduction equation, which is a second-order partial differential equation:

$$\frac{\partial u(\vec{x},t)}{\partial t} = \nabla \cdot k(\vec{x},t)\nabla T(\vec{x},t) \tag{2.2}$$

Within the context of subsurface heat transfer, vertical gradients are usually larger then lateral gradients, and the subsurface thermal properties differ mostly along the vertical direction. Hence, we subsequently consider only the vertical ($z-$) direction of the problem.

In ground with variable volumetric liquid water content ($\theta_\mathrm{w}(z,t)$ [-]) due to freezing and thawing processes, the internal energy (u) can change through sensible heat transfer, expressed in a change in temperature, as well as through latent heat transfer, expressed in a change in liquid water content. Taking these considerations into account, one arrives at the following, one-dimensional heat conduction equation for variably-saturated ground due to the phase change of water:

$$\rho_\mathrm{w} L_\mathrm{sl} \frac{\partial \theta_\mathrm{w}}{\partial t} + C(z,t) \frac{\partial T}{\partial t} = \frac{\partial}{\partial z} \left(k(z,t) \frac{\partial T}{\partial z} \right) \tag{2.3}$$

where ρ_w [$\mathrm{kg\,m^{-3}}$] is the density of water, L_sl [$\mathrm{J\,kg^{-1}}$] the specific latent heat of fusion of water, and $C(z,t)$ [$\mathrm{J\,K^{-1}\,m^{-3}}$] the volumetric heat capacity of the ground.

For the numerical solution of Equation (2.3) it is helpful to express the latent heat conversion during the phase change of water in terms of an “effective” heat capacity (C_eff) of the ground. Using a differential relation $\left(\frac{\partial \theta_\mathrm{w}}{\partial t} = \frac{\partial \theta_\mathrm{w}}{\partial T} \frac{\partial T}{\partial t} \right)$, one obtains:

$$\underbrace{\left(\rho_\mathrm{w} L_\mathrm{sl} \frac{\partial \theta_\mathrm{w}}{\partial T} + C(z,t) \right)}_{C_\mathrm{eff}(\theta_\mathrm{w},z,t)} \frac{\partial T}{\partial t} = \frac{\partial}{\partial z} \left(k(z,t) \frac{\partial T}{\partial z} \right) \tag{2.4}$$

In porous media like soil, the phase change of water occurs gradually, when the temperature falls below the freezing point. This means that in soil colder than 0 °C, there is a certain fraction of liquid water remaining in the soil pores. To describe this behaviour mathematically, a common assumption is that the *freezing* of soil can be described in the same way as the *drying* of soils (Dall’Amico et al., 2011). Under this assumption, the generalized Clapeyron equation can be used, to derive a relation between the matric potential (ψ) of the soil and its temperature ($\psi = \psi(T)$). Employing empirical formulations of the soil water retention curve (SWRC), which relates the liquid water content with the matric potential ($\theta_\mathrm{w} = \theta_\mathrm{w}(\psi)$), allows to obtain the so-called soil freezing characteristic curve (SFCC), which relates the liquid water content with the soil temperature ($\theta_\mathrm{w} = \theta_\mathrm{w}(T)$). In CryoGrid 3, the SFCC is parameterized according to the Van Genuchten model (Genuchten, 1980). The shape of the SFCC is depending on the soil texture, i.e., the size distribution of the soil grains. CryoGrid 3 provides a predefined set of parameter values to distinguish between sandy and silty soil textures, following Dall’Amico et al., (2011).

The soil thermal properties – the volumetric heat capacity $C(z,t)$ and the thermal conductivity $k(z,t)$ – depend on the constituents of the soil, i.e., the volumetric fractions of mineral (θ_m), organic (θ_o), liquid water (θ_w), ice (θ_i), and air (θ_a) (Westermann et al., 2013). The composition of the solid soil constituents (mineral and organic) can change with depth as specified by the soil stratigraphy. The contents of liquid water and air are variable with depth and in time due to both thermal and hydrological processes (see Section 2.4.4). The volumetric heat capacity is obtained as the weighted sum of all constituents $\alpha \in \{\mathrm{m,o,w,i,a}\}$:

$$C = \sum_\alpha \theta_\alpha C_\alpha \,, \tag{2.5}$$

where the C_α are the volumetric heat capacities of the respective constituents. The thermal conductivity is parameterized according to (COSENZA et al., 2003):

$$k = \left(\sum_{\alpha} \theta_{\alpha} \sqrt{k_{\alpha}} \right)^2 , \tag{2.6}$$

where the k_{α} are the thermal conductivities of the respective constituents.

To solve Equation (2.4), one needs to specify thermal boundary conditions for the upper and lower end of the model domain. The lower boundary condition in CryoGrid 3 is specified by a constant geothermal heat flux (Q_{geo} [$\mathrm{W\,m^{-2}}$]), which depends on the tectonic activity in the geographical region of the study area. However, the geothermal heat flux is of minor importance in regions with little tectonic activity like northeast Siberia, and when considering time scales in the order of a century. The upper boundary condition exerts a strong control on the near-surface thermal regime. In CryoGrid 3, it is provided by the ground heat flux (Q_{g} [$\mathrm{W\,m^{-2}}$]), which is obtained by solving the surface energy balance (SEB), as described in the next section.

2.4.2 Surface energy balance

CryoGrid 3 uses meteorological forcing data as an input to solve the energy balance of the ground surface, in order to derive the ground heat flux (Q_{g}). The SEB scheme is implemented in a similar way as in LSMs, such that it could in principle provide the turbulent heat fluxes – the sensible heat flux Q_{h} and the latent heat flux Q_{e} – as a lower boundary condition to atmospheric models. The full SEB comprises heat fluxes due to radiation, turbulent convection, and conduction, and reads as follows:

$$0 = \underbrace{S_{\mathrm{in}} + S_{\mathrm{out}} + L_{\mathrm{in}} + L_{\mathrm{out}}}_{\text{radiative}} + \underbrace{Q_{\mathrm{h}} + Q_{\mathrm{e}}}_{\text{turbulent}} + \underbrace{Q_{\mathrm{g}}}_{\text{conductive}} , \tag{2.7}$$

where fluxes are defined as positive, if they point towards the ground surface, and negative if the point away from the ground surface.

S_{in} and L_{in} denote the short- and long-wave incoming radiation, respectively, and are provided by the meteorological forcing data. The outgoing shortwave (S_{out}) radiation is obtained by multiplying the incoming shortwave radiation with the albedo of the surface (α), which can change depending on whether the surface is covered by snow, water, ice, etc.:

$$S_{\mathrm{out}} = -\alpha S_{\mathrm{in}} . \tag{2.8}$$

The outgoing longwave radiation (L_{out}) is obtained by summing up the reflection of incoming longwave radiation and the emission of longwave radiation from the surface, following the laws of Kirchoff and Stefan–Boltzmann:

$$L_{\mathrm{out}} = -(1-\varepsilon)L_{\mathrm{in}} - \varepsilon\sigma T_{\mathrm{surf}}^4 \tag{2.9}$$

where ε is the emissivity of the ground surface, σ the Stefan–Boltzmann constant, and T_{surf} the ground surface temperature (in $[K]$).

The turbulent heat fluxes (Q_{h},Q_{e}) are calculated according to the Monin-Obukhov similarity theory (MONIN et al., 1954):

$$Q_{\mathrm{h}} = \frac{\rho_{\mathrm{a}}\, c_{\mathrm{p}}}{r_{\mathrm{a}}^{\mathrm{H}}} \left(T_{\mathrm{air}}(h) - T_{\mathrm{surf}}\right) , \tag{2.10}$$

$$Q_{\mathrm{e}} = \frac{\rho_{\mathrm{a}}\, L_{\mathrm{lg}}}{r_{\mathrm{a}}^{\mathrm{E}} + r_{\mathrm{s}}} \left(q(h) - q_{\mathrm{surf}}\right) . \tag{2.11}$$

with ρ_{a} the density of air, c_{p} the specific (isobaric) heat capacity of air, and L_{lg} the specific latent heat of vaporization of water. $T_{\mathrm{air}}(h)$ is the air temperature and $q(h)$ is the specific humidity at height h above the surface; both are provided as meteorological forcing data. The resistance terms r in the denominators of Equations (2.10) and (2.11) describe the aerodynamic resistance of the lower atmosphere to turbulent heat transfer ($r_{\mathrm{a}}^{\mathrm{H,E}}$), and the resistance of the surface against evaporation (r_{s}). While r_{s} is a parameter that is specified depending on the surface condition (snow, water, soil, etc.), the aerodynamic resistances are calculated in dependence of the atmospheric stability. The specific humidity directly above the surface (q_{surf}) can be obtained from the surface temperature and the atmospheric pressure (see WESTERMANN et al., (2016) for details).

Finally, the ground heat flux (Q_{g}) can be obtained as the residual of Equation (2.7) and serves as an upper boundary condition to Equation (2.3). For this thesis, the surface energy balance scheme of CryoGrid 3 has been modified such that the latent heat flux (Q_{e}) is determined depending on the availability of water in unfrozen soil (see Article 1).

2.4.3 Snow

CryoGrid 3 has a dedicated snow scheme that simulates the dynamic build-up due to snowfall, and ablation due to melt and sublimation of the snowpack (WESTERMANN et al., 2016). It comprises the infiltration and refreezing of rain and meltwater, and associated changes in density of the snow (ρ_{snow}). Most importantly, the snowpack acts as an insulating layer between the ground and the atmosphere during the snow-covered period of the year. When a snowpack is present, the heat conduction equation (2.3) is solved for the joint soil and snow domains (see also Figure 2.8). The heat capacity of snow is parameterized in analogy to Equation (2.5) for the snow constituents ice, water, and air. The thermal conductivity of snow is parameterized according to (YEN, 1981) as follows:

$$k_{\mathrm{snow}} = k_{\mathrm{i}} \left(\frac{\rho_{\mathrm{snow}}}{\rho_{\mathrm{w}}}\right)^{1.88} . \tag{2.12}$$

2.4.4 Water balance

While previous versions of CryoGrid 3 (Langer et al., 2016; Westermann et al., 2016) did not include an explicit water balance calculation, a simple hydrology scheme for unfrozen conditions was introduced into the model within the scope of this thesis (see Article 1 for a detailed description). Unlike more sophisticated hydrology schemes which solve Richard's equation for unsaturated flow in soils (Richards, 1931; Richardson, 1922), an instantaneous infiltration scheme is employed in CryoGrid 3. Infiltrating water is routed downwards in the unfrozen part of the ground, raising the water content to the soil's field capacity (θ_{fc}). Excess water is then routed upwards, leading to the formation of a water table either within the unfrozen ground or above the ground surface (Figure 2.8).

2.4.5 Excess ice melt

CryoGrid 3 has a dedicated scheme describing the subsidence of ground resulting from excess ice melt which enables the investigation of thermokarst processes (Langer et al., 2016; Lee et al., 2014; Westermann et al., 2016). It assumes that once a soil layer containing excess ice thaws, the excess water is instantaneously routed upwards, while mineral and organic constituents from the above-lying layers are routed downwards, such that the resulting soil layer has a predefined "natural" porosity (ϕ_{nat}). If a soil layer of thickness Δz and volumetric ice content θ_{i} thaws, this results in ground subsidence Δs by the following amount:

$$\Delta s = \Delta z \frac{\theta_{\mathrm{i}} - \phi_{\mathrm{nat}}}{1 - \phi_{\mathrm{nat}}} \,. \tag{2.13}$$

Depending on the hydrological boundary conditions for lateral water fluxes, excess ice melt can lead to the formation of a water body atop the soil surface, or mere subsidence of the soil surface without water ponding at the surface.

2.4.6 Spatial heterogneity and lateral fluxes

In the context of this thesis, I have extended the one-dimensional version of CryoGrid 3 as described above and in (Westermann et al., 2016), to also simulate lateral fluxes of heat, water, snow, and sediment between adjacent parts of the landscape. For this, the tiling concept (Section 2.3) which was first introduced into CryoGrid 3 by Langer et al., (2016) has been employed and enhanced. The description of the schemes used to calculate lateral fluxes of heat, water, and snow is provided in Section 2.2.4 of Article 1, and the scheme describing lateral transport of sediment is described in the Methods section as well as in the Supplementary Methods 2 of Article 2. Finally, I have extended the tiling concept to incorporate landscape heterogeneity at multiple spatial scales, with a focus on surface and subsurface lateral water transport as described in Section 2.3.1 of Article 3.

CHAPTER 3

Summary of Research

In the previous Chapters, I have outlined the research objectives of my thesis and provided background information on the theory and methodology which I used to address the objectives. In this Chapter, I briefly summarize each of the three research articles which are part of my dissertation, and explain how the individual articles build on each other. As an orientation, Table 3.1 gives an overview of the scope and the methodological approach pursued in each of the articles. The complete research articles are provided in Part II (Chapters 5 to 7) of my dissertation.

	Article 1 (Chapter 5)	**Article 2** (Chapter 6)	**Article 3** (Chapter 7)
study area	Samoylov Island	Northeast Siberian lowlands	Samoylov Island
thermokarst processes	ice-wedge degradation	ice-wedge degradation and stabilization, thaw lake formation	ice-wedge degradation and stabilization, thaw lake formation and drainage
model developments	water balance, lateral fluxes	lateral sediment fluxes	multi-scale tiling, surface water fluxes
scale of heterogeneity	micro	micro	micro, meso
lateral fluxes	heat, water, snow	heat, water, snow, sediment	heat, water, snow, sediment
climatic forcing	recent (1980–2014)	future scenarios (RCP2.6, RCP4.5, RCP8.5)	future scenario (RCP8.5)
sensitivities explored	hydrological conditions	hydrological conditions, excess ice distribution	micro- and meso-scale heterogeneities
model diagnostics	landscape evolution, thaw depth, water table depth, snow height, evapotranspiration, runoff	landscape evolution, permafrost degradation, subsidence, saturation, thaw-affected carbon	landscape evolution, permafrost degradation, subsidence

Table 3.1: Overview of the scope and the methodology of each of the three research articles.

3.1 Article 1

Pathways of ice-wedge degradation in polygonal tundra under different hydrological conditions

For the first article, I have developed a tile-based model set-up which represents the spatial heterogeneity in surface and subsurface characteristics associated with ice-wedge polygons. This model set-up builds the methodological basis for all three research articles of my thesis. I have advanced the one-dimensional version of the CryoGrid 3 permafrost model by a hydrology scheme that simulates water infiltration into unfrozen ground, and by parameterizations of lateral fluxes of heat, water, and snow among adjacent tiles. The model was set up for Samoylov Island in the Lena River delta and driven by meteorological forcing data reflecting present-day climatic conditions.

I have evaluated the model simulations by comparing them to field measurements of soil temperatures, soil moisture levels, snow depths, water levels, surface energy fluxes. I have demonstrated that the tile-based model is capable of reflecting the spatial variability of these parameters which is associated with the microtopography of polygonal tundra, i.e., polygon centres, polygon rims, and inter-polygon troughs. I have further shown that the model is able to simulate the geomorphological transition of ice-wedge polygons form a low-centred to a high-centred microtopography. The timing and the rate of this process was found to depend on the hydrological conditions in the inter-polygon troughs, with wetter conditions leading to an earlier and more rapid degradation of the ice wedges. Finally, I have shown that the transition of the polygon morphology from a low-centred to a high-centred relief induces a shift in the spatial patterns of the subsurface thermal and hydrological regimes, as well as in the overall water balance of polygonal tundra.

The findings presented in the first article provide an explanation for the diverse degradation stages of ice-wedge polygons observed on Samoylov Island at present. Deviations between observations and modelling as well as limitations of the model set-up are further discussed. One of these limitations lies in the insufficient representation of processes which potentially have a stabilizing effect on ice wedges and are thus required to assess long-term responses of ice-wedge polygons under warming climatic conditions. These issues I have addressed in the second research article.

3.2 Article 2

Fast response of cold ice-rich permafrost in northeast Siberia to a warming climate

Building on the model set-up developed and validated within the scope of the first article, the second study of my dissertation addressed the response of ice-rich permafrost in northeast Siberia to different scenarios of twenty-first century climate-warming (RCP2.6, RCP4.5, RCP8.5).

For this, I have complemented the tile-based version of CryoGrid 3 by a lateral transport scheme for sediment, allowing to capture potentially stabilizing effects due to sediment accumulation in ice-wedge troughs. Due to the marked sensitivity of ice-wedge stability to hydrological conditions which was found in the first study, the simulations were carried out under contrasting hydrological conditions which served as confining cases for future pathways of landscape evolution. Furthermore, the amounts and the distribution of excess ice were varied, in order to assess the response of representative present-day configurations of ice-rich permafrost landscapes in northeast Siberia, including a set-up reflecting Yedoma deposits. In addition, I have up-scaled the results of the model projections to assess potentially thaw-affected carbon stocks in the lowlands of northeast Siberia. These stocks were compared to projections using simplistic permafrost representations which disregard thermokarst-inducing processes.

The simulations revealed a wide range of landscape evolution pathways, depending on the hydrological conditions, the ground ice distribution, and the warming scenario. Under well-drained conditions, ice-wedge thermokarst led to the development of high-centred polygons, which developed a more pronounced relief under stronger warming and higher excess ice contents. Under water-logged conditions, ice-wedge thermokarst initiated the formation of surface water bodies which evolved into thaw lakes of several meters depth and a talik underneath. Furthermore, I have found, that whether or not the laterally transported sediment provides sufficient stabilization after initial ice-wedge melt, depends on the prescribed warming scenario. Under RCP2.6, the landscapes remained largely stable in the simulations, while thermokarst activity was projected for the RCP4.5 and RCP8.5 warming scenarios. However, under RCP4.5, sediment deposition in the troughs led to a stabilization of the landscape, while positive feedbacks on permafrost thaw outpaced negative ones under RCP8.5, corresponding to widespread landscape collapse in the projections. With respect carbon pools in the lowlands of northeast Siberia, I have found that by 2100 up to three-fold (twelve-fold) could be affected by thaw, of what is projected in simulations which disregard thermokarst-inducing processes under RCP4.5 (RCP8.5).

The findings presented in the second article demonstrate a considerable potential for permafrost degradation through thermokarst which is not captured by the conventional one-dimensional representation of permafrost in the land surface schemes of ESMs. The uncertainty range of projected thaw-affected carbon stocks increases with the strength of the warming scenario due to entirely different pathways of landscape evolutions under the contrasting hydrological conditions considered. Constraining this uncertainty further and capturing a wider range of feedbacks through landscape dynamics requires to include landscape heterogeneity at a larger scale into the model. This is what I have pursued in the third article.

3.3 Article 3

Effects of multi-scale heterogeneity on the simulated evolution of ice-rich permafrost lowlands under a warming climate

While I have put a focus on the micro-scale heterogeneity of ice-rich permafrost landscapes in the first two articles, I have extended the landscape tiling concept for the third article to also incorporate heterogeneities at larger scales (meso-scale). In the article, I suggest a multi-scale hierarchical tiling concept that allows to capture micro-scale heterogeneities as associated with ice-wedge polygons, and at the same time takes into account lateral fluxes at the meso-scale, such as water transport along slopes. Within this model framework, hydrological conditions in different parts of the landscape are simulated dynamically, instead of being prescribed through static boundary conditions as in the first two studies. This allows to constrain the uncertainty range associated with the simulations under contrasting hydrological conditions in the preceding articles. In the simulations I have conducted for the third article, I have systematically explored, how projections of ice-rich permafrost landscape evolution under a warming climate depend on the representation of micro- and meso-scale heterogeneities.

The simulation results presented in the article demonstrated additional complexity and feedbacks in the landscape evolution, if meso-scale heterogeneities are taken into account. With the model setup, it is possible to simulate pathways of landscape evolution, which have not been possible to capture using the model set-up of the first two articles. For example, it was possible to simulate the landscape-scale drainage of polygonal tundra, as a consequence of ice-wedge degradation in several parts of the simulated landscape. Similarly, the formation and the gradual drainage of thaw lakes were possible to capture, if meso-scale interactions were considered. I have furthermore shown, that the way in which landscape heterogeneity is represented at different scales has an effect on the projections of permafrost thaw and ground subsidence under climate-warming. Another finding was, that explicit representation of lateral fluxes on both the micro- and the meso-scale makes the response of permafrost to climate-warming more gradual, compared to relatively abrupt changes which were simulated in model setups that ignored these heterogeneities.

Overall, in the third article, I have provided a comprehensive model framework for the simulation of degradation pathways in ice-rich permafrost lowlands, with a specific focus on polygonal tundra. I discuss the results regarding their potential to constrain uncertainties in the response of ice-rich permafrost to a warming climate, and I connect the capacities of the model framework to the general concepts ice-wedges and thaw-lake cycles in thermokarst terrain. Together with the research I have conducted for the first and second article of this thesis, the work presented in the third article constitutes substantial progress towards (i) the modelling of ice-rich permafrost landscape evolution under changing climates, and (ii) the computationally efficient representation of subgrid-scale processes like thermokarst in the land surface components of ESMs.

CHAPTER 4

Synthesis and Outlook

The research I conducted within the scope of this dissertation addressed three major objectives, which were outlined in Section 1.4. Each of the three research articles summarized in Chapter 3 and provided in Part II of this thesis, contributed to each of the three major objectives, while putting a focus on different aspects and defining more specific objectives. Subsequently, I synthesize the main conclusions of each article with respect to each of the three major research objectives.

4.1 Understanding controls and feedbacks in ice-rich permafrost landscapes

The first major objective of this thesis was to use a tailored numerical permafrost model to obtain an improved understanding of physical processes and feedbacks which are involved in the degradation of ice-rich permafrost landscapes, with a specific focus on ice-wedge thermokarst in continuous permafrost lowlands.

With respect to the first objective, the numerical modelling work I conducted for the three research articles suggests, that lateral processes and the distribution of excess ice play a key role in the pathways of landscape evolution and permafrost degradation in ice-rich terrain. My findings emphasize the importance of representing these complexities in large-scale models used to assess the fate of permafrost in a warming Arctic.

A key insight of my thesis is, that lateral processes on spatial scales from meters to hundreds of meters exert a strong influence on the evolution of ice-rich permafrost landscapes, and can constitute both positive and negative feedbacks on permafrost degradation. In polygonal tundra, the hydrological conditions prevailing in the inter-polygonal troughs affect the timing and the speed of ice-wedge degradation, with inundated troughs causing earlier and faster degradation relative to well-drained troughs (Article 1). The hydrological conditions in the troughs are affected by lateral water fluxes, both at the micro-scale, i.e., between polygon centers and troughs (Article 1), and at the meso-scale, i.e., between different parts of the landscape (Article 3). The transition of ice-wedge polygons from a low-centred to a high-centred relief with advancing ice-wedge degradation causes lateral water fluxes and landscape runoff to increase (Articles 1 and 3). However, when drainage is precluded, new thermokarst lakes can form in ice-rich terrain under a warming climate at a rate which is determined by the excess ice content and the strength of the warming scenario (Articles 2 and 3). Besides the hydrological conditions, lateral snow redistribution according to the micro-scale topography exerts a strong positive feedback on ice-wedge degradation, as more snow accumulates in deepening troughs, providing more insulation and increasing temperatures in the active layer above the ice wedge (Articles 1, 2, and 3). The research for this thesis further identified lateral sediment transport as a potential negative feedback processes, which slows down ice-wedge degradation (Article 2 and 3) and can cause landscapes to stabilize after initial degradation. Hence, the numerical simulations suggested, that the lateral transport of heat, water, snow, and sediment influences pathways of landscape evolution in ice-rich permafrost lowlands, and exerts feedbacks on the timing and the magnitude of permafrost degradation under climate warming (Articles 1,2 and 3).

My research has further revealed that – in addition to the crucial role played by different lateral transport processes – the spatial distribution and the content of excess ice in the subsurface have major consequences for the landscape evolution and permafrost degradation in response to a warming climate. In numerical simulations, heterogeneously distributed excess ice, reflecting the subsurface conditions in ice-wedge terrain, gives rise to pathways of landscape evolution which are different from those emerging in simulations with homogeneously distributed excess ice. Neglecting these micro-scale heterogeneities in numerical simulations, precludes simulation of landscape-wide drainage patterns associated with the transition from low-centred to high-centred polygons (Article 3). Furthermore, the excess ice content, which can vary substantially depending on climate and sediment deposition in the past, preconditions present-day ice-rich permafrost lowlands to different pathways of landscape evolution in the future. Thermokarst lakes and taliks are more likely to develop in landscapes with very high excess ice contents such as undegraded Yedoma deposits, than in landscapes with lower excess ice contents such as drained lake basins (Article 2).

4.2 Constraining the response of ice-rich permafrost to a warming climate

The second major objective of this thesis was to constrain the relevance of thermokarst processes for future projections of permafrost thaw, hydrological regimes, and thaw-affected carbon stocks under a warming climate, with a specific focus on ice- and organic-rich permafrost deposits in northeast Siberia.

With respect to the second objective, my research has revealed, that substantially more permafrost carbon could be subject to thaw under a warming climate, than projected using simplistic models that ignore thermokarst-inducing processes. Even though my modelling results do not allow final conclusions about the most likely response of the ground hydrological regime of ice-rich permafrost lowlands to climate-warming, I have developed numerical modelling techniques which allow to further constrain remaining uncertainties in this regard.

My research findings provide significant evidence that thermokarst-related processes cause changes in the energy and water balances of ice-rich terrain, which result in substantially larger amounts of projected permafrost degradation and thaw-affected carbon under a warming climate, compared to projections for ice-poor terrain (Article 2). Ignoring the presence of excess ice and thermokarst processes in large-scale model assessments, could thus cause considerable bias in projections of permafrost thaw, soil moisture, and thaw-affected carbon, given the abundance of excess ice in vast parts of the continuous permafrost region. The deviation between projections with and without thermokarst-inducing projections is most pronounced for the strong warming scenario (RCP8.5). For this scenario, thaw-affected carbon stocks in northeast Siberia would be at least two-fold, and up to twelve-fold by 2100, of the respective projections ignoring excess ice. For a moderate warming scenario (RCP4.5), the relative increase of thaw-affected carbon under consideration of thermokarst-inducing processes ranged between factors of 1.2 and 3.4. Only under an ambitious mitigation scenario (RCP2.6), ice-rich permafrost landscapes in northeast Siberia are projected to remain largely unaffected by thermokarst, and thaw-affected carbon stocks would not increase due to thermokarst activity (Article 2).

Furthermore, in each of the three Articles I have identified a strong interrelation between ice-wedge thermokarst and permafrost hydrology. On the one hand, I showed that contrasting hydrological conditions provide constraints on projections of permafrost degradation, as they give rise to radically different pathways of landscape evolution (Article 1 and 2). The uncertainty associated with these contrasting hydrological conditions exceeds the uncertainty associated with the different warming scenarios (RCPs) for the twenty-first century (Article 2). Incorporating a representation of landscape heterogeneity and lateral water fluxes at the meso-scale (hundreds to thousands of meters) is necessary to further constrain projections of permafrost degradation (Article 3). On the other hand, my modelling work has demonstrated that ice-wedge thermokarst crucially affects the hydrology in permafrost landscapes. The transition from low-centred to high-centred polygons as a result of ice-wedge degradation leads to increased lateral runoff, and an overall intensification of the water cycle in tundra lowlands (Article 1). If lateral drainage is precluded, ice-wedge thermokarst in sufficiently ice-rich terrain leads to the formation of new thermokarst lakes under climate warming scenarios, and thus affects surface water coverage (Articles 2 and 3). Irrespective of the concrete pathway of landscape evolution, my research suggests that warming-induced ice-wedge thermokarst causes a reorganization of landscape hydrology which will affect the cycling carbon and intensify the cycling of water in Arctic lowlands in the future (Articles 1, 2, and 3).

4.3 Employing laterally coupled tiles to represent subgrid-scale processes in land surface models

The third major research objective addressed in this thesis was to develop modelling techniques to efficiently represent subgrid-scale heterogeneity and lateral processes that are affecting permafrost thaw dynamics within the structure of global-scale land surface models.

With respect to the third objective, I have demonstrated that laterally coupled landscape tiles constitute an effective method to assess the effect of small-scale processes on permafrost thaw in ice-rich terrain. The approach constitutes a computationally affordable way to represent these subgrid-scale processes within the lands surface schemes of Earth system models.

In this thesis, I have successfully used laterally coupled tiles to reflect the spatial heterogeneity and lateral fluxes characteristic to ice-rich permafrost landscapes, and I have shown that they can capture manifold degradation pathways in these landscapes. The spatial variability of the subsurface thermal and hydrological regimes, the snow cover, and surface energy fluxes of polygonal tundra can be effectively captured by lateral coupling of three landscape tiles that reflect polygon centres, rims, and troughs (Article 1). Within this tile-based model set-up, it is possible to simulate the transition from low-centred to high-centred polygons which is associated with the degradation of ice wedges, and to represent lateral fluxes of heat, water, snow, and sediment, which give rise to positive and negative feedbacks on ice-wedge degradation (Article 1 and 2). The tile-based set-up for polygonal tundra was adapted to simulate the landscape evolution in Yedoma deposits, which bear relict ice wedges in the subsurface without exhibiting the characteristic surface micro-topography of polygonal tundra (Article 2). In addition to representing micro-scale landscape heterogeneities, the tiling approach was also used to incorporate lateral fluxes and heterogeneities at the meso-scale (Article 3). Combining tile-based representations of the micro- and meso-scale allows to capture a wide range of landscape evolution pathways and associated feedbacks on permafrost degradation. Hence, with only a low number of laterally coupled realizations of a one-dimensional permafrost model, complex patterns and pathways of ice-rich permafrost landscape evolution under a warming climate were simulated.

I further conclude, that the tile-based modelling approach which I pursued and enhanced in this thesis, constitutes an effective method for incorporating subgrid-scale processes in land surface models. Process-based tiling models are thus a promising candidate to bridge the scale-gap between coupled thermal-hydrological models with a high lateral resolution on the one hand, and land surface models employed at global scales on the other hand (see Figure 1.5). For ice-rich permafrost lowlands, a low number ($\lesssim 10$) of laterally coupled tiles is sufficient to capture key processes and feedbacks which are not possible to resolve in one-dimensional schemes. In a first-order approximation, the additional computational demand scales linearly with the number of tiles used to represent the subgrid-heterogeneity. In view of the substantial impact of subgrid-processes on the projections of permafrost thaw, hydrological regimes, and thawed carbon which was revealed in this thesis, an increased focus on the improvement of land surface schemes seems advisable.

Through the model development for the articles of this thesis as well as through closely related studies I was involved in (AAS et al., 2019; MARTIN et al., 2019; ZWEIGEL et al., 2020), I have contributed to the improvement of the numerical permafrost model CryoGrid 3. These contributions include (i) the introduction of a simple hydrology scheme, (ii) schemes for the lateral transport of heat, snow, water, and sediment, and (iii) a framework for dealing with landscape heterogeneities at different spatial scales. These model developments constitute the basis for the improvement of other numerical models used to investigate land surface processes in periglacial environments.

4.4 Outlook

In the previous sections I have synthesized the main conclusions of my work with respect to the research objectives posed in Section 1.4. The work I conducted within the scope of this thesis has improved the understanding of small-scale physical processes and feedbacks which affect how ice-rich permafrost landscapes evolve under a warming climate. Moreover, I have demonstrated that thermokarst processes substantially contribute to the overall amounts of permafrost degradation in response to warming, and I have contributed to the development of novel modelling approaches to represent these subgrid-scale processes in large-scale climate models.

To conclude my thesis, I would like to recommend possible directions of future research, for which the work presented in this thesis constitutes a solid basis. One logical next step of research would be, to adapt the tile-based modelling approach to reflect also permafrost degradation pathways and associated landforms observed in ice-rich uplands. These include, for example, the development of thermo-erosional gullies and retrogressive thaw slumps, which have in common that mass-wasting processes are a key driver of landscape change and permafrost loss. Besides the adaption to different landforms, the model set-up developed in this thesis could readily be applied to other sites in the Arctic which are characterized by ice-rich lowlands. Such efforts would allow to further evaluate the model's capacities, to improve its parameterizations, and to obtain improved projections of permafrost thaw in response to warming in those regions. Yet another direction of future research lies in the development of numerical schemes which would simulate the formation and the growth of excess ice. Such developments would allow to investigate landscape evolution pathways also under climatic conditions which favour the aggradation of permafrost, and might thus allow to assess the centennial- to millennial-scale dynamics of periglacial landscapes. These modeling capacities would not only allow an improved understanding of permafrost environments in the past, but also enhance future projections of permafrost thaw. Ultimately, the proposed modelling concept of laterally coupled landscape tiles bears a lot of potential for application in the land surface schemes of ESMs, where it might also be employed to represent subgrid-scale heterogeneities and lateral processes outside the periglacial realm.

Part II

Articles

CHAPTER 5

Pathways of ice-wedge degradation in polygonal tundra under different hydrological conditions

Nitzbon, J., Langer, M., Westermann, S., Martin, L. C. P., Aas, K. S., Boike, J.

The Cryosphere (2019), 13(4), 1089–1123. DOI: 10.5194/tc-13-1089-2019

The Cryosphere, 13, 1089–1123, 2019
https://doi.org/10.5194/tc-13-1089-2019
© Author(s) 2019. This work is distributed under
the Creative Commons Attribution 4.0 License.

The Cryosphere
Open Access
EGU

Pathways of ice-wedge degradation in polygonal tundra under different hydrological conditions

Jan Nitzbon[1,2,3], Moritz Langer[1,2], Sebastian Westermann[3], Léo Martin[3], Kjetil Schanke Aas[3], and Julia Boike[1,2]

[1]Alfred Wegener Institute, Helmholtz Centre for Polar and Marine Research, Telegrafenberg A45, 14473 Potsdam, Germany
[2]Geography Department, Humboldt-Universität zu Berlin, Unter den Linden 6, 10099 Berlin, Germany
[3]Department of Geosciences, University of Oslo, Sem Sælands vei 1, 0316 Oslo, Norway

Correspondence: Jan Nitzbon (jan.nitzbon@awi.de)

Received: 28 September 2018 – Discussion started: 7 November 2018
Revised: 27 February 2019 – Accepted: 4 March 2019 – Published: 4 April 2019

Abstract. Ice-wedge polygons are common features of lowland tundra in the continuous permafrost zone and prone to rapid degradation through melting of ground ice. There are many interrelated processes involved in ice-wedge thermokarst and it is a major challenge to quantify their influence on the stability of the permafrost underlying the landscape. In this study we used a numerical modelling approach to investigate the degradation of ice wedges with a focus on the influence of hydrological conditions. Our study area was Samoylov Island in the Lena River delta of northern Siberia, for which we had in situ measurements to evaluate the model. The tailored version of the CryoGrid 3 land surface model was capable of simulating the changing microtopography of polygonal tundra and also regarded lateral fluxes of heat, water, and snow. We demonstrated that the approach is capable of simulating ice-wedge degradation and the associated transition from a low-centred to a high-centred polygonal microtopography. The model simulations showed ice-wedge degradation under recent climatic conditions of the study area, irrespective of hydrological conditions. However, we found that wetter conditions lead to an earlier onset of degradation and cause more rapid ground subsidence. We set our findings in correspondence to observed types of ice-wedge polygons in the study area and hypothesized on remaining discrepancies between modelled and observed ice-wedge thermokarst activity. Our quantitative approach provides a valuable complement to previous, more qualitative and conceptual, descriptions of the possible pathways of ice-wedge polygon evolution. We concluded that our study is a blueprint for investigating thermokarst landforms and marks a step forward in understanding the complex interrelationships between various processes shaping ice-rich permafrost landscapes.

1 Introduction

Many landscapes in the terrestrial Arctic are changing rapidly due to the thawing of ice-rich permafrost and subsequent ground subsidence, a process referred to as thermokarst (French, 2007; Rowland et al., 2010). Thermokarst activity is apparent from various landforms including the formation of lakes, thaw slumps and thermo-erosional gullies (Kokelj and Jorgenson, 2013; Olefeldt et al., 2016). Another manifestation of thermokarst is the degradation of ice-wedge polygons, which is expressed by the formation of water-filled pits and troughs in polygonal tundra. Advanced degradation of ice wedges can lead to a transition in the surface microtopography, from low-centred polygons to high-centred polygons (French, 2007). There is evidence from across almost all of the Arctic for increasing thermokarst activity in general (Kokelj and Jorgenson, 2013) and ice-wedge degradation in particular (Liljedahl et al., 2016) over the past few decades.

Ice-rich thermokarst landscapes are estimated to cover about 20 % of the Northern Hemisphere's permafrost region but to store about half of the below-ground organic carbon of that region (Olefeldt et al., 2016). Because ice-wedge polygonal tundra is widespread in thermokarst landscapes it is of particular relevance to the local, regional, and possibly global cycling of energy, water, and carbon (Muster et al., 2012). The water and energy balances of polygonal tun-

Published by Copernicus Publications on behalf of the European Geosciences Union.

dra are characterized by small-scale spatial heterogeneities (Langer et al., 2011b), which are influenced by the microtopography of the terrain. The degradation of ice wedges and concomitant microtopographic changes could therefore significantly alter water and energy fluxes in polygonal tundra (Liljedahl et al., 2016), with implications for a range of ecosystem functions such as, for example, the decomposition of organic matter (Lara et al., 2015). However, the implications of ice-wedge degradation for land–atmosphere and land–land energy, water, and carbon fluxes remain poorly constrained.

Ice-wedge degradation has been documented through in situ measurements at, and remote-sensing observations over, a number of different Arctic areas (Jorgenson et al., 2006; Kokelj et al., 2014; Liljedahl et al., 2016; Fraser et al., 2018), and the biogeophysical processes controlling the evolution of ice-wedge polygons on different temporal scales have been described by conceptual models (Jorgenson et al., 2015; Kanevskiy et al., 2017). However, the prediction of thermokarst landscape evolution (as demanded by Rowland and Coon, 2015) requires numerical models capable of simulating the dominant processes associated with thermokarst landforms such as ice-wedge polygonal tundra (Painter et al., 2013). A variety of numerical modelling studies have addressed different aspects of a broad range of biogeophysical processes associated with the evolution of ice-wedge polygons. Cresto Aleina et al. (2013) presented a data-driven, scalable approach to assessing the hydrological connectivity of polygonal tundra and reported a non-linear hydrological control on methane fluxes. Several studies have noted the influence of microtopography and lateral fluxes on subsurface thermal and hydrological regimes, as well as on the biogeochemical processes in polygonal tundra areas (Kumar et al., 2016; Grant et al., 2017a, b; Bisht et al., 2018; Abolt et al., 2018). Liljedahl et al. (2016) investigated the hydrological implications of a transition from low-centred polygons to high-centred polygons and noted the important influence of spatially heterogeneous snow distribution. Abolt et al. (2017) investigated the ability of a hillslope diffusion approach to describe the geomorphological transition from low-centred polygons to high-centred polygons.

While all of these studies have improved our understanding of certain aspects of polygonal tundra systems, none used numerical models that could simulate the thermal and hydrological processes in polygonal tundra in combination with its dynamically changing microtopography due to melting of excess ground ice and successive ground subsidence (i.e. thermokarst formation). Furthermore, most numerical models previously used to investigate ice-wedge polygons involved two- or three-dimensional fine-scale representations of the terrain, thereby significantly limiting the spatial features (a few metres across) and temporal periods (a few years) that could be simulated.

In this paper we present a modelling approach that is able to represent the landscape dynamics of polygonal tundra, thereby taking into account transient microtopographic changes due to subsidence of ice-rich ground, as well as accounting for lateral fluxes of heat, water, and snow. Using a tiling approach to represent different parts of polygonal tundra allowed long-term (several decades) simulations on a landscape scale (several polygonal structures). We took advantage of a detailed in situ data record from a site in the Lena River delta of northern Siberia (Boike et al., 2019), which was used to provide model parameters and meteorological forcing data, as well as for comparisons between actual measurements and the simulation results. Our main objectives were

1. to demonstrate the ability of our tile-based modelling approach to simulate the process of ice-wedge degradation and the associated transition from low-centred polygons to high-centred polygons.
2. to assess the stability and the evolution of ice wedges in the study area under present-day climatic conditions but different site-specific hydrological conditions.
3. to quantify the implications of ice-wedge degradation for land–atmosphere and lateral (land-land) water and energy fluxes.

For this we performed and analysed numerical simulations, using a tailored version of the CryoGrid 3 land surface model (Westermann et al., 2016). Our investigations aimed at understanding the evolution of ice wedges in polygonal tundra in equilibrium with the recent climatic conditions, while we did not address projections of ice-wedge development in a changing future climate.

2 Methods

2.1 Study area

Our study area was Samoylov Island in the Lena River delta, northern Siberia (72.36972° N, 126.47500° E), which lies within the lowland tundra vegetation zone and is underlain by continuous permafrost. The climate on the island is Arctic continental with a mean annual air temperature (MAAT) below $-12\,°\mathrm{C}$, minimum temperatures below $-45\,°\mathrm{C}$, and maximum temperatures above $25\,°\mathrm{C}$ (Boike et al., 2013, 2019). The average annual liquid precipitation is approximately 169 mm. There is typically continuous snow cover from the end of September to the end of May, with a mean end-of-winter thickness of about 0.3 m; the remaining months are mostly snow-free. The permafrost in the Lena River delta extends to depths of between 400 and 600 m (Yershov et al., 1999) with ground temperatures (in 2006) at a depth of 27 m of about $-9\,°\mathrm{C}$ (2006) (Boike et al., 2019).

Samoylov Island belongs to the first river terrace of the Lena River delta, which was formed by fluvial erosion and sedimentation during the Holocene. The sediments in the upper soil layers have a silty to sandy texture with variable mineral (20 %–40 % by volume) and organic contents (5 %–10 % by volume) (Boike et al., 2013). Peat layers of variable thickness with higher organic contents have accumulated at the surface. These Holocene deposits are supersaturated with ice, with an average volumetric ice content of at least 60 %–70 % (Zubrzycki et al., 2013). The spatial distribution of ground ice is highly variable due to the presence of ice wedges underlying most of the island. The presence of ice wedges is expressed at the ground surface by a polygonal-patterned landscape, formed as a result of repeated frost-cracking of the ground and subsequent infiltration and freezing of water. Apart from a few large thermokarst lakes, Samoylov Island is largely covered by ice-wedge polygons whose surface features vary greatly across the island (Fig. 1). Some areas are covered with un-degraded low-centred polygons (LCPs; Fig. 1d), while initial degradation features, as described by Liljedahl et al. (2016) and Kanevskiy et al. (2017), are visible in other parts of the island (Fig. 1b). Due to advanced degradation of ice wedges, some polygons feature a reversed, high-centred relief (high-centred polygons: HCPs) and interconnected troughs that can be either dry or water-filled (Fig. 1a and c). The polygonal tundra on Samoylov Island has been previously investigated in a number of studies, with a particular focus on measuring its water and energy balances (Boike et al., 2008; Langer et al., 2011a, b; Helbig et al., 2013). Moisture levels on the island are spatially variable with a high abundance of polygonal ponds and a few larger water bodies in its central part and dryer, well-drained areas towards the margins of the island (Muster et al., 2012).

The diversity of ice-wedge polygons that evolved under identical climatic conditions on Samoylov Island makes it a highly suitable location for studying the factors affecting the evolution of polygonal tundra. The long-term monitoring of meteorological and ground conditions (Boike et al., 2013, 2019) also provides valuable in situ baseline data (see Fig. 1 for the location of long-term measurement station). These data have been used as input for permafrost models in a number of modelling studies (Westermann et al., 2016, 2017; Langer et al., 2016; Gouttevin et al., 2018), as well as for their validation.

2.2 Model description

2.2.1 Tile-based representation of polygonal tundra

The subgrid-scale heterogeneity of land surfaces (e.g. with regard to vegetation or snow cover) has previously been taken into account in LSMs using tiling approaches (Avissar and Pielke, 1989; Koster and Suarez, 1992; Aas et al., 2017). In this study we have used a similar approach to represent the spatial heterogeneity of permafrost landscapes, with each landscape tile representing a distinct part of the polygonal tundra (Fig. 2a). We subdivided the polygonal patterned landscape into three landscape units according to what we refer to as its microtopography: polygon centres (C), elevated rims (R), and a network of troughs (T) that spreads among the distinct polygonal structures (Fig. 2b). A similar partitioning of polygonal tundra has been used previously (Muster et al., 2012; Kumar et al., 2016; Grant et al., 2017a, b). Each of these landscape units constitutes a certain *areal fraction* γ of the overall landscape. We further simplified the partitioned landscape by assuming that it was made up of equally sized hexagons arranged on a regular grid (Fig. 2c). This assumption allowed us to derive topological relationships among the different landscape units, in particular lateral *distances* D and *contact lengths* L (see Appendix C for details and equations). Each of the landscape units (C, R, and T) was integrated into a single representative tile (Fig. 2d). The land-

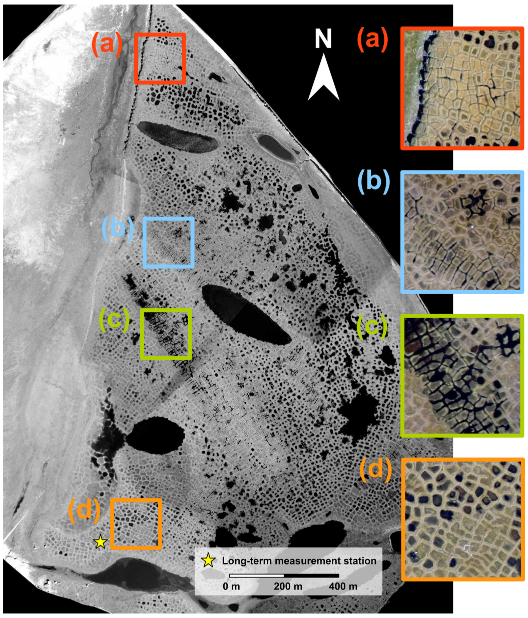

Figure 1. Aerial image of Samoylov Island with enlargements showing various types of ice-wedge polygons in different parts of the island, all of which evolved under identical climatic conditions: **(a)** high-centred polygons with drained troughs; **(b)** water-filled troughs that are indicative of initial ice-wedge degradation; **(c)** high-centred polygons with water-filled troughs; **(d)** low-centred polygons with wet or water-covered centres. The central part of the island is relatively wet and contains a large number of water bodies, while the surrounding areas are drier and in part drain into the surrounding river delta. The location of the long-term measurement station for soil and meteorological conditions described in Boike et al. (2019) is indicated by a yellow star.

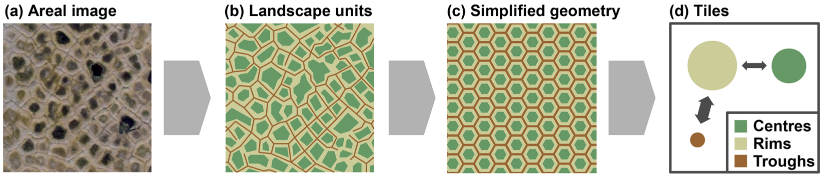

Figure 2. In our model framework the spatial heterogeneity of polygonal tundra microtopography is represented by three landscape tiles (polygon centres, C; polygon rims, R; troughs, T). The assumption of equally sized hexagons arranged on a regular grid makes it possible to quantify lateral transport processes among the tiles.

scape tiles were coupled by lateral transport processes whose magnitudes were determined by the topological relationships among the relevant tiles (Sect. 2.2.4). Note that apart from the partitioning into centres, rims, and troughs, our approach did not take into account topographic features of individual polygons. Instead, we assumed that larger areas with multiple polygons of similar topography and subject to similar hydrological conditions can be described via a single "effective" polygon composed of the three tiles.

In order to reflect microtopographic differences within the polygonal tundra landscape, each tile was associated with a particular surface altitude (a).[1] We defined three types of ice-wedge polygonal tundra based on the soil surface altitudes of the tiles. We designated the state in which the centre tile had the lowest elevation as low-centred polygonal tundra (LCP):

$$\mathrm{LCP}:\ a_{\mathrm{C}} \leq \min\left(a_{\mathrm{R}}, a_{\mathrm{T}}\right). \qquad (1)$$

Initial ice-wedge degradation is typically characterized by subsidence of the soil surface within the troughs. Those configurations in which the troughs subsided below the level of the centre but with the rims remaining elevated relative to the centre were designated intermediate-centred polygonal tundra (ICP):

$$\mathrm{ICP}:\ a_{\mathrm{T}} < a_{\mathrm{C}} < a_{\mathrm{R}}. \qquad (2)$$

Finally, configurations in which the centre tile had the highest elevation were designated high-centred polygonal tundra (HCP):

$$\mathrm{HCP}:\ a_{\mathrm{C}} \geq \max\left(a_{\mathrm{R}}, a_{\mathrm{T}}\right). \qquad (3)$$

These definitions of polygonal tundra microtopography (LCP → ICP → HCP) correspond approximately to the three stages of ice-wedge degradation qualitatively depicted by Liljedahl et al. (2016) in their Fig. 1c and to the definitions of polygon types by MacKay (2000).[2]

2.2.2 CryoGrid 3 Xice land surface model

To simulate the ground thermal regime of polygonal tundra, we used a parallelized version of the CryoGrid 3 land surface model in which each of the tiles described in Sect. 2.2.1 (C, R, and T) was assigned a one-dimensional representation of the subsurface (see Westermann et al., 2016, for a detailed description, and Nitzbon et al., 2019a, for the model source code). The numerical model simulates the temporal evolution of the ground temperature profile ($T(z)$) by solving the one-dimensional heat conduction equation, taking into account the phase change of water through an effective heat capacity:

$$\left(C(z,T)+\rho_{\mathrm{w}}L_{\mathrm{sl}}\frac{\partial\theta_{\mathrm{w}}}{\partial T}\right)\frac{\partial T}{\partial t}=\frac{\partial}{\partial z}\left(k(z,T)\frac{\partial T}{\partial z}\right), \qquad (4)$$

where θ_{w} is the volumetric water content, ρ_{w} the density of water, and L_{sl} the latent heat of fusion of water. The thermal properties of the soil cells (volumetric heat capacity $C(z,T)$ and thermal conductivity $k(z,T)$) are derived from the volumetric fractions of mineral, organic, water, ice, and air (see Westermann et al., 2013, for details). The lower boundary condition is prescribed by a constant geothermal heat flux (Q_{geo}), while the boundary condition at the surface is given by the ground heat flux (Q_{g}), which is obtained by explicitly solving the surface energy balance (SEB) equations from the meteorological forcing data. The model further simulates the build-up and ablation of the snowpack, heat conduction within the snow, and water infiltration and refreezing within the snowpack. CryoGrid 3 uses a first-order forward Euler algorithm with adaptive time step for the numerical integration of the heat conduction equation.

The unique feature of CryoGrid 3 that enables it to simulate the evolution of ice-wedge polygons is its excess ground ice scheme ("Xice"), which uses a simple parameterization for excess ice melt and the resulting ground subsidence and water body formation, based on an algorithm proposed by Lee et al. (2014). This involves each cell of the discrete one-dimensional grid that represents the subsurface in the model being assigned a "natural" porosity (ϕ_{nat}). Frozen grid cells for which the volumetric water content (θ_{w}) exceeds ϕ_{nat} are considered to contain excess ice. Once a grid cell containing excess ice thaws, the excess water ($\theta_{\mathrm{w}}-\phi_{\mathrm{nat}}$) is routed upwards while the solid soil matrix material of the cells above is routed downwards such that it occupies the natural volumetric matrix fraction $(1-\phi_{\mathrm{nat}})$. Continued thawing of excess ice cells results in a net subsidence of the soil surface and potentially in the formation of a water body at the surface, depending on the treatment of excess water.

---

[1] Throughout this paper we used the term altitude (a) when referring to the height above sea level and the term elevation (e) when referring to the height above the initial position of the centre tile (a_{C}), which serves as a reference height.

[2] Note that we excluded the case $a_{\mathrm{R}} < a_{\mathrm{C}} < a_{\mathrm{T}}$ from these definitions as it corresponds to a state that is not observed in nature.

2.2.3 Hydrology scheme for unfrozen ground

To simulate the subsurface hydrological regime of the active layer we enhanced CryoGrid 3 with a hydrology scheme for unfrozen ground conditions. We used an instantaneous infiltration scheme which assumes rapid vertical water flow compared to the rates of other processes represented in the model. This is a valid assumption for the upper soil layers of tundra wetlands, which are typically characterized by large hydraulic conductivities (Boike et al., 2008) and in which infiltration into the active layer is mainly controlled by thaw depth (Zhang et al., 2010).

Given the preconditions of a snow-free and unfrozen soil surface, the hydrology scheme simulates the change in water content (θ_{w}) of each grid cell (within the soil domain and water bodies atop the soil surface) resulting from precipitation, evapotranspiration, and infiltration (Fig. 3). Water gained from rainfall (and snowmelt) is added to the uppermost soil grid cell. Reductions in soil water content due to evaporation and transpiration are distributed down to a characteristic evaporation depth (d_{E}) and root depth (d_{T}). An infiltration algorithm is then used to take into account the changes in water content due to precipitation and evapotranspiration; this first routes water downwards to the bottom of the active layer, setting the soil water content of all grid cells at maximum to the field capacity (θ_{fc}). Potential excess water is then pooled upwards by successively saturating the grid cells, which leads to the formation of a water table within the active layer (or even above the soil surface). Note that no sensible heat is transported with the infiltrating water; i.e. the process of heat advection is not taken into account by CryoGrid 3. A quantitative description of the hydrology scheme is given in Appendix A.

We note that the employed hydrology scheme is rather simplistic compared to other schemes available (e.g. Painter et al., 2016). We confirmed, however, that the employed scheme, in combination with the lateral water transport scheme detailed in Sect. 2.2.4, was sufficiently suited to reflect the spatial heterogeneity of the subsurface hydrological regime of polygonal tundra (see Sect. 3).

2.2.4 Lateral transport of heat, water, and snow among tiles

We further enhanced CryoGrid 3 by taking into account lateral subsurface heat and water fluxes among the landscape tiles, as well as snow redistribution. Topological characteristics of and relationships among the tiles (area A, thermal distance D^{th}, hydraulic distance D^{hy}, contact length L) were used to quantify the magnitudes of the lateral fluxes.

Lateral transport of heat. The lateral heat flux between adjacent tiles is computed for each cell of the vertically discretized grid of all tiles, according to Fourier's law. The heat flux $q^{\mathrm{th}}_{\alpha,i}$ $(\mathrm{J\,s^{-1}})$ to the cell with index i of tile α from all adjacent tiles is given as

$$q^{\mathrm{th}}_{\alpha,i}=\sum_{\beta\in\mathcal{N}(\alpha)}k^{i}_{\alpha\beta}\frac{T^{i}_{\beta}-T^{i}_{\alpha}}{D^{\mathrm{th}}_{\alpha\beta}}L_{\alpha\beta}\Delta^{i}_{\alpha}\,, \tag{5}$$

where $\mathcal{N}(\alpha)$ denotes all tiles adjacent to α, $k^{i}_{\alpha\beta}$ is the effective lateral thermal conductivity (Eq. B1 in Appendix B), T^{i} refers to the temperature, and Δ^{i} refers to the height of grid cell i. The lateral heat fluxes are added after each lateral transport time step Δt_{lat} to the vertical heat fluxes resulting from heat conduction and boundary fluxes (i.e. geothermal and ground heat fluxes).

Lateral transport of water between tiles. Lateral water fluxes between adjacent tiles are calculated as bulk fluxes, based on Darcy's law. Given the precondition of a snow-free and unfrozen land surface, the lateral water flux q^{hy}_{α} $(\mathrm{m\,s^{-1}})$ to tile α from all adjacent tiles is given as

$$q^{\mathrm{hy}}_{\alpha}=\sum_{\beta\in\mathcal{N}(\alpha)}K_{\alpha\beta}\frac{w_{\beta}-\max\left(w_{\alpha},f_{\alpha}\right)}{D^{\mathrm{hy}}_{\alpha\beta}}\frac{H_{\alpha\beta}L_{\alpha\beta}}{A_{\alpha}}\,, \tag{6}$$

where $K_{\alpha\beta}$ is the saturated hydraulic conductivity between tiles α and β, w_{α} the elevation of the water table of tile α, and f_{α} the elevation of the frost table (i.e. the bottom of the active layer) of tile α. $H_{\alpha\beta}$ is the hydraulic contact height between tiles α and β, which is obtained as follows:

$$H_{\alpha\beta}=\min\left[w_{\beta}-\max\left(w_{\alpha},f_{\alpha}\right),w_{\beta}-f_{\beta}\right]. \tag{7}$$

The bulk lateral fluxes q^{hy}_{α} are applied to each tile α after each lateral transport time step Δt_{lat} using the instantaneous infiltration scheme described in Sect. 2.2.3. Note that a tile for which no water table forms above the frost table can only receive lateral water fluxes. To ensure conservation of water, lateral fluxes are proportionally reduced if insufficient water is available in those tiles that "lose" water.

Exchange of water with the surrounding terrain. The trough tile is hydrologically connected to a theoretical external "water reservoir" that has a constant water level (w_{res}).[3] This water level serves as a hydrological boundary condition between the modelled polygonal tundra and the surrounding terrain. A low water level in the external water reservoir leads to drainage of the troughs while a high water level results in their inundation. The lateral water fluxes from the reservoir

---

[3] Note that we used the symbol e_{res} when the reservoir water level is given relative to the initial altitude of the centre tile ($e_{\mathrm{res}}=w_{\mathrm{res}}-a_{\mathrm{C}}$).

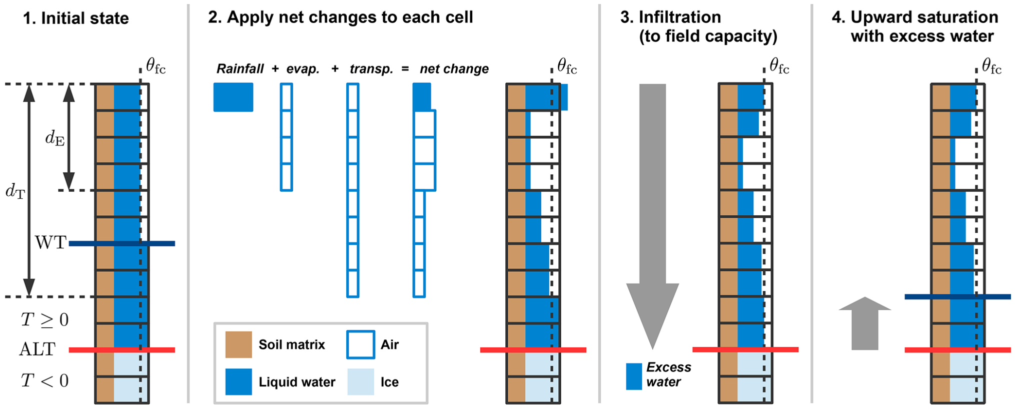
1. Initial state
2. Apply net changes to each cell
3. Infiltration (to field capacity)
4. Upward saturation with excess water
θ_{fc}
d_{E}
d_{T}
WT
$T \geq 0$
ALT
$T < 0$
Rainfall + evap. + transp. = net change
Soil matrix
Air
Liquid water
Ice
Excess water

Figure 3. Schematic illustration of the hydrology scheme for unfrozen ground conditions. The net changes due to precipitation and evapotranspiration are calculated during each time step of the model. The instantaneous infiltration routine involves downwards routing of water to the bottom of the active layer (ALT) and saturation with excess water from the bottom upwards. The water table (WT) forms above the uppermost water-saturated grid cell. Details on the hydrology scheme are given in Appendix A.

to the troughs ($q_{\mathrm{res}}^{\mathrm{hy}}$) are calculated in a similar way to those in Eq. (6), as follows:

$$q_{\mathrm{res}}^{\mathrm{hy}} = K_{\mathrm{res}} \frac{\left(w_{\mathrm{res}} - \max\left[w_{\mathrm{T}}, f_{\mathrm{T}}\right]\right)^2}{A_{\mathrm{T}}}, \qquad (8)$$

where K_{res} is the reservoir hydraulic conductivity that, compared to the saturated hydraulic conductivity K, also incorporates the topological parameters for hydraulic distance (D^{hy}) and contact length (L) between the reservoir and the trough tile.

Lateral transport of snow. Snow redistribution due to wind drift is assumed to occur among all tiles. A terrain index (I_α) that depends on the difference of the snow surface elevation (a_α) and the mean surface elevation ($\overline{a}$) is calculated and indicates whether tile α loses or gains snow due to snow redistribution. The mobile snow of the more elevated tiles is redistributed amongst the less elevated tiles while at the same time taking into account the conservation of mass, leading to a levelling out of the snow surfaces, The "snow catch" effect of vegetation is taken into account by treating only snow above a threshold height ($h_\alpha^{\mathrm{catch}}$) as "mobile" snow. Furthermore, lateral snow transport does not occur during melting conditions, i.e. if any snow cell has a positive temperature ($T^i > 0$) or contains liquid water. The governing equations of the lateral snow transport scheme are provided in Appendix B.

2.3 Model setup and simulations

2.3.1 Topology

As described in Sect. 2.2.1, we represented the spatial heterogeneity of the polygonal tundra landscape using three tiles (C, R, and T) and a theoretical, external water reservoir (denoted with subscript "res"). Figure 4 provides a schematic representation of the lateral connections among these tiles and indicates important parameters used to characterize the topology and microtopography in the model setup. Polygon centres are adjacent only to the rims, while the rims are also connected to the troughs. The troughs are hydrologically connected to the external water reservoir, which makes it possible to exchange water with the surrounding terrain (Fig. 4). We derived the topological relationships among the tiles (areas, contact lengths, and distances) based on an assumed regular hexagonal grid (see Fig. 2c). We estimated the areal fraction (γ) of the tiles (Table 1) on the basis of land cover classifications for Samoylov Island by Muster et al. (2012). The contact lengths ($L_{\alpha\beta}$), thermal distances (D^{th}), and hydraulic distances (D^{hy}) between adjacent tiles were calculated on the basis of geometric assumptions (i.e. regular hexagonal grid) and the mean size of polygons on Samoylov Island given by Muster et al. (2012) (see Fig. 4 and Appendix C for details).

2.3.2 Microtopography

The lateral fluxes of snow, water, and heat are also influenced by the microtopography of the terrain, which is reflected in the different relative elevations of the tiles. We assumed that the initial elevation of the rims (e_{R}) of intact low-centred polygons relative to the centres was 0.4 m (Boike et al., 2019) and that the troughs were initially 0.1 m lower than the polygon rims (Table 1). The water level in the external water reservoir relative to the initial altitude of the polygon centres (e_{res}) was varied among different runs. In order to take into account variability in the polygon topology and micro-

Table 1. Parameters used to specify the topology and the microtopography for the tile-based model of polygonal tundra. Note that the initial altitude of the tiles can change due to ground subsidence. Lateral distances and contact lengths are calculated from these values using the formulas in Appendix C.

Parameter	Symbol	Unit	Centre	Rim	Trough	Total	Reference
Altitude (initial)	a	m	20	20.4	20.3	–	Boike et al. (2013)
Area	A_{tot}	m^2	–	–	–	140	Muster et al. (2012)
Areal fraction	γ	–	0.3	0.6	0.1	1	Muster et al. (2012), Langer et al. (2011b)

Table 2. New parameters introduced with the hydrology scheme and the lateral transport schemes described in this paper.

Parameter	Symbol	Default value	Unit	Reference
Hydrology scheme				
Field capacity/water holding capacity	θ_{fc}	0.50	–	
Root depth	d_{T}	0.1 (R)	m	Boike et al. (2019)
		0.2 (C, T)	m	Boike et al. (2019)
Evaporation depth	d_{E}	0.1	m	
Lateral transport schemes				
Catch height snow	h^{catch}	0.1	m	Boike et al. (2019)
Saturated hydraulic conductivity	K	1×10^{-5}	$\mathrm{m\,s^{-1}}$	Boike et al. (2019)
Reservoir hydraulic conductivity	K_{res}	5×10^{-5}	$\mathrm{m\,s^{-1}}$	Boike et al. (2019)
Lateral transport time step	Δt_{lat}	0.25	day	

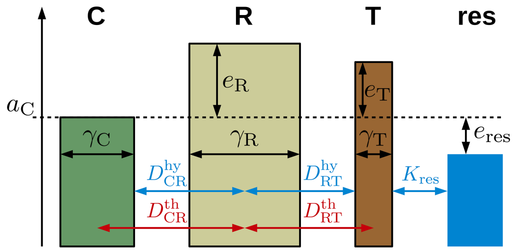

Figure 4. Setup of the coupled tiles (centres, C; rims, R; troughs, T) with parameters specifying the topology (reflected by areal fractions, γ; hydrological distances, D^{hy}; and thermal distances, D^{th}) and microtopography (reflected by elevations, e, relative to the altitude of the centre tile, a_{C}) of the polygonal tundra landscape. Each tile was assigned a one-dimensional representation of the subsurface, for which a parallelized version of the CryoGrid 3 land surface model was used. Water can also be exchanged with the surrounding terrain, which is represented by a theoretical water reservoir (res) with a fixed water level (e_{res}) and a hydraulic conductivity (K_{res}). Subscripts denote the tile(s) the parameters are relating to.

topography we conducted a sensitivity test and compared the modelled results with in situ measurements (see Sect. 3).

2.3.3 Parameters

Many of our model parameters were adopted from previous studies of the same study area that also used CryoGrid 3 (see Table D1 in Appendix D). The parameters introduced with the hydrology scheme (Sect. 2.2.3) and the lateral transport scheme (Sect. 2.2.4) are summarized in Table 2, which also includes the default values and ranges assumed in this study. We assumed a field capacity for the upper soil layers (θ_{fc}) of 0.50, which is in agreement with typical volumetric water contents in unsaturated soil layers, measured during the summer (Boike et al., 2019, Table 1). The root depth (d_{T}) was set to 0.2 m for the polygon centres and troughs, which are typically covered with mosses and sedges, and to 0.1 m for the rims, where the mosses have shallower roots. The evaporation depth (d_{E}) was set uniformly to 0.1 m for all tiles. The saturated soil hydraulic conductivity (K) among all connected tiles was set to $1 \times 10^{-5}\,\mathrm{m\,s^{-1}}$ and the reservoir hydraulic conductivity (K_{res}) was set to $5 \times 10^{-5}\,\mathrm{m\,s^{-1}}$; both values were of the same order of magnitude as the various estimates for the uppermost soil layers in the same study area (1.09–$46.3 \times 10^{-5}\,\mathrm{m\,s^{-1}}$; Boike et al., 2019). The lateral transport schemes were run in intervals of 6 h ($\Delta t_{\mathrm{lat}} = 0.25$ day). Those parameters for which no published values were available have been estimated by the authors who have long-time field experience in the study area.

2.3.4 Soil stratigraphies

The soil stratigraphies were based on the stratigraphy provided in Westermann et al. (2016) for a polygon centre on Samoylov Island. However, we modified the stratigraphies for the different tiles to reflect the spatially heterogeneous

Table 3. Overview of the soil stratigraphies used for polygon centres, rims, and troughs. Excess ice layers ($\theta_w^0 > \phi_{nat}$) are shown in bold. Depths are relative to the initial altitude (a) of the respective tile.

Depth (m)	Mineral θ_m	Organic θ_o	Nat. porosity ϕ_{nat}	Soil type	Initial water θ_w^0
Centre ($a_C = 20.0$ m)					
0–0.15	0	0.15	0.85	sand	0.85
0.15–0.30	0.20	0.05	0.75	sand	0.75
0.30–0.90	0.30	0.05	0.65	silt	0.65
0.90–9.00	**0.30**	**0.05**	**0.55**	**sand**	**0.65**
> 9.00	0.70	0	0.30	sand	0.30
Rim ($a_R = 20.4$ m)					
0–0.10	0.10	0.15	0.75	sand	0.50
0.10–0.60	0.30	0.05	0.65	silt	0.65
0.60–9.40	**0.20**	**0.05**	**0.55**	**sand**	**0.75**
> 9.40	0.70	0	0.30	sand	0.30
Trough ($a_T = 20.3$ m)					
0–0.20	0	0.15	0.85	sand	0.50
0.20–0.50	**0.20**	**0.05**	**0.55**	**sand**	**0.75**
0.50–9.30	**0.05**	**0.05**	**0.55**	**sand**	**0.90**
> 9.30	0.70	0	0.30	sand	0.30

ground ice distribution, which is linked to the surface microtopography expressed as polygon centres, rims, and troughs (see Table 3). The position of excess ground ice layers was crucial for the geomorphological dynamics simulated by the subsidence scheme. In these layers the volumetric water content exceeds the natural porosity (ϕ_{nat}), for which we assumed a conservative value of 0.55. In an idealized polygonal tundra, ice wedges are located beneath the troughs, where frost cracks occur during cold winters. We assumed that the ice wedges consisted of almost pure ice ($\theta_w^0 = 0.90$, i.e. 35 % excess ice) and that they extended from a depth of 0.5 m down to 9.3 m. An intermediate layer with less excess ice ($\theta_w^0 = 0.75$, i.e. 20 % excess ice) was placed between 0.2 and 0.5 m in depth, serving as a protective layer between the active layer and the ice wedge (see the conceptual model by Kanevskiy et al., 2017). Above these excess ice layers, the troughs were covered with an insulating organic soil layer 0.2 m thick. Since ice wedges typically extend laterally beneath the polygon rims (which is causal for their elevation above polygon centres), we assigned high excess ice contents to the rim tile over the full vertical extent of the ice wedges. We therefore placed an excess ice layer with $\theta_w^0 = 0.75$ (i.e. 20 % excess ice) between 0.6 and 9.4 m in depth. A silty mineral layer was placed above that excess ice layer, covered by an organic-rich layer 0.1 m thick. The stratigraphy for the polygon centres was chosen to be identical to that in Westermann et al. (2016), with a layer of 10 % excess ice starting at a depth of 0.9 m and extending downwards to 9.0 m. Note that the excess ice domain of all tiles ends at the same absolute depth and that this depth corresponds to the recorded depth of ice wedges on Samoylov Island. The upper organic layer of the centre tile had a thickness of 0.15 m. A bedrock layer with no organic constituents and a lower ice content of (θ_w^0) of 0.30 was assumed to extend from the bottom of the ice-rich layer down to the lower end of the model domain for all tiles (C, R, and T).

2.3.5 Forcing data

The model required meteorological data (including air temperature, humidity, pressure, wind speed, rain and snow precipitation, and incoming long-wave and short-wave radiation) to provide the atmospheric forcing at the upper boundary of the model domain. We used the same forcing dataset as Westermann et al. (2016), which covers the period from 1979 to 2014. These data are based on in situ observations from Samoylov Island for the period from 2002 to 2014 (Boike et al., 2019). Downscaled ERA-Interim reanalysis data were used to infill gaps during this period and to obtain forcing data for the period from 1979 to 2002 (see Westermann et al., 2016 for details). In order to allow long-term simulations under present-day climatic conditions, the dataset was extended to 2040 by repeated appending of the forcing data from the period between January 2000 and December 2014 to the end of the original forcing dataset. Note that due to a lack of consistent in situ data the precipitation forcing (rain and snow) was taken from the reanalysis product for the entire forcing period.

2.3.6 Simulations

An overview of the different model runs and specific parameter settings is provided in Table 4.

Validation runs. We conducted six 7-year validation runs for the period from October 2007 to December 2014, for which there is a good coverage of in situ data available. All runs were initialized with a typical temperature profile for the beginning of October, based on borehole measurements from 2006 and an extrapolation assuming a typical geothermal temperature gradient (0 m depth: 0.0 °C; 2 m: -2.0 °C; 5 m: -7.0 °C; 10 m: -9.0 °C; 25 m: -9.0 °C; 100 m: -8.0 °C; 1100 m: $+10.2$ °C). The initial soil water content of the active layer was based on the end-of-season soil moisture measured for the centre and rim profiles in 2007 (Boike et al., 2019). We allowed the state variables to adjust to the climatic conditions during an entire winter season before comparing model output with measurements. We confirmed that this spin-up period was sufficient for the near-surface processes of interest by evaluating the same period after a 10-year spin-up with the meteorological forcing of 2007, but this did not change the evaluation results significantly. We used a number of validation runs to test the model's sensitivity to variations in microtopography ($\gamma_{\mathrm{C/R/T}}$, e_{R}), snow properties (ρ_{snow}), and hydrological parameters (θ_{fc}, K) as detailed in Table 4 (VALIDATION). We then compared the results from the six validation runs with in situ measurements (see Sect. 3).

Long-term runs. To study the long-term (i.e. over multiple decades) evolution of polygonal tundra under different hydrological conditions, we conducted a number of 60-year runs for the period from October 1979 to December 2039. The soil temperatures were initialized to the same profile as used for the validation runs. The initial soil water contents were as shown in Table 3. The first 3 months (October 1979–December 1979) of the simulations were not considered in order to allow the state variables to adjust to the climatic forcing. We confirmed that this spin-up period was sufficient by running the model with a 20-year spin-up using the meteorological forcing of the 1979–1989 decade, which did not significantly change the results for the analysis period starting from 1980. The lateral topology and microtopography of the polygonal tundra were estimated based on available in situ data given and referenced in Table 1. To investigate the susceptibility of the evolution of polygonal tundra to the hydrological conditions, the elevation of the external water reservoir (e_{res}) was varied between -1.5 and $+0.5$ m (Table 4, LONGTERM-XICE), where low values correspond to drainage of the troughs and higher values to their inundation. To isolate the effects of subsidence we conducted control runs with the subsidence due to excess ice melt disabled (Table 4, LONGTERM-CONTROL). For these runs the initial LCP microtopography was static during the entire simulation period.

3 Model validation

In order to justify the tile-based representation of a permafrost landscape within our modelling framework we assessed its ability to reproduce the spatial heterogeneity in the thermal and hydrological characteristics of polygonal tundra by comparing the model results with in situ measurements from Samoylov Island.

3.1 In situ measurements

The in situ measurement data came mainly from the long-term records of the Samoylov Permafrost Observatory described in Boike et al. (2019). This dataset contains vertical soil temperature and soil moisture profiles of different microtopographic units of the polygonal tundra (one profile for centre, slope, rim, and ice wedge, respectively; see Fig. 1 for the location of the measurement polygon), as well as water table (WT) records for an adjacent polygon centre. We also used the active layer thickness (ALT) time series from the Samoylov Circumpolar Active Layer Monitoring (CALM) site which cover different microtopographic units of polygonal tundra, including polygon centres ("wet tundra", $n = 39$ measurement points) and rims ("dry tundra", $n = 80$ measurement points) (Boike et al., 2013). Most of the data cover the period from 2002 to 2017 (with a few gaps), but WT measurements are only available from 2007 to 2017. In order to evaluate the simulated spatial heterogeneity of the surface energy balance (SEB) of polygonal tundra, we took surface energy flux measurements and Bowen ratios recorded in summer 2008 on Samoylov Island by Langer et al. (2011b). These data include a separation of wet tundra and dry tundra surface energy fluxes which was based on a linear decomposition of measurements conducted in different parts of Samoylov Island with variable areal coverages of wet and dry tundra (see Langer et al., 2011b, for details). We used spatially distributed snow depth (SD) measurements obtained in spring 2008 from different parts of the polygonal tundra, including polygon rims and polygon centres (Boike et al., 2013), for comparison with the modelled spatial distribution of snow.

3.2 Comparison of model results and in situ measurements

3.2.1 Ground thermal regime

We compared the modelled and measured evolution of ALT for polygon centres and rims during all years of the validation period, i.e. from 2008 to 2014 (Fig. 5). For the polygon centres both the progression of the thaw front and the maximum ALT of all model runs lay mostly within 1 standard deviation from the mean of the measurements. During the last 4 years of the validation period (2011–2014) the ALT progression in the centres between all model runs showed a large variability and some runs simulated ALTs that were too shallow

Table 4. Overview of the configurations used for validation and long-term model runs. Each of the default parameters shown in bold has been varied during the validation runs to the value specified in the line below while the remaining parameters were kept at their default values.

Run name	Xice	Simulation period	$\gamma_C : \gamma_R : \gamma_T$ (–)	e_R (m)	ρ_{snow} ($kg\,m^{-3}$)	θ_{fc} (–)	K ($m\,s^{-1}$)	e_{res} (m)
VALIDATION (default)	off	Oct 2007–Dec 2014	**0.3 : 0.6 : 0.1**	**0.4**	**200**	**0.50**	$\mathbf{1 \times 10^{-5}}$	0.0
individual variations			0.5 : 0.4 : 0.1	0.2	250	0.40	1×10^{-6}	
LONGTERM-XICE	on	Oct 1979–Dec 2039	0.3 : 0.6 : 0.1	0.4	200	0.50	1×10^{-5}	[−1.5, …, 0.5]
LONGTERM-CONTROL	off	Oct 1979–Dec 2039	0.3 : 0.6 : 0.1	0.4	200	0.50	1×10^{-5}	[−1.5, …, 0.5]

compared to the measured values. For 2013 all model runs significantly underestimated the maximum ALT of the centres (by about 0.3 m) compared to the measured values. This can probably be attributed to too little precipitation in the forcing data, leading to an overly dry, and hence insulating, upper organic soil layer. The ALTs of the simulations with an increased areal fraction of the centres ($\gamma_C = 0.50$) and with lower-elevated rims ($e_R = 0.20$ m) were particularly shallow during the final 3 years of the validation period, highlighting the sensitivity of the thermal regime to microtopographic characteristics.

The modelled ALT progressions for polygon rims were within the range of available measurements during all years of the validation period, resulting in good agreement with respect to both the timing of thawing and the maximum ALT. The underestimation of ALT for the centres that occurred in 2013 was not observed for the rims. There was generally a very low variability among the validation runs, indicating that the modelled ALTs for the rims were less susceptible to changes in the varied parameters ($\gamma_{C/R/T}$, e_R, ρ_{snow}, θ_{fc}, K) than those simulated for the centres. This can probably be attributed to larger differences among the hydrological regimes of the centres among the different validation runs.

In addition to the ALT, we also compared modelled and measured soil temperatures within the active layer, for both polygon centres and polygon rims (see Fig. E1 in Appendix E). A detailed assessment of the model performance in terms of root-mean-squared error (RMSE), bias, and coefficient of determination (R^2) is provided in Tables F1 and F2 in Appendix F. For the default parameters, there was a slight cold bias (≥ -0.4 °C) for the simulated rim temperatures while the centre temperatures showed a slight warm bias (≤ 0.52 °C). R^2 values were in the range of 0.69 to 0.83 for the centres and between 0.79 and 0.90 for the rims, indicating an overall good reproduction of the temperature evolutions.

3.2.2 Ground hydrological regime

The hydrology scheme incorporated into CryoGrid 3 (see Sect. 2.2.3) made it possible to simulate a dynamic water table; we compared the modelling results with in situ WT measurements from a polygon on Samoylov Island (see Fig. 1 for the location of the measurement polygon). Figure 6 shows the modelled and measured WT evolution in the polygon centre during the summer months of the validation period. With the exception of 2013, the simulated WT evolutions showed a large range of about 0.1 to 0.2 m among the most extreme runs. For some years (e.g. 2011) there were runs in which the centres were water-covered throughout the entire summer while for the runs with $\gamma_C = 0.50$ and $e_R = 0.20$ m WT was mostly below the soil surface. This suggests that the simulated WT of the centres is very sensitive to the topology and microtopography of the polygonal tundra and feeds back on the simulated ALT as mentioned above. Note that for these runs the RMSE was smaller for the simulated WTs but larger for the simulated ALT of the centres (Table F1) compared to the remaining runs, indicating the complex interplay among microtopography, hydrology, and the active layer. There was a general pattern in the simulated WT evolutions that was independent of the year and the parameter setting used: WTs were high immediately after snowmelt, usually followed by a decrease over the summer months after which the WTs stabilized towards the end of summer or increased again in response to major precipitation events.

The measured WTs lay mostly within the range of the simulated WTs. During most summers the measured WTs were partly above and partly below the soil surface. In most years the measured WT evolutions revealed a similar pattern to the modelled evolutions, with high WTs after snowmelt followed by a decrease towards the end of the summer. However, the measurements showed a more pronounced intra-annual variability than the individual model runs. In contrast, the inter-annual variability appeared to be slightly greater in the model runs. The remaining mismatches between modelling results and measurements were attributed to a variety of factors including (i) site-specific characteristics of the measurement polygon, (ii) the accuracy of the precipitation forcing data used in the model, (iii) the accuracy of measured WT values, and (iv) the simplistic representation of vertical and lateral water fluxes in the model.

Apart from WT we also compared modelled and measured soil moisture levels within the active layer, for both polygon centres and polygon rims (see Fig. E2 in Appendix E). There was a good agreement between modelled and measured soil moisture levels for the mostly water-saturated centre, while

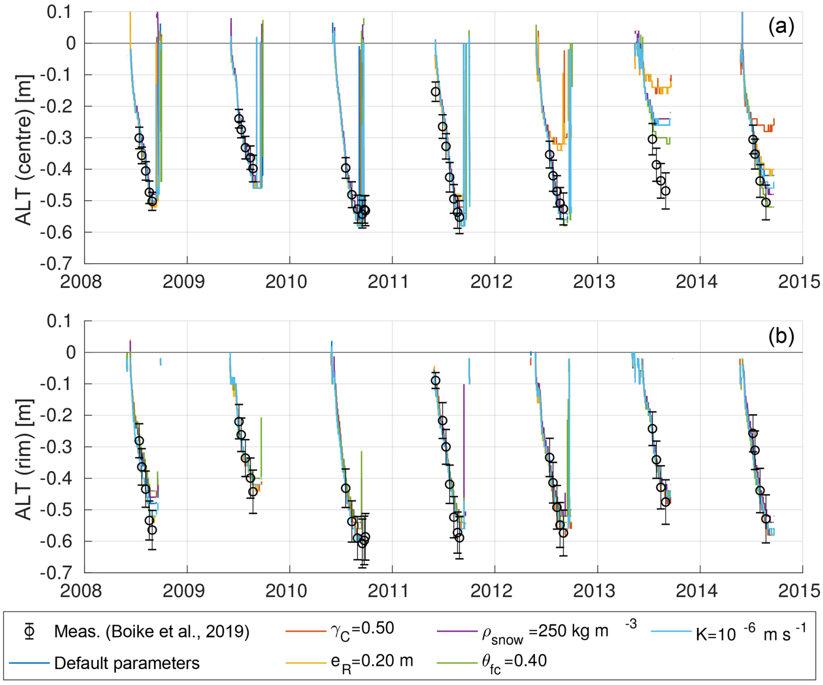

Figure 5. Modelled and measured progression of the active layer thicknesses (ALTs) of polygon centres **(a)** and rims **(b)** for the 7-year period of the validation runs. The black markers represent the means and standard deviations of categorized CALM data ($n = 39$ measurement points for centres, $n = 80$ for rims) described in Boike et al. (2019). Coloured lines correspond to the individually modelled ALTs of the six validation runs (see Table 4 VALIDATION for default parameter values.). Note that the ALTs refer to unfrozen soil, excluding water bodies, so that positive values of ALT may occur if a water body is present.

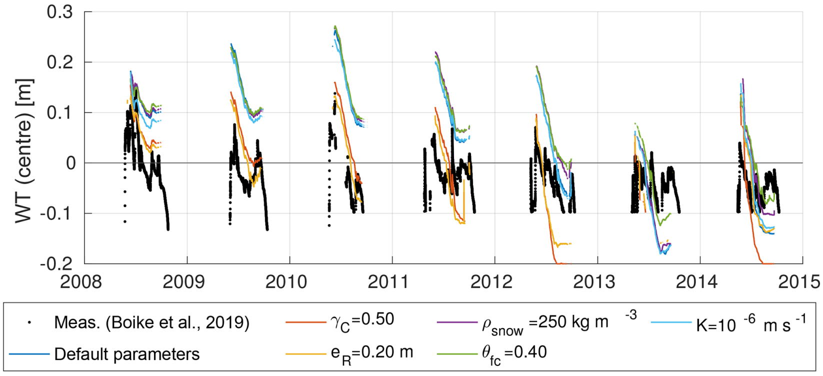

Figure 6. Modelled versus measured water tables (WTs) relative to the soil surface of a polygon centre for the 7-year period of the validation runs. The measured data are for a particular polygon centre on Samoylov Island described by Boike et al. (2019). Coloured lines correspond to the individually modelled WTs of the six validation runs (see Table 4 VALIDATION for default parameter values). Note that minimum WT measurements are limited to a level of -0.120 m until 2009 and to -0.095 m from 2010.

the model underestimated soil moisture by about 10 % close to the surface of the rim profile. The latter can be attributed to uncertainty in the parameters (e.g. θ_{fc}, Table 2) and the assumption of instantaneous infiltration.

The model performance in terms of RMSE, bias, and R^2 for the simulated ground hydrological regime, is presented in Tables F1 and F3 in Appendix F. The simulated WT had a positive bias (0.06 m) for the default parameters, while it was slightly negative-biased for the runs with $\gamma_{\mathrm{C}} = 0.50$ and $e_{\mathrm{R}} = 0.20$ m. Simulated soil moisture values showed mostly low dry-biases (≥ -0.08) and fair R^2 values ranging from 0.39 to 0.76 for the centres and from 0.57 to 0.74 for the rims.

3.2.3 Summer surface energy balance

We used eddy-covariance measurements from Samoylov Island obtained between 7 June and 30 August 2008 (Langer et al., 2011b) to assess the model's ability to reproduce the spatial heterogeneity in the SEB of polygonal tundra. We first compared measured mean surface energy fluxes[4] (net radiation Q_{net}, sensible heat flux Q_{h}, latent heat flux Q_{e}, ground heat flux Q_{g}) with the modelled area-weighted mean fluxes for the same period in the validation runs (Fig. 7, left-hand side). The variability in all SEB components among the different model runs was low and they were all close to, or within, the uncertainty range of the measured fluxes. The measured summer Bowen ratio was 0.50, which compares reasonably well with the mean modelled value of 0.64. Note that the low variability in the modelled SEB partitioning indicates that it is robust against variations in the topology and microtopography of the polygonal tundra, as well as snow properties and hydrological parameters.

We next compared the turbulent heat fluxes (Q_{h}, Q_{e}) of wet tundra estimated from field measurements with those modelled for the centre tile (Fig. 7, central part). While the modelled fluxes lay within the large uncertainty range of the fluxes measured in the field, the mean modelled summer Bowen ratio of 0.40 was larger than the measured value of 0.02. However, the SEB partitioning for the centre tile in the model was significantly distinct from the area-weighted mean SEB.

Similarly, the modelled turbulent heat fluxes for the rim tile were of comparable magnitude to the fluxes for dry tundra estimated from field measurements (Fig. 7, right-hand side). The mean summer Bowen ratio for the rims in the model runs was 0.89, while the measured value was 1.29. Like for the wet tundra described above, the model was able to reproduce a SEB partitioning for the rim tile that was distinct from the area-weighted mean SEB.

Although the spatial heterogeneity was more pronounced in the measured data than in the modelling results, the model was able to reproduce spatially heterogeneous patterns of turbulent heat fluxes while also robustly reflecting the mean summer SEB partitioning of the polygonal tundra.

3.2.4 Snow redistribution

To assess the ability of the snow redistribution scheme to reproduce actual, spatially heterogeneous SD distributions, we compared modelled and measured SDs for spring 2008 in polygon centres and rims as well as the areal mean SD (Fig. 8). The modelled areal mean SDs of the validation runs were close (≤ 0.07 m) to the measured value of 0.31 m. Modelled areal mean SDs were slightly higher for those runs with lower snow density ($\rho_{\mathrm{snow}} = 200\,\mathrm{kg\,m^{-3}}$) and agreed very well with the measured value for the run with $\rho_{\mathrm{snow}} = 250\,\mathrm{kg\,m^{-3}}$. The modelled SDs for polygon centres were consistently higher (mean of all runs: 0.60 m) than the measurements which had a mean of about 0.46 m. Similarly, the modelled SDs of the rims were on average (mean of all runs: 0.23 m) higher than the measurements (mean: 0.18 m), but were overall closer to the field data than those for the centres. The parameter variations further revealed that while the areal mean SDs are only sensitive to snow density, the spatial distribution of SDs is critically influenced by variations in the topology ($\gamma_{\mathrm{C/R/T}}$) and microtopography (e_{R}) of polygonal tundra. The comparison showed that the model was able to realistically reproduce the spatial heterogeneity in SD. Furthermore, the variability within the validation runs was similar to that found in the measurement data collected from an area that contained several polygons.

3.3 Summary

The comparison of modelled and measured ALT, WT, SEB, and SD (plus soil temperature and soil moisture in Appendix E) justified the use of a tile-based modelling approach as the measured spatial heterogeneities in (i) the subsurface thermal and hydrological regimes, (ii) the surface energy balance, and (iii) the snow distribution of polygonal tundra were well reproduced in the model validation runs. The sensitivity tests revealed that the simulated ALT and WT evolutions are robust against variations in snow and hydrological parameters (ρ_{snow}, θ_{fc}, K), while the polygon microtopography (γ_{C}, e_{R}) had a significant impact on simulated SD, WT, and ALT.

4 Results

4.1 Ice-wedge degradation under intermediate hydrological conditions ($e_{\mathrm{res}} = 0.0$ m)

The primary objective of our study was to simulate the transient process of ice-wedge degradation in a tile-based model of polygonal tundra. For this we conducted 60-year runs of our model setup with the excess ice module being enabled (see Table 4, LONGTERM-XICE). The run with an interme-

---

[4] The eddy-covariance measurement footprint was about 200 m in diameter.

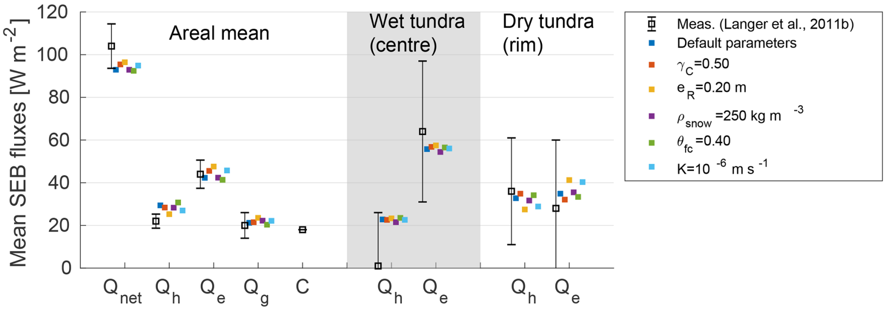

Figure 7. Modelled and measured partitioning of the mean surface energy balance (SEB) during summer 2008 (7 June–30 August). Modelled values are displayed in individual colours for each of the six validation runs (see Table 4 VALIDATION for default parameter values). The measured data are mean summer fluxes from Langer et al. (2011b) and the error bars indicate the estimated accuracies provided in that publication. The left-hand side (white background) shows the overall SEB (area-weighted mean of all tiles for the model), the central part of the figure (grey background) shows turbulent fluxes for wet tundra (centre tile for the model), and the right-hand side (white background) shows turbulent fluxes for dry tundra (rim tile for the model).

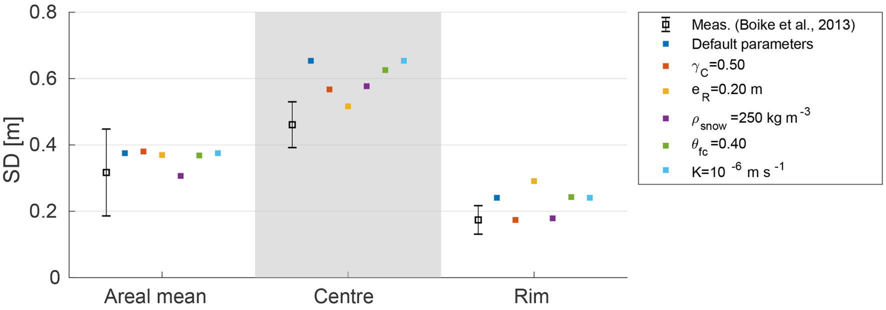

Figure 8. Modelled and measured snow depths (SDs) for polygon centres and polygon rims, together with the areal mean. The data from Boike et al. (2013) show the mean and standard deviation of spatially distributed point measurements obtained between 25 April and 2 May 2008. Modelled values correspond to SDs on 1 May 2008 and are displayed in individual colours for each of the six validation runs (see Table 4 VALIDATION for default parameter values).

diate water level in the external water reservoir (e_{res}) of 0.0 m illustrated the degradation process and the associated microtopographic changes very well (Fig. 9). The Supplement to this article contains an animated video showing the results of this simulation run.

LCP phase. During the first decade of the simulation period (1980–1990) the modelled polygonal tundra was low-centred (LCP, according to Eq. 1 above). During this period the centre tile was (over-)saturated with water, resulting in surface water of 0.05 to 0.2 m in depth. The rims were rather dry with end-of-summer WTs about 0.2–0.3 m below the surface. The absolute altitude of the modelled end-of-summer WT was almost identical for the centre (1986: $\mathrm{WT_C} = 20.20$ m) and rim tile (1986: $\mathrm{WT_R} = 20.15$ m), indicating lateral water fluxes that lead to a levelling out of the WT within the active layer between the different tiles. During the LCP phase the troughs showed a very shallow ALT of about 0.2 m in depth and their active layer was mostly dry with water tables either absent or just above the frost table. Note that during the first 9 years of the simulation period the active layer of the trough tile did not extend below the water level in the external water reservoir (20.0 m a.s.l.), so that any water in the troughs drained into the external reservoir.

Transition. During the last 5 years of the LCP phase (1986 to 1990) the troughs started to subside as soon as the active layer extended into the intermediate excess ice layer, which lay between 0.2 and 0.5 m in depth and contained 20 % excess ice (see Table 3). Concurrent with the subsidence of the ground surface the end-of-summer ALT almost doubled from 0.20 m in 1986 to 0.38 m in 1991. During these years the water saturation in the active layer beneath the troughs increased (with the WT lying above ALT) due to the addition of water from the melting of excess ice and lateral fluxes from the rims, which occur every summer as soon as the frost table of the troughs sinks below the water table of the rims. The increased amount of liquid water in the active layer beneath

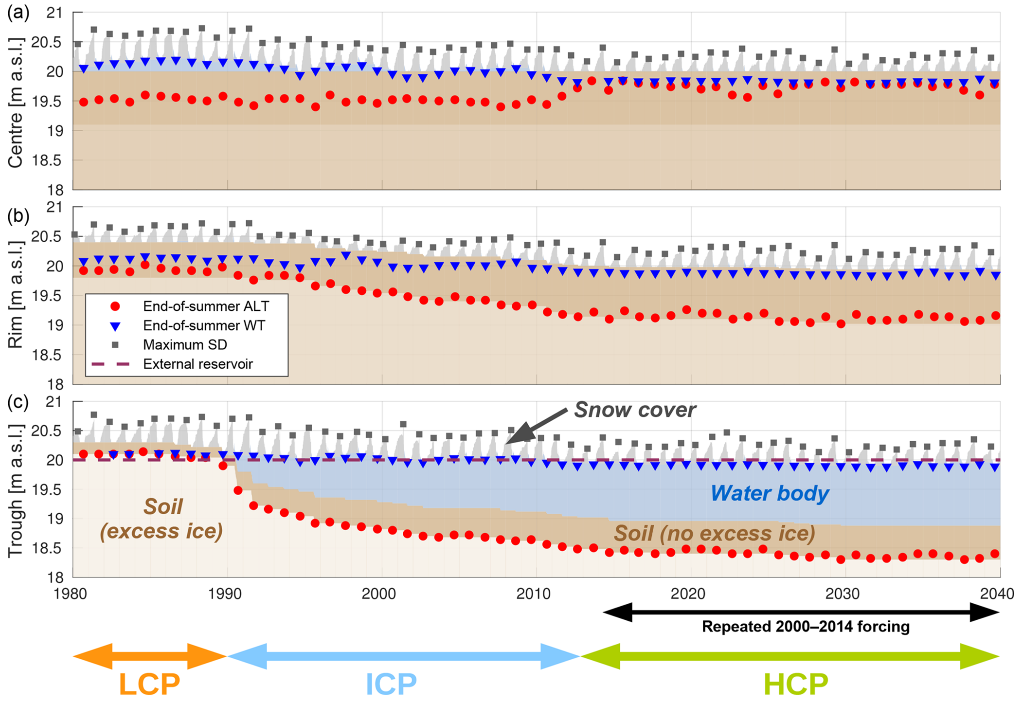

Figure 9. Evolution of the polygonal tundra tiles for the 60-year run (from 1980 to 2040) with $e_{\mathrm{res}} = 0.0\,\mathrm{m}$ (see Table 4, LONGTERM-XICE). Each panel displays the temporal evolution of the vertical extents of snow cover, water body, and soil domains (excess ice and no excess ice) for the different tiles (**a**: centre; **b**: rim; **c**: trough). For the excess ice layers, lighter colours indicate larger amounts of excess ice. The end-of-summer (maximum) active layer depth (ALT), the end-of-summer water table (WT), and the maximum snow depth (SD) are also indicated for each year. The initial low-centred polygon (LCP) phase lasted for about 11 years, followed by a transitional phase of ice-wedge degradation and ground subsidence (ICP) until the start of the high-centred polygon (HCP) phase. Note that the meteorological forcing after 2014 consisted of repeated appending of the forcing between 2000 and 2014. A condensed plot of the results is shown in Fig. 10. The Supplement to this article contains an animated video showing the results of this simulation run.

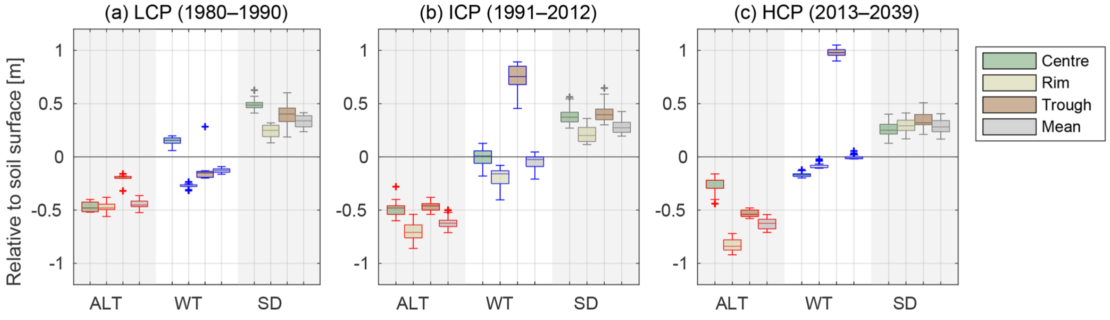

Figure 10. Box plots of the distributions of maximum ALT, WT, and SD for each tile and the area-weighted means from all years of the respective phases of the polygonal tundra, from the LCP phase **(a)**, through the ICP phase **(b)**, to the HCP phase **(c)**. The transition from LCP to HCP implies shifts in the thermal and hydrological regimes of the different landscape tiles; it also affects the snow distribution. The results are for the long-term run with $e_{\mathrm{res}} = 0.0\,\mathrm{m}$, which is also shown in Fig. 9.

the troughs increased its thermal conductivity, resulting in increased ground heat flux (with the mean summer Q_g in the trough tile increasing from about 8 W m^{-2} in 1986 to about 36 W m^{-2} in 1991) which in turn resulted in a further increase in the ALT. This positive feedback led to continued melting of excess ice and subsequent ground subsidence in the following years. In the year 1989 of the simulation the thaw front extended into the ice-rich layer representing the ice-wedge which contained 35 % of excess ice (see Table 3). The increased amount of melted excess ice pooled up in the active layer and enhanced the positive feedback described above.

ICP. During the summer of 1990 of the simulation the soil altitude of the troughs subsided below that of the centre tile, such that the polygons represented by the tiles were classified as ICPs, according to Eq. (2) above. After the first 2 years of the ICP phase (1990–1991), during which the troughs subsided very rapidly (about 0.2–0.3 m a^{-1}), the subsidence rate decreased to about 0.05–0.1 m a^{-1} in subsequent years, with a number of summers recording no ground subsidence at all. The total subsidence of the troughs between 1990 and 2012 amounted to about 1.0 m. The depth of the water body ponded in the troughs was about 1.0 m in 2012. During the ICP phase the rims also started to subside as soon as the active layer extended into the excess ice layer for the first time (extending downwards from 0.6 m in depth with 20 % excess ice; see Table 3). The subsidence continued for about 2 decades but at a lower rate than the troughs, which had a higher excess ice content. During the simulation period from 1990 to 2012 the polygon rims subsided by a total of 0.4 m, reaching the level of the centre tile, so that the modelled polygonal tundra was subsequently centred high (HCP, according to Eq. 3 above). Note that during the ICP phase the active layer of the polygon rims became wetter as the absolute altitude of the WT remained more or less constant while the soil surface subsided. The polygon centres remained mostly water-saturated during the ICP phase, with their WT sinking below the soil surface in only a few of the summers.

HCP. The HCP phase lasted from 2012 until the end of the simulation period in 2040. The subsidence rates for both rim and trough tiles were significantly lower than during the ICP phase. No ground subsidence occurred in any of the tiles during the last decade of the simulation. The water levels in all tiles also stabilized and showed less inter-annual variability. As soon as the centres became the highest part of the landscape their WT dropped to about 0.2 m below the surface. The resulting organic-rich dry upper layer had an insulating effect so that the maximum ALT of the centre tile was substantially lower during the HCP phase than during the preceding LCP and ICP phases.

All of the stages of polygonal tundra evolution defined in Sect. 2.2.1 occurred during the 60-year simulation period of the run with an intermediate water level in the external water reservoir ($e_{\mathrm{res}} = 0.0$ m): the LCP phase lasted for 10 years, from the start of the simulation in 1980 until the summer of 1990, followed by the ICP phase that lasted for 22 years (until summer 2012) and the HCP phase that continued for the remaining 27 years. The key characteristics of the different phases are summarized in Fig. 10, which shows box plots of the distributions of end-of-summer ALT, end-of-summer WT, and maximum SD for each tile, together with the area-weighted means for the entire landscape. The transition from LCP to HCP led to an increase in the maximum ALT for polygon rims and troughs but a reduced maximum ALT for the polygon centres. These changes were directly linked to the changes in WTs, which fell from above the surface of the centres during the LCP phase to below the surface during the HCP phase. For the polygon rims and troughs the WT increased such that the landscape-mean WT elevation relative to the soil surface increased slightly, indicating that the polygonal tundra was becoming wetter. The snow distribution, which was heterogeneous during the LCP phase with a high SD for centres and troughs, becomes increasingly homogeneous during the HCP phase in which the surface altitudes of the three tiles were similar.

In summary, the run with intermediate hydrological conditions ($e_{\mathrm{res}} = 0.0$ m) demonstrated that the tile-based approach to modelling a polygonal tundra landscape is able to simulate the degradation of ice wedges and the associated geomorphological transition from low-centred polygons to high-centred polygons.

4.2 Variation in the hydrological conditions

The second objective of our study was to investigate the control that hydrological conditions exert on the evolution of polygonal tundra. For this we considered the results of additional long-term runs with different water levels in the external water reservoir (e_{res}; see Table 4, LONGTERM-XICE). To contrast the results for the run with $e_{\mathrm{res}} = 0.0$ m discussed in Sect. 4.1, we analysed in detail another model run with a rather low value for e_{res} of −1.0 m, corresponding to draining hydrological conditions (Sect. 4.2.1). We also compared the evolution of the polygonal tundra in all runs with the excess ice scheme enabled, covering a broad range of hydrological conditions (Sect. 4.2.2).

4.2.1 Draining hydrological conditions ($e_{\mathrm{res}} = -1.0$ m)

The temporal evolution of the tiles is shown in Fig. 11 and the characteristics of the different phases are summarized in Fig. 12. The Supplement to this article contains an animated video showing the results of this simulation run.

LCP. The landscape evolution for this setting can be divided into two phases. During the first 3 decades of the simulation period (1980–2010) the polygonal tundra remained centred low, with the polygon centres being water-covered, the rims were stable (i.e. not subsiding) with an end-of-summer WT about 0.3 m below the surface, and the troughs

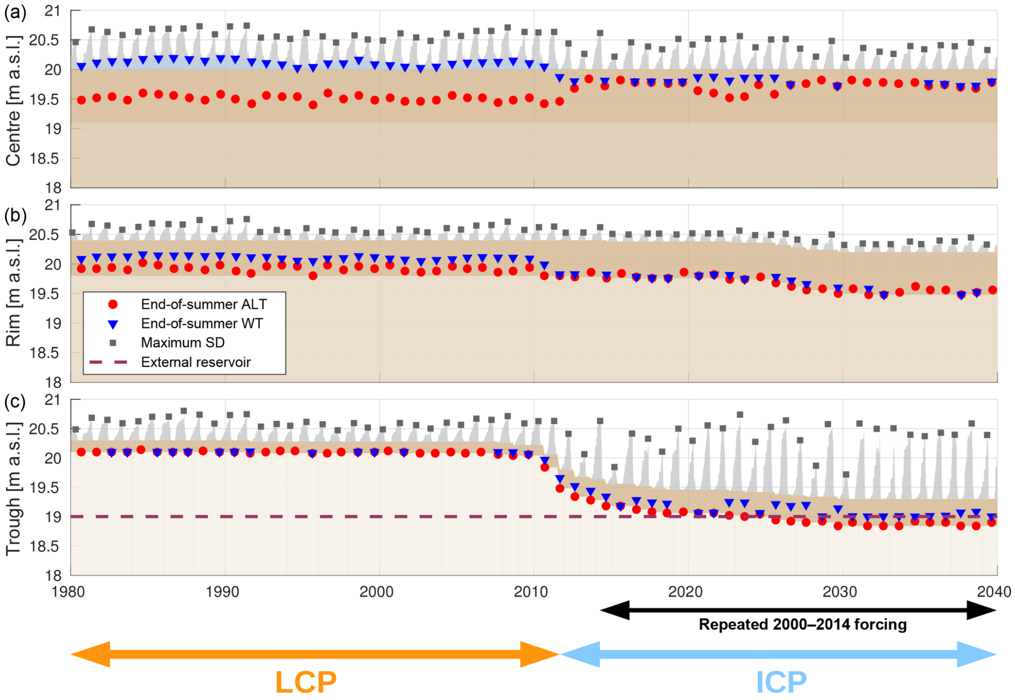

Figure 11. Evolution of the polygonal tundra tiles for the 60-year run (from 1980 to 2040) and well-drained hydrological conditions ($e_{\mathrm{res}} = -1.0\,\mathrm{m}$). Ice-wedge degradation started about 2 decades later than in the run with a water level in the external reservoir ($e_{\mathrm{res}} = 0.0\,\mathrm{m}$ – Fig. 9), ultimately leading to an overall lowering of the water tables and effective drainage of the landscape. Note that the meteorological forcing after 2014 consisted of repeated appending of the forcing between 2000 and 2014. A condensed plot of the results is shown in Fig. 12. The Supplement to this article contains an animated video showing the results of this simulation run.

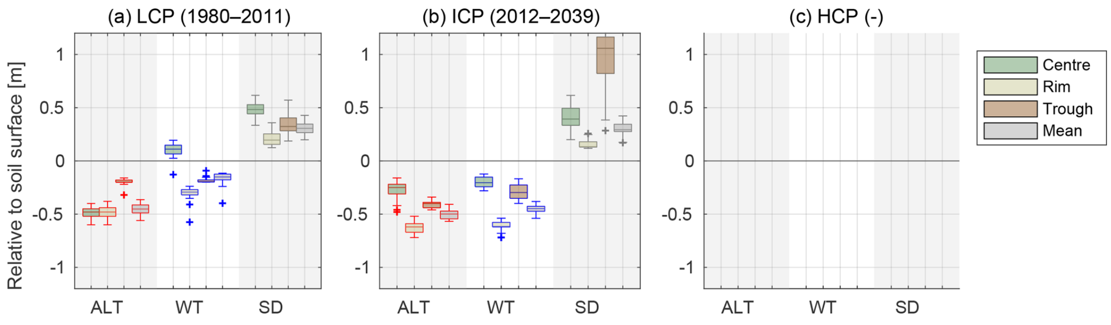

Figure 12. Box plots of the distributions of maximum ALT, WT, and SD for each tile and the area-weighted means from all years of the respective phases of polygonal tundra, from the LCP phase **(a)** to the ICP phase **(b)**. Note that the HCP phase is not attained during this run. The results are for the long-term run with $e_{\mathrm{res}} = -1.0\,\mathrm{m}$, which is also shown in Fig. 11.

were dry, draining into the external water reservoir. During this phase the troughs subsided slightly (by 0.05 to 0.1 m) due to thawing of excess ice in the intermediate excess ice layer, which extended from 0.2 to 0.5 m in depth (see Table 3). The thawing of excess ice in the trough tile accelerated towards the end of the third decade of the simulation period (between 2007 and 2010). This resulted in an increase in the amount of liquid water in the active layer of the trough tile, which was not compensated for by the runoff into the external water reservoir. A positive feedback through increasing thermal conductivities and ground heat fluxes, analogous to that described in Sect. 4.1, was thus initiated, which in turn resulted in sustained ice-wedge degradation over the next 2 decades.

ICP. The ICP phase started with subsidence of the troughs to below the level of the centre tile in summer 2011 and continued until the end of the simulation period in 2040. The positive feedback described above caused the troughs to continue subsiding despite the drainage of the trough network into the external water reservoir. The SD in the deepening troughs increased from a maximum of about 0.3 m during the LCP phase to one of about 1.0 m during the ICP phase. This resulted in increased liquid water input from snowmelt into the active layer of the troughs, thus enhancing the positive feedback through thermal conductivities and ground heat fluxes. During the ICP phase the water tables receded in both centre and rim tiles. The lower WT in the centres (WT was about 0.2 m below the surface) compared to the LCP phase (when the centres were mostly water-covered) indicated that the rims, despite their relative elevation (e_R) of 0.40 m, did not prevent the centres from being drained by lateral subsurface water fluxes. With WTs about 0.6 m below the surface, the active layer of the rim tile was also well drained during the ICP phase. While the rims subsided very little (only about 0.05 m) until year 2025 of the simulation, this was followed by a phase of accelerated excess ice melt with about 0.15 m of ground subsidence between 2025 and 2030. The landscape stabilized during the last decade of the simulation period (2030–2040), with no subsidence occurring in any of the tiles. Until the end of the 60-year run the rims remained elevated by about 0.2 m above the centres, so that the HCP phase was not attained for the run with $e_{\mathrm{res}} = -1.0$ m.

The changes in ALT, WT, and SD associated with the landscape evolution of the run with draining hydrological conditions are summarized in Fig. 12. Although the mean ALT did not change much with the transition from LCP to ICP, the spatial pattern changed substantially, with an increase in ALT for polygon rims and troughs compensated for by a marked reduction for the polygon centres. While the LCP microtopography resulted in isolated, water-saturated centres, their end-of-summer WT fell significantly during the ICP phase to about 0.2 m below the surface. The end-of-summer WT of the rims also decreased by about 0.2 m with degradation of the ice wedges. The mean water level fell from about −0.1 m relative to the soil surface to almost −0.5 m, indicating an overall drying of the landscape. The change in snow cover was most pronounced for the troughs. In the drained troughs above the degraded ice wedges up to about 1.0 m of snow accumulated during the winters of the ICP phase.

4.2.2 Comparison among all runs under different hydrological conditions

The presented results of the two model runs for (i) an intermediate water level in the external water reservoir (e_{res}) of 0.0 m (see Sect. 4.1) and (ii) a rather low external water reservoir level of −1.0 m (see Sect. 4.2.1) revealed that the hydrological conditions exerted a strong influence on the evolution of the polygonal tundra. While ice-wedge degradation occurred in both runs, the timing and the speed of this process varied among the runs, as indicated by the timing and duration of the different phases (LCP, ICP, and HCP). Ice-wedge degradation (i.e. the transition from LCP to ICP) in the wetter setting (with $e_{\mathrm{res}} = 0.0$ m) started about 2 decades earlier (in 1990) than in the dryer setting (with $e_{\mathrm{res}} = -1.0$ m), where it occurred in 2011. The excess ice melt in troughs and rims was more rapid during the wet setting (with $e_{\mathrm{res}} = 0.0$ m), in which the ICP phase lasted 22 years, compared to the dry setting (with $e_{\mathrm{res}} = -1.0$ m) in which it lasted more than 29 years.

To illustrate the dependency of ice-wedge stability on the hydrological conditions, we compared the evolution of polygonal tundra among all runs at different levels of e_{res} (see Table 4 for the parameter values and Fig. 13 for the results). Since the transition from the LCP phase to the ICP phase marks the initiation of ice-wedge degradation, its timing is indicative of the stability of the original LCP landscape. For $e_{\mathrm{res}} > 0.1$ m excess ice melt began immediately after the start of the simulations, such that the transition to the ICP phase occurred within the first 2 years. For intermediate external water reservoir levels ($e_{\mathrm{res}} = 0.1$ m and $e_{\mathrm{res}} = 0.0$ m) ice-wedge degradation started within the first decade of the simulation period. For all runs with lower water levels in the external water reservoir ($e_{\mathrm{res}} < 0.0$ m) the transition from LCP to ICP occurred after about 3 decades of simulation time in the summer of 2011.

The duration of the ICP phase, which terminates as soon as the rim tile subsides below the centre tile, can be used as an indicator of the speed of ice-wedge degradation. The ICP phase was generally shorter for those runs with inundating hydrological conditions (e.g. for $e_{\mathrm{res}} = 0.5$ m the ICP phase lasted about 15 years) than for the dryer settings (e.g. for $e_{\mathrm{res}} = -0.5$ m the ICP phase lasted more than 29 years), for which the HCP phase was not adopted until the end of the simulation period. However, for intermediate water levels in the external water reservoir ($e_{\mathrm{res}} = 0.1$ m and $e_{\mathrm{res}} = 0.0$ m) the HCP phase was reached by 2012, 1 year later than in the run with $e_{\mathrm{res}} = 0.2$ m, meaning a shorter duration for the ICP phase. This is opposite to the general trend of slower degradation with lower water levels in the external water reservoir but can probably be explained by exceptionally high

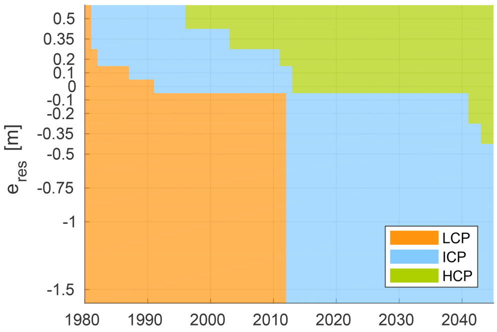

Figure 13. The phases of polygonal tundra evolution from low-centred polygons (LCP), through intermediate-centred polygons (ICP), to high-centred polygons (HCP), with respect to the hydrological condition reflected in e_{res}. Drainage (low values of e_{res}) generally stabilizes the ice wedges and slows down excess ice melt. Exceptional meteorological conditions can, however, trigger or accelerate ice-wedge degradation (e.g. between 2010 and 2012). The results are for all long-term runs with an enabled excess ice module (see Table 4, LONGTERM-XICE).

excess ice melt in the 2010–2012 period, which is about at the time that the ICP phase was reached in the runs with $e_{\mathrm{res}} \leq -0.1$ m.

Hydrological conditions that led to a drainage of the troughs were generally found to stabilize the landscape and to slow down the melting of excess ground ice. Exceptionally extreme meteorological conditions can, however, initiate or accelerate ice-wedge degradation, irrespective of the hydrological conditions.

4.3 Implications of ice-wedge degradation for water and energy fluxes

After investigating the evolution of polygonal tundra under different hydrological conditions, our third objective was to quantify the effect of ice-wedge degradation on the water and energy fluxes in polygonal tundra. We observed significant changes to both land–atmosphere fluxes (reflected by evapotranspiration) and land–land fluxes (reflected by external runoff), induced by the degradation of ice wedges and the associated changes in microtopography. While these fluxes showed a very low sensitivity to the hydrological conditions if a static LCP microtopography was assumed, ice-wedge degradation was found to increase the susceptibility of the fluxes to the hydrology, but in a non-linear fashion.

4.3.1 Evapotranspiration

To investigate the implications of ice-wedge degradation for land–atmosphere fluxes, we looked at the differences between accumulated summer (i.e. snow-free period) evapotranspiration (ET) for runs with the excess ice module enabled (LONGTERM-XICE) and with the module disabled (LONGTERM-CONTROL); in addition we varied the water level in the external water reservoir (see Table 4). Since the microtopography remained static when the excess ice module was disabled, the polygonal tundra remained in the LCP phase over the entire simulation period in all runs. For all of the runs with the excess ice module enabled, however, ice-wedge degradation was observed during the 60-year simulation period (i.e. the transition from LCP to ICP occurred; see Fig. 13). In order to exclude the influences of the meteorological forcing and isolate the effect of microtopographic changes, we compared ET during the last 10 years (2030–2039) of the runs with the excess ice module enabled with those when it was disabled (Fig. 14a).

In the control runs the ET showed no significant dependence on the hydrological conditions for low and intermediate e_{res}. For $e_{\mathrm{res}} \leq 0.1$ m the ET ranged between 125 and 150 mm, while for higher water levels in the external reservoir ($e_{\mathrm{res}} \geq 0.2$ m) the ET increased up to about 200 mm for $e_{\mathrm{res}} = 0.5$ m. Note that the relative elevation of the rims (e_{R}) was 0.4 m, so that external water levels above this level led to an entirely water-covered landscape. We observed significant changes to the ET in runs with the excess ice module enabled, with a non-linear dependence on e_{res}. For runs with low e_{res} values (≤ -0.35 m) the ET was about 10–20 mm lower than in those runs with static microtopography. For runs with high e_{res} values (≥ 0.1 m) the ET increased significantly (i.e. by more than 50 mm) to above 200 mm. For runs with intermediate e_{res} values the results showed a marked increase in the ET as the e_{res} increased.

4.3.2 Runoff

In conjunction with our investigations into the changes of land–atmosphere fluxes (as reflected in ET), we also investigated changes in the lateral (i.e. land–land) water fluxes between the model domain and its surrounding terrain. For this we looked at the accumulated summer (i.e. snow-free period) runoff (R) from the troughs to the external water reservoir. To exclude the effects of the meteorological forcing we again compared the runoff for the same simulation period (2030–2039) between runs with the excess ice module disables (LONGTERM-CONTROL) and the excess ice module enabled (LONGTERM-XICE) (Fig. 14b).

For the control runs with low and intermediate e_{res} the external runoff was mostly positive (i.e. net flux from the model domain to the external water reservoir), with mean accumulated annual fluxes on the order of 5 mm during the last 10 years of the simulation period. Only for high water levels in the external water reservoir ($e_{\mathrm{res}} \geq 0.2$ m), did R decrease to negative values (i.e. net flux from the external water reservoir to the model domain). For most e_{res} values we observed significant changes to R within the same period, if the microtopographic changes induced by ice-wedge degradation were taken into account (i.e. with enabled excess ice module). For

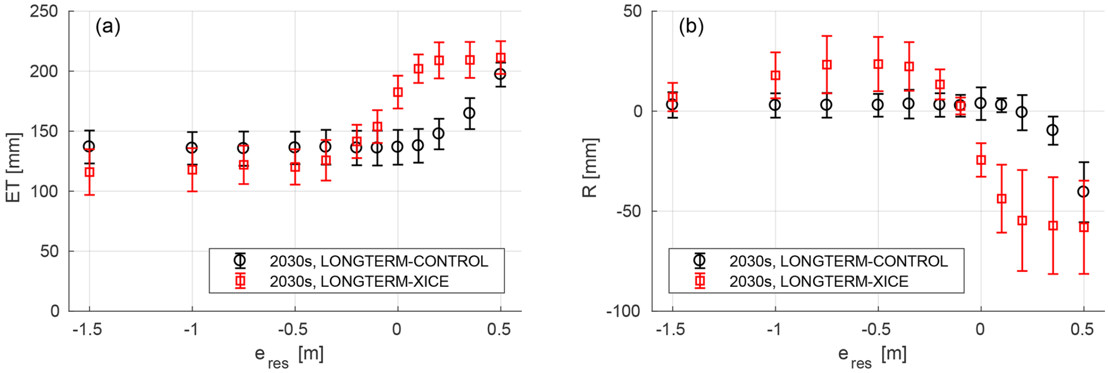

Figure 14. Changes to evapotranspiration (ET, **a**) and external runoff (R, **b**) induced by the degradation of ice wedges, for different hydrological conditions. Black markers show the means and standard deviations of the respective fluxes during the final 10 years of the simulation period (2030–2039) ignoring any ground subsidence (i.e. with disabled excess ice module). Red markers show the same for runs with enabled excess ice module, during which ice-wedge degradation occurred within the simulation period.

$-1.0\,\mathrm{m} \leq e_{\mathrm{res}} \leq -0.35\,\mathrm{m}$ there was a significant increase in R to mean annual values of about 25 mm. For high reservoir levels ($e_{\mathrm{res}} \geq 0.1$ m), however, R decreased substantially to mean values of about -50 mm if ground subsidence was enabled. There was a sharp reduction in R for intermediate values of e_{res}, yielding an overall non-linear relationship between the two quantities.

It is noteworthy that for $e_{\mathrm{res}} = -1.5$ m R increased only slightly to about 10 mm if the excess ice module was enabled, while the increase in runoff was larger for higher water levels in the external reservoir (e.g. $e_{\mathrm{res}} = -0.5$ m). This could probably be attributed to the slower degradation of the ice wedges for this very low value of e_{res} (see the results in Sect. 4.2.2), resulting in higher rims during the period under consideration, which would in turn impede lateral water fluxes from the polygon centres into the troughs. Note that for most e_{res} values the absolute value of R (i.e. its modulus) was multiple times higher for the runs with the enabled excess ice module than for the runs with static microtopography. Only for $e_{\mathrm{res}} = -0.1$ m did R not change significantly when ground subsidence was taken into account.

5 Discussion

5.1 Ice-wedge degradation as a transient phase in the evolution of polygonal tundra

There is a lack of reliable, long-term measurements of ground subsidence for the different microtopographic units of polygonal tundra in our study area, which makes quantitative comparisons with the modelled landscape evolution unfeasible. However, Boike et al. (2019) reported recent (2013 to 2017) subsidence rates on Samoylov Island to be on the order of $0.04\,\mathrm{m\,a^{-1}}$ for polygon rims and $< 0.01\,\mathrm{m\,a^{-1}}$ for polygon centres. These figures are in agreement with the modelled subsidence characteristics, with rates of about $0.02\,\mathrm{m\,a^{-1}}$ for the rim tiles and no subsidence for the centre tiles (see Figs. 9 and 11). While the modelled ground subsidence seems to be reasonable, the available measurements did not allow for a quantitative comparison of the degradation rates of ice wedges underneath the troughs. The long-term (60-year) runs with variable hydrological conditions demonstrated, however, that our model framework is able to reflect the process of ice-wedge degradation and the associated changes to the microtopography of polygonal tundra as described in other studies (e.g. Liljedahl et al., 2016) in a qualitatively realistic way.

During the initial years of the two extensively discussed modelling runs (see Sect. 4.1 and 4.2.1), the low-centred polygonal tundra prevailed with similar characteristics among the runs regarding the active layer thickness (ALT), water tables (WTs), and snow depth (SD) (see LCP phase in Figs. 10 and 12). The timing of the initiation of ice-wedge degradation, i.e. the time at which the active layer in the trough tile extended down to the ice-rich layer representing the ice wedge (see Table 3), was found to depend on the hydrological conditions (reflected in e_{res}), with higher water levels in the external water reservoir leading to an earlier onset of degradation and lower water levels (i.e. drainage conditions) having a stabilizing effect (see Fig. 13). This suggests that ice-wedge degradation is triggered by the hydrological regime in the troughs above the ice wedges, which results from a combination of the hydrological conditions (i.e. the hydrological “forcing”) and the meteorological forcing of the relevant year. As suggested by Kanevskiy et al. (2017), ice-wedge degradation may therefore be initiated by extreme meteorological conditions in certain years, such as major precipitation events or high air temperatures, which would result in exceptionally large ALTs. This is supported by our finding that the intermediate-centred polygon (ICP) phase started in the same year in all runs with $e_{\text{res}} \leq 0.1$ m (see Fig. 13). Our results suggest that those parts of the polygonal tundra that are well-drained are less susceptible to ice-wedge degradation than wetter parts, irrespective of any meteorological forcing, and that the rate of excess ice melt is lower under dryer conditions. It should be noted that – apart from the hydrological conditions reflected in e_{res} – other parameters of the model, including snow properties, the soil stratigraphy, and the depth and amount of excess ice, are likely to affect the timing of the onset of ice-wedge degradation.

Once the degradation process was initiated, the simulations showed continuing degradation and ground subsidence of the troughs in subsequent years. This rapid degradation was observed to be independent of the hydrological conditions and to continue for 2 or 3 decades, until a new equilibrium state was reached. We suspect that this process is driven by a positive feedback loop, with meltwater resulting from the melting of excess ice being routed upwards and thus increasing the thermal conductivity within the active layer; this would increase the ground heat flux, which would in turn result in an increased ALT, leading to further melting of excess ice. The feedback would be slowed down as the solid soil material stored in the excess ice layers accumulates to a soil layer without excess ice and a new "equilibrium ALT" is established. The presence of ponded water within the troughs for the run with intermediate hydrological conditions ($e_{\text{res}} = 0.0$ m; Fig. 9) would not inhibit this process because of the efficient temperature mixing that occurs during summer and the insulating effect of the water body during freeze-back. Since rapid subsidence of the troughs was also observed for draining hydrological conditions ($e_{\text{res}} = -1.0$ m; Fig. 11), this appears to indicate that the drainage of water from the troughs into the external reservoir is not sufficient to break this feedback loop. Indeed, the lower part of the active layer beneath the troughs was found to be saturated during the ICP phase, even under draining conditions (see Fig. 11, years 2010 to 2020). This fact may relate to increased snow accumulation in the deepening troughs as a result of lateral transport from the polygon centres and rims, leading to increased amounts of meltwater in the active layer beneath the troughs during spring.

With the establishment of a new equilibrium ALT beneath the troughs and rims, the landscape dynamics reached a new equilibrium state with characteristics that were strongly controlled by the hydrological conditions, in contrast to the initial LCP phase. For the run with $e_{\text{res}} = 0.0$ m a HCP landscape was established with water-filled troughs, water-saturated rims, and relatively dry centres, corresponding to an "inversion" of the hydrological regime during the LCP phase. If the melting of excess ground ice were to continue – for example, induced by a warming climate – this could possibly lead to the development of a thermokarst lake on longer (multi-decadal to centennial) timescales; this was, however, not observed within the 60-year simulation period. For the run with $e_{\text{res}} = -1.0$ m the polygonal landscape stabilized in the ICP phase, with well-drained active layers in all landscape tiles.

The evolution of the polygonal tundra with the phases described above is conceptually depicted in Fig. 15, which has been adapted from Jorgenson et al. (2015). We have demonstrated in this study that the presented model framework can be used to simulate the evolution from un-degraded ice wedges (with overlying LCP microtopography), through a phase with initial degradation features (overlying ICP microtopography), to either advanced degraded ice wedges (with overlying inundated HCP microtopography) or interrupted degradation (with overlying drained ICP microtopography). However, it is not yet possible to take into account the feedbacks that lead to long-term (multi-decadal to centennial) stabilization and potential aggradation of ice wedges previously reported by Kanevskiy et al. (2017). The processes involved in these negative feedbacks include the establishment of insulating aquatic vegetation within water-filled troughs and the deposition of laterally transported organic and mineral material above the ice wedges. The development of thermokarst lakes within the model framework is in theory possible (Westermann et al., 2016; Langer et al., 2016) but would require extended simulation periods and appropriate meteorological forcing. We note that while Jorgenson et al. (2015) and Kanevskiy et al. (2017) developed a qualitative, conceptual model for the evolution of ice wedges, our model framework allows a quantitative assessment of the processes and feedbacks involved. It is thus also suitable for the prediction of the future evolution of ice wedges, which is, however, beyond the scope of this study.

5.2 Present-day state of polygonal tundra on Samoylov Island

The ice-wedge polygonal tundra on Samoylov Island is characterized by a large spatial variability, with different types of polygons (low-centred, high-centred) and different moisture levels (drained, inundated). The presence of both water-filled and drained troughs (see Fig. 1a and c) is indicative of former ice-wedge thermokarst activity. Our model results have improved our understanding of the concurrence of degradation features with un-degraded ice wedges under the same climatic conditions, by linking it to the spatial variability in site-specific hydrological conditions.

The initial LCP phase, with wet or water-covered centres, was associated with the un-degraded LCP microtopography, which is abundant on the island – particularly in its southern and eastern parts (see Fig. 1d). Degradation features such as disconnected, water-filled troughs are apparent locally in the central part of the island (see Fig. 1b). These features are reminiscent of the ICP phase of the run with intermediate hydrological conditions ($e_{\text{res}} = 0.0$ m; Fig. 9), during which the ice wedge melted and the overlying soil layers

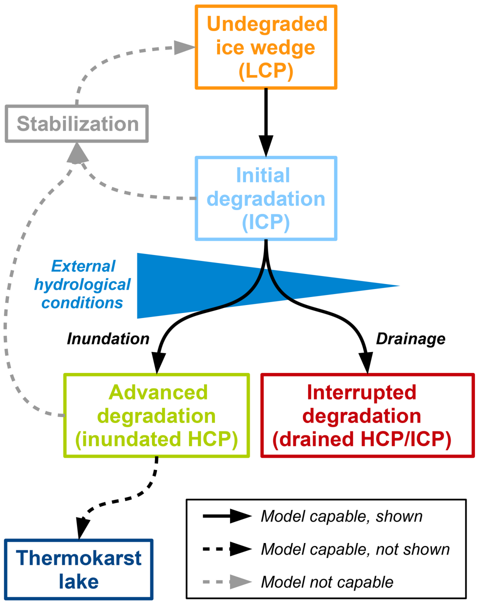
Undegraded ice wedge (LCP)
Stabilization
Initial degradation (ICP)
External hydrological conditions
Inundation
Drainage
Advanced degradation (inundated HCP)
Interrupted degradation (drained HCP/ICP)
Thermokarst lake
Model capable, shown
Model capable, not shown
Model not capable

Figure 15. Pathways of polygonal tundra landscape evolution, adapted from Jorgenson et al. (2015). While the presented model framework is able to reflect the transition from low-centred polygon terrain to high-centred polygon terrain for various hydrological conditions, it is not able to take into account the long-term stabilization and aggradation of ice wedges.

subsided. Continued ice-wedge degradation in this model run led to collapse of the rims to levels below those of the centres and inundation of the entire landscape during the HCP phase. This is reminiscent of the advanced degradation features shown in Fig. 1c. This part of the island currently appears to be very wet and if melting of excess ice continues (as would be particularly likely under a warming climate) then further collapse may occur, leading to the formation of a thermokarst lake. Lastly, drained troughs with LCP and ICP microtopography are present in the northern part of the island (see Fig. 1a). These features correspond to the final equilibrium state that is attained in the well-drained run with $e_{\mathrm{res}} = -1.0\,\mathrm{m}$ (Fig. 11), indicating that ice-wedge degradation may have occurred in this part of the island either concurrently with or prior to a drainage of the polygonal tundra through the trough network. While Liljedahl et al. (2016) describe this drained ICP–HCP state as representing the final phase of polygonal tundra evolution, in our simulations it is only attained in the runs with draining hydrological conditions. Our numerical modelling results thus correspond well with the conceptual models by Jorgenson et al. (2015) and Kanevskiy et al. (2017), which suggest a number of pathways of ice-wedge evolution that are sometimes cyclic, in contrast to the one-directional evolution suggested by Liljedahl et al. (2016).

In summary, by making a time-by-space substitution and considering different site-specific hydrological conditions in different parts of the island, our modelling runs have revealed the potential to reproduce a number of observed features of polygonal tundra of Samoylov Island by varying only a single parameter that is reflecting the hydrological conditions in the surroundings of the model domain (e_{res}).

In the past few decades, ice-wedge thermokarst has only been locally recorded on Samoylov Island, and at only a moderate rate compared to other sites in the Arctic (Liljedahl et al., 2016). Our modelling results, however, showed rapid ice-wedge degradation under recent climatic forcing for all tested hydrological conditions. This apparent discrepancy may have a number of possible explanations.

- First, ice wedges on Samoylov Island may have already passed through the rather short transitional phase from the initial LCP state to a new equilibrium state in those parts of the island that were particularly susceptible to ice-wedge degradation in the past. In this case no ice-wedge thermokarst activity would be visible in these parts of the island at present (see the final decade of the model run shown in Fig. 9).
- Second, ice wedges in some parts of Samoylov Island may still be stable because no initial perturbation of sufficient strength has occurred within the recent past (e.g. due to extreme weather events).
- Third, Liljedahl et al. (2016) detected ice-wedge thermokarst by comparing aerial image time series, which mainly relied on widening of the troughs. The deepening of troughs beneath a water body and the subsidence of rims are, however, not directly detectable using this method.
- Fourth, another possible explanation for the discrepancy is the presence of protective intermediate layers between the active layer and the ice wedges, as described by Kanevskiy et al. (2017). Although we assumed such a layer in the soil stratigraphy for the trough tiles (see Table 3), it may in reality extend to greater depths, which would lead to a temporal retardation in thermokarst activity.
- Finally, as well as the uncertainty regarding the effect of a protective layer, there are also other processes that can have a stabilizing effect on ice wedges which our current model version does not take into account. These include the formation of ground ice and ice-wedge growth, the insulating effects of aquatic vegetation that develops in troughs, and the deposition of organic and mineral material above the ice wedges, e.g. due to lateral erosion of soil from the rims (see Abolt et al., 2017, for a modelling approach). The importance of taking

> into account these stabilizing feedbacks in any long-term numerical modelling that aims to predict the future evolution of polygonal tundra needs to be stressed.

In summary, our modelling results can explain the spatial heterogeneity in the polygonal tundra on Samoylov Island under present-day climatic conditions by relating it to variability in site-specific hydrological conditions. The apparent discrepancy between the ice-wedge degradation simulated by model runs and the low levels of thermokarst activity reported by Liljedahl et al. (2016) can be ascribed to a combination of insufficient in situ monitoring of ice-wedge thermokarst and an incomplete representation of relevant biogeophysical processes in the model.

5.3 Possible implications of ice-wedge degradation for ecosystem functions

The presented model framework makes it possible to quantify changes in the subsurface thermal and hydrological conditions of polygonal tundra in response to the degradation of ice wedges and consequent changes in the microtopography. That these changes can be substantial and are strongly dependent on the hydrological conditions is emphasized by the changes in land–atmosphere and land–land water fluxes (see Fig. 14). The modelling results have shown that the degradation of ice wedges increases the susceptibility of polygonal tundra to the hydrology of the surrounding terrain. While the elevated rims in the LCP microtopography serve as natural barriers to lateral water fluxes into or out of the polygon centres, ice-wedge degradation leads to subsidence of the rims and thus improved (i.e. occurring earlier in the summer) lateral water flux pathways between polygon centres and the network of troughs.

The increase in total water fluxes (as exemplified by evapotranspiration and runoff) associated with ice-wedge degradation can be interpreted as resulting from an intensification of the water cycling in polygonal tundra, which holds true irrespective of the hydrological conditions. On a larger scale, such changes in a landscape's water and energy fluxes could induce regional feedbacks to the atmosphere (for example, changes in evapotranspiration affecting cloud formation and hence incoming radiation) and thus ultimately lead to changes in the atmospheric forcing variables that in turn drive the subsurface dynamics (Göckede et al., 2017).

Although our modelling results do not allow us to draw any conclusions regarding the large-scale implications of ice-wedge degradation, any changes in the subsurface thermal and hydrological regimes of polygonal tundra could result in associated changes to biogeochemical cycling within the active layer, mainly through their control on the decomposition of soil organic carbon (Elberling et al., 2013; Knoblauch et al., 2018; Cresto Aleina et al., 2013; Lara et al., 2015; Grant et al., 2017a). The impacts of global warming on the terrestrial hydrology and ecosystems in the Arctic (e.g. the question of whether ground conditions in certain regions will become dryer or wetter) remain unclear (AMAP, 2017). Our results suggest that permafrost degradation is characterized by small-scale spatial heterogeneity that may be amplified by increases in thermokarst formation. This makes robust predictions of, for example, the permafrost–carbon feedback even more difficult.

Our modelling results support the hypothesis that small-scale changes in the microtopography of ice-rich permafrost landscapes may induce larger-scale feedbacks to the regional ecosystem by altering the water, energy, and carbon fluxes, both within the terrestrial domain and across the surface–atmosphere interface. Since these small-scale features are not taken into account by the one-dimensional land surface schemes used in climate models, their projections of the future state of permafrost could be biased. Inclusion of small-scale heterogeneity and lateral fluxes in the land surface components of Earth system models (ESMs) is therefore highly desirable for any future model developments. The companion paper by Aas et al. (2019) presents a concrete step in this direction.

5.4 Advantages over related numerical models of ice-wedge polygonal tundra

A number of numerical modelling approaches have highlighted the important influence exerted by microtopography and small-scale spatial variability in polygonal tundra on different biogeophysical and biogeochemical processes. The studies by Liljedahl et al. (2016), Bisht et al. (2018), and Abolt et al. (2018) have all identified the influence of spatially heterogeneous snow distributions on subsurface thermal and hydrological regimes and runoff. Kumar et al. (2016), Grant et al. (2017b), and Bisht et al. (2018) also pointed out the crucial influence of lateral subsurface water fluxes on the subsurface thermal state and active layer thickness. Our model complements and enhances these approaches as it allows investigations to be made into all of the processes and feedbacks mentioned above and is also able to include dynamical topography through its excess ice module (Westermann et al., 2016).

All the above-mentioned investigations have in common that their respective numerical models use two- or three-dimensional spatial domains for subsurface representations. The targeted accuracy of reflecting actual field topographies, however, comes at a large computational cost that renders long-term (multi-decadal) simulations unfeasible. Techniques to reduce the spatial dimension of numerical permafrost models are therefore now being developed (Langer et al., 2016; Jan et al., 2018; Aas et al., 2019). The tiling approach of laterally coupled, one-dimensional subsurface representations, which was used in this study, is a trade-off between an accurate reflection of spatial heterogeneity on the one hand (see Sect. 3) and long-term simulations (covering decades or centuries) on the other hand (see Sect. 4). Our approach is furthermore promising with regard to the upscaling small-scale processes for inclusion in LSMs, as demonstrated in the companion study by Aas et al. (2019). Because of its independence of lateral scale, the tiling concept is easily transferable to other, in particular larger, landforms, without increasing the computational demands. It could therefore be used to investigate other thermokarst landforms such as lakes (see Langer et al., 2016), retrogressive thaw slumps, or thermo-erosional valleys, without increasing the computational costs.

Another aspect that distinguishes the model framework presented in this paper from the above-mentioned approaches is the dynamic simulation of changes in microtopography due to excess ice melt, which is not possible in static terrain representations such as those used in other permafrost models (e.g. Kumar et al., 2016; Bisht et al., 2018; Abolt et al., 2018). Previous modelling studies have taken into account different polygonal tundra microtopographies (e.g. low-centred and high-centred polygons) by using separate model runs for different topographies. Our approach, however, allows us to investigate the dynamic landscape transition from low-centred polygons to high-centred polygons and the associated transient and asymptotic subsurface thermal and hydrological dynamics. Our results support the findings by Lee et al. (2014) regarding the importance of taking into account excess ground ice in future predictions for permafrost regions. We acknowledge, however, that our model does not take into account other geomorphological processes, such as lateral erosion or sedimentation, in the way that landscape evolution models are able to do (e.g. Coulthard, 2001).

Although the most relevant thermal and hydrological processes, as well as some geomorphological processes, can be taken into account in the CryoGrid 3 model, because it is a purely physical model it does not include any parameterization for soil biogeochemistry (such as, for example, in Grant et al., 2017a) or a dynamic vegetation component such as is included in most LSMs used for large-scale assessments of permafrost regions (e.g. Schaphoff et al., 2013; Chadburn et al., 2015). In reality, the change in the subsurface hydrological regimes resulting from ice-wedge degradation (e.g. the drying of polygon centres; Fig. 9), would also imply an adaption of the vegetation (Wolter et al., 2016). This in turn would affect the surface energy balance through changes to the evapotranspiration in a non-trivial way. The development of aquatic vegetation which is also not represented would have an isolating and thus stabilizing effect on ice wedges (Kanevskiy et al., 2017).

The model setup used in this study makes idealized assumptions on the hydrological connectivity and the hydrological boundary conditions of the polygonal tundra. The connectivity of inter-polygonal troughs which we assumed to be given throughout the simulations might in reality only develop with advancing degradation of ice wedges. The assumption of a static external reservoir proved to be useful for comparing contrasting hydrological conditions but is an idealization which neglects the hydrological dynamics of the surrounding terrain. However, if specific study cases (opposed to our idealized test cases) would require the above-mentioned processes to be taken into account, these could readily be implemented within the CryoGrid 3 model framework.

5.4.1 Comparison with the companion paper by Aas et al. (2019)

While our study focused on improving our understanding of the processes controlling the evolution of polygonal tundra, a companion paper by Aas et al. (2019) addressed how such small-scale processes could be incorporated into land surface models (LSMs) that can be used for online simulations as part of an ESM. Our findings complement those of by Aas et al. (2019), who used a similar tiling approach within the Noah-MP LSM (Niu et al., 2011). They applied their modelling approach to polygonal tundra in the continuous permafrost zone of northern Siberia as well as to peat plateaus in the sporadic permafrost zone of northern Norway. Although the modelling approach of that study has much in common with the approach used in our study (e.g. the tiling concept, the excess ice scheme, and the lateral flux schemes), there are considerable differences between the employed modelling tools, resulting in different, but complementary, objectives of the two papers.

CryoGrid 3 is a rather simple LSM that is dedicated to permafrost applications and offers a large flexibility, allowing the design of specific model experiments like the three-tile representation of polygonal tundra, coupled to an external water reservoir. Our study using CryoGrid 3 hence focused on an improved quantitative understanding of physical permafrost processes on small spatial scales. Our model setup could be easily transferred to other, in particular ice-rich, permafrost landscapes like, for example, peat plateaus in the sporadic permafrost zone.

Noah-MP, however, is a more sophisticated LSM designed to be used on larger spatial scales, for example, within the scope of numerical weather prediction. The study by Aas et al. (2019) using Noah-MP hence focused on demonstrating the universality of the tiling concept for taking into account small-scale lateral processes in an efficient way by applying it to two entirely different study areas and landforms.

With respect to polygonal tundra, Aas et al. (2019) were also able to simulate the transition from low-centred polygons to high-centred polygons. In their laterally coupled simulations, however, the polygonal rims are stable under present-day climatic conditions and start to subside around 2030 in a RCP4.5 scenario for Samoylov Island. This difference can likely be attributed to different parameterizations employed in the models, e.g. of the subsurface hydrology. Despite the different timing of excess ice melt, both studies find a similar shift in the patterns of the ground hydrological regimes and surface energy fluxes of polygon centres and rims, induced by the changes in polygon microtopography.

Taken together, the two papers improved both our understanding of small-scale spatial heterogeneity in permafrost landscapes and the representation of this heterogeneity in LSMs, in a complementary way. While both studies demonstrated the capabilities of the tiling concept, they also shed light on the remaining difficulties of the implementation and the upscaling of this concept within ESMs. These last two issues comprise the spatial variability of hydrological conditions and the initial presence of different polygon types within one grid cell. Combining the tiling approach with ensembles of simulations might constitute a possibility to bridge this scaling gap.

6 Conclusions

Our main conclusions from the presented investigations are as follows.

1. A tile-based numerical modelling approach, which takes into account lateral fluxes of heat, water, and snow, is capable of accurately reflecting the spatial heterogeneities in (i) the subsurface thermal and hydrological regimes, (ii) the surface energy balance, and (iii) the snow distribution of polygonal tundra, which are observed in field measurements. In addition, it is capable of simulating the degradation of ice wedges and the associated changes in microtopography, from low-centred polygons to high-centred polygons.

2. The timing and speed of ice-wedge degradation is critically affected by the hydrological regime in the active layer beneath the polygon troughs; wetter conditions have a destabilizing effect on ice wedges and lead to a more rapid degradation than occurs in well-drained landscapes.

3. The spatial variability in the types of ice-wedge polygons observed in the study area (Samoylov Island in the Lena River delta of northern Siberia) can be linked to the spatial variability in the hydrological conditions.

4. Microtopographic changes associated with ice-wedge degradation have substantial implications for land–land and land–atmosphere water and energy fluxes and may also contribute to an intensification of the water cycle in lowland permafrost landscapes.

5. There is a two-way coupling between permafrost hydrology and surface microtopography since the hydrological conditions control permafrost degradation and the resulting ground subsidence in turn has a significant effect on the subsurface hydrological regimes.

In summary, our study provides a blueprint for modelling thermokarst landforms and thus helps to disentangle the complex interrelationships among various physical processes shaping ice-rich permafrost landscapes, in both the past and the future. Together with the companion paper by Aas et al. (2019), this work marks a significant step forward for the representation of small-scale spatial heterogeneity in permafrost landscapes within the land surface schemes of ESMs.

Code and data availability. The model source code used for the simulations in this work has been archived on Zenodo (Nitzbon et al., 2019a). The measurement data from Boike et al. (2019) used for evaluation of the model results are available from PANGAEA (Boike et al., 2018).

Appendix A: Detailed description of the hydrology scheme

The subsurface hydrology scheme introduced to CryoGrid 3 for this study is run at each simulation time step, given the preconditions for infiltration (i.e. no snow cover on unfrozen ground surface). With the introduction of this scheme the (total) volumetric water content (θ_w) of the unfrozen soil cells becomes variable, in contrast to previous versions of CryoGrid 3 in which it remained constant. The hydrology scheme computes the changes in water contents due to (i) rainfall, (ii) evapotranspiration, and (iii) infiltration.

Rainfall. The rainfall is obtained from the forcing data and is initially put into the uppermost cell (index 1) of the discretized soil grid:

$$\delta\theta^1_{\mathrm{w,P}} = \frac{p\Delta t}{\Delta^1}, \tag{A1}$$

where $\delta\theta^1_{\mathrm{w,P}}$ denotes the change in water content in the uppermost cell due to precipitation, p is the precipitation rate ($\mathrm{m\,s^{-1}}$), Δt is the time step (s), and Δ^1 is the height of the uppermost cell (m).

Evapotranspiration. The changes in soil water content resulting from evaporation and transpiration (δw^i_{ET}) are determined as part of the surface energy balance calculations. The (liquid) water available in the upper part of the soil determines the magnitude of the latent surface heat flux (Q_e), which in turn affects the soil water content near the surface.

Q_e is calculated from the individual evaporation and transpiration contributions but is limited to the potential evaporation from an unfrozen water surface (Q^*_e), which takes into account the atmospheric stability:

$$Q_\mathrm{e} = Q^*_\mathrm{e} \cdot \min\left[1, \eta_\mathrm{E} + \eta_\mathrm{T}\frac{r}{1-r}\right], \tag{A2}$$

$$Q_\mathrm{e,E} = \frac{\eta_\mathrm{E}}{\eta_\mathrm{E} + \eta_\mathrm{T}\frac{r}{1-r}} Q_\mathrm{e}, \tag{A3}$$

$$Q_\mathrm{e,T} = \frac{\eta_\mathrm{T}}{\eta_\mathrm{E} + \eta_\mathrm{T}\frac{r}{1-r}} Q_\mathrm{e}, \tag{A4}$$

where η_E and η_T denote the efficiencies of evaporation and transpiration, respectively, and $0 \leq r < 1$ is a parameter controlling the areal contributions of these processes.

Q^*_e is calculated according to Westermann et al. (2016). The maximum index of the soil cells that are subject to E and T are then calculated as follows:

$$i_\mathrm{E} = \min\left(i_\mathrm{E,max}, i_\mathrm{AL}\right), \tag{A5}$$

$$i_\mathrm{T} = \min\left(i_\mathrm{T,max}, i_\mathrm{AL}\right), \tag{A6}$$

where $i_\mathrm{E,max}$ and $i_\mathrm{T,max}$ denote the indices of the lowermost grid cells affected by evaporation and transpiration, respectively (corresponding to root depth, d_T, and evaporation depth, d_E) and i_AL denotes the index of the lowermost cell of the active layer.

With this the overall efficiencies of E and T are calculated as follows:

$$\eta_\mathrm{E} = \frac{\sum_{i=1}^{i_\mathrm{E}} \sigma^i \Delta^i}{\sum_{i=1}^{i_\mathrm{E}} \Delta^i}, \tag{A7}$$

$$\eta_\mathrm{T} = \frac{\sum_{i=1}^{i_\mathrm{T}} \sigma^i \Delta^i}{\sum_{i=1}^{i_\mathrm{T}} \Delta^i}, \tag{A8}$$

where $\sigma^i = \sigma(\theta^i_\mathrm{w})$, and

$$\sigma(\theta_\mathrm{w}) = \begin{cases} 1 & \text{if} \quad \theta_\mathrm{w} \geq \theta_\mathrm{fc} \\ 0.25\left(1 - \cos\left(\pi\frac{\theta_\mathrm{w}}{\theta_\mathrm{fc}}\right)\right)^2 & \text{if} \quad \theta_\mathrm{w} < \theta_\mathrm{fc} \end{cases} \tag{A9}$$

is a function used to determine the reduction in evaporation and transpiration with decreasing water availability. The same function (σ) is chosen for E and T, but generally different functions could be used for E and for T.

The water flux associated with Q_e is then uniformly distributed over those parts of the soil that contribute to evaporation and transpiration:

$$\delta\theta^i_{\mathrm{w,E}} = -\frac{\sigma^i}{\sum_{i=1}^{i_\mathrm{E}} \Sigma^i \Delta^i} \frac{Q_\mathrm{e,E}}{\rho_\mathrm{w} L_\mathrm{lg}}, \tag{A10}$$

$$\delta\theta^i_{\mathrm{w,T}} = -\frac{\sigma^i}{\sum_{i=1}^{i_\mathrm{T}} \Sigma^i \Delta^i} \frac{Q_\mathrm{e,T}}{\rho_\mathrm{w} L_\mathrm{lg}}, \tag{A11}$$

$$\delta\theta^i_{\mathrm{w,ET}} = \delta\theta^i_{\mathrm{w,E}} + \delta\theta^i_{\mathrm{w,T}}, \tag{A12}$$

where σ^i is determined according to Eq. (A9), and i_E and i_T denote the index of the grid cells that coincide with the evaporation depth (d_E) and the root depth (d_T), respectively.

Note that Eqs. (A2) and (A10) to (A12) are only used if the surface cell is an unfrozen soil cell. For frozen soil cells a surface resistance to evapotranspiration of $r_\mathrm{s} = 50\,\mathrm{s\,m^{-1}}$ is assumed and the water content remains unchanged. For an unfrozen water surface $r_\mathrm{s} = 0$ is used (i.e. $Q_\mathrm{e} = Q_\mathrm{e,pot}$) and the associated change in water content is applied only to the surface cell.

Infiltration. After determining the changes in water content due to rainfall ($\delta\theta^1_{\mathrm{w,P}}$) and evapotranspiration ($\delta\theta^i_{\mathrm{w,ET}}$), water is instantaneously infiltrated into the subsurface. The amount of water per cell in excess of its field capacity (θ_fc) is first moved downwards until a frozen cell or the maximum infiltration limit is reached. If there is excess water available the cells are saturated from the bottom upwards, leading to the formation of a water table above the frost table. If there is excess water present after saturating the pore space of the soil, this is either pooled above the soil surface to form a water body or removed as surface runoff depending on the model configuration.

Appendix B: Details on the lateral transport schemes

B1 Lateral transport of heat

The cell-wise effective lateral thermal conductivity ($k^i_{\alpha\beta}$) between tiles α and β is calculated from the weighted reciprocal sum of the individual thermal conductivities:

$$k^i_{\alpha\beta} = \frac{A_\alpha + A_\beta}{\frac{A_\alpha}{k^i_\alpha} + \frac{A_\beta}{k^i_\beta}} . \tag{B1}$$

B2 Lateral transport of snow

The redistribution of snow due to wind drift occurs between all tiles of the landscape, irrespective of whether or not they are adjacent. A terrain index (I_α) is first calculated for all tiles; it depends on the relative differences between the surface altitudes (a_α) at the time of snow transport:

$$\widetilde{I}_\alpha = \frac{a_\alpha - \overline{a}}{\sigma_\mathrm{a}} , \tag{B2}$$

$$I_\alpha = \frac{\widetilde{I}_\alpha}{\sum_{\{\alpha | \widetilde{I}_\alpha > 0\}} \widetilde{I}_\alpha} , \tag{B3}$$

where $\overline{a} = \sum_\alpha (a_\alpha A_\alpha) / \sum_\alpha A_\alpha$ denotes the area-weighted mean surface altitude and σ_a the area-weighted standard deviation of the surface altitudes of all tiles. Tiles with a positive terrain index ($I_\alpha > 0$) are losing snow, which is then deposited in those tiles that have a negative terrain index ($I_\alpha < 0$). Tiles with $I_\alpha = 0$ have no net change in their snow cover due to lateral transport.

After determining the terrain indices, the volume of drift snow (V^D) is accumulated from all tiles with a positive terrain index:

$$V^\mathrm{D} = \sum_{\{\alpha | I_\alpha > 0\}} \mathrm{SWE}^\mathrm{D}_\alpha A_\alpha , \tag{B4}$$

where SWE^D denotes the snow water equivalent that is mobile due to wind drift.

The drift snow is then redistributed among the receiving tiles according to their terrain indices:

$$\delta \mathrm{SWE}_\alpha = \frac{I_\alpha V^\mathrm{D}}{A_\alpha} \quad \forall\, \alpha \in \{\alpha \mid I_\alpha < 0\} . \tag{B5}$$

The snow catch effect of vegetation is taken into account by treating only that part of the snowpack above the maximum vegetation height (h^catch_α) as “mobile”. Furthermore, lateral snow transport does not occur during melting conditions, i.e. if a cell i of the snowpack has a positive temperature (i.e. $T^i > 0$) or contains liquid water.

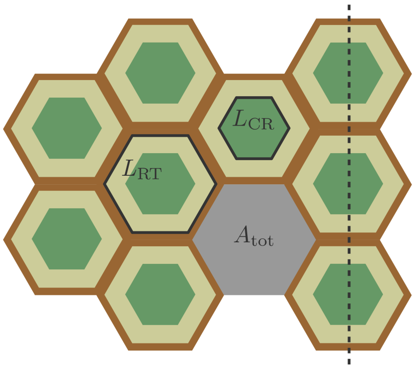

Figure C1. Simplified two-dimensional lateral geometry of the polygonal tundra assumed to calculate the contact lengths (L) between adjacent tiles.

Appendix C: Derivation of topological relationships among the landscape tiles

The topological relationships among the landscape tiles are quantified based on the assumption of a regular hexagonal structure and on estimates of the (typical) polygon size (A_tot) and the relative areal fractions of centres (γ_C), rims (γ_R), and troughs (γ_T).

The areas A_α of the tiles are given as follows:

$$A_\mathrm{C} = \gamma_\mathrm{C} A_\mathrm{tot} , \tag{C1}$$

$$A_\mathrm{R} = \gamma_\mathrm{R} A_\mathrm{tot} , \tag{C2}$$

$$A_\mathrm{T} = \gamma_\mathrm{T} A_\mathrm{tot} . \tag{C3}$$

The lateral geometry of “nested” hexagons is uniquely determined by their area (Fig. C1). The contact lengths between adjacent (L) tiles correspond to the perimeters of the respective hexagons:

$$L_\mathrm{CR} = 6 \sqrt{\frac{2}{3\sqrt{3}} A_\mathrm{C}} , \tag{C4}$$

$$L_\mathrm{RT} = 6 \sqrt{\frac{2}{3\sqrt{3}} (A_\mathrm{C} + A_\mathrm{R})} . \tag{C5}$$

The hydraulic distances (D^hy) and thermal distances (D^th) between adjacent tiles need to be specified. For this we considered a one-dimensional cross section through the hexagonal structures (see the dashed line in Figs. C1 and C2). Next we considered the smallest sequence of tiles that is repeated along this cross section (see the box in Fig. C2). We assumed this minimal sequence (which is representative for one polygon) to be of the length $\sqrt{A_\mathrm{tot}}$, and that the lengths of the tiles it consists of are proportional to their respective areal fraction (γ). For the hydraulic distances (D^hy) we took the distances among the central point of the rims and the edges

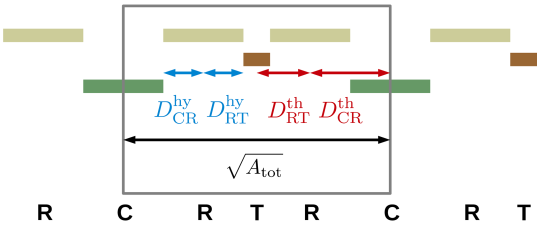
$D^{\mathrm{hy}}_{\mathrm{CR}}$
$D^{\mathrm{hy}}_{\mathrm{RT}}$
$D^{\mathrm{th}}_{\mathrm{RT}}$
$D^{\mathrm{th}}_{\mathrm{CR}}$
$\sqrt{A_{\mathrm{tot}}}$
R C R T R C R T

Figure C2. Simplified one-dimensional lateral geometry of the polygonal tundra assumed to calculate the distances (D) between adjacent tiles.

Table C1. Topological parameter values assumed for the long-term (60-year) runs in this study. The total area of a polygonal structure ($A_{\mathrm{tot}} = 140\,\mathrm{m}^2$) and the areal fractions γ_α are based on estimates for Samoylov Island given in Muster et al. (2012). All other topological parameters are calculated from these estimates using the formulas given in Appendix C.

Parameter	Symbol	Unit	Tiles (α, $\alpha\beta$)				
			C	CR	R	RT	T
Areal fraction	γ_α	–	0.3	–	0.6	–	0.1
Area	A_α	m^2	42	–	84	–	14
Contact length	$L_{\alpha\beta}$	m	–	24.1	–	41.8	–
Thermal distance	$D^{\mathrm{th}}_{\alpha\beta}$	m	–	3.5	–	2.4	–
Hydraulic distance	$D^{\mathrm{hy}}_{\alpha\beta}$	m	–	1.8	–	1.8	–

of the centres and troughs, thereby assuming a constant hydraulic pressure throughout the centres and troughs. For the thermal distances (D^{th}) we took the distances between the central points of each pair of adjacent tiles. Thus we obtained the following relationships for the lateral distances between the tiles:

$$D^{\mathrm{th}}_{\mathrm{CR}} = \left(\frac{\gamma_{\mathrm{C}}}{2} + \frac{\gamma_{\mathrm{R}}}{4}\right)\sqrt{A_{\mathrm{tot}}}, \tag{C6}$$

$$D^{\mathrm{th}}_{\mathrm{RT}} = \left(\frac{\gamma_{\mathrm{T}}}{2} + \frac{\gamma_{\mathrm{R}}}{4}\right)\sqrt{A_{\mathrm{tot}}}, \tag{C7}$$

$$D^{\mathrm{hy}}_{\mathrm{CR}} = \frac{\gamma_{\mathrm{R}}}{4}\sqrt{A_{\mathrm{tot}}}, \tag{C8}$$

$$D^{\mathrm{hy}}_{\mathrm{RT}} = \frac{\gamma_{\mathrm{R}}}{4}\sqrt{A_{\mathrm{tot}}}. \tag{C9}$$

The topological parameter values used for the long-term runs in this study are given in Table C1.

Appendix D: Parameter overview

An overview of all model parameters of the previous version of CryoGrid 3 Xice is provided in Table D1, together with the values used in the present study.

Table D1. Parameters used for CryoGrid 3 Xice. For all listed parameters we used the same values as documented in Westermann et al. (2016).

Parameter	Symbol	Default value	Unit
Surface properties			
Albedo fresh snow	$\alpha_{\mathrm{snow,max}}$	0.85	–
Albedo old snow	$\alpha_{\mathrm{snow,min}}$	0.50	–
Albedo soil	α_{soil}	0.20	–
Albedo water – unfrozen	α_{water}	0.07	–
Albedo water – frozen	α_{ice}	0.20	–
Time constant of snow albedo change - non-melting	$\tau_{\alpha,\mathrm{f}}$	0.008	day^{-1}
Time constant of snow albedo change - melting	$\tau_{\alpha,\mathrm{m}}$	0.24	day^{-1}
Emissivity snow	ϵ_{snow}	0.99	–
Emissivity soil	ϵ_{soil}	0.97	–
Emissivity water – unfrozen	$\epsilon_{\mathrm{water}}$	0.99	–
Emissivity water – frozen	ϵ_{ice}	0.98	–
Roughness length snow	$z_{0,\mathrm{snow}}$	0.0005	m
Roughness length soil	$z_{0,\mathrm{soil}}$	0.0010	m
Roughness length water – unfrozen	$z_{0,\mathrm{water}}$	0.0005	m
Roughness length water – frozen	$z_{0,\mathrm{ice}}$	0.0005	m
Resistance against evapotranspiration snow	$r_{\mathrm{s,snow}}$	0	$\mathrm{s\,m^{-1}}$
Resistance against evapotranspiration soil – frozen	$r_{\mathrm{s,frozensoil}}$	50	$\mathrm{s\,m^{-1}}$
Resistance against evapotranspiration water – frozen	$r_{\mathrm{s,ice}}$	0	$\mathrm{s\,m^{-1}}$
SW radiation extinction coefficient	β_{SW}	25	$\mathrm{m^{-1}}$
Material properties			
Density water	ρ_{w}	1000	$\mathrm{kg\,m^{-3}}$
Density ice	ρ_{i}	1000	$\mathrm{kg\,m^{-3}}$
Density air	ρ_{a}	1.293	$\mathrm{kg\,m^{-3}}$
Volumetric heat capacity water	C_{w}	4.2×10^6	$\mathrm{J\,K^{-1}m^{-3}}$
Volumetric heat capacity ice	C_{i}	1.9×10^6	$\mathrm{J\,K^{-1}m^{-3}}$
Volumetric heat capacity air	C_{a}	1.3×10^3	$\mathrm{J\,K^{-1}m^{-3}}$
Volumetric heat capacity mineral soil	C_{m}	2.0×10^6	$\mathrm{J\,K^{-1}m^{-3}}$
Volumetric heat capacity organic soil	C_{o}	2.5×10^6	$\mathrm{J\,K^{-1}m^{-3}}$
Thermal conductivity water	k_{w}	0.57	$\mathrm{W\,m^{-1}\,K^{-1}}$
Thermal conductivity ice	k_{i}	2.20	$\mathrm{W\,m^{-1}\,K^{-1}}$
Thermal conductivity air	k_{a}	0.0243	$\mathrm{W\,m^{-1}\,K^{-1}}$
Thermal conductivity mineral soil	k_{m}	3.00	$\mathrm{W\,m^{-1}\,K^{-1}}$
Thermal conductivity organic soil	k_{o}	0.25	$\mathrm{W\,m^{-1}\,K^{-1}}$
Latent heat of fusion water	L_{sl}	0.334×10^6	$\mathrm{J\,kg^{-1}}$
Latent heat of vaporization	L_{lg}	2.501×10^6	$\mathrm{J\,kg^{-1}}$
Latent heat of sublimation	L_{sg}	2.835×10^6	$\mathrm{J\,kg^{-1}}$
Natural constants			
Von Kármán constant	κ	0.4	–
Gravitational acceleration	g	9.81	$\mathrm{m\,s^{-2}}$
Pressure at sea level	p_0	100 500	Pa
Freezing point of water at normal pressure	T_{f}	273.15	K
Specific gas constant of air	R	287.058	$\mathrm{J\,K^{-1}\,kg^{-1}}$
Stefan–Boltzmann constant	σ	5.6704×10^{-8}	$\mathrm{W\,m^{-2}\,K^{-4}}$
Location-specific parameters			
Geothermal heat flux	Q_{geo}	0.05	$\mathrm{W\,m^{-2}}$

Appendix E: Modelled and measured active layer temperatures and soil water contents

E1 Soil temperatures

Figure E1 shows the modelled and measured soil temperatures (T) for a polygon centre at depths of 0.20 and 0.40 m, and for a polygon rim at depths of 0.21 and 0.38 m, during the 7-year validation period from 2008 to 2014.

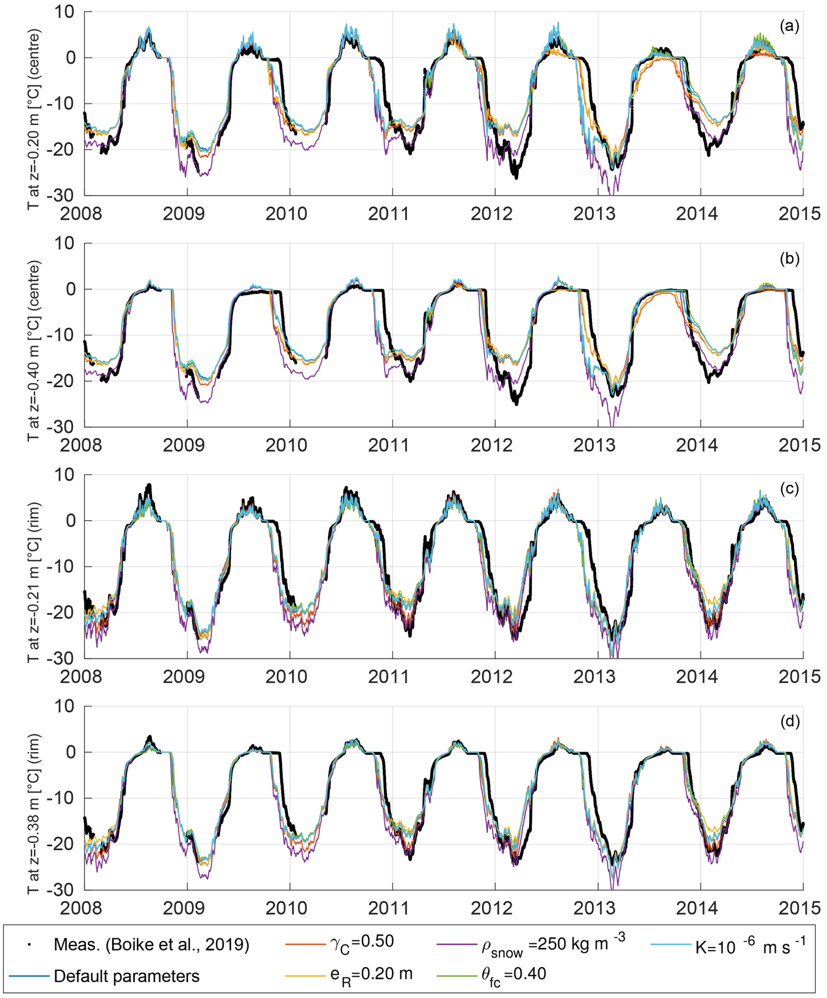

Figure E1. Modelled versus measured soil temperatures for a polygon centre at depths of 0.20 m **(a)** and 0.40 m **(b)**, and a polygon rim at depths of 0.21 m **(c)** and 0.38 m **(d)**, for 2008 to 2014. Measurement data from Boike et al. (2019). Model results are for all validation runs (see Table 4, VALIDATION).

E2 Soil moisture levels

Figure E2 shows the modelled and measured volumetric soil liquid water contents (θ_w) for a polygon centre at depths of 0.23 and 0.43 m, and for a polygon rim at depths of 0.22 and 0.37 m, during the 7-year validation period from 2008 to 2014.

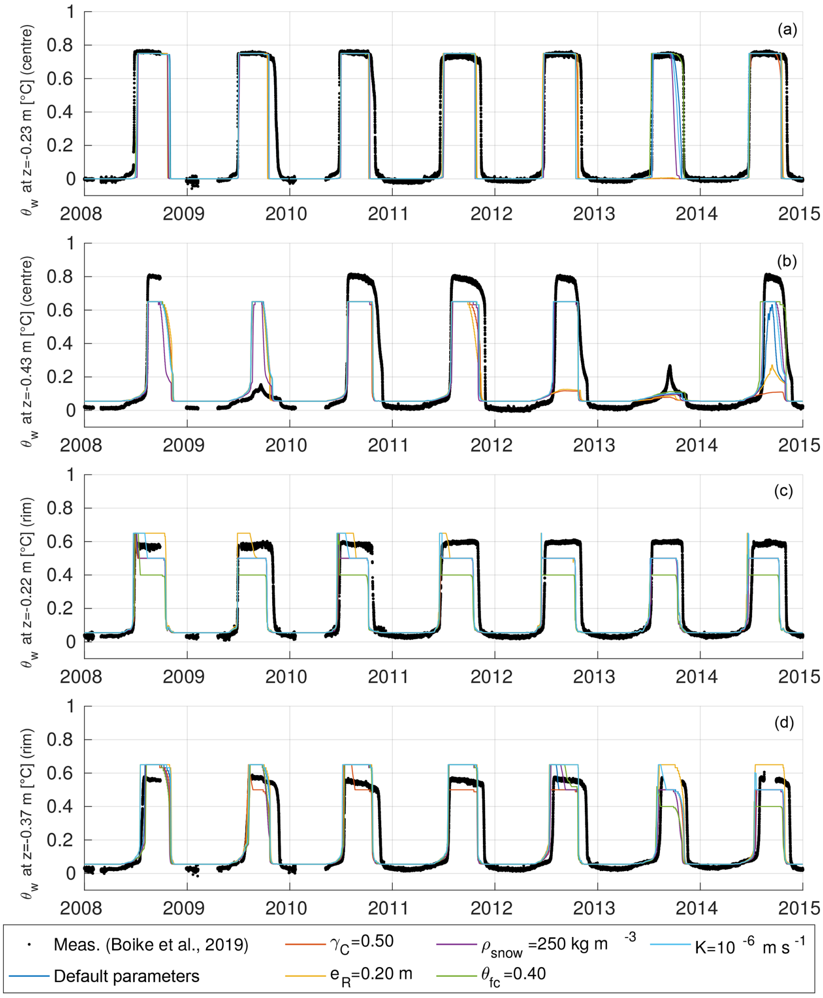

Figure E2. Modelled versus measured soil moisture levels for a polygon centre at depths of 0.23 m **(a)** and 0.43 m **(b)**, and for a rim at depths of 0.22 m **(c)** and 0.37 m **(d)**, for 2008 to 2014. Measurement data from Boike et al. (2019). Model results are for all validation runs (see Table 4, VALIDATION).

Appendix F: Model performance assessment

We assessed the ability of the model to reproduce measurements of ALT, WT, soil temperatures, and soil moisture levels by calculating the root-mean-squared error (RMSE), the model bias, and the coefficient of determination (R^2) for all validation runs. The respective scores are provided in Table F1 for ALT and WT, in Table F2 for soil temperatures, and in Table F3 for soil moisture levels.

Table F1. Model performance in terms of root-mean-squared error (RMSE) and model bias for the simulated evolutions of active layer thicknesses (ALT) and water tables (WT) displayed in Figs. 5 and 6. All scores are computed from all available measurement data during the 7-year validation period (2008–2014).

	WT (centre)		ALT (centre)		ALT (rim)	
Run	RMSE (m)	Bias (m)	RMSE (m)	Bias* (m)	RMSE (m)	Bias* (m)
Default parameters	0.11	0.06	0.067	0.028	0.036	0.004
$\gamma_{\mathrm{C}} = 0.50$	0.09	−0.02	0.126	0.079	0.038	0.004
$e_{\mathrm{R}} = 0.20\,\mathrm{m}$	0.07	−0.01	0.114	0.067	0.032	−0.003
$\rho_{\mathrm{snow}} = 250\,\mathrm{kg\,m^{-3}}$	0.12	0.08	0.072	0.045	0.043	0.026
$\theta_{\mathrm{fc}} = 0.40$	0.12	0.09	0.055	0.020	0.051	0.017
$K = 10^{-6}\,\mathrm{m\,s^{-1}}$	0.11	0.06	0.067	0.027	0.031	−0.005
Mean	0.10	0.04	0.083	0.044	0.039	0.007

* Note that ALT is defined negative, such that a positive bias corresponds to shallower thaw depths in the simulations.

Table F2. Model performance in terms of root-mean-squared error (RMSE), bias, and coefficient of determination (R^2) for the simulated soil moisture levels displayed in Fig. E1. All scores are computed from all available measurement data during the 7-year validation period (2008–2014).

	T at $z = 0.20\,\mathrm{m}$ (centre)			T at $z = 0.40\,\mathrm{m}$ (centre)			T at $z = 0.21\,\mathrm{m}$ (rim)			T at $z = 0.38\,\mathrm{m}$ (rim)		
Run	RMSE (°C)	Bias (°C)	R^2	RMSE (°C)	Bias (°C)	R^2	RMSE (°C)	Bias (°C)	R^2	RMSE (°C)	Bias (°C)	R^2
Default parameters	4.02	0.40	0.79	3.73	0.52	0.78	3.04	−0.40	0.90	3.06	−0.28	0.87
$\gamma_{\mathrm{C}} = 0.50$	3.74	−0.03	0.82	3.49	0.20	0.81	3.14	−0.65	0.89	3.18	−0.53	0.86
$e_{\mathrm{R}} = 0.20\,\mathrm{m}$	3.65	0.23	0.83	3.41	0.44	0.82	3.02	−0.06	0.90	3.03	0.04	0.87
$\rho_{\mathrm{snow}} = 250\,\mathrm{kg\,m^{-3}}$	4.84	−1.70	0.70	4.45	−1.52	0.69	3.81	−1.83	0.84	3.87	−1.72	0.79
$\theta_{\mathrm{fc}} = 0.40$	4.11	0.47	0.79	3.81	0.56	0.77	3.22	−0.49	0.89	3.16	−0.34	0.86
$K = 10^{-6}\,\mathrm{m\,s^{-1}}$	4.08	0.41	0.79	3.78	0.54	0.78	2.96	−0.32	0.90	2.99	−0.21	0.88
Mean	4.07	−0.04	0.79	3.78	0.12	0.78	3.20	−0.62	0.89	3.21	−0.51	0.86

Table F3. Model performance in terms of root-mean-squared error (RMSE), bias, and coefficient of determination (R^2) for the simulated soil moisture levels displayed in Fig. E2. All scores are computed from all available measurement data during the 7-year validation period (2008–2014).

	θ_w at $z = 0.23$ m (centre)			θ_w at $z = 0.43$ m (centre)			θ_w at $z = 0.22$ m (rim)			θ_w at $z = 0.37$ m (rim)		
Run	RMSE (–)	Bias (–)	R^2	RMSE (–)	Bias (–)	R^2	RMSE (–)	Bias (–)	R^2	RMSE (–)	Bias (–)	R^2
Default parameters	0.18	−0.05	0.75	0.17	−0.02	0.68	0.14	−0.04	0.72	0.14	0.00	0.60
$\gamma_C = 0.50$	0.24	−0.08	0.56	0.23	−0.05	0.39	0.13	−0.04	0.74	0.14	−0.02	0.62
$e_R = 0.20\,\mathrm{m}$	0.23	−0.07	0.58	0.22	−0.05	0.45	0.14	−0.02	0.69	0.15	0.02	0.57
$\rho_{\mathrm{snow}} = 250\,\mathrm{kg\,m^{-3}}$	0.20	−0.06	0.69	0.15	−0.02	0.74	0.14	−0.04	0.72	0.14	−0.01	0.60
$\theta_{\mathrm{fc}} = 0.40$	0.17	−0.04	0.76	0.15	0.00	0.73	0.17	−0.07	0.58	0.15	−0.01	0.57
$K = 10^{-6}\,\mathrm{m\,s^{-1}}$	0.19	−0.05	0.73	0.16	−0.01	0.72	0.14	−0.03	0.70	0.15	0.01	0.57
Mean	0.20	−0.06	0.68	0.18	−0.03	0.62	0.14	−0.04	0.69	0.15	0.00	0.59

Video supplement. The supplement to this article (Nitzbon et al., 2019b, c) contains two animated videos showing the results of the simulations described in Sect. 4.1 and 4.2.1.

Author contributions. JN designed the study, carried out the simulations, and wrote the paper. JN and LM implemented the model code. All authors interpreted the results and contributed to the paper. SW and JB secured the funding for the project.

Competing interests. Julia Boike and Moritz Langer are members of the editorial board of *The Cryosphere*. All other authors declare that they have no conflict of interest.

Acknowledgements. Jan Nitzbon is thankful to the POLMAR graduate school and the Geo.X Young Academy for providing a supportive framework for his PhD project. Jan Nitzbon is thankful to Tress Academic for helpful courses on scientific writing and project management. The authors gratefully acknowledge the Climate Geography Group at the Humboldt University of Berlin for providing resources on their high-performance-computer system. This work was supported by the Research Council of Norway through the PERMANOR project (no. 255331). This work was supported by the Federal Ministry of Education and Research (BMBF) of Germany through a grant to Moritz Langer (no. 01LN1709A).

The article processing charges for this open-access
publication were covered by a Research
Centre of the Helmholtz Association.

Review statement. This paper was edited by Christian Beer and reviewed by two anonymous referees.

References

Aas, K. S., Gisnås, K., Westermann, S., and Berntsen, T. K.: A Tiling Approach to Represent Subgrid Snow Variability in Coupled Land Surface–Atmosphere Models, J. Hydrometeorol., 18, 49–63, https://doi.org/10.1175/JHM-D-16-0026.1, 2017.

Aas, K. S., Martin, L., Nitzbon, J., Langer, M., Boike, J., Lee, H., Berntsen, T. K., and Westermann, S.: Thaw processes in ice-rich permafrost landscapes represented with laterally coupled tiles in a land surface model, The Cryosphere, 13, 591–609, https://doi.org/10.5194/tc-13-591-2019, 2019.

Abolt, C. J., Young, M. H., and Caldwell, T. G.: Numerical Modelling of Ice-Wedge Polygon Geomorphic Transition, Permafrost Periglac., 28, 347–355, https://doi.org/10.1002/ppp.1909, 2017.

Abolt, C. J., Young, M. H., Atchley, A. L., and Harp, D. R.: Microtopographic control on the ground thermal regime in ice wedge polygons, The Cryosphere, 12, 1957–1968, https://doi.org/10.5194/tc-12-1957-2018, 2018.

AMAP: Snow, Water, Ice and Permafrost in the Arctic (SWIPA) – 2017, Arctic Monitoring and Assessment Programme, Oslo, Norway, oCLC: 1038467657, 2017.

Avissar, R. and Pielke, R. A.: A Parameterization of Heterogeneous Land Surfaces for Atmospheric Numerical Models and Its Impact on Regional Meteorology, Mon. Weather Rev., 117, 2113–2136, https://doi.org/10.1175/1520-0493(1989)117<2113:APOHLS>2.0.CO;2, 1989.

Bisht, G., Riley, W. J., Wainwright, H. M., Dafflon, B., Yuan, F., and Romanovsky, V. E.: Impacts of microtopographic snow redistribution and lateral subsurface processes on hydrologic and thermal states in an Arctic polygonal ground ecosystem: a case study using ELM-3D v1.0, Geosci. Model Dev., 11, 61–76, https://doi.org/10.5194/gmd-11-61-2018, 2018.

Boike, J., Wille, C., and Abnizova, A.: Climatology and summer energy and water balance of polygonal tundra in the Lena River Delta, Siberia, J. Geophys. Res., 113, G03025, https://doi.org/10.1029/2007JG000540, 2008.

Boike, J., Kattenstroth, B., Abramova, K., Bornemann, N., Chetverova, A., Fedorova, I., Fröb, K., Grigoriev, M., Grüber, M., Kutzbach, L., Langer, M., Minke, M., Muster, S., Piel, K., Pfeiffer, E.-M., Stoof, G., Westermann, S., Wischnewski, K., Wille, C., and Hubberten, H.-W.: Baseline characteristics of climate, permafrost and land cover from a new permafrost observatory in the Lena River Delta, Siberia (1998–2011), Biogeosciences, 10, 2105–2128, https://doi.org/10.5194/bg-10-2105-2013, 2013.

Boike, J., Nitzbon, J., Anders, K., Grigoriev, M. N., Bolshiyanov, D. Y., Langer, M., Lange, S., Bornemann, N., Morgenstern, A., Schreiber, P., Wille, C., Chadburn, S., Gouttevin, I., and Kutzbach, L.: Measurements in soil and air at Samoylov Station (2002–2018), PANGAEA, https://doi.org/10.1594/PANGAEA.891142, 2018.

Boike, J., Nitzbon, J., Anders, K., Grigoriev, M., Bolshiyanov, D., Langer, M., Lange, S., Bornemann, N., Morgenstern, A., Schreiber, P., Wille, C., Chadburn, S., Gouttevin, I., Burke, E., and Kutzbach, L.: A 16-year record (2002–2017) of permafrost, active-layer, and meteorological conditions at the Samoylov Island Arctic permafrost research site, Lena River delta, northern Siberia: an opportunity to validate remote-sensing data and land surface, snow, and permafrost models, Earth Syst. Sci. Data, 11, 261–299, https://doi.org/10.5194/essd-11-261-2019, 2019.

Chadburn, S. E., Burke, E. J., Essery, R. L. H., Boike, J., Langer, M., Heikenfeld, M., Cox, P. M., and Friedlingstein, P.: Impact of model developments on present and future simulations of permafrost in a global land-surface model, The Cryosphere, 9, 1505–1521, https://doi.org/10.5194/tc-9-1505-2015, 2015.

Coulthard, T. J.: Landscape evolution models: a software review, Hydrol. Proc., 15, 165–173, https://doi.org/10.1002/hyp.426, 2001.

Cresto Aleina, F., Brovkin, V., Muster, S., Boike, J., Kutzbach, L., Sachs, T., and Zuyev, S.: A stochastic model for the polygonal tundra based on Poisson–Voronoi diagrams, Earth Syst. Dynam., 4, 187–198, https://doi.org/10.5194/esd-4-187-2013, 2013.

Elberling, B., Michelsen, A., Schädel, C., Schuur, E. A. G., Christiansen, H. H., Berg, L., Tamstorf, M. P., and Sigsgaard, C.: Long-term CO_2 production following permafrost thaw, Nat. Clim. Change, 3, 890–894, https://doi.org/10.1038/nclimate1955, 2013.

Fraser, R., Kokelj, S., Lantz, T., McFarlane-Winchester, M., Olthof, I., Lacelle, D., Fraser, R. H., Kokelj, S. V., Lantz, T. C., McFarlane-Winchester, M., Olthof, I., and Lacelle, D.: Climate Sensitivity of High Arctic Permafrost Terrain Demonstrated by Widespread Ice-Wedge Thermokarst on Banks Island, Remote Sensing, 10, 954, https://doi.org/10.3390/rs10060954, 2018.

French, H. M.: The periglacial environment, John Wiley and Sons, Chichester, England; Hoboken, NJ, 3rd edn., oCLC: ocm70407762, 2007.

Gouttevin, I., Langer, M., Löwe, H., Boike, J., Proksch, M., and Schneebeli, M.: Observation and modelling of snow at a polygonal tundra permafrost site: spatial variability and thermal implications, The Cryosphere, 12, 3693–3717, https://doi.org/10.5194/tc-12-3693-2018, 2018.

Grant, R. F., Mekonnen, Z. A., Riley, W. J., Arora, B., and Torn, M. S.: Mathematical Modelling of Arctic Polygonal Tundra with Ecosys: 2. Microtopography Determines How CO_2 and CH_4 Exchange Responds to Changes in Temperature and Precipitation, J. Geophys. Res.-Biogeo., 122, 3174–3187, https://doi.org/10.1002/2017JG004037, 2017a.

Grant, R. F., Mekonnen, Z. A., Riley, W. J., Wainwright, H. M., Graham, D., and Torn, M. S.: Mathematical Modelling of Arctic Polygonal Tundra with Ecosys: 1. Microtopography Determines How Active Layer Depths Respond to Changes in Temperature and Precipitation, J. Geophys. Res.-Biogeo., 122, 3161–3173, https://doi.org/10.1002/2017JG004035, 2017b.

Göckede, M., Kittler, F., Kwon, M. J., Burjack, I., Heimann, M., Kolle, O., Zimov, N., and Zimov, S.: Shifted energy fluxes, increased Bowen ratios, and reduced thaw depths linked with drainage-induced changes in permafrost ecosystem structure, The Cryosphere, 11, 2975–2996, https://doi.org/10.5194/tc-11-2975-2017, 2017.

Helbig, M., Boike, J., Langer, M., Schreiber, P., Runkle, B. R. K., and Kutzbach, L.: Spatial and seasonal variability of polygonal tundra water balance: Lena River Delta, northern Siberia (Russia), Hydrogeol. J., 21, 133–147, https://doi.org/10.1007/s10040-012-0933-4, 2013.

Jan, A., Coon, E. T., Painter, S. L., Garimella, R., and Moulton, J. D.: An intermediate-scale model for thermal hydrology in low-relief permafrost-affected landscapes, Computat. Geosci., 22, 163–177, https://doi.org/10.1007/s10596-017-9679-3, 2018.

Jorgenson, M. T., Shur, Y. L., and Pullman, E. R.: Abrupt increase in permafrost degradation in Arctic Alaska, Geophys. Res. Lett., 33, L02503, https://doi.org/10.1029/2005GL024960, 2006.

Jorgenson, M. T., Kanevskiy, M., Shur, Y., Moskalenko, N., Brown, D. R. N., Wickland, K., Striegl, R., and Koch, J.: Role of ground ice dynamics and ecological feedbacks in recent ice wedge degradation and stabilization, J. Geophys. Res.-Earth, 120, 2280–2297, https://doi.org/10.1002/2015JF003602, 2015.

Kanevskiy, M., Shur, Y., Jorgenson, T., Brown, D. R., Moskalenko, N., Brown, J., Walker, D. A., Raynolds, M. K., and Buchhorn, M.: Degradation and stabilization of ice wedges: Implications for assessing risk of thermokarst in northern Alaska, Geomorphology, 297, 20–42, https://doi.org/10.1016/j.geomorph.2017.09.001, 2017.

Knoblauch, C., Beer, C., Liebner, S., Grigoriev, M. N., and Pfeiffer, E.-M.: Methane production as key to the greenhouse gas budget of thawing permafrost, Nat. Clim. Change, 8, 309–312, https://doi.org/10.1038/s41558-018-0095-z, 2018.

Kokelj, S. V. and Jorgenson, M. T.: Advances in Thermokarst Research, Permafrost Periglac., 24, 108–119, https://doi.org/10.1002/ppp.1779, 2013.

Kokelj, S. V., Lantz, T. C., Wolfe, S. A., Kanigan, J. C., Morse, P. D., Coutts, R., Molina-Giraldo, N., and Burn, C. R.: Distribution and activity of ice wedges across the forest-tundra transition, western Arctic Canada, J. Geophys. Res.-Earth, 119, 2032–2047, https://doi.org/10.1002/2014JF003085, 2014.

Koster, R. D. and Suarez, M. J.: Modeling the land surface boundary in climate models as a composite of independent vegetation stands, J. Geophys. Res., 97, 2697–2715, https://doi.org/10.1029/91JD01696, 1992.

Kumar, J., Collier, N., Bisht, G., Mills, R. T., Thornton, P. E., Iversen, C. M., and Romanovsky, V.: Modeling the spatiotemporal variability in subsurface thermal regimes across a low-relief polygonal tundra landscape, The Cryosphere, 10, 2241–2274, https://doi.org/10.5194/tc-10-2241-2016, 2016.

Langer, M., Westermann, S., Muster, S., Piel, K., and Boike, J.: The surface energy balance of a polygonal tundra site in northern Siberia – Part 2: Winter, The Cryosphere, 5, 509–524, https://doi.org/10.5194/tc-5-509-2011, 2011a.

Langer, M., Westermann, S., Muster, S., Piel, K., and Boike, J.: The surface energy balance of a polygonal tundra site in northern Siberia – Part 1: Spring to fall, The Cryosphere, 5, 151–171, https://doi.org/10.5194/tc-5-151-2011, 2011b.

Langer, M., Westermann, S., Boike, J., Kirillin, G., Grosse, G., Peng, S., and Krinner, G.: Rapid degradation of permafrost underneath waterbodies in tundra landscapes – Toward a representation of thermokarst in land surface models, J. Geophys. Res.-Earth, 121, 2446–2470, https://doi.org/10.1002/2016JF003956, 2016.

Lara, M. J., McGuire, A. D., Euskirchen, E. S., Tweedie, C. E., Hinkel, K. M., Skurikhin, A. N., Romanovsky, V. E., Grosse, G., Bolton, W. R., and Genet, H.: Polygonal tundra geomorphological change in response to warming alters future CO_2 and CH_4 flux on the Barrow Peninsula, Glob. Change Biol., 21, 1634–1651, https://doi.org/10.1111/gcb.12757, 2015.

Lee, H., Swenson, S. C., Slater, A. G., and Lawrence, D. M.: Effects of excess ground ice on projections of permafrost in a warming climate, Environ. Res. Lett., 9, 124006, https://doi.org/10.1088/1748-9326/9/12/124006, 2014.

Liljedahl, A. K., Boike, J., Daanen, R. P., Fedorov, A. N., Frost, G. V., Grosse, G., Hinzman, L. D., Iijma, Y., Jorgenson, J. C., Matveyeva, N., Necsoiu, M., Raynolds, M. K., Romanovsky, V. E., Schulla, J., Tape, K. D., Walker, D. A., Wilson, C. J., Yabuki, H., and Zona, D.: Pan-Arctic ice-wedge degradation in warming permafrost and its influence on tundra hydrology, Nat. Geosci., 9, 312–318, https://doi.org/10.1038/ngeo2674, 2016.

MacKay, J. R.: Thermally induced movements in ice-wedge polygons, western arctic coast: a long-term study, Geogr. Phys. Quatern., 54, 41–68, https://doi.org/10.7202/004846ar, 2000.

Muster, S., Langer, M., Heim, B., Westermann, S., and Boike, J.: Subpixel heterogeneity of ice-wedge polygonal tundra: a multi-scale analysis of land cover and evapotranspiration in the Lena River Delta, Siberia, Tellus B, 64, 17301, https://doi.org/10.3402/tellusb.v64i0.17301, 2012.

Nitzbon, J., Langer, M., Westermann, S., and Martin, L.: CryoGrid/CryoGrid3: CryoGrid 3 set-up for ice-wedge polygons, Zenodo, https://doi.org/10.5281/zenodo.2601973, 2019a.

Nitzbon, J., Langer, M., Westermann, S., Martin, L., Aas, K. S., and Boike, J.: Simulation of ice-wedge degradation under intermediate hydrological conditions, Copernicus Publications, https://doi.org/10.5446/39651, 2019b.

Nitzbon, J., Langer, M., Westermann, S., Martin, L., Aas, K. S., and Boike, J.: Simulation of ice-wedge degradation under draining hydrological conditions, Copernicus Publications, https://doi.org/10.5446/39652, 2019c.

Niu, G.-Y., Yang, Z.-L., Mitchell, K. E., Chen, F., Ek, M. B., Barlage, M., Kumar, A., Manning, K., Niyogi, D., Rosero, E., Tewari, M., and Xia, Y.: The community Noah land surface model with multiparameterization options (Noah-MP): 1. Model description and evaluation with local-scale measurements, J. Geophys. Res., 116, D12109, https://doi.org/10.1029/2010JD015139, 2011.

Olefeldt, D., Goswami, S., Grosse, G., Hayes, D., Hugelius, G., Kuhry, P., McGuire, A. D., Romanovsky, V. E., Sannel, A. B. K., Schuur, E. A. G., and Turetsky, M. R.: Circumpolar distribution and carbon storage of thermokarst landscapes, Nat. Commun., 7, 13043, https://doi.org/10.1038/ncomms13043, 2016.

Painter, S. L., Moulton, J. D., and Wilson, C. J.: Modeling challenges for predicting hydrologic response to degrading permafrost, Hydrogeol. J., 21, 221–224, https://doi.org/10.1007/s10040-012-0917-4, 2013.

Painter, S. L., Coon, E. T., Atchley, A. L., Berndt, M., Garimella, R., Moulton, J. D., Svyatskiy, D., and Wilson, C. J.: Integrated surface/subsurface permafrost thermal hydrology: Model formulation and proof-of-concept simulations, Water Resour. Res., 52, 6062–6077, https://doi.org/10.1002/2015WR018427, 2016.

Rowland, J. C. and Coon, E. T.: From documentation to prediction: raising the bar for thermokarst research, Hydrogeol. J., 24, 645–648, https://doi.org/10.1007/s10040-015-1331-5, 2015.

Rowland, J. C., Jones, C. E., Altmann, G., Bryan, R., Crosby, B. T., Hinzman, L. D., Kane, D. L., Lawrence, D. M., Mancino, A., Marsh, P., McNamara, J. P., Romanvosky, V. E., Toniolo, H., Travis, B. J., Trochim, E., Wilson, C. J., and Geernaert, G. L.: Arctic Landscapes in Transition: Responses to Thawing Permafrost, Eos T. Am. Geophys. Un., 91, 229–230, https://doi.org/10.1029/2010EO260001, 2010.

Schaphoff, S., Heyder, U., Ostberg, S., Gerten, D., Heinke, J., and Lucht, W.: Contribution of permafrost soils to the global carbon budget, Environ. Res. Lett., 8, 014026, https://doi.org/10.1088/1748-9326/8/1/014026, 2013.

Yershov, E. D., Kondrat'yeva, K. A., Loginov, V. F., and Sychev, I. K.: Geocryological map of Russia and neighbouring republics. Lomonosov Moscow State University, Russian Ministry of Geology, 1999.

Westermann, S., Schuler, T. V., Gisnås, K., and Etzelmüller, B.: Transient thermal modeling of permafrost conditions in Southern Norway, The Cryosphere, 7, 719–739, https://doi.org/10.5194/tc-7-719-2013, 2013.

Westermann, S., Langer, M., Boike, J., Heikenfeld, M., Peter, M., Etzelmüller, B., and Krinner, G.: Simulating the thermal regime and thaw processes of ice-rich permafrost ground with the land-surface model CryoGrid 3, Geosci. Model Dev., 9, 523–546, https://doi.org/10.5194/gmd-9-523-2016, 2016.

Westermann, S., Peter, M., Langer, M., Schwamborn, G., Schirrmeister, L., Etzelmüller, B., and Boike, J.: Transient modeling of the ground thermal conditions using satellite data in the Lena River delta, Siberia, The Cryosphere, 11, 1441–1463, https://doi.org/10.5194/tc-11-1441-2017, 2017.

Wolter, J., Lantuit, H., Fritz, M., Macias-Fauria, M., Myers-Smith, I., and Herzschuh, U.: Vegetation composition and shrub extent on the Yukon coast, Canada, are strongly linked to ice-wedge polygon degradation, Polar Res., 35, 27489, https://doi.org/10.3402/polar.v35.27489, 2016.

Zhang, Y., Carey, S. K., Quinton, W. L., Janowicz, J. R., Pomeroy, J. W., and Flerchinger, G. N.: Comparison of algorithms and parameterisations for infiltration into organic-covered permafrost soils, Hydrol. Earth Syst. Sci., 14, 729–750, https://doi.org/10.5194/hess-14-729-2010, 2010.

Zubrzycki, S., Kutzbach, L., Grosse, G., Desyatkin, A., and Pfeiffer, E.-M.: Organic carbon and total nitrogen stocks in soils of the Lena River Delta, Biogeosciences, 10, 3507–3524, https://doi.org/10.5194/bg-10-3507-2013, 2013.

CHAPTER 6

Fast response of cold ice-rich permafrost in northeast Siberia to a warming climate

Nitzbon, J., Westermann, S., Langer, M., Martin, L. C. P., Strauss, J., Laboor, S., Boike, J.

Nature Communications (2020), 11, 2201. DOI: 10.1038/s41467-020-15725-8

The Supplementary Information for this article are provided in Appendix A.

nature COMMUNICATIONS

ARTICLE

https://doi.org/10.1038/s41467-020-15725-8 OPEN

Check for updates

Fast response of cold ice-rich permafrost in northeast Siberia to a warming climate

Jan Nitzbon [1,2,3]✉, Sebastian Westermann[3], Moritz Langer[1,2], Léo C. P. Martin [3], Jens Strauss [1], Sebastian Laboor [1] & Julia Boike [1,2]

The ice- and organic-rich permafrost of the northeast Siberian Arctic lowlands (NESAL) has been projected to remain stable beyond 2100, even under pessimistic climate warming scenarios. However, the numerical models used for these projections lack processes which induce widespread landscape change termed thermokarst, precluding realistic simulation of permafrost thaw in such ice-rich terrain. Here, we consider thermokarst-inducing processes in a numerical model and show that substantial permafrost degradation, involving widespread landscape collapse, is projected for the NESAL under strong warming (RCP8.5), while thawing is moderated by stabilizing feedbacks under moderate warming (RCP4.5). We estimate that by 2100 thaw-affected carbon could be up to three-fold (twelve-fold) under RCP4.5 (RCP8.5), of what is projected if thermokarst-inducing processes are ignored. Our study provides progress towards robust assessments of the global permafrost carbon-climate feedback by Earth system models, and underlines the importance of mitigating climate change to limit its impacts on permafrost ecosystems.

---

[1] Permafrost Research Section, Alfred Wegener Institute Helmholtz Centre for Polar and Marine Research, Telegrafenberg A45, 14473 Potsdam, Germany. [2] Geography Department, Humboldt-Universität zu Berlin, Unter den Linden 6, 10099 Berlin, Germany. [3] Department of Geosciences, University of Oslo, Sem Sælands vei 1, 0316 Oslo, Norway. ✉email: jan.nitzbon@awi.de

Today's permafrost landscapes have been shaped by climatic, geomorphic and ecological processes during the Last Glacial Period and the Holocene[1–5]. In unglaciated regions, climate-driven accumulation and melting of ground ice have been key processes in the evolution of these landscapes, resulting in history-dependent landscapes and landforms with distinct ground ice distributions[6–9]. There is emerging evidence that the present-day ground ice distribution governs permafrost thaw pathways, and thus how landscapes evolve in the future[10–13]—particularly given the expected warming of the Arctic climate[14,15]. Thawing of ice-rich permafrost and melting of massive ground ice induce landscape change termed thermokarst, which results in characteristic landforms across ice-rich permafrost terrain[16] (see Supplementary Notes 1 for definitions). In the continuous permafrost zone, thermokarst is expressed in the transition from low-centred to high-centred ice-wedge polygons[12,17], or the formation of thaw lakes and thermo-erosional gullies[16,18,19], thereby causing landscape-scale feedbacks on hydrology and carbon decomposition[12,20,21]. In contrast to the gradual thawing of permafrost in ice-poor terrain, thermokarst processes can cause severe permafrost degradation within few years or decades, and have thus been referred to as rapid or abrupt thaw[11,22,23]. The contribution of thermokarst processes to global-scale permafrost degradation in the future is highly uncertain[11,22]. Recent efforts using simple conceptual models allow first-order estimates and emphasise the global relevance of abrupt thaw in thermokarst terrain[23], but are at the same time limited by strong assumptions on model parameters that mask the underlying physical processes. To date, process-based Earth system models (ESMs) lack the structure and physical processes relevant to represent thermokarst, and might thus substantially underestimate future permafrost degradation and the permafrost carbon–climate feedback.

Permafrost in the northeast Siberian Arctic lowlands (NESAL, Fig. 1a, see "Methods" for definition) is highly susceptible to thermokarst[18], as the landscapes' history led to abundance of ice- and organic-rich permafrost deposits[3,24] (Fig. 1b; Supplementary Fig. 1). The NESAL comprise large parts of the Yedoma domain[25,26], which has been hypothesised to exhibit large-scale tipping behaviour under strong regional climate warming[27]. Permafrost deposits in the NESAL are estimated to store about 100 GtC, corresponding to an increase in atmospheric CO_2 of about 24 ppm if it were all to be released into the atmosphere (Supplementary Methods 1). Despite recent warming trends observed in boreholes (about 0.9 °C per decade[28,29]), permafrost temperatures in the NESAL are yet amongst the coldest in the Arctic with observed and simulated present-day mean annual ground temperatures lying mostly within the range -8 to -12 °C[30]. In projections of ESMs, the NESAL are one of the most stable permafrost regions, with near-surface permafrost largely remaining thermally stable beyond 2100, even under the strong RCP8.5 warming scenario[31–34]. However, these models do not take into account thermokarst-inducing processes and associated feedbacks, which can be expected to occur in the NESAL due to the abundance of massive ground ice in form of ice wedges[11,12,22,23], making the model projections highly questionable.

Recent developments constitute significant progress towards the process-based simulation of subgrid-scale heterogeneity and ground subsidence[10,13,35–37], allowing a more realistic evaluation of ice-rich permafrost thaw dynamics. Here, we extend and apply the CryoGrid 3 permafrost model[13] to investigate how the present-day ground ice distribution in the NESAL, which is inherited from the landscape history, affects pathways of landscape evolution, the magnitude and pace of permafrost degradation, and the amount of currently freeze-locked permafrost carbon that becomes subject to thawed conditions, in the course of the twenty-first century. Our focus here is on vast lowlands (covering about 493,000 km^2) that are underlain by massive ice wedges in the subsurface, as wedge ice constitutes the dominant

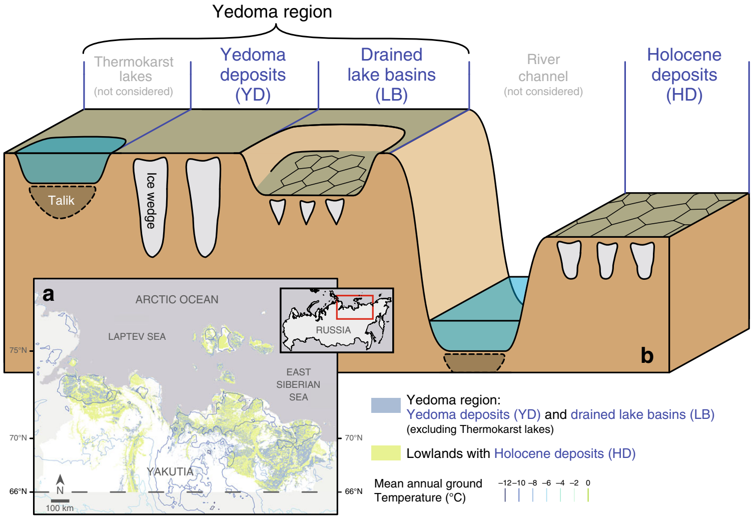

Fig. 1 Map and schematic of ice-rich permafrost landscapes. a Map showing the extent of ice-rich lowlands and mean annual ground temperatures[30] in northeast Siberia. See Supplementary Fig. 2 for an enlarged map of the study region. **b** Climate-driven landscape evolution during the last glacial period and the Holocene has led to diverse types of ice-rich permafrost landscapes. At present, ice wedges are the most common form of excess ground ice, but there is large variability in the volume and thickness of wedge ice. We assumed ice wedges to increase in lateral size and depth from drained lake basins (LB), over Holocene deposits (HD), to undisturbed Yedoma deposits (YD). While LB and HD feature active ice-wedge polygons with a patterned surface microtopography, YD host relict ice-wedge polygons which are covered by younger deposits. Note that we excluded from our analysis old thermokarst lakes and large water bodies already existing in the study region. See Supplementary Fig. 1 for an extended version of the schematic.

type of excess ground ice in the NESAL[3,38] (see Supplementary Notes 2). Consequently, the initiation and development of thermokarst can be assumed to involve melting of ice wedges at the microscale. Acknowledging the landscape evolution throughout the Holocene, we distinguish three major types of present-day landscapes, with marked differences in the wedge-ice volumes and the thickness of ice-rich deposits (Fig. 1b). Intact Late Pleistocene deposits within the Yedoma region are underlain my wide and deep ice wedges (Yedoma deposits, YD), while large parts of the Yedoma region have been affected by degradation processes during the Holocene, involving the formation of thermokarst lakes and their drainage. Refrozen drained lake basins (LB) are underlain by thin and shallow ice wedges. Active ice-wedge polygons are also abundant in lowlands outside the Yedoma region, which we designated as Holocene deposits (HD). To broadly explore possible landscape responses, the present-day landscapes are subjected to different hydrological conditions (water-logged versus well-drained) and future climate scenarios following different representative concentration pathways (RCP2.6, RCP4.5 and RCP8.5). Our model explicitly takes into account the spatial heterogeneity in surface topography and subsurface stratigraphies of ice-rich permafrost terrain, ground subsidence due to melting of excess ice, as well as feedbacks exerted through small-scale lateral fluxes of heat, water and snow. In addition, lateral sediment transport is reflected in our model, which is a key processes for the stabilisation of ice wedges after initial degradation[39]. To allow for comparison with the simplistic representation of permafrost in ESMs, we conducted reference runs which do not take into account thermokarst-inducing processes, such as excess ice melt and small-scale lateral fluxes. We demonstrate that our numerical modelling approach can retrace a multitude of landscape evolution and degradation pathways characteristic to ice-wedge terrain in the continuous permafrost zone. Projected permafrost degradation in the NESAL during the twenty-first century is substantially increased when thermokarst-inducing processes are taken into account. The response of ice-rich terrain differs considerably for different future warming scenarios, ranging from mostly stable landscapes (RCP2.6) to widespread landscape collapse (RCP8.5). We find that lateral sediment transport moderates thaw after initial ice-wedge degradation, leading to stabilised landscapes by 2100 under RCP4.5. For RCP8.5, we find that substantial amounts of the NESAL's organic carbon stocks might be affected by thaw within the present century, despite the projected stability of the region in previous ESM projections. This study emphasises the necessity of representing thermokarst-inducing processes in ESMs and provides significant progress towards achieving this goal. More broadly, our results underline the importance of mitigating climate change if we are to limit its impacts on permafrost ecosystems.

Results and discussion

Landscape evolution. Our numerical model uses the concept of laterally coupled tiles[35–37] to represent the spatial heterogeneity in surface and subsurface characteristics of ice-wedge terrain, which is typically characterised by polygonal patterned ground (see "Methods"; Supplementary Methods 2). We classified the geomorphological state of the landscape according to the relative positions of the tiles' soil surface altitudes, thereby distinguishing between relict polygons (RP), low-centred polygons (LCP), intermediate-centred polygons (ICP), high-centred polygons (HCP) and water bodies (WB) (see "Methods" for definitions). For each type of ice-wedge terrain (lake basins (LB), Holocene deposits (HD) and Yedoma deposits (YD)), we assessed the future landscape evolution, starting from the representative present-day state of the landscape (Fig. 2b, c; Supplementary Fig. 3; Supplementary Movies). Note that while our model allows for the formation of surface water bodies through ice-wedge thermokarst, the evolution of already existing old thaw lakes is not considered in this study.

Under the RCP2.6 scenario, all landscape types (LB, HD, YD) remained stable throughout the simulation period, with the exception of water-logged YD where shallow surface water bodies formed. We thus restrict the following analysis of the landscape evolution to the warming scenarios RCP4.5 and RCP8.5. The simulations for LB and HD were initialised with undegraded LCPs, featuring water-covered centres and elevated rims overlaying intact ice wedges (Fig. 2b; Supplementary Fig. 4a). Within the simulation period, ice-wedge degradation occurred and altered the initial landscape configuration under both warming scenarios (RCP4.5 and RCP8.5), and irrespective of the hydrological conditions (Fig. 2a). However, the initiation of ice-wedge degradation, which is indicated by the transition from LCP to ICP microtopography, was found to occur about two decades earlier under RCP8.5 than under RCP4.5, as well as about two decades earlier under water-logged compared with well-drained settings. Hence, the LB and HD landscapes were most stable under RCP4.5 and well-drained conditions, for which the simulated landscape by 2100 showed little sign of permafrost degradation (Fig. 2d). Under RCP8.5 and well-drained conditions, in turn, more substantial melting of ice wedges was simulated, indicated by subsiding rims of polygons and the resulting development of HCPs (Fig. 2e). When drainage was impeded, strong warming (RCP8.5) led to a collapse of ice-wedge polygons and the formation of surface water bodies (Fig. 2f). These water bodies are the initial stage for the formation of larger thermokarst lakes. In the RCP8.5 simulations, water bodies reach mean depths of ~1 m (LB), 2 m (HD) and 4 m (YD) within a few decades, and cause the development of continuously unfrozen zones (taliks) that were 3 m (LB) to 5 m (YD) thick (Supplementary Fig. 5m, n, o). Notably, the high-centred topography is preserved at the bottom of the water bodies, indicating that the lateral sediment transport does not keep pace with the ground subsidence due to excess ice melt. This agrees with features observed at lake bottoms in the study area (Supplementary Fig. 4c, d).

Yedoma deposits, which in their undegraded state have a negligible microtopography (Fig. 2c) and contain the largest amounts of excess ground ice (Table 1), showed the most pronounced changes in the landscape configuration. Here, the timing of initial and advanced degradation was mainly dependent on the hydrological conditions (Fig. 2a). Under water-logged conditions, initial degradation occurred a few years after the start of the simulation, and water bodies formed after two to three decades of simulation time. Irrespective of the warming scenario, the landscape turned into a water body by the end of the twenty-first century, but a talik formed only under RCP8.5 warming (Supplementary Fig. 5l, o). Under well-drained conditions, initial degradation occurred after about two decades, and HCPs evolved after six to seven decades under both warming scenarios. Under RCP8.5, the final state of the landscape was characterised by massive subsidence of polygon troughs and rims, leaving a pronounced high-centred relief. This is reminiscent of conical thermokarst mounds (termed baidzharakhs), which can already today be observed at local Yedoma exposures and on top of Yedoma deposits[7] (Supplementary Figs. 4b, 5i).

Under variation of ground ice contents and hydrological conditions, our model can reproduce a multitude of degradation pathways for ice-rich permafrost landscapes underlain by ice wedges, which have recently been observed as widespread degradation features at other sites in the continuous permafrost zone[12,40,41]. Within the NESAL, such thaw phenomena do occur

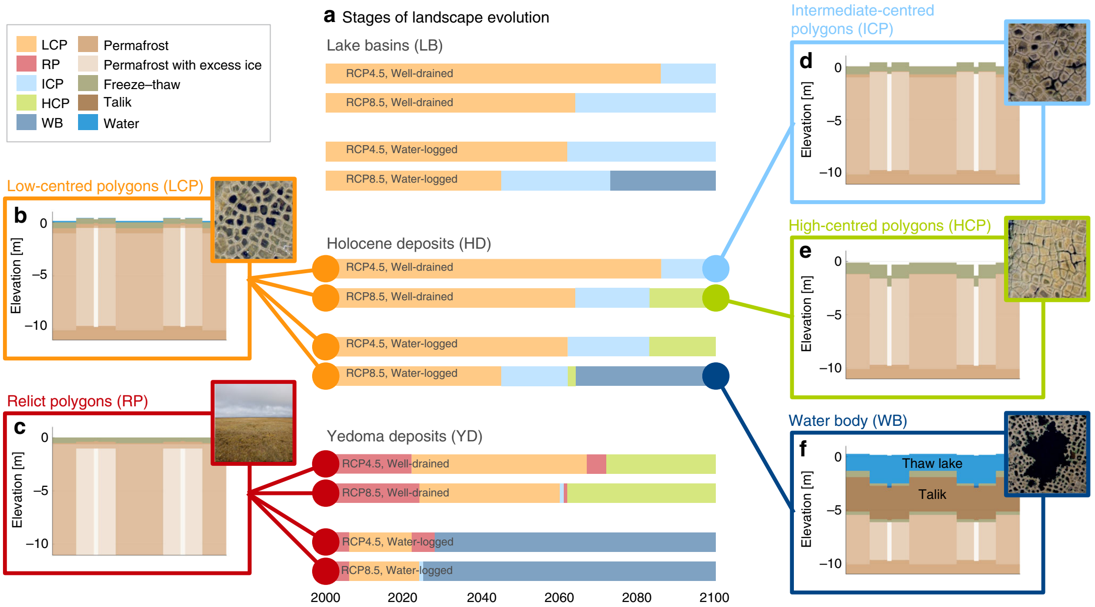
a Stages of landscape evolution
Lake basins (LB)
Holocene deposits (HD)
Yedoma deposits (YD)
RCP4.5, Well-drained
RCP8.5, Well-drained
RCP4.5, Water-logged
RCP8.5, Water-logged
2000
2020
2040
2060
2080
2100
LCP
RP
ICP
HCP
WB
Permafrost
Permafrost with excess ice
Freeze–thaw
Talik
Water
Low-centred polygons (LCP)
b
Relict polygons (RP)
c
Intermediate-centred polygons (ICP)
d
High-centred polygons (HCP)
e
Water body (WB)
f
Thaw lake
Talik
Elevation [m]
0
−5
−10

Fig. 2 Simulated evolution of ice-rich permafrost landscapes. Active low-centred polygons of drained lake basins and Holocene deposits (LCP, **b**), as well as relict polygons of Yedoma deposits (RP, **c**), initially host undegraded ice wedges. Melting of ice wedges under warming climatic conditions causes subsidence of the ground and a change in the microtopographic state of the landscape (**a**). Depending on the strength of the warming (RCP4.5 versus RCP8.5) and the hydrological conditions (well-drained versus water-logged), the landscapes evolve into intermediate-centred polygons (ICP, **d**), high-centred polygons (HCP, **e**) or water bodies (WB, **f**) by the end of the twenty-first century. Insets show aerial images of different states of ice-wedge terrain from study sites in northeast Siberia (Samoylov Island and Kurungnakh Island in the central Lena River delta). The initial and final states of the landscapes as well as detailed trajectories of the soil surface altitudes are provided in Supplementary Figs. 3 and 5.

Table 1 Surface and subsurface characteristics, areal coverage and number of soil samples of the different landscape types of the NESAL.

Parameter	Unit	Lake basins (LB)	Holocene deposits (HD)	Yedoma deposits (YD)
Initial topography	-	**LCP**	**LCP**	**RP (flat)**
Ice-wedge depth	m	3.8	10	20
Wedge-ice volume	%	10	30	50
Excess ice content	%	13	19	25
Ground ice content	%	68	74	80
Full stratigraphy	-	Supplementary Table 3	Supplementary Table 4	Supplementary Table 5
Number of soil samples	-	199	200	585
Total area	km^2	140,000	290,000	63,000

locally[12], but are either restricted to extreme site-specific conditions or induced by disturbances of natural or anthropogenic origin. Examples include the accumulation of snow in topographic depressions[12,42], the removal of protective organic layers or vegetation[43], tundra and forest fires[44], or vehicle tracks. When introducing such conditions or disturbances into our model, the simulated timing of permafrost degradation markedly shifts to earlier years[37]—in agreement with observations[12]. Here, however, we concentrated on undisturbed initial conditions and evaluate the impact of climate warming.

The correspondence between simulated and observed degradation pathways, together with the comprehensive site-level comparison between simulated and observed permafrost characteristics conducted in a preceding work[37], build confidence in that our simulations represent true end-members of landscape evolution in the NESAL under projected twenty-first century climate warming. We note that the processes represented in our model are tailored for its application on decadal-to-centennial time-scales. If the approach was applied to millenial time-scales, comprising also extended periods of colder climatic conditions, the accumulation of ground ice would need to be taken into account, as it counter-acts the melting of ice wedges[39]. Even though our numerical model does not explicitly incorporate meso-scale landscape features (e.g., thermo-erosional valleys) and their lateral interactions (e.g., drainage of thermokarst lakes), the simulations under contrasting hydrological conditions are reflective of a broad range of permafrost thaw dynamics at the microscale.

Permafrost thaw and ground subsidence. Next, we assess the degradation of permafrost that is associated with the dynamic

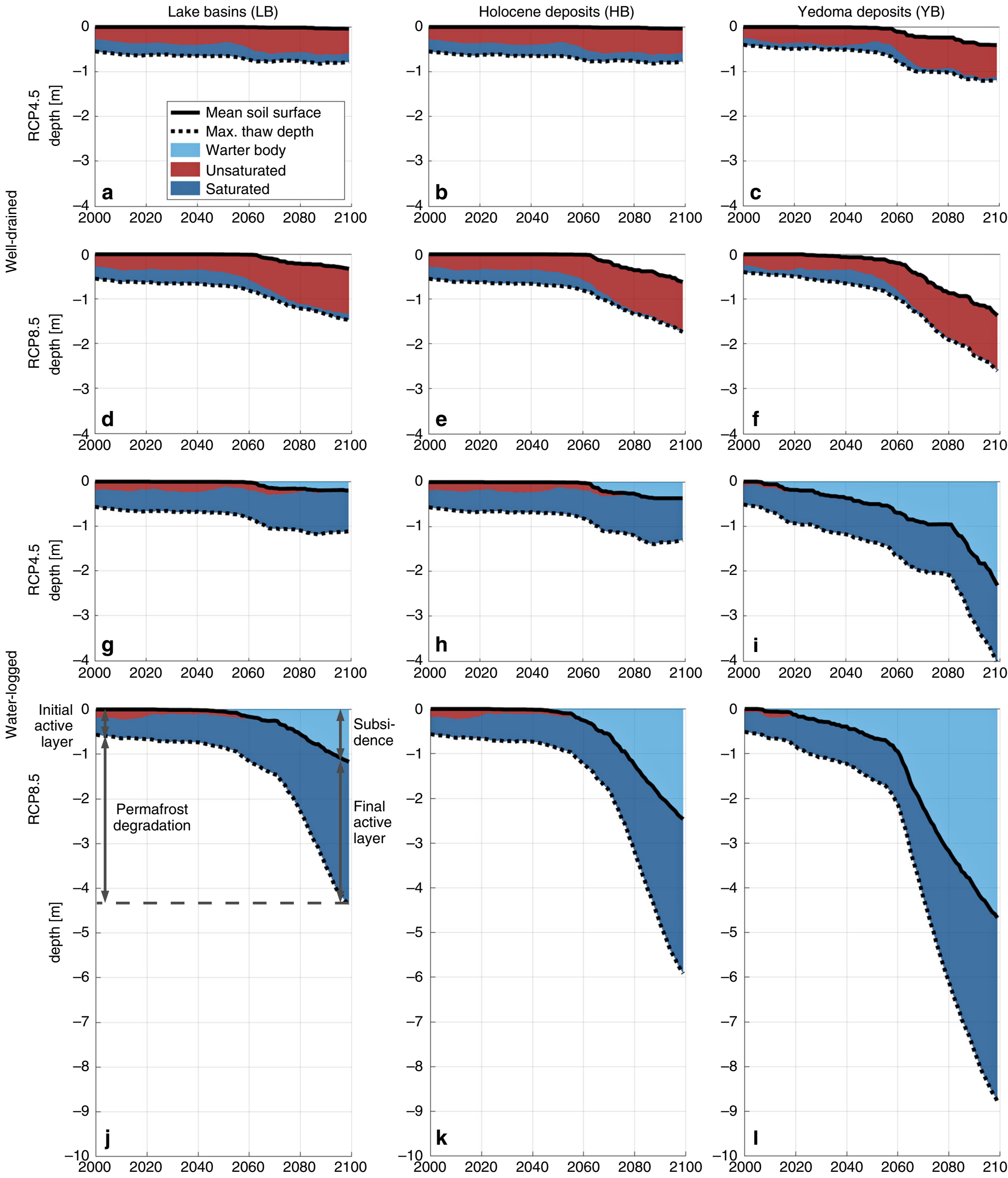

Fig. 3 Simulated permafrost degradation and ground saturation. The panels **a** to **l** show the accumulated mean ground subsidence and 11-year running mean of the maximum annual thaw depth for all settings (area-weighted means of the three tiles). Coloured areas indicate the fractions of unsaturated (red) and saturated (dark blue) conditions prevailing in the thawed ground throughout each year. Under water-logged conditions, surface water bodies form atop subsiding ground (light blue). Both ground subsidence and active-layer deepening cause permafrost degradation (see illustration in panel **j**). Corresponding plots for the reference runs without excess ice and the RCP2.6 runs are provided in Supplementary Figs. 6 and 7.

evolution of the different types of ice-wedge terrain. Figure 3 shows the temporal evolution of the maximum annual thaw depths as well as the mean ground subsidence (area-weighted means of the three tiles), for all landscape types and hydrological conditions under the RCP4.5 and RCP8.5 warming scenarios. Our numerical simulations provide an improved understanding of the dynamics and controls of ice-rich permafrost thaw and allow a comparison with more simplistic model representations which only simulate gradual thawing of permafrost, ignoring thermokarst-inducing processes (Supplementary Methods 3 and Supplementary Fig. 6). Subsequently, we discuss four key results, which allow conclusions about the process of ice-rich permafrost thaw in general, and about its relevance within the NESAL in particular.

First, substantial permafrost degradation was projected under the RCP4.5 and RCP8.5 warming scenarios, which is reflected in both increasing thaw depth relative to the soil surface, and ground subsidence resulting from excess ice melt. Simulated maximum thaw depths increased significantly within the twenty-first century (Fig. 3a–l), with relative increases ranging from factors of 1.3 (well-drained LB, RCP4.5) to 8.0 (water-logged YD, RCP8.5). Within the same period, thaw depths increased by factors of 1.7 (RCP4.5) and 2.3 (RCP8.5) in the corresponding reference runs, which do not represent thaw processes related to excess ground ice (Supplementary Fig. 6). These reference simulations do not reflect ground subsidence, which led to additional permafrost degradation of 0.2 m (well-drained LB, RCP4.5) to 4.7 m (water-logged YD, RCP8.5) by 2100 in the simulations with excess ice.

The degradation of ice wedges, which has so far only been observed locally within the study area[12], can be expected to occur as a widespread phenomenon across the cold permafrost of the NESAL within the twenty-first century, if warming exceeds RCP2.6 projections. Similar degradation of very cold, ice-rich permafrost has recently been reported for the High Canadian Arctic[41]. Both simulations and observations highlight the particular vulnerability of ice-rich permafrost landscapes to climate warming, which is despite very low permafrost temperatures at present[30]. It should be stressed that permafrost models without representation of excess ground ice can only simulate the gradual increase in thaw depth, but not the additional degradation through ground subsidence and associated feedbacks.

Second, after initial degradation, stabilisation of permafrost was projected towards the end of the twenty-first century under the moderate RCP4.5 warming scenario, but permafrost continued to degrade beyond 2100 under the strong RCP8.5 warming scenario. This qualitative difference between these two warming scenarios was found for all landscape types and hydrological conditions, except for water-logged Yedoma deposits. Under RCP4.5, the maximum thaw depths did not increase significantly during the final one to two decades of the simulations (Fig. 3a–c, g, h), while active-layer deepening and ground subsidence occurred during that period in all of the RCP8.5 simulations (Fig. 3d–f, j–l). Simulations for the ambitious mitigation scenario RCP2.6 revealed that ice-rich permafrost remained largely stable throughout the simulation period (Supplementary Methods 4 and Supplementary Fig. 7).

The stabilisation of the landscape under the warming scenarios depends on whether a sufficiently thick ice-poor layer consisting of thawed-out and laterally transported sediment accumulates. Such a layer would prevent the thaw front from reaching soil layers containing excess ice, i.e., a new active layer in equilibrium with the warming climate is established. On the one hand, the lateral transport of sediment (e.g., from polygon rims into deepening troughs) and the accumulation of sediment from melted excess ice layers promote the stabilisation of the landscape[39] (Supplementary Fig. 3). On the other hand, positive feedbacks induced by melting of excess ice cause an increase in thaw depths[39]. These include, for instance, soil warming resulting from increased snow depth in deepening troughs, and enhanced ground heat fluxes resulting from increased thermal conductivity of the active layer[37]. These results suggest that the possibility of permafrost stabilisation in the NESAL is linked to a critical threshold in the rate of climate warming reflected in the different warming scenarios. Under the strong and rapid warming of the RCP8.5 scenario, the system exceeds a tipping point beyond which stabilising feedbacks do not keep pace with positive feedbacks that accelerate permafrost degradation. Under the moderate warming of the RCP4.5 scenario, negative feedbacks slow down permafrost degradation such that a new equilibrium active layer establishes towards the end of the simulation period. Our results thus emphasise the necessity of representing thermally stabilising and destabilising feedback processes in numerical permafrost models used to project the stability of near-surface permafrost in the future. Typically, these feedback processes involve lateral fluxes of mass and energy on spatial scales far below the grid size of current ESMs. Beyond this, our findings provide evidence that climate change mitigation according to the RCP2.6 or RCP4.5 scenarios could significantly limit the impacts of permafrost thaw on ecosystems and infrastructure in northeast Siberia, but most likely also in other Arctic regions hosting ice-rich permafrost.

Third, the abundance of excess ground ice exerts a strong control on the rate and magnitude of permafrost thaw. For instance, under well-drained conditions and RCP8.5 (Fig. 3d–f), the different landscape types showed a similar increase in maximum thaw depth during the simulation period, while the simulated subsidence increased from landscapes with low (LB) over intermediate (HD) to high (YD) excess ice contents. A similar relation was found under water-logged conditions and RCP8.5 (Fig. 3j–l), where subsidence is reflected in the deepening of thaw lakes forming during the simulation period. While a simple linear relation between total permafrost degradation and excess ground ice content can be established under the idealised assumptions of our numerical model (see Supplementary Notes 3 and Supplementary Fig. 8), the actual timing and the temporal evolution of permafrost thaw is further affected by site-specific factors, the incidence of extreme weather conditions, as well as hydrophysical and ecological feedback processes. In our simulations, this is illustrated by the formation of a deepening thaw lake for water-logged Yedoma deposits under RCP2.6 (Supplementary Fig. 7f) and RCP4.5 (Fig. 3i), which is not projected for landscapes with lower excess ice contents (Fig. 3g, h).

Our results underline the important role played by the present-day ground ice distribution, which is a product of climate-driven landscape evolution in the past, for permafrost thaw under a changing future climate. For landscapes with low abundance of wedge ice (e.g., drained lake basins), ground ice content has less influence on the magnitude and pace of permafrost degradation than in landscapes with high ice abundance (e.g., Yedoma deposits), where positive feedback mechanisms produce more rapid thawing, resulting in severe permafrost degradation and landscape collapse. Hence, robust projections of permafrost thaw require knowledge of present-day ground ice distribution[9] and numerical models that represent thermokarst-inducing processes in ice-rich terrain. Models lacking these processes likely underestimate permafrost thaw systematically. This is supported by the results of the reference runs with a simplistic representation of permafrost thaw dynamics (Supplementary Fig. 6), in which projected permafrost degradation was significantly lower compared with the simulations which include heterogeneously distributed excess ice.

Fourth, the hydrological regime of thawed ground tipped as a consequence of ice-wedge degradation to a dominance of either saturated or unsaturated conditions, depending on the specified hydrological conditions. At the beginning of the simulations, the fractions of saturated and unsaturated conditions in the thawed ground were of comparable magnitude, irrespective of whether the system is water-logged or well-drained. This was particularly the case for landscapes with undegraded ice-wedge polygons, i.e., pronounced LCP microtopography (LB and HD). Note that the presence of saturated ground conditions in the well-drained settings is possible, for instance, due to wet conditions after snowmelt and precipitation events, or due to higher water levels in the depressed polygon centres, which are hydrologically isolated from the well-drained troughs. The subsidence of ground above melting ice wedges changes lateral water fluxes, mainly due to subsiding polygon rims no longer acting as barriers between polygon centres and inter-polygonal troughs. Under water-logged conditions, thaw subsidence led to inundation of the entire model domain, reflected in vanishing fractions of unsaturated conditions as soon as excess ice melt occurred (Fig. 3g–l). Under well-drained conditions, melting of ice wedges had a contrasting effect on the ground hydrological regime. Here, thaw subsidence of polygon rims improved the drainage of the landscape, leading to predominantly unsaturated conditions prevailing in thawed ground (Fig. 3a–f), particularly for those settings with emergent HCP microtopography (Fig. 3c, e, f).

These findings highlight the crucial role of ice-wedge thermokarst for the hydrological regime of the active layer and landscape hydrology. Melting of ice wedges and associated ground subsidence increase the lateral hydrological connectivity of the landscape[12], making the hydrological regime more sensitive to the surrounding conditions[37]. The water-logged cases correspond to situations where ice-wedge degradation leads to the development of deep water-filled troughs, and potentially the formation of thermokarst ponds and lakes. As soon as inter-polygonal troughs connect to an external drainage point, this can cause drainage of the entire landscape[12], leaving unsaturated high-centred polygons, drained troughs or conical thermokarst mounds (YD, Supplementary Fig. 4b). Overall, our results emphasise that the subsurface hydrology is crucially influenced by heterogeneous microtopography, lateral hydrological connectivity and ground subsidence. One-dimensional permafrost models that lack these complexities are thus inherently unsuitable for reliable projections of the hydrological regime of the active layer[21,45].

Thaw-affected organic carbon stocks. By scaling the simulated amounts of thawed organic carbon (per unit area) with the estimated total areas of each landscape type (LB, HD, YD) within the NESAL (see “Methods”, Table 1), we estimated the proportion of the region’s carbon pool that becomes subject to thawed conditions in the course of the twenty-first century under different warming scenarios (RCP2.6, RCP4.5 and RCP8.5; Fig. 4). Here, we distinguish between the simulations with excess ground ice and lateral fluxes, and the reference runs that reflect the typical representation of permafrost in ESMs. For the model runs with excess ground ice, the simulations under contrasting hydrological conditions (water-logged versus well-drained) provide a confining range for our estimates, acknowledging that the actual landscape evolution takes place under a range of different and dynamically changing hydrological conditions.

At the beginning of the twenty-first century ~7–8 Gt of organic carbon (GtC) were contained in the active layers of the simulated landscapes, and thus potentially accessible for microbial decomposition. Deepening of the active layers in combination with melting of excess ground ice caused thawing of additional carbon that was initially stored in perennially frozen soil layers. During the first half of the twenty-first century, the amounts of thawed organic carbon were projected to increase steadily, and the differences between the runs with excess ice and the reference simulations were small. By 2050, an additional 1.7 GtC (RCP2.6), 1.8 GtC (RCP4.5) and 2.5 GtC (RCP8.5), respectively, became subject to thawed conditions according to the reference runs. These numbers are within the respective ranges projected by the simulations with excess ice, reflecting that the increase was mainly attributable to active-layer deepening. However, during the second half of the twenty-first century excess ice melt set in under the RCP4.5 and RCP8.5 scenarios, leading to ground subsidence and an acceleration of permafrost thaw due to positive feedbacks (Fig. 3). Thereby, deep organic carbon stocks were subjected to thaw and would potentially become accessible for microbial decomposition. Hence, under the RCP4.5 and RCP8.5 scenario, after 2060 the projected range of thawed carbon was substantially higher in the runs with excess ice, compared with the respective reference runs. Under RCP4.5, by 2100 an additional 3.2–9.3 GtC were affected by thaw, if excess ice melt was taken into account, significantly exceeding the 2.7 GtC projected by the corresponding reference run. While stabilising feedback processes slowed down thawing rates under RCP4.5, positive feedbacks sustained rapid thawing under RCP8.5, exposing 12.5–64.4 GtC to thawed conditions by 2100, substantially exceeding the 5.3 GtC projected by the reference runs. Under the ambitious mitigation scenario RCP2.6, no widespread occurrence of excess ice melt was simulated (Supplementary Fig. 7), and consequently the amounts of carbon affected by thaw by 2100 (0.8–2.0 GtC) did not exceed the respective projection of the reference run (1.3 GtC). Overall, the deviation of the simulations with excess ice from the respective reference runs was found to increase with the strength of the warming scenario, reflecting that the contribution of thermokarst-inducing processes increased under stronger climate warming.

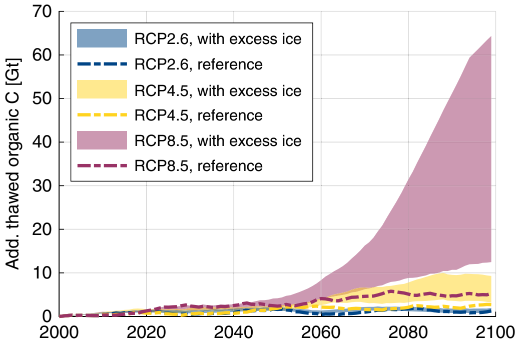

Fig. 4 Projection of thaw-affected organic carbon stocks. The estimates were obtained by scaling the simulation results using representative stratigraphies and the total areal extent of each landscape type within the northeast Siberian lowlands (see “Methods”). For each warming scenario, the indicated ranges correspond to 11-year running means of the annual maximum of thawed organic carbon under contrasting hydrological conditions. The reference runs without excess ice reflect the simplistic representation of permafrost in ESMs.

These results suggest that in regions like the NESAL which host cold, ice- and organic-rich permafrost deposits, substantially larger amounts of permafrost organic matter could thaw and expose carbon to mineralisation than what is projected by models like ESMs that employ a simplistic representation of permafrost thaw dynamics. Such global-scale models project significant amounts of thaw-affected permafrost carbon for the end of the twenty-first century (~140–400 GtC, depending on the scenario and the model[46,47]), but do not take into account thermokarst-inducing processes and deep carbon stocks which would become accessible through these processes. This is particularly problematic for cold permafrost regions like the NESAL where—even under RCP8.5—projected gradual thaw is limited (only ~5.3% of the NESAL’s carbon pools become subject to thaw in our reference runs), but thermokarst-inducing process could cause thawing of 2–12 times (i.e., up to two-thirds of the NESAL’s carbon pool) of the amount projected for gradual thaw only. ESMs might thus substantially underestimate the amounts of carbon becoming accessible for microbial decomposition under a warming climate, particularly in cold and seemingly stable permafrost regions like the NESAL.

Our simulations further revealed that thermokarst-inducing processes are not only relevant for the deposits of the Yedoma domain which bear substantial amounts of well-preserved organic matter as well as relict wedge ice down to large depths[26] but also for landscapes hosting active ice-wedge polygons (LB and HD), where the same feedbacks cause rapid and deep thaw (Supplementary Fig. 8). Hence, in regions with ice-rich deposits prone to thermokarst processes[18], permafrost thaw through ice-wedge degradation needs to be taken into account in addition to gradual thaw through active-layer-deepening, when assessing the potential mobilisation of permafrost carbon pools under a warming climate. Since ice-wedge degradation constitutes a spacious process, it potentially affects larger areas and carbon stocks than localised or linear thermokarst features, such as retrogressive thaw slumps or coastal erosion. While these mass-wasting process might constitute an efficient pathway for the lateral export and the potential mobilisation of organic carbon[48], the total area and carbon pools affected by these processes are small[49,50] compared with the vast terrain underlain by ice wedges addressed in this study. We note that permafrost degradation beneath existing thermokarst lakes was not considered in this study, but constitutes another pathway of unlocking frozen carbon stocks that is typically ignored by ESMs[19,35].

Under RCP4.5 and RCP8.5, the spread between the simulations under contrasting hydrological conditions increased during the second half of the simulation period (Fig. 4), concurrent to the occurrence of ice-wedge degradation and associated ground subsidence (Fig. 3). This reflects that different pathways of ice-rich permafrost thaw under contrasting hydrological conditions affect substantially different amounts carbon, with water-logged conditions generally leading to deeper thaw than in well-drained settings (Supplementary Fig. 9). Moreover, the spread in thaw-affected carbon stocks was further found to increase with the strength of the warming scenarios. The spread in the projections can be interpreted as the uncertainty range of our simulations with respect to the preconditioning of the landscape hydrology and its response to a warming climate. In order to further constrain our estimates, more dedicated modelling studies are needed that recognise the spatial variability of the present-day landscapes' topography and hydrology (which have been affected by thermokarst and thermoerosion in the past), and at the same time realistically reflect the meso-scale hydrological and geomorphological responses to future permafrost degradation, such as the expansion and drainage of thermokarst lakes. Meso-scale snow redistribution (e.g., blowing snow from frozen lake surfaces) constitutes another process which can affect the thermal and hydrological state and thaw dynamics of permafrost. Constraining the hydrological response of Arctic lowlands to thawing of permafrost appears even more important when considering that lateral hydrological export might constitute also an important direct pathway for soil carbon loss[51].

Finally, the hydrological conditions do not only affect the total amounts of thawed organic carbon but also exert control over its potential decomposition pathways[11,52–54]. With advanced melting of excess ice, water-logged conditions will lead to a dominance of saturated active layers, and hence favour anaerobic decomposition pathways; well-drained conditions in turn will favour unsaturated soils, in which carbon decomposition occurs aerobically, especially if a high-centred microtopography with improved landscape drainage emerges[12] (Supplementary Fig. 9). The quantification of microbial decomposition, turnover into greenhouse gases, and potential gas fluxes into the atmosphere is, however, beyond the scope of this study, and would require the extension of our physical process model with suitable biogeochemistry schemes. It should be stressed, that the overall carbon balance of permafrost ecosystems under a changing climate is depending on various processes besides permafrost thaw, including, for example, carbon uptake by vegetation. Our simulations do not allow conclusions about which portion of the thaw-affected carbon stocks presented in Fig. 4 could end up as greenhouse gases in the atmosphere, and whether the study region would evolve into a carbon source or sink.

In conclusion, the process-based simulations presented in this study provide evidence for a substantial potential for unlocking of vast amounts of currently frozen organic carbon pools in cold ice-rich lowlands, through thermokarst-related permafrost thaw in response to a warming climate. Thermokarst-inducing processes merit representation in ESMs as they could significantly contribute to the global permafrost carbon–climate feedback[11,23] already during the twenty-first century, and also at lower warming levels than previously thought[55]. According to our results, mitigation of climate change could save ecosystems in northeast Siberia from severe permafrost degradation and landscape collapse that are likely to occur under a high emissions scenario (RCP8.5).

Methods

Numerical model of ice-wedge terrain. We used a version of the CryoGrid 3 land surface model[13] that represents the surface topography of ice-wedge terrain using three tiles[37]: polygon centres, polygon rims and inter-polygonal troughs. Each tile has a one-dimensional vertical representation of the subsurface, for which the thermal and hydrological dynamics were simulated by solving the heat-conduction equation with phase change, combined with a hydrology scheme for unfrozen ground[37,56]. The snow scheme simulated the dynamic build-up and ablation of the snow pack as well as infiltration and refreezing of rain and meltwater. The model takes into account lateral fluxes of heat, water and snow between the tiles, assuming a circular symmetry for individual ice-wedge polygons (see Fig. 5; Supplementary Methods 2, Supplementary Fig. 10 and Supplementary Table 1). Lateral drainage of water from the troughs into an external reservoir is also possible. The elevation of this reservoir (e_{res}) was varied between different model runs in order to prescribe different hydrological conditions.

The geomorphological evolution of ice-wedge terrain was represented in our model by the combination of two process. First, we used the excess ground ice scheme introduced by Lee et al.[10], which was implemented into CryoGrid[13,35] to simulate the subsidence of the soil surface resulting from melting of excess ground ice. Soil layers with ice contents above the natural porosity were considered to contain excess ice. Excess water is moved upwards upon thawing of soil layers containing excess ice, while mineral and organic sediment is routed downwards. This scheme reflects the main process causing the degradation of ice-wedge polygons[37]. Second, we used the non-linear hillslope diffusion scheme by Roering et al.[57], which has been adapted for periglacial environments in previous studies[58,59]. This scheme describes the lateral erosion of mineral and organic sediment, which is an important process promoting the stabilisation of ice-wedge polygons[39].

For this study, we introduced the lateral sediment transport scheme into CryoGrid 3, by prescribing a slope-dependent lateral sediment flux $q^{\mathrm{sed}}_{i\leftarrow j}$ [m s^{-1}] between two adjacent tiles i and j. We neglected diffusive contributions to q^{sed}, and restricted the lateral sediment transport to advective fluxes, which occur after rapid ground subsidence that gives rise to steep terrain gradients. Advective fluxes were calculated as follows (see Supplementary Methods 2 for details):

$$q^{\mathrm{adv}}_{i\leftarrow j} = K_{\mathrm{eff}} \frac{a_j - a_i}{D_{ij}} \frac{\alpha^2}{\alpha^2_{\mathrm{crit}} - \alpha^2} \frac{L_{ij}}{A_i} \quad (1)$$

where $a_{i,j}$ is the soil surface altitude of the tiles, $\alpha = \arctan\left(\frac{a_j - a_i}{D_{ij}}\right)$ is the angle of the slope between the tiles and α_{crit} a critical slope angle at which advective fluxes diverge (Supplementary Fig. 11). The topological relations among the tiles involved are reflected by their respective distances (D_{ij}), contact lengths (L_{ij}) and areas (A_i). K_{eff} [m^2 s^{-1}] is a transport coefficient composed of a subaerial (K_{land}) and a subaqueous (K_{water}) part, depending on the surface conditions of both tiles (Supplementary Fig. 12). We set $\alpha_{\mathrm{crit}} = 45°$, $K_{\mathrm{land}} = 3 \times 10^{-10}$ m^2 s^{-1}, and $K_{\mathrm{water}} = 3 \times 10^{-8}$ m^2 s^{-1}, following previous studies in periglacial environments[58,59] (Supplementary Table 2).

Ground stratigraphies and further parameters. The three different landscape types (Fig. 1; two from the Yedoma region including Late Pleistocene Yedoma deposits (YD) and drained lake basins (LB), and Holocene Deposits (HD)) differ in

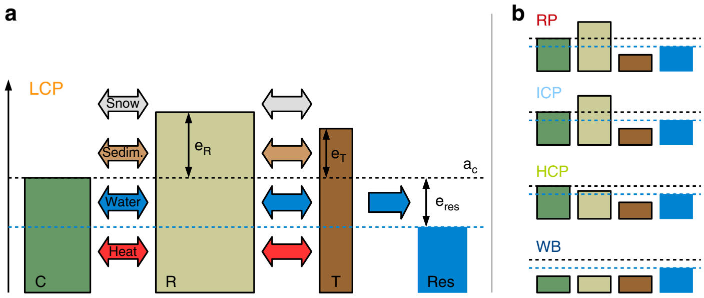

Fig. 5 Schematic of the model set-up. a Coupled tiles (polygon centres (C), polygon rims (R) and troughs (T)) and an external water reservoir (res) are used to represent surface and subsurface heterogeneities of ice-wedge terrain. The surface microtopography is reflected in different initial elevations (e) relative to the altitude of the centres (a_C). Different subsurface stratigraphies are provided in Supplementary Tables 3–5. Lateral fluxes of heat, water, snow and sediment between the tiles were calculated taking into account topological relationships among the tiles (see Supplementary Methods 2 and Supplementary Fig. 10 for details). The parameter e_{res} was used to specify the hydrological conditions. **b** The microtopographic state of the landscape is defined according to Eqs. (2) to (6) as relict polygons (RP), low-centred polygons (LCP), intermediate-centred polygons (ICP), high-centred polygons (HCP) or water body (WB), depending on the soil surface altitudes of the tiles ($a_{C,R,T}$) and the elevation of the external water reservoir (e_{res}).

their surface and subsurface characteristics. For LB and HD, which are characterised by active ice-wedge polygons, we assumed a low-centred surface microtopography ($e_R = 0.4$ m, $e_T = 0.3$ m). Undegraded YD, which are underlain by relict ice-wedge polygons, do not show a pronounced surface microtopography, so we assumed a flat surface ($e_R = 0.0$ m, $e_T = 0.0$ m).

The subsurface ground ice distributions of LB, HD and YD were reflected by setting up the model with different cryostratigraphies. For this, we used representative values[25,60] for wedge-ice volumes, ice-wedge depths and ground ice contents (Table 1). While we assumed homogeneous ice-wedge dimensions with depth for HD and YD, the pronounced wedge-shape of ice wedges in LB was reflected by reducing ground ice contents of the trough tile in deeper soil layers. An ice-rich intermediate layer[39] of 0.2 m (LB, HD) to 0.4 m (YD) thickness was placed above the ice wedges of all types. Organic, mineral and ice contents of LB, HD and YD were based on a total of 984 soil samples from different sites of all landscape types within the NESAL (see Table 1 for the number of samples per landscape type); the samples were measured with carbon–nitrogen (elementar vario EL III) and total organic carbon (elementar vario MAX C) analysers. Based on these data, we specified the soil stratigraphies in the model which we consider to be representative for the respective landscape type within the entire study area. Detailed stratigraphies are provided in Supplementary Tables 3–5.

In agreement with observations[29], the density of snow at deposition was set to $\rho_{snow} = 250\,\mathrm{kg\,m^{-3}}$, and the natural porosity of soil layers containing excess ice was set to $\phi_{nat} = 0.55$. All other model parameter values are provided in the Supplementary Information, or were set to the same values as in previous studies for the same study area[13,37].

Forcing data. We used meteorological forcing data for the central Lena River delta; these data have been used in previous studies using CryoGrid 3[13,35]. The forcing data covered the period from 1901 until 2100, and were composed of downscaled CRU-NCEP v5.3 data for the 1901 to 2014 period, and additionally applied anomalies from CCSM4 projections under the RCP4.5 and RCP8.5 scenarios (see ref. [13]. for details). For the RCP2.6 scenario, we took anomalies from CCSM4 projections and applied them repeatedly to the period from 2000 until 2014 of the RCP4.5 forcing data. Due to the central location of the Lena River delta within the NESAL, we assumed the current climate characteristics and future climate trends throughout the NESAL to be comparable with those expected for the Lena River delta. Differences in current climate characteristics within the NESAL were assumed to be negligible compared with the differences expected from the climate warming scenarios.

Simulations and spin-up. For each landscape type (LB, HD and YD), we conducted simulations under three climatic forcing scenarios (RCP2.6, RCP4.5 and RCP8.5) and two contrasting hydrological conditions (water-logged, well-drained). The two contrasting hydrological conditions were prescribed through fixed elevations of the external water reservoir (e_{res}), which was connected to the trough tile (Fig. 5). We set $e_{res} = 0.0$ m (LB, HD) or $e_{res} = -0.2$ m (YD) to reflect water-logged, and $e_{res} = -10.0$ m to reflect well-drained hydrological conditions. The initial temperature profiles of all 12 simulations were based on the borehole data, and a subsequent 50-year spin-up period using historical forcing data (10/1949-12/1999). The analysed period of the simulations was from 01/2000 until 12/2099.

In addition to the runs with the tiled set-up, we conducted reference runs under the three climatic forcing scenarios (RCP2.6, RCP4.5 and RCP8.5) with a setting of CryoGrid 3, which is comparable with the design of ESM land surface schemes. These runs were conducted using a one-dimensional subsurface representation without excess ice (Supplementary Table 6) and without taking into account lateral fluxes (see Supplementary Methods 3 for details).

Model evaluation and sensitivity analysis. The model set-up for ice-wedge terrain was evaluated against field measurements from a study site in the central Lena River delta[29] in a preceding study[37]. The study showed that simulated soil temperatures, thaw depths, soil moisture levels, water tables, snow heights and surface energy fluxes for different microtopographic features of ice-wedge terrain (polygon centres and rims) agreed well with observations. The correspondence between simulated and observed degradation pathways and landforms provides further evidence for the validity of our modelling approach (see main text, Fig. 2 and Supplementary Fig. 4).

In order to ensure the robustness of our results and to identify critical processes, we conducted a sensitivity analysis in which single-model parameters deviated from their default values. The parameters were related to different processes, and included the fresh snow density (ρ_{snow}), the sediment transport coefficients (K_{land}, K_{water}), the field capacity (θ_{fc}) and the natural porosity of ice-rich soil layers (ϕ_{nat}). Results of the sensitivity analysis are provided in Supplementary Fig. 13, and discussed in the Supplementary Notes 4.

Model diagnostics. During the simulations the topography of the landscape was altered due to ground subsidence resulting from excess ice melt and loss, as well as lateral sediment fluxes between adjacent tiles. While ground subsidence is indicative of permafrost degradation, lateral sediment fluxes smooth out the topography and potentially stabilise low-lying tiles. This process can counteract ice-wedge degradation[39]. Depending on the soil surface altitude of the three tiles ($a_{C,R,T}$) and the altitude of the external water reservoir ($a_{res} = a_C + e_{res}$), we distinguished five different states of the surface microtopography (Fig. 5), each corresponding to different landforms:

$$\text{Relict polygons (RP:)}\, a_T = a_C = a_R, \tag{2}$$

$$\text{Low-centred polygons (LCP):}\, a_C < \min(a_R, a_T), \tag{3}$$

$$\text{Intermediate-centred polygons (ICP):}\, a_T < a_C < a_R, \tag{4}$$

$$\text{High-centred polygons (HCP):}\, a_C > \max(a_R, a_T), \tag{5}$$

$$\text{Water body (WB):}\, \max(a_C, a_R, a_T) < a_{res}. \tag{6}$$

Maximum thaw depths are the area-weighted mean of the maximum thaw depth of each tile for each year. The proportion of unsaturated conditions corresponds to the fraction of thawed soil cells (above the permafrost) throughout each year that contain a non-zero fraction of air; the remaining fraction of thawed cells is saturated. Note that this definition takes into account changing thaw depths and changing water table levels throughout the year.

Areal extent and carbon stocks of the NESAL. Our overall region of interest is the northeast Siberian Arctic, defined as all landmass north of 66°N within the political borders of Yakutia (~1,462,000 km^2; Fig. 1a; Supplementary Fig. 2). Within this region, we identified three types of ice-rich lowlands underlain by ice wedges (LB, HD and YD), and the union of these constitute the northeast Siberian

Arctic lowlands (NESAL). Based on different sources[25,26,61], drained lake basins (LB, ~140,000 km^2) were assumed to comprise 69% of the mapped Yedoma region[62] (excluding existing lakes), while the remaining 31% of were considered as undisturbed Yedoma deposits (YD, ~63,000 km^2; Table 1). The area of lowlands with ice-rich deposits outside the Yedoma region (Holocene deposits, HD) was estimated based on a digital elevation model (DEM), which had a spatial resolution of 3 arc seconds[63]. We assumed ice-wedge polygonal tundra to be present in terrain with an altitude between 5 and 100 m above sea level, and a slope ≤ 4°. This region covers ~290,000 km^2 of the northeast Siberian Arctic. By using these criteria, we excluded low-lying terrain like floodplains, as well as slopes and mountain regions. The areal coverage of HD was validated using another DEM compiled from TanDEM-X data[64], yielding a relative difference in the HD area of < 3%. We excluded large water bodies (old thaw lakes, larger rivers) from the area estimates for all landscape types. In total, the NESAL cover about 493,000 km^2 (34%) of the overall study region. Note that the NESAL region mapped according to the criteria above largely falls into regions with high or very high thermokarst landscape coverage of types Lake and Hillslope mapped in an expert assessment[18].

The organic carbon contents assumed for the ground stratigraphies of the different landscape types in the simulations were based on a large number of soil samples from several study sites within the NESAL (Table 1). The ground stratigraphies were thus considered to be representative for the entire NESAL. We estimated the NESAL's thaw-affected carbon pool by scaling the amounts of organic carbon per unit area simulated for each landscape type at a single location with the total areas of the respective landscape types (LB, HD and YD) within the NESAL (Table 1).

Data availability

The data that support the findings of this study are available from the corresponding author upon reasonable request.

Code availability

The model code and the settings to reproduce the numerical simulations are available from https://doi.org/10.5281/zenodo.3648266. The code is published under a GNU General Public License v3.0.

Received: 18 September 2019; Accepted: 25 March 2020;
Published online: 04 May 2020

References

1. Burn, C. R. Cryostratigraphy, paleogeography, and climate change during the early Holocene warm interval, western Arctic coast, Canada. *Can. Earth Sci.* **34**, 912–925 (1997).
2. Grosse, G. et al. Geological and geomorphological evolution of a sedimentary periglacial landscape in Northeast Siberia during the Late Quaternary. *Geomorphology* **86**, 25–51 (2007).
3. Schirrmeister, L. et al. Periglacial landscape evolution and environmental changes of Arctic lowland areas for the last 60 000 years (western Laptev Sea coast, Cape Mamontov Klyk). *Polar Res.* **27**, 249–272 (2008).
4. Kanevskiy, M. et al. Cryostratigraphy and permafrost evolution in the lacustrine lowlands of West-Central Alaska. *Permafr. Periglac. Process.* **25**, 14–34 (2014).
5. Gilbert, G. L., Cable, S., Thiel, C., Christiansen, H. H. & Elberling, B. Cryostratigraphy, sedimentology, and the late Quaternary evolution of the Zackenberg River delta, northeast Greenland. *Cryosphere* **11**, 1265–1282 (2017).
6. Fortier, D. & Allard, M. Late Holocene syngenetic ice-wedge polygons development, Bylot Island, Canadian Arctic Archipelago. *Can. Earth Sci.* **41**, 997–1012 (2004).
7. Gilbert, G. L., Kanevskiy, M. & Murton, J. B. Recent advances (2008-2015) in the study of ground ice and cryostratigraphy. *Permafr. Periglac. Process.* **27**, 377–389 (2016).
8. Christiansen, H. H., Matsuoka, N. & Watanabe, T. Progress in understanding the dynamics, internal structure and palaeoenvironmental potential of ice wedges and sand wedges. *Permafr. Periglac. Process.* **27**, 365–376 (2016).
9. O'Neill, H. B., Wolfe, S. A. & Duchesne, C. New ground ice maps for Canada using a paleogeographic modelling approach. *Cryosphere* **13**, 753–773 (2019).
10. Lee, H., Swenson, S. C., Slater, A. G. & Lawrence, D. M. Effects of excess ground ice on projections of permafrost in a warming climate. *Environ. Res. Lett.* **9**, 124006 (2014).
11. Schuur, E. A. G. et al. Climate change and the permafrost carbon feedback. *Nature* **520**, 171–179 (2015).
12. Liljedahl, A. K. et al. Pan-Arctic ice-wedge degradation in warming permafrost and its influence on tundra hydrology. *Nat. Geosci.* **9**, 312–318 (2016).
13. Westermann, S. et al. Simulating the thermal regime and thaw processes of ice-rich permafrost ground with the land-surface model CryoGrid 3. *Geosci. Model Dev.* **9**, 523–546 (2016).
14. AMAP. *Snow, Water, Ice and Permafrost in the Arctic (SWIPA) 2017* (Arctic Monitoring and Assessment Programme, Oslo, Norway, 2017).
15. Pörtner, H.-O. et al. (eds) in *IPCC Special Report on the Ocean and Cryosphere in a Changing Climate* (IPCC, 2019).
16. Kokelj, S. V. & Jorgenson, M. T. Advances in thermokarst research. *Permafr. Periglac. Process.* **24**, 108–119 (2013).
17. Jorgenson, M. T., Shur, Y. L. & Pullman, E. R. Abrupt increase in permafrost degradation in Arctic Alaska. *Geophysical Res. Lett.* **33**, L02503 (2006).
18. Olefeldt, D. et al. Circumpolar distribution and carbon storage of thermokarst landscapes. *Nat. Commun.* **7**, 13043 (2016).
19. Walter Anthony, K. et al. 21st-century modeled permafrost carbon emissions accelerated by abrupt thaw beneath lakes. *Nat. Commun.* **9**, 3262 (2018).
20. Lara, M. J. et al. Polygonal tundra geomorphological change in response to warming alters future CO_2 and CH_4 flux on the Barrow Peninsula. *Glob. Change Biol.* **21**, 1634–1651 (2015).
21. Walvoord, M. A. & Kurylyk, B. L. Hydrologic impacts of thawing permafrost—a review. *Vadose Zone* **15**, 1–20 vzj2016.01.0010 (2016).
22. Turetsky, M. R. et al. Permafrost collapse is accelerating carbon release. *Nature* **569**, 32–34 (2019).
23. Turetsky, M. R. et al. Carbon release through abrupt permafrost thaw. *Nat. Geosci.* **13**, 138–143 (2020).
24. Schirrmeister, L. et al. Fossil organic matter characteristics in permafrost deposits of the northeast Siberian Arctic. *J. Geophys. Res.: Biogeosci.* **116**, G00M02 (2011).
25. Strauss, J. et al. The deep permafrost carbon pool of the Yedoma region in Siberia and Alaska. *Geophys. Res. Lett.* **40**, 6165–6170 (2013).
26. Strauss, J. et al. Deep Yedoma permafrost: a synthesis of depositional characteristics and carbon vulnerability. *Earth-Sci. Rev.* **172**, 75–86 (2017).
27. Lenton, T. M. Arctic climate tipping points. *AMBIO* **41**, 10–22 (2012).
28. Biskaborn, B. K. et al. Permafrost is warming at a global scale. *Nat. Commun.* **10**, 264 (2019).
29. Boike, J. et al. A 16-year record (2002-2017) of permafrost, active-layer, and meteorological conditions at the Samoylov Island Arctic permafrost research site, Lena River delta, northern Siberia: an opportunity to validate remote-sensing data and land surface, snow, and permafrost models. *Earth Syst. Sci. Data* **11**, 261–299 (2019).
30. Obu, J. et al. Northern hemisphere permafrost map based on TTOP modelling for 2000-2016 at 1 km^2 scale. *Earth-Sci. Rev.* **193**, 299–316 (2019).
31. Koven, C. D. et al. Permafrost carbon-climate feedbacks accelerate global warming. *Proc. Natl Acad. Sci. USA* **108**, 14769–14774 (2011).
32. Lawrence, D. M., Slater, A. G. & Swenson, S. C. Simulation of present-day and future permafrost and seasonally frozen ground conditions in CCSM4. *J. Clim.* **25**, 2207–2225 (2012).
33. Slater, A. G. & Lawrence, D. M. Diagnosing present and future permafrost from climate models. *J. Clim.* **26**, 5608–5623 (2013).
34. Koven, C. D., Lawrence, D. M. & Riley, W. J. Permafrost carbon–climate feedback is sensitive to deep soil carbon decomposability but not deep soil nitrogen dynamics. *Proc. Natl Acad. Sci. USA* **112**, 3752–3757 (2015).
35. Langer, M. et al. Rapid degradation of permafrost underneath waterbodies in tundra landscapes—toward a representation of thermokarst in land surface models. *J. Geophys. Res.: Earth Surf.* **121**, 2446–2470 (2016).
36. Aas, K. S. et al. Thaw processes in ice-rich permafrost landscapes represented with laterally coupled tiles in a land surface model. *Cryosphere* **13**, 591–609 (2019).
37. Nitzbon, J. et al. Pathways of ice-wedge degradation in polygonal tundra under different hydrological conditions. *Cryosphere* **13**, 1089–1123 (2019).
38. Fedorov, A. N. et al. Permafrost-landscape map of the Republic of Sakha (Yakutia) on a scale 1:1,500,000. *Geosciences* **8**, 465 (2018).
39. Kanevskiy, M. et al. Degradation and stabilization of ice wedges: implications for assessing risk of thermokarst in northern Alaska. *Geomorphology* **297**, 20–42 (2017).
40. Fraser, R. et al. Climate sensitivity of high arctic permafrost terrain demonstrated by widespread ice-wedge thermokarst on Banks Island. *Remote Sens.* **10**, 954 (2018).
41. Farquharson, L. M. et al. Climate change drives widespread and rapid thermokarst development in very cold permafrost in the Canadian high arctic. *Geophys. Res. Lett.* **46**, 6681–6689 (2019).
42. Abolt, C. J., Young, M. H., Atchley, A. L. & Harp, D. R. Microtopographic control on the ground thermal regime in ice wedge polygons. *Cryosphere* **12**, 1957–1968 (2018).
43. Nauta, A. L. et al. Permafrost collapse after shrub removal shifts tundra ecosystem to a methane source. *Nat. Clim. Change* **5**, 67–70 (2015).
44. Jones, B. M. et al. Recent Arctic tundra fire initiates widespread thermokarst development. *Sci. Rep.* **5**, 15865 (2015).

45. Andresen, C. G. et al. Soil moisture and hydrology projections of the permafrost region—a model intercomparison. *Cryosphere* **14**, 445–459 (2020).
46. Burke, E. J., Hartley, I. P. & Jones, C. D. Uncertainties in the global temperature change caused by carbon release from permafrost thawing. *Cryosphere* **6**, 1063–1076 (2012).
47. Kleinen, T. & Brovkin, V. Pathway-dependent fate of permafrost region carbon. *Environ. Res. Lett.* **13**, 094001 (2018).
48. Tanski, G. et al. Rapid CO_2 release from eroding permafrost in seawater. *Geophys. Res. Lett.* **46**, 11244–11252 (2019).
49. Günther, F., Overduin, P. P., Sandakov, A. V., Grosse, G. & Grigoriev, M. N. Short- and long-term thermo-erosion of ice-rich permafrost coasts in the Laptev Sea region. *Biogeosciences* **10**, 4297–4318 (2013).
50. Nitze, I., Grosse, G., Jones, B. M., Romanovsky, V. E. & Boike, J. Remote sensing quantifies widespread abundance of permafrost region disturbances across the Arctic and Subarctic. *Nat. Commun.* **9**, 5423 (2018).
51. Plaza, C. et al. Direct observation of permafrost degradation and rapid soil carbon loss in tundra. *Nat. Geosci.* **12**, 627–631 (2019).
52. Elberling, B. et al. Long-term CO_2 production following permafrost thaw. *Nat. Clim. Change* **3**, 890–894 (2013).
53. Schädel, C. et al. Potential carbon emissions dominated by carbon dioxide from thawed permafrost soils. *Nat. Clim. Change* **6**, 950–953 (2016).
54. Knoblauch, C., Beer, C., Liebner, S., Grigoriev, M. N. & Pfeiffer, E.-M. Methane production as key to the greenhouse gas budget of thawing permafrost. *Nat. Clim. Change* **8**, 309–312 (2018).
55. Khvorostyanov, D. V., Ciais, P., Krinner, G. & Zimov, S. A. Vulnerability of east Siberia's frozen carbon stores to future warming. *Geophys. Res. Lett.* **35**, L10703 (2008).
56. Martin, L. C. P. et al. Stability conditions of peat plateaus and palsas in Northern Norway. *J. Geophys. Res.: Earth Surface* **124**, 705–719 (2019).
57. Roering, J. J., Kirchner, J. W. & Dietrich, W. E. Hillslope evolution by nonlinear, slope-dependent transport: steady state morphology and equilibrium adjustment timescales. *J. Geophys. Res.: Solid Earth* **106**, 16499–16513 (2001).
58. Plug, L. J. & West, J. J. Thaw lake expansion in a two-dimensional coupled model of heat transfer, thaw subsidence, and mass movement. *J. Geophys. Res.: Earth Surface* **114**, F01002 (2009).
59. Kessler, M. A., Plug, L. J. & Anthony, K. M. W. Simulating the decadal- to millennial-scale dynamics of morphology and sequestered carbon mobilization of two thermokarst lakes in NW Alaska. *J. Geophys. Res.: Biogeosci.* **117**, G00M06 (2012).
60. Ulrich, M., Grosse, G., Strauss, J. & Schirrmeister, L. Quantifying wedge-ice volumes in Yedoma and thermokarst basin deposits. *Permafr. Periglac. Process.* **25**, 151–161 (2014).
61. Morgenstern, A., Grosse, G., Günther, F., Fedorova, I. & Schirrmeister, L. Spatial analyses of thermokarst lakes and basins in Yedoma landscapes of the Lena Delta. *Cryosphere* **5**, 849–867 (2011).
62. Strauss, J. et al. Database of ice-rich Yedoma permafrost (IRYP). *PANGAEA* https://doi.org/10.1594/pangaea.861733 (2016).
63. de Ferranti, J. Digital elevation data. http://viewfinderpanoramas.org/dem3.html (2014).
64. Rizzoli, P. et al. Generation and performance assessment of the global TanDEM-X digital elevation model. *ISPRS Photogramm. Remote Sens.* **132**, 119–139 (2017).

Acknowledgements

The authors gratefully acknowledge the Climate Geography Group at the Humboldt University of Berlin for providing resources on their high-performance-computer system. We thank Lutz Schirrmeister for providing soil organic carbon data and Alexander Oehme for processing the RCP2.6 forcing data. This work was supported by a grant of the Research Council of Norway (project PERMANOR, grant no. 255331). J.N. was supported by a grant of the German Academic Exchange Service (DAAD) for a research stay at the University of Oslo, and by the Geo.X Research Network. S.W. acknowledges funding through Nunataryuk (EU grant agreement no. 773421). M.L. was supported by a BMBF grant (project PermaRisk, grant no. 01LN1709A). J.S. was supported by a NERC-BMBF grant (project CACOON, grant no. 03F0806A) and the International Permafrost Association (Action Group The Yedoma Region). This work was supported by funding from the Helmholtz Association in the framework of MOSES (Modular Observation Solutions for Earth Systems).

Author contributions

J.N. designed the study, developed and implemented the numerical model, carried out and analysed the simulations, prepared the results figures and led the paper preparation. S.W., M.L. and J.B. co-designed the study, and interpreted the results. L.M. contributed to the development and implementation of the numerical model, and prepared schematic figures. J.S. contributed soil organic carbon and ice-wedge data, field observations and set the selection criteria for landscape-type mapping. S.L. did GIS analysis and mapping, and prepared geospatial figures. All authors contributed to the writing and editing of the paper.

Competing interests

The authors declare no competing interests.

Additional information

Supplementary information is available for this paper at https://doi.org/10.1038/s41467-020-15725-8.

Correspondence and requests for materials should be addressed to J.N.

Reprints and permission information is available at http://www.nature.com/reprints

Peer review infromation *Nature Communications* thanks Merritt Turetsky and other, anonymous, reviewers for their contributions to the peer review of this work. Peer review reports are available.

Publisher's note Springer Nature remains neutral with regard to jurisdictional claims in published maps and institutional affiliations.

Open Access This article is licensed under a Creative Commons Attribution 4.0 International License, which permits use, sharing, adaptation, distribution and reproduction in any medium or format, as long as you give appropriate credit to the original author(s) and the source, provide a link to the Creative Commons license, and indicate if changes were made. The images or other third party material in this article are included in the article's Creative Commons license, unless indicated otherwise in a credit line to the material. If material is not included in the article's Creative Commons license and your intended use is not permitted by statutory regulation or exceeds the permitted use, you will need to obtain permission directly from the copyright holder. To view a copy of this license, visit http://creativecommons.org/licenses/by/4.0/.

© The Author(s) 2020

CHAPTER 7

Effects of multi-scale heterogeneity on the simulated evolution of ice-rich permafrost lowlands under a warming climate

Nitzbon, J., Langer, M., Martin, L. C. P., Westermann, S., Schneider von Deimling, T., Boike, J.

Submitted to *The Cryosphere*.

Effects of multi-scale heterogeneity on the simulated evolution of ice-rich permafrost lowlands under a warming climate

Jan Nitzbon[1,2,3], Moritz Langer[1,2], Léo C. P. Martin[3], Sebastian Westermann[3], Thomas Schneider von Deimling[1,2], and Julia Boike[1,2]

[1]Permafrost Research, Alfred Wegener Institute Helmholtz Centre for Polar and Marine Research, Potsdam, Germany
[2]Geography Department, Humboldt-Universität zu Berlin, Berlin, Germany
[3]Department of Geosciences, University of Oslo, Oslo, Norway

Correspondence: Jan Nitzbon (jan.nitzbon@awi.de)

Abstract. Thawing of ice-rich permafrost deposits can cause the formation of thermokarst terrain, thereby involving ground subsidence and feedbacks to the thermal and hydrological regimes of the subsurface. Thermokarst activity can entail manifold pathways of landscape evolution and cause rapid permafrost thaw in response to a warming climate. Numerical models that realistically capture these degradation pathways and represent the involved feedback processes at different spatial scales, are required to assess the threats and risks that thermokarst processes pose to the functioning of ecosystems and human infrastructure in the Arctic. In this study, we therefore introduce a multi-scale tiling scheme to the CryoGrid 3 permafrost model which allows to represent the spatial heterogeneities of surface and subsurface conditions, together with lateral fluxes of heat, water, snow, and sediment, at spatial scales not resolved in Earth system models (ESMs). We applied the model setup to a lowland tundra landscape in northeast Siberia characterized by ice-wedge polygons at various degradation stages. We present numerical simulations under a climate-warming scenario and investigate the sensitivity of projected permafrost thaw to different terrain heterogeneities, on both a micro-scale (ice-wedge polygons) and a meso-scale (low-gradient slopes). We found that accounting for both micro- and meso-scale heterogeneities yields the most realistic possibilities for simulating landscape evolution. Simulations that ignored one or the other of these scales of heterogeneity were unable to represent all of the possible spatio-temporal feedbacks in ice-rich terrain. For example, we show that the melting of ice wedges in one part of the landscape can result in the drainage of other parts, where surface water has been impounded a number of decades earlier as a result of ice-wedge thermokarst. We also found that including subgrid-scale heterogeneities in the simulations resulted in a more gradual response in terms of ground subsidence and permafrost thaw, compared to the more abrupt changes in simple one-dimensional simulations. Our results suggest that, under a warming climate, the investigated area is more likely to experience widespread drainage of polygonal wetlands than the formation of new thaw lakes, which is in general agreement with evidence from previous field studies. We also discuss how the presented model framework is able to capture a broad range of processes involved in the cycles of ice-wedge and thaw-lake evolution. The results of this study improve our understanding of how micro- and meso-scale processes control the evolution of ice-rich permafrost landscapes. Furthermore, the methods that we have developed allow improved representation of subgrid-scale processes such as thermokarst in ESMs.

1 Introduction

Thawing of permafrost in response to climatic change, poses a threat to ecosystems, infrastructure, and indigenous communities in the Arctic (AMAP, 2017; Vincent et al., 2017; Schuur and Mack, 2018; Hjort et al., 2018). Permafrost degradation involves a wide range of feedback process from local to global scales, including widespread changes in soil moisture (Andresen et al., 2020), and the potential liberation of greenhouse gases, posing a positive feedback to climate warming (Schuur et al., 2015; Schneider von Deimling et al., 2015). However, the large-scale models used to project the response of permafrost to climate warming, employ a simplistic representation of permafrost thaw dynamics, which only reflects gradual top-down thawing of frozen ground (Lawrence et al., 2012; Slater and Lawrence, 2013; Andresen et al., 2020). In particular, such models lack representation of thaw processes in ice-rich permafrost deposits that cause localized and rapid landscape changes called thermokarst (Kokelj and Jorgenson, 2013). Thermokarst activity is induced on small spatial scales that are not resolved in large-scale Earth system models (ESMs), but it can have widespread effects on the ground thermal and hydrological regimes (Fortier et al., 2007; Liljedahl et al., 2016), soil erosion (Godin et al., 2014), and on carbon decomposition pathways (Lara et al., 2015; Turetsky et al., 2020). In addition, thermokarst features can induce positive feedback processes leading to accelerated permafrost degradation and landscape collapse (Walter Anthony et al., 2018; Turetsky et al., 2019; Farquharson et al., 2019; Nitzbon et al., 2020), but also stabilizing feedbacks have been observed (Jorgenson et al., 2015; Kanevskiy et al., 2017), overall establishing thermokarst as a key factor of uncertainty in any future projections of how permafrost and hydrology respond to Arctic climate change.

To address these issues, numerical models resolving heterogeneities at the spatial scales of thermokarst features and representing the vertical and lateral physical processes that give rise to the complex pathways of permafrost landscape evolution observed in the real world are required (Rowland et al., 2010). In recent years, substantial progress has been made in the development of numerical models to study the thermal and hydrological dynamics of permafrost terrain on small scales (Painter et al., 2016; Jafarov et al., 2018), and to identify important feedbacks associated with various thermokarst landforms such as ice-wedge polygons (Abolt et al., 2018; Nitzbon et al., 2019; Abolt et al., 2020) or peat plateaus (Martin et al., 2019). The development of numerical schemes simulating ground subsidence resulting from excess ice melt (Lee et al., 2014; Westermann et al., 2016) enabled the assessment of transient changes of thermokarst terrain using dedicated permafrost models (Langer et al., 2016; Nitzbon et al., 2019), but also more broadly using ESM framworks (Aas et al., 2019).

Using a tile-based modelling approach to represent lowlands underlain by massive ice wedges, Nitzbon et al. (2020) recently suggested the potential for substantial permafrost degradation in northeast Siberia in response to a warming climate, which is not captured by large-scale models that ignore thermokarst-inducing processes. These projections revealed a considerable uncertainty range associated with different hydrological boundary conditions in the simulations, that gave rise to contrasting pathways of landscape evolution, ranging from the development of high-centred polygons (HCPs) to the formation of thaw lakes. This uncertainty can be attributed to the fact that while the numerical model explicitly incorporates the micro-scale heterogeneity of ice-wedge polygon terrain (i.e., meters to tens of meters), it did not explicitly reflect meso-scale (i.e., hundreds to thousands of meters) landscape dynamics (see Table 1 for the terminology used to refer to different spatial scales). For example, kilometer-scale mapping of ice-wedge polygon types at different Arctic sites revealed, that polygons of the same degradational stage are located close to each other, but that there is a variability of different polygon types at the meso-scale (Kartoziia, 2019; Abolt and Young, 2020). These patterns could thus be linked to lateral surface and subsurface water fluxes which follow the terrain's topography and affect the degradation of ice wedges (Nitzbon et al., 2019). Moreover, excess ice melt on the micro-scale, can lead to the emergence of thaw features and feedbacks on the meso-scale, such as the formation of drainage networks (Liljedahl et al., 2016), laterally expanding thaw lakes, or thermo-erosional gullies. These features have the potential to interact with each other, thereby adding more complexity to the landscape evolution, for example, when a thaw lake drains upon incision of the thermo-erosional gully. Hence, in order to constrain the most likely landscape evolution and permafrost degradation pathways further, landscape heterogeneity and lateral processes at the meso-scale need to be considered. Tiling schemes which proved successful in realistically reflecting micro-scale permafrost dynamics (Aas et al., 2019), constitute a promising approach to also capture meso-scale processes in order to constrain those uncertainties further while keeping computational costs low.

In this study, we employ a multi-scale hierarchical tiling approach to investigate the transient response of ice-rich permafrost lowlands in northeast Siberia to projected twenty-first century climate warming. Specifically, we address the following objectives:

1. To investigate the transient evolution of ice-rich permafrost landscapes in response to climate warming using different representations of micro- and meso-scale heterogeneity, thereby identifying degradation pathways and feedback processes associated with lateral fluxes on these different spatial scales.
2. To quantify the sensitivity of projected permafrost thaw and ground subsidence to different representations of micro- and meso-scale heterogeneity.

Overall, our study intends to provide a transferable and scalable framework for more robustly assessing ice-rich permafrost landscape evolution, and at the same time aims at reducing sources of uncertainty in the projections of ice-rich permafrost response to a warming climate presented by Nitzbon et al. (2020). Instead of providing quantitative site-specific projections, the presented simulations should thus be considered as numerical experiments to explore important scales and controls of ice-rich permafrost landscape dynamics in response to a warming climate.

2 Methods

2.1 Terminology for spatial scales

Throughout the manuscript we use a consistent terminology to refer to different characteristic length scales of landscape features and processes. This terminology is summarized in Table 1.

Terminology	Superscript	Length scale	Example
subgrid	–	$\lesssim 10^5\,\mathrm{m}$	all mentioned below
micro	μ	$\simeq 10^0 - 10^1\,\mathrm{m}$	Ice-wedge polygon micro-topography
meso	m	$\simeq 10^2 - 10^3\,\mathrm{m}$	Thermo-erosion catchments, thaw lakes
macro	–	$\simeq 10^4 - 10^5\,\mathrm{m}$	River delta, ESM grid cell

Table 1. Overview of the terminology used in this manuscript to refer to the spatial scale of permafrost landscape features and processes.

2.2 Study area

While the the scientific objectives and the modelling concept pursued in this study are general and applicable to any ice-rich continuous permafrost terrain, we chose Samoylov Island in the Lena river delta in northeast Siberia as our focus study area ($72.36972\,^\circ$N, $126.47500\,^\circ$E). The island is located in the central southern part of the Lena River delta within the lowland tundra vegetation zone and features cold continuous permafrost (mean annual ground temperature of about $-9\,^\circ$C (Boike et al., 2019)), which has been warming rapidly in recent years (about $0.9\,^\circ$C per decade (Biskaborn et al., 2019)).

Samoylov Island belongs to the first terrace of the Lena River delta which formed during the Holocene (Schwamborn et al., 2002). The fluvial deposits contain substantial amounts of excess ice, mainly in form of ice wedges up to $10\,$m deep, which can be of epigenetic and syngenetic type. The surface of the island is characterized by ice-wedge polygons and water bodies of different sizes, ranging from ponds in polygon troughs and centers to thermokarst lakes several hundred meters in diameter (Figure 1 a). While the low-lying western part of Samoylov Island is regularly flooded in spring, the eastern part is more elevated but with an overall very flat topography (Fig. 1 a). Ice-wedge polygons show different features across different parts of the island, including mostly low-centered polygons with water-covered centers, but also water-filled troughs indicative of ice-wedge degradation, and some high-centered polygons with drained troughs. Polygons of different geomorphological type tend to occur as grouped “clusters” in the same areas of the island (Kartoziia, 2019), and the pre-dominant types differ along gently-sloped (about 0.1%) transects across the island (Fig. 1 b).

Meteorological and ground conditions have been measured on Samoylov Island for almost two decades, establishing it as a key site for the long-term monitoring of permafrost and the validation of numerical models (Boike et al., 2013, 2019). Various field studies addressed the climatology, hydrology, and geomorphology of the Island on different scales (Boike et al., 2008; Langer et al., 2011a, b; Muster et al., 2012), allowing the calibration and evaluation of numerical models used to assess

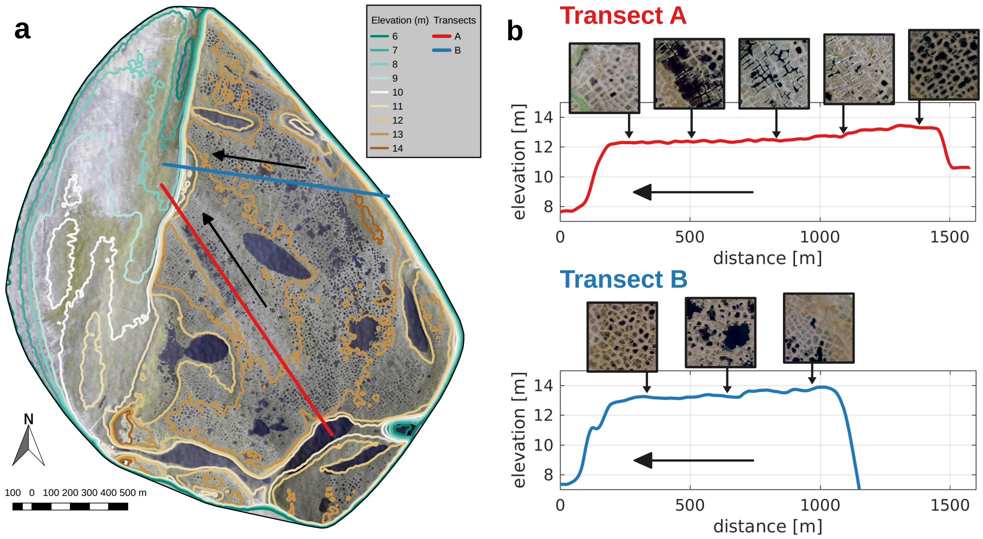
a
Elevation (m)
6
7
8
9
10
11
12
13
14
Transects
A
B
N
100 0 100 200 300 400 500 m
b
Transect A
elevation [m]
14
12
10
8
0
500
1000
1500
distance [m]
Transect B
elevation [m]
14
12
10
8
0
500
1000
1500
distance [m]

Figure 1. a: Aerial photography of Samoylov Island with elevation contour lines based on the ArcticDEM. The study area is covered with water bodies of different sizes and ice-wedge polygons of different geomorphological stages. b: Two (arbitrary) examples of transects across the island, reflecting the gently-sloped terrain with steep cliffs at the margins. The inlets are details (about 100 m in diameter) of the aerial photography, reflecting polygon clusters of similar stages along the transects. Arrows point towards the main drainage direction. Note that ice-wedge polygons show little signs of degradation in the highest-elevated parts and close to the margins of the island (first and last inlet of both Transects). Along Transect A, the abundance of thermokarst troughs increases in the downstream direction of the slope. Small water bodies are visible in the central part of Transect B.

permafrost dynamics in northeast Siberia under recent (Gouttevin et al., 2018; Nitzbon et al., 2019) and future (Westermann et al., 2016; Langer et al., 2016; Nitzbon et al., 2020) climatic conditions.

2.3 Model description

2.3.1 Process representations (CryoGrid 3 Xice)

For the numerical experiments in this study, we used the CryoGrid 3 (Xice) permafrost model, which is a physical process-based land surface model tailored for applications in permafrost environments (Westermann et al., 2016). CryoGrid 3 has a one-dimensional representation of the subsurface for which it computes the subsurface temperatures ($T(z,t)$ [$°C$]) by solving the heat diffusion equation, thereby taking into account the phase change of soil water (θ_{w} [-]) through an effective heat capacity:

$$\left(C(z,T) + \rho_w L_{\mathrm{sl}} \frac{\partial \theta_{\mathrm{w}}}{\partial T}\right) \frac{\partial T}{\partial t} = \frac{\partial}{\partial z}\left(k(z,T)\frac{\partial T}{\partial z}\right) . \tag{1}$$

In Equation (1), $C(z,T)$ is the volumetric heat capacity of the soil, $k(z,T)$ the thermal conductivity of the soil, both parameterized depending on the soil constituents.ρ_{w} $[\mathrm{kg\,m^{-3}}]$ is the density of water, and L_{sl} $[\mathrm{J\,kg^{-1}\,K^{-1}}]$ the specific latent heat of fusion of water. The upper boundary condition to Eq. (1) is prescribed as a ground heat flux which is obtained by solving the surface energy balance (Westermann et al., 2016). CryoGrid 3 simulates the dynamic build-up and ablation of a snow pack above the surface, heat conduction through the snowpack, changes to the snowpack due to infiltration and refreezing of rain and meltwater, and changes in snow albedo due to aging (Westermann et al., 2016). Snow is deposited at a constant density ($\rho_{\mathrm{snow}} = 250\,\mathrm{kg\,m^{-3}}$) which can effectively increase due to infiltration and refreezing of water. The model further employs a simple vertical hydrology scheme to represent changes in the ground hydrological regime due to infiltration of rain or meltwater, and evapotranspiration (Martin et al., 2019; Nitzbon et al., 2019). Excess water is allowed to pond above the surface, and heat transfer through unfrozen surface water bodies is represented assuming complete mixing of the water column throughout the ice-free period (Westermann et al., 2016). The field capacity parameter was set to $\theta_{\mathrm{fc}} = 0.5$.

CryoGrid 3 represents a range of physical processes which enable it to simulate the formation of thermokarst in ice-rich permafrost deposits Westermann et al. (2016); Langer et al. (2016); Nitzbon et al. (2019, 2020). Soil layers which have an ice content (θ_{i}) exceeding the natural porosity (ϕ_{nat}) of the soil constituents, are treated as excess ice layers. Once an excess ice layer thaws, the resulting excess water $\theta_{\mathrm{i}} - \phi_{\mathrm{nat}}$ is routed upwards, while above-lying soil constituents are routed downwards, following the scheme proposed by Lee et al. (2014). Thawing of an excess ice layer of thickness Δp thus results in a net subsidence (Δs) of the ground surface:

$$\Delta s = \Delta p \underbrace{\frac{\theta_{\mathrm{i}} - \phi_{\mathrm{nat}}}{1 - \phi_{\mathrm{nat}}}}_{\theta_{\mathrm{x}}} , \tag{2}$$

where θ_{x} denotes the excess ice content of the ice-rich soil layer.

The thermal regime and thaw processes in ice-rich permafrost are further controlled by lateral fluxes of mass and energy at subgrid-scales. We used the concept of laterally coupled tiles (Langer et al., 2016; Nitzbon et al., 2019) to represent subgrid heterogeneity of permafrost terrain (see Section 2.3.2 for details). We followed Nitzbon et al. (2019) to represent lateral fluxes of heat, water, and snow between adjacent tiles at the micro-scale. Furthermore, we included micro-scale advective sediment transport due to slumping, following the scheme introduced by Nitzbon et al. (2020). For this study, we advanced the model capacities by taking into account lateral fluxes of water on the meso-scale, for which we further distinguished between surface fluxes and subsurface contributions. Both surface and subsurface fluxes were calculated according to a gradient in water table elevations following Darcy's law, but the hydraulic conductivities differed considerably ($K^{\mathrm{subs}} = 10^{-5}\,\mathrm{m\,s^{-1}}$, $K^{\mathrm{surf}} = 10^{-2}\,\mathrm{m\,s^{-1}}$; see Appendix A for details). Finally, our model allowed for lateral drainage of water, by assuming an external reservoir at a fixed elevation (e_{res}) and a constant effective hydraulic conductivity ($K_{\mathrm{res}} = 2\pi K_{\mathrm{subs}}$) as hydrological boundary condition for a tile.

2.3.2 Multi-scale hierarchical tiling

For the present study, we extended the concept of laterally coupled tiles (Langer et al., 2016; Nitzbon et al., 2019) to a multi-scale hierarchical approach that allows to represent the subgrid-scale heterogeneity of permafrost terrain in general, and of thermokarst processes in particular. The multi-scale tiling hierarchy can flexibly be adapted to represent heterogeneous permafrost landscapes and features across several spatial scales. Different numbers of micro-scale tiles (N^{μ}) and meso-scale tiles (N^{m}) are used to reflect heterogeneity at different subgrid-scales. Each of the tiles is associated with a one-dimensional representation of the subsurface.

While the concept of the multi-scale tiling is very general, we applied it for the present study to create the subsequent four model setups (see Figure 2):

- *Homogeneous* ($N^{\mu} = 1$, $N^{\mathrm{m}} = 1$, Figure 2 a): This is the most simple case which reflects homogeneous surface and subsurface conditions across all spatial scales via only one tile (H). Water can drain laterally into an external reservoir at a fixed elevation (e_{res}). This setup comes closest to the simplistic representation of permafrost in ESMs and corresponds to the set-up for the simulations presented in Westermann et al. (2016).

- *Polygon* ($N^{\mu} = 3$, $N^{\mathrm{m}} = 1$, Figure 2 b): This setting reflects the micro-scale heterogeneity associated with ice-wedge polygons via three tiles: polygon centers (C), polygon rims (R) and inter-polygonal troughs (T). The heterogeneity of the surface topography is expressed in different initial elevations of the soil surface of the tiles. The subsurface stratigraphies of the tiles differ with respect to the depth (d_{x}) and amount (θ_{x}) of excess ice, reflecting the network of ice wedges linked to the polygonal surface pattern. Lateral fluxes of heat, water, snow, and sediment is enabled among the tiles, and the trough tile is connected to an external water reservoir. This configuration has been used by Nitzbon et al. (2019) and Nitzbon et al. (2020). The characteristics of the polygon setting are summarized in Table 3.

- *Homogeneous landscape* ($N^{\mu} = 1$, $N^{\mathrm{m}} = 3$, Figure 2 c): This setup reflects a meso-scale gradient of slope S^{m}, for which the outer tile (H^{o}) is connected to a low-lying reservoir (well-drained). The intermediate (H^{m}) and inner (H^{i}) tiles represent the landscape upslope of the well-drained tile (drainage point) at constant distances (D^{m}). The setting assumes a translational symmetry perpendicular to the direction of the slope, i.e. each tile represents an equal total area at the meso-scale. Lateral surface and subsurface water fluxes are enabled among the meso-scale tiles, while lateral heat fluxes as treated by Langer et al. (2016) were not considered in this study.

- *Polygon landscape* ($N^{\mu} = 3$, $N^{\mathrm{m}} = 3$, Figure 2 d): This setup reflects a meso-scale slope featuring ice-wedge polygons at the micro-scale. Each meso-scale tile is represented by three tiles (C,R,T) at the micro-scale, corresponding to the *polygon* setup described above. However, only the trough tile of the outer polygon (T^{o}) is connected to a low-lying reservoir (well-drained), and the intermediate and inner troughs are hydrologically connected along the meso-scale slope.

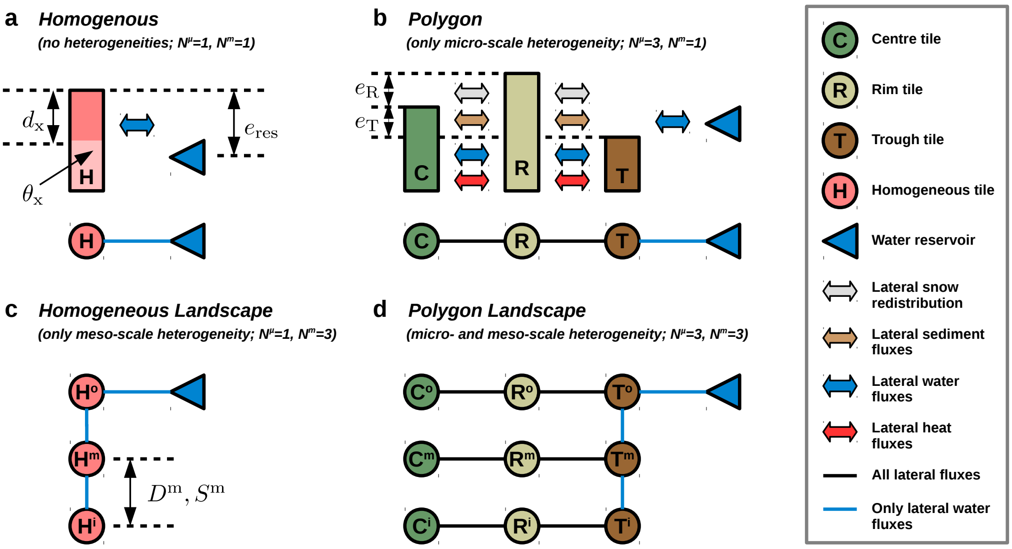
a Homogenous
(no heterogeneities; Nμ=1, Nm=1)
d_x
θ_x
e_{res}
H
b Polygon
(only micro-scale heterogeneity; Nμ=3, Nm=1)
e_R
e_T
C
R
T
c Homogeneous Landscape
(only meso-scale heterogeneity; Nμ=1, Nm=3)
Ho
Hm
Hi
D^m, S^m
d Polygon Landscape
(micro- and meso-scale heterogeneity; Nμ=3, Nm=3)
Co Ro To
Cm Rm Tm
Ci Ri Ti
C Centre tile
R Rim tile
T Trough tile
H Homogeneous tile
Water reservoir
Lateral snow redistribution
Lateral sediment fluxes
Lateral water fluxes
Lateral heat fluxes
All lateral fluxes
Only lateral water fluxes

Figure 2. Overview of the the different tile-based model setups used to represent heterogeneity at micro- and meso-scales. The depth of excess ice (d_x) and the excess ice content (θ_x) determine the distribution of excess ground ice in each of the tiles. An external reservoir (blue triangle) at a fixed elevation (e_{res}) prescribes the hydrological boundary conditions. Note that d_x and θ_x for the simple tile are chosen such that they correspond to the area-weighted mean of the three tiles of the polygon setup.

a: The *homogeneous* setup used only one tile (H) and does not reflect any subgrid-scale heterogeneity.

b: The *polygon* setup reflects micro-scale heterogeneity of topography and ground ice distribution associated with ice-wedge polygons via three tiles: polygon centres (C), polygon rims (R) and inter-polygonal troughs (T). The parameters e_R and e_T indicate the (initial) elevation of rims and troughs relative to the center. The micro-scale tiles are interacting through lateral fluxes of heat, water, snow, and sediment.

c: The *homogeneous landscape* setup reflects meso-scale heterogeneity of an ice-rich lowland via three tiles ($H^{o,m,i}$) of which the outer one (H^o) is connected to a draining reservoir. The intermediate (H^m) and inner tiles (H^i) are located at distances D^m along a low-gradient slope S^m. The meso-scale tiles are interacting through lateral surface and subsurface water fluxes.

d: The *polygon landscape* setup incorporates heterogeneities at both micro- and meso-scales via a total of nine tiles.

2.4 Model settings and simulations

2.4.1 Soil stratigraphies and ground ice distribution

The subsurface of all tiles is represented via a generic soil stratigraphy (Table 2). The stratigraphy is based on previous studies using CryoGrid 3 for the same study area (Nitzbon et al., 2019, 2020). It consists of two highly porous layers of 0.1 m thickness which reflect the surface vegetation and an organic-rich peat layer. Below that a mineral layer with silty texture follows. An excess ice layer of variable ice content θ_i extends from a variable depth d_x down to a depth of $10.0\,\mathrm{m}$. Between the variable excess ice layer and the mineral layer, an ice-rich intermediate layer of $0.2\,\mathrm{m}$ thickness is placed. Below the variable excess ice layer follow an ice-poor layer and bedrock down to the end of the model domain.

The default ice content assumed for the excess ice layer of homogeneous tiles (no micro-scale heterogeneity) was $\theta_\mathrm{i}^\mathrm{H} = 0.75$ and the default depth of this layer was $d_\mathrm{x} = 0.9\,\mathrm{m}$. To reflect the heterogeneous excess ice distribution associated with ice-wedge polygons, different ice contents were assumed for the excess ice layers of polygon centres ($\theta_\mathrm{i}^\mathrm{C} = 0.65$), rims ($\theta_\mathrm{i}^\mathrm{R} = 0.75$), and troughs ($\theta_\mathrm{i}^\mathrm{T} = 0.95$). However, the area-weighted mean excess ice content of ice-wedge polygon terrain is identical to the default value assumed for simple tiles (Table 3).

Table 2. Generic soil stratigraphy used to represent the subsurface of all tiles. An ice-rich layer of variable ice content (θ_i) is located at variable depth (d_x) from the surface. Note that the effective excess ice content (θ_x) is linked to the absolute ice content (θ_i) and the natural porosity (ϕ_nat) via the relation given in Equation (2). The soil texture is only used to parameterize the freezing-characteristic curve of the respective layer.

Depth from [m]	Depth to [m]	Mineral θ_m	Organic θ_o	Nat. por. ϕ_nat	Soil texture	Water θ_w^0	Comment
0	0.1	0	0.15	0.85	sand	0.85	Vegetation layer
0.1	0.2	0.10	0.15	0.75	sand	0.75	Organic layer
0.2	$d_\mathrm{x} - 0.2$	0.25	0.10	0.65	silt	0.65	Mineral layer
$d_\mathrm{x} - 0.2$	d_x	0.20	0.15	0.55	sand	0.65	Intermediate layer
d_x	10	$\frac{1.05-\theta_\mathrm{i}}{2}$	$\frac{0.95-\theta_\mathrm{i}}{2}$	0.55	sand	θ_i	Variable excess ice layer
10	30	0.50	0.05	0.45	sand	0.45	Ice-poor layer (Taberit)
30	1000	0.90	0	0.10	sand	0.10	Bedrock

2.4.2 Topography

For the *homogeneous* setup (Figure 2 a) the initial altitude of the soil surface was assumed to be $20.0\,\mathrm{m}$ above sea level, corresponding roughly to the altitude of the study area (see Section 2.2). This value does not affect the simulation results, but it serves as a reference for the variation of the micro- and meso-scale topographies. For the *polygon* setup (Figure 2 b) we assumed that the rims were elevated by $e_\mathrm{R} = 0.2\,\mathrm{m}$ relative to the polygon centres, while the troughs had the same altitude as the centres ($e_\mathrm{T} = 0.0\,\mathrm{m}$). While this choice of parameters varies slightly from the values assumed in previous studies (Nitzbon et al., 2019, 2020), it allows for consistent comparability to the setups without micro-scale heterogeneity (Table 3).

The meso-scale topography in the *homogeneous landscape* setup (Figure 2 c) was obtained by multiplying the meso-scale distances (D^m) with the slope of the terrain (S^m). We set $D^\mathrm{m} = 100\,\mathrm{m}$ and $S^\mathrm{m} = 0.001$ for all *landscape* setups, yielding elevations of $0.1\,\mathrm{m}$ and $0.2\,\mathrm{m}$ relative to the outer tile for the intermediate and inner tiles, respectively. The micro-scale topography of the *polygon landscape* setup (Figure 2 d) was obtained by adding up the relative topographic elevations of the meso- and micro-scales.

2.4.3 Topology

We made simplifying assumptions to determine the adjacency and geometrical relations such as distances and contact lengths between the tiles at the micro- and meso-scale. These topological characteristics determine the magnitude of lateral fluxes between the tiles, and only need to be specified if more than one tile is used to represent the respective scale. For the polygon setup at the micro-scale we assumed a geometry of a circle (C) surrounded by rings (R,T), following Nitzbon et al. (2020). This geometry is fully defined by specifying the total area (A^{μ}) of a single polygonal structure and the areal fractions ($\gamma_{\mathrm{C,R,T}}$) of the three tiles. Here we chose values which constitute a compromise between observations from the study area and comparability to the setups without micro-scale heterogeneity (Table 3). For this geometry, the micro-scale distances D^{μ} and contact lengths L^{μ} can be calculated as provided in the Supplementary Information to Nitzbon et al. (2020).

For the *landscape* setups with three meso-scale tiles we assumed translational symmetry of the landscape in the direction perpendicular to the direction of the gradient. Furthermore, the three meso-scale tiles were assumed to be at equal distances of $D^{\mathrm{m}} = 100\,\mathrm{m}$ from each other. Hence, each meso-scale tile is representative for the same areal fraction of the overall landscape. For the translational symmetry, it is sufficient to specify D^{m} in order to calculate the lateral surface and subsurface water fluxes.

Parameter	Symbol	Unit	Tile				
			C	R	T	∅ / Σ	H
Stratigraphy							
Depth of excess ice layer	d_{x}	[m]	1.0	0.9	0.7	0.9	0.9
Ice content of excess ice layer	θ_{i}	[-]	0.65	0.75	0.95	0.75	0.75
Topography and Topology							
Areal fraction	γ	[-]	$\frac{1}{3}$	$\frac{1}{2}$	$\frac{1}{6}$	1	1
Total area	A^{μ}	[m^2]	–	–	–	140	1
Initial elevation	e	[m]	0.0	0.2	0.0	0.1	0.0
Hydrological boundary conditions							
Reservoir elevation poorly-drained	$e_{\mathrm{res}}^{\mathrm{pd}}$	[m]	–	–	0.0	0.0	-0.1
Reservoir elevation well-drained	$e_{\mathrm{res}}^{\mathrm{wd}}$	[m]	–	–	-10.0	-10.0	-10.0

Table 3. Overview of the model parameters for different representations of the micro-scale. Elevation values are given relative to the initial altitude of the center tile ($a_{\mathrm{C}} = 20.0\,\mathrm{m}$). Note that on average the *polygon* setup (C,R,T) exhibits the same characteristics as the *homogeneous* setup (H). Note that setting the area of the simple tile to $A^{\mu} = 1\,\mathrm{m}^2$ is an arbitrary choice, as it cancels out during the calculation of the meso-scale fluxes due to the assumed symmetry.

2.4.4 Forcing data

We used the same meteorological forcing dataset which has been used in preceding studies based on CryoGrid 3 for the same study area (Westermann et al., 2016; Langer et al., 2016; Nitzbon et al., 2020). The dataset spans the period from 1901 until 2100 and is based on down-scaled CRU-NCEP v5.3 data for the period until 2014. For the period after 2014 climatic anomalies obtained from CCSM4 projections for the RCP8.5 scenarios were applied to a repeatedly appended base climatological period. A detailed description of how the forcing dataset was generated is provided by Westermann et al. (2016).

2.4.5 Simulations

To investigate the sensitivity to the micro-scale representation and to compare the *landscape* setup to the setups without meso-scale heterogeneity we conducted a total of six simulations. For each micro-scale representation (*homogeneous* versus *polygon*) we conducted three simulations under the RCP8.5 warming scenario: *well-drained*, *poorly-drained*, *landscape*. The well-drained and poorly-drained cases for the *polygon* setup correspond to the confining cases considered in Nitzbon et al. (2020), and reflect contrasting hydrological boundary conditions (Table 3). For the well-drained case, the elevation of external reservoir was set to $e_{\mathrm{res}}^{\mathrm{wd}} = -10.0\,\mathrm{m}$, independent of the micro-scale representation. For the poorly-drained case, the elevation of the external reservoir was set to $e_{\mathrm{res}}^{\mathrm{pd}} = -0.1\,\mathrm{m}$ (*homogeneous*) and $e_{\mathrm{res}}^{\mathrm{pd}} = 0.0\,\mathrm{m}$ (*polygon*), respectively. For the *landscape* simulations, only one tile ($\mathrm{H^o}$ and $\mathrm{T^o}$, respectively) was connected to an external reservoir (Fig. 2 c,d; $e_{\mathrm{res}}^{\mathrm{wd}} = -10.0\,\mathrm{m}$), while the hydrological boundary fluxes of the intermediate and inner tiles resulted from adjacent tiles only.

The subsurface temperatures of each model run were initialized in 10/1999 with a typical temperature profile for that time of year which was based on long-term borehole measurements from the study area (Boike et al., 2019). Using multi-year spin-up periods did not result in significant changes to the near-surface processes investigated in this study so that uncertainty related to the initial condition can be excluded. The analyzed simulation period was the twenty-first century from 01/2000 until 12/2099.

3 Results

3.1 Landscape evolution

3.1.1 Simulations without micro-scale heterogeneity

The simulated landscape evolution for selected years throughout the twenty-first century under RCP8.5 for all runs with a homogeneous micro-scale representation (setups presented in Fig. 2 a,c) is visualized in Figure 3.

Single-tile simulations: Until 2050 no excess ice melt and associated ground subsidence occur in both the well-drained and the poorly-drained single-tile simulations (Fig. 3 a–c, first and fifth column). Between 2050 and 2075 excess ice melt occurs in both single-tile simulations and leads to ground subsidence by about 0.2 m in the well-drained case, and by about 0.5 m in the poorly-drained case (Fig. 3 d, first and fifth column). In the poorly-drained simulation excess ice melt leads to the formation of a shallow surface water body. By 2100 total ground subsidence reaches almost 1.0 m in the well-drained simulation (Fig. 4 e, first column). In the poorly-drained simulation, excess ice melt proceeds faster than in the well-drained case, causing the surface water body to deepen, and to reach a depth of about 2.0 m by 2100 (Fig.3 e, fifth column). A talik of about about 1.5 m thickness has formed in this simulation by the end of the simulation period.

Landscape simulations: The simulated evolution of the outer tile in the landscape simulation is very similar to that of the well-drained single-tile throughout the simulation period (Fig. 3 first and second column). In the intermediate and inner tiles of the landscape simulation, melting of excess ice and associated ground subsidence occur during the first half of the simulation period, and there is a shallow layer of surface water (about 0.2 m) in these tiles (Fig. 3 a–c, third and fourth column). After 2050 excess ice melt proceeds faster and the surface water body in the intermediate and inner tiles reaches a depth of almost 1 m by 2075 (Fig. 3 d, third and fourth column). The permafrost table in these tiles lowered by about 2 m relative to its initial position. Between 2075 and 2100 a talik of about 2 m thickness forms beneath the water body in the two inland tiles (Fig. 3 e, third and fourth column). By 2100 the water body has a depth of about 1.5 m in both tiles.

The ground subsidence in the outer tile during the second half of the simulation leads to a lowering of the water level of the surface water body in the intermediate and inner tiles (Fig. 3 d–e). As a result, the surface water body depth by 2100 is about 1.5 m in the landscape simulation, while it is about 2.0 m in the poorly-drained single-tile simulation (Fig. 3 e, third to fifth column). This difference in water body depths is observed despite excess ice melt and surface water formation in the landscape simulation set on several decades earlier than in the poorly-drained single-tile simulation.

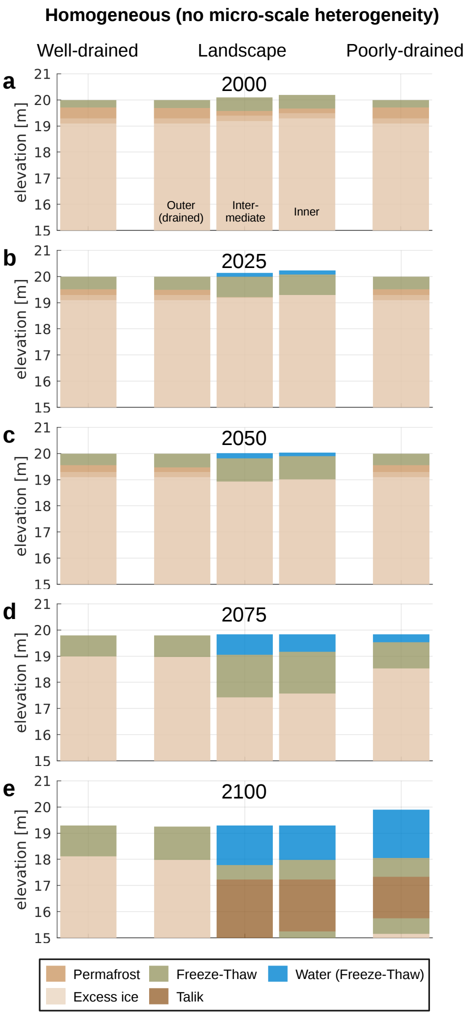

Figure 3. Landscape evolution in the simulations with a homogeneous micro-scale representation under the RCP8.5 warming scenario. The well-drained and poorly-drained cases correspond to the model setup without micro- or meso-scale heterogeneity (Fig. 2 a) and the landscape case corresponds to the model setup with only meso-scale heterogeneity (Fig. 2 c).

3.1.2 Simulations with micro-scale heterogeneity reflecting ice-wedge polygons

In analogy to Figure 3, Figure 4 illustrates the landscape evolution throughout the twenty-first century under RCP8.5 for the simulations with the micro-scale heterogeneity reflecting ice-wedge polygons. In addition, it shows the geomorphological state of the polygon micro-topography, i.e., whether it is low-centered (LCP), intermediate-centered (ICP), or high-centered (HCP), or turned into a water body (WB), according to the definitions in Nitzbon et al. (2020). Initially, all simulations feature undegraded ice-wedge polygons with an LCP micro-topography (Fig. 4 a).

Single-polygon simulations: Between 2000 and 2050, initial ice-wedge degradation occurs in the well-drained single-polygon simulation, indicated by subsiding troughs and a transition from the LCP to the ICP micro-topography (Fig. 4 a–c, first column). Between 2050 and 2075, substantial excess ice melt occurs in the trough and rim tile, leading to a transition to a pronounced HCP micro-topography for the well-drained polygons (Fig. 4 d, first column). The degradation continues until 2100, when the trough tile has subsided by about $2\,\mathrm{m}$, the rim tile by about $1\,\mathrm{m}$, and the center tile by more than $0.2\,\mathrm{m}$. As a consequence of the connection to a low-lying external reservoir (see Table 3) the well-drained polygon does not show any surface water formation throughout the simulation period.

In contrast, a shallow surface water body of about $0.5\,\mathrm{m}$ depth forms between 2000 and 2025 in the poorly-drained single-polygon simulation, as a result of excess ice melt in the center, rim, and trough tiles (Fig. 4 b, fifth column). The bottom of the water body has a high-centered topography. Little excess ice melt occurs in this polygon between 2025 and 2050 (Fig. 4 c, fifth column). After 2050 excess ice melt proceeds faster, causing the water body to deepen, reaching a depth between 1 m (center tile) and more than 2 m (trough tile) by 2075 (Fig. 4 d, fifth column). Until 2100 excess ice melt proceeds further, resulting in a water body depth of $2-4\,\mathrm{m}$ and the formation of an extended talik underneath (Fig. 4 e, fifth column). By the end of the simulation period, the lake is not entirely bottom-freezing in winter.

Polygon landscape simulation: The outer polygon in the landscape simulation shows a very similar evolution to the well-drained single-polygon throughout the entire simulation period (Fig. 4, first and second column). The intermediate and inner polygons show an evolution which is similar to each other, but different from both single-polygon simulations (Fig. 4, third and fourth column). Between 2000 and 2025 excess ice melt in the rim and trough tiles cause the ponding of surface water in the intermediate and inner polygons (Fig. 4 b, third and fourth column) with the surface of the center being close to or elevated above the water table. Besides a lowering of the water table, the configuration of these high-centered polygons does not change much until 2050 (Fig. 4 c, third and fourth column). Between 2050 and 2075, excess ice melt continues, leading to a pronounced high-centered topography (Fig. 4 d, third and fourth column). Meanwhile, the surface water disappears from the rim and trough tiles, as a consequence of marked ice-wedge degradation in the outer polygon (Fig. 4 d, second column). The elevation in the trough tiles increases toward the inland tiles, allowing an efficient drainage of the entire landscape. After 2075 all polygons of the landscape simulation show a similar evolution, resulting in pronounced high-centered topographies with troughs about 2 m deep and rims that subsided by about 1 m by 2100. Note that between 2075 and 2100 the troughs of the intermediate and inner polygons subsided more than that of the outer polygon, so that the drainage efficiency is decreased and surface water starts to pond again in the intermediate and inner troughs (Fig. 4 e, third and fourth column).

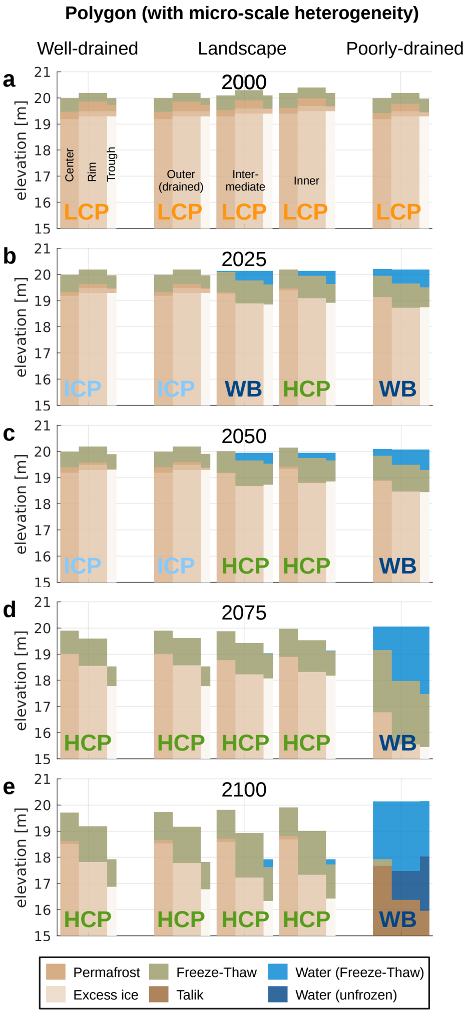

Figure 4. Landscape evolution in the simulations with a polygon micro-scale representation under the RCP8.5 warming scenario. The well-drained and poorly-drained cases correspond to the model setup with only micro-scale heterogeneity (Fig. 2 b) and the landscape case corresponds to the model setup with both micro- and meso-scale heterogeneity (Fig. 2 d). Note that the horizontal width of the tiles does not match with the vertical scale. Based on the relative soil surface elevations of the polygons, these were classified in to low-centered (LCP), intermediate-centered (ICP), high-centered (HCP), and water body (WB), following the definitions in Nitzbon et al. (2020). The same legend as in Fig. 3 applies.

3.2 Permafrost thaw and ground subsidence

The changes in the landscape configuration described in the previous section are linked to the degradation of ice-rich rich permafrost, which causes ground subsidence and alters lateral hydrological fluxes in the multi-tile settings. The projected quantitative changes in terms of maximum thawed ground depth and accumulated ground subsidence are displayed in more detail in Figure 5. Note that the sum of thaw-depth increase (i.e., active-layer-deepening) and accumulated ground subsidence correspond to the absolute lowering of the permafrost table.

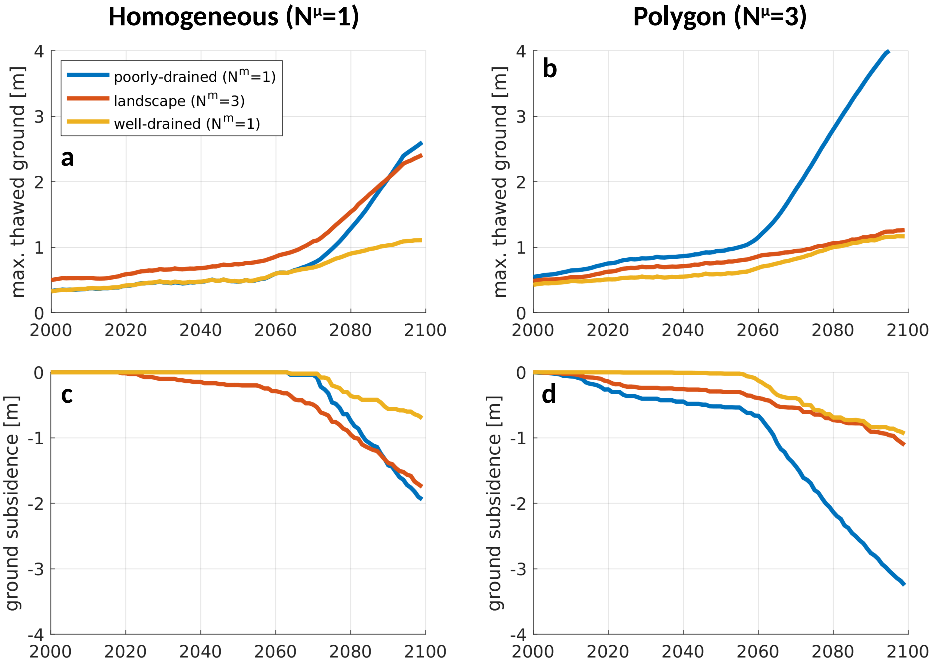

Figure 5. 11-year running mean of maximum annual thawed ground extent (a,b) and the accumulated ground subsidence (c,d) for different micro-scale representations (homogeneous and polygon).

3.2.1 Simulations without micro-scale heterogeneity

Maximum thawed ground: In all simulations without micro-scale heterogeneity, the maximum thawed ground extent increases steadily from less than 0.5 m in the year 2000 until it roughly has doubled around the years 2070 (Fig. 5 a). Throughout this period, thawed ground is slightly higher in the landscape simulation than in the single-tile simulations. The thawed ground extents in the single-tile simulations diverge during the last three decades of the simulation, with the increase being about two to three times faster in the poorly-drained (about 2.6 m in 2100) than in the well-drained simulation (about 1.1 m in 2100). Thawed ground extent in the landscape simulation also accelerates in the last three decades, to an intermediate increase rate, such that by 2100 it is about 2.4 m and thus lies within the range spanned by the two single-tile simulations under contrasting hydrological conditions, but closer to the poorly-drained simulation.

Ground subsidence: While ground subsidence starts already after about two decades in the landscape simulation, no subsidence occurs until about 2060 in both single-tile simulations (Fig. 5 c). The accumulated mean ground subsidence in the landscape simulation reaches about 0.3 m in 2060, and accelerates afterwards, reaching about 1.8 m in 2100. Ground subsidence in the single tile simulations sets on abruptly around the year 2070 and is about three times faster in the poorly-drained than in the well-drained simulation. By 2100, it reaches about 2.0 m in the poorly-drained case, and about 0.7 m in the well-drained, such that the landscape simulation is within the range spanned by the single-tile simulations, but closer to the poorly-drained simulation.

3.2.2 Simulations with micro-scale heterogeneity reflecting ice-wedge polygons

Maximum thawed ground: All simulations with polygons as the micro-scale representation, had a similar maximum thawed ground extent of about 0.5 m in 2000 (Fig. 5 b). This amount increased steadily until about 2060, but at different rates among the three simulations. The permafrost thaw rate is fastest for the poorly-drained single-polygon where the maximum thawed ground reaches about 1.2 m in 2060, and it is slowest for the well-drained single-polygon for which it reaches about 0.7 m by the same time. After 2060 the increase in the simulated thawed ground extents becomes faster in the single-tile simulations. By 2100 it reaches about 1.2 m in the well-drained simulation, and more than 4 m in the poorly-drained simulation. The mean thawed ground in the polygon landscape simulation lies within the range spanned by the two single-polygon simulations throughout the 21st century. However, during the last three to four decades, the increase does not accelerate such that it aligns more with the well-drained simulation, reaching a value of about 1.3 m by 2100. As a general pattern, thaw depths are consistently larger in the single-polygon simulations than in the single-tile simulations with homogeneous micro-scale representation. In contrast, the thaw depths in the polygon landscape simulation are consistently lower than in the homogeneous landscape simulation, particularly during the last three decades.

Ground subsidence: Excess ice melt and associated ground subsidence occur within the first decade in the poorly-drained single-polygon simulation and in the polygon landscape simulation, while the ground does not subside before 2050 in the poorly-drained polygon simulation (Fig. 5 d). As for the thawed ground discussed above, mean ground subsidence in the polygon landscape simulation is constrained by the two single-polygon simulations. By 2060, mean ground subsidence in the polygon landscape reaches about 0.4 m. During the last four decades, ground subsidence sets in and proceeds in the well-drained single-polygon simulation, reaching a value of about 1.0 m by 2100. In the poorly-drained single-polygon simulation, subsidence rates are about three times faster, reaching more than 3 m by 2100. In the polygon landscape simulation, subsidence rates do not accelerate markedly during the last decades and the mean total subsidence is close to that of the well-drained polygon by 2100. A similar general pattern as for the thaw depths is found for the accumulated subsidence. Simulated ground subsidence in the single-polygon simulations consistently exceeds the respective projections of the homogeneous single-tile simulations, while the mean ground subsidence by 2100 is substantially larger in the homogeneous landscape than in the polygon landscape.

4 Discussion

4.1 Simulating landscape degradation pathways under consideration of micro- and meso-scale heterogeneity

The multi-scale tiling approach employed in this study (see Section 2.3.2) facilitates the simulation of degradation pathways of ice-rich permafrost landscapes in response to a warming climate, under consideration of feedback processes emerging from heterogeneities and lateral fluxes on subgrid-scales. The most idealized cases considered were one-tile simulations without heterogeneities on the micro- or meso-scale (Fig. 2 a; Fig. 3 first and fifth column). Depending on the hydrological boundary conditions, these simulations reflect different real-world cases. Under well-drained conditions, the simulation reflects an “upland” setting for which steady ground subsidence was projected under RCP8.5 during the second half of the twenty-first century and no surface water can form. If drainage was precluded, the simulations projected the formation of a thaw lake to occur during the second half of the twenty-first century. While these model configurations correspond to the two cases considered by Westermann et al. (2016), the response of the presented simulations in this study differs both qualitatively and quantitatively. Overall, the projected permafrost degradation in this study is considerably lower than in the projections of Westermann et al. (2016) who assumed similar excess ice contents and used the same meteorological forcing data. This can most likely be attributed to the inclusion of a water balance into CryoGrid 3 (Nitzbon et al., 2019; Martin et al., 2019).

These simple cases, however, do not reflect a lot of processes observed in real-word landscapes, such as dynamically changing hydrological conditions due to lateral water fluxes. These have been taken into account in the homogeneous landscape setting (Fig. 2 c, 3 second to fourth column). Compared to the single-tile cases, the landscape evolution is affected by lateral interactions between different parts of the simulated landscape. Surface water formation in the inland parts is projected to occur earlier than in poorly-drained single-tile case, which can be attributed to very poor drainage along the low-gradient slope. Furthermore, the subsiding outer part causes a gradual drainage of the thaw lake in the inner part, such that it is substantially more shallow by the end of the simulation than in the poorly-drained single-tile case. Shallow water bodies favor bottom-freezing, such that the gradual lake drainage would constitute a stabilizing feedback on the ground thermal regime in the simulations. However, real world thaw lakes are also known to drain “catastrophically”, for example, upon the incision of a thermo-erosional gully as a result of either gully growth or lake expansion (Jones et al., 2011; Kessler et al., 2012). Both are a consequence of lateral erosion which is not represented in our model at the meso-scale. Besides feedbacks through meso-scale water fluxes, previous modeling studies demonstrated that the stability and the thermal regime of permafrost in the vicinity of thaw lakes is affected by meso-scale heat fluxes from taliks forming underneath the lakes (Rowland et al., 2011; Langer et al., 2016). These effects have not been considered in this study.

As suggested by several studies (Nitzbon et al., 2019; Abolt et al., 2020), the degradation pathways of ice-rich permafrost become more involved, if the micro-scale heterogeneity associated with ice-wedge polygons is taken into account, for example due to the lateral rerouting of surface and subsurface water according to the micro-scale topography. Here, we took into account micro-scale lateral fluxes of heat, water, snow, and sediment (see Fig. 2 b). The single-polygon simulations in this study correspond to the simulations for “Holocence Deposits” presented in Nitzbon et al. (2020) in terms of the ground ice distribution and the meteorological forcing data. Consequently, qualitatively identical landscape evolution pathways have been simulated (Fig. 4 first and fifth column). Under well-drained conditions the low-centred polygons evolve into high-centred polygons with a pronounced relief, while a deep thaw lake underlain by a talik has been simulated to from, under poorly-drained conditions. These two cases span a wide range of uncertainty in terms of projected permafrost degradation.

The simulation of the polygon landscape that takes into account meso-scale water fluxes (Fig. 2 d, Fig. 4 second to fourth column) has been conducted to provide a more realistic representation of heterogeneity in ice-rich terrain, and it revealed a subtle transient landscape evolution in response to climate warming. In that simulation surface water ponds early in the inland parts of the landscape, associated with initial ice-wedge degradation. The degradation is slowed down, however, by lateral transport of sediment (slumping) from the rims into the troughs (see Fig. 4 b–c, fourth column), such that the high-centred polygons are stabilized temporarily. During the second half of the twenty-first century, rapid ice-wedge degradation occurs in the outer part of the landscape, and the entire landscape drains as a consequence. Overall, the simulation reflects a transition from a low-gradient landscape of undegraded low-centered polygons to well-drained high-centered polygons within less than a century. This transient simulation thus corresponds to the schematic landscape evolution depicted by Liljedahl et al. (2016). This constitutes a significant improvement over the previous versions of the model (Nitzbon et al., 2019, 2020), for which it was not possible to simulate this type of landscape dynamics. It should further be noted that the simulated shifts in the subsurface hydrological regime have important consequences for whether the decomposition of soil organic carbon occurs under aerobic or anaerobic conditions (Lara et al., 2015; Schuur et al., 2015; Schädel et al., 2016; Knoblauch et al., 2018).

4.2 Constraining the response of ice-rich permafrost to a warming climate

Depending on the inclusion of landscape heterogeneities at different scales, the presented simulations reveal very different permafrost degradation trajectories (Fig. 5). Irrespective of the representation of micro-scale heterogeneity, the simulations under well-drained and poorly-drained conditions provide outer boundaries in terms of thaw and subsidence for the landscape simulations. The landscape-scale mean of the three-tile simulation without representation of micro-scale heterogeneity, revealed permafrost degradation trajectories which proceed slower than the poorly-drained case, but align closer to it than to the well-drained case. However, when the micro-scale was represented as ice-wedge polygons, the resulting degradation trajectories aligned closer to the well-drained case, as a consequence of the drainage network formation described in the previous section. The simulations thus indicate that the overall (landscape-mean) permafrost degradation, is crucially affected by small-scale heterogeneities, and that model projections have to be considered with care in light of these complexities. Hence, our simulations do not allow a final judgment with respect to whether the formation of new thaw lakes and taliks, or the formation of new drainage systems will dominate the evolution of real-world permafrost lowlands under a warming climate. For a more realistic assessment of the most likely response of ice-rich permafrost to climate warming, additional configurations than the two exemplary cases presented here would need to be considered, for example by incorporating also different meso-scale topologies which could correspond to different catchment geometries. This could also help to test the hypotheses on thaw lake abundance which underlie other models' projections of greenhouse gas emissions from thermokarst terrain (Schneider von Deimling et al., 2015; Walter Anthony et al., 2018).

Our simulations further suggest, that abrupt degradation of ice-rich permafrost across entire landscapes is less likely than spatially distributed and gradual degradation dynamics. When either micro- or meso-scale heterogeneities (or both) are taken into account in the simulations, the projected degradation trajectories are more gradual and steady than in the overly simplistic one-tile simulations (Fig. 5). The one-tile simulations show a relatively abrupt onset of subsidence and thaw-depth increase, and similar abrupt changes in ground thermal and hydrological regimes have been found using similarly simplistic model setup (Teufel and Sushama, 2019). We interpret our findings to suggest that abrupt responses of permafrost terrain to climate warming may occur locally, but are not likely at regional or even global scales.

4.3 Simulating the cyclic evolution of ice wedges and thaw lakes in thermokarst terrain

It has been suggested that thermokarst terrain evolves in a cyclic manner on centennial-to-millennial timescales. For example, the cycles of degradation and stabilization have been suggested to describe the evolution of ice wedges (Jorgenson et al., 2006, 2015; Kanevskiy et al., 2017) on these time scales. Similarly, but at a larger spatial scale, the cyclic evolution of thaw lakes has been hypothesized (Billings and Peterson, 1980) (see Grosse et al. (2013) for a review of the hypothesis). While we do not want to discuss to which extent ice-rich permafrost landscapes have been evolving or are evolving according to these models, we would like to point out that the model framework presented in this study, is in principle able to capture a wide range of the processes involved in these cycles. Figure 6 provides a schematic of the cyclic evolution of thermokarst terrain based and highlights the capacities of our model to simulate different pathways.

The initial and advanced degradation of ice wedges and the associated transition from low-centered to high-centered polygons was captured by the model setup by Nitzbon et al. (2019). Nitzbon et al. (2020) complemented this by the stabilizing of ice wedges due to sediment accumulation in the troughs, and also showed that it is possible to simulate ice-wedge collapse and thaw lake formation in response to climate warming scenarios. The simulations with representation of landscape heterogeneity and lateral water fluxes at the meso-scale, which are presented in this study, allow to capture further feedbacks. First, the formation of efficient drainage pathways through degrading ice-wedge networks, as depicted by Liljedahl et al. (2016), was qualitatively captured by the simulation using the polygon landscape setup (Fig. 2 d). While this drainage did not completely interrupt the ice-wedge degradation (as indicated in Fig. 6), it did lead to a significantly slower degradation compared to the simulations without meso-scale heterogeneity (Fig. 5 b,c). Second, representing meso-scale lateral water fluxes (Fig. 2 c,d) enables our model in principle to simulate the drainage of thaw lakes, which would result in the exposure of unfrozen ground (talik) to the atmosphere. While it is not possible to simulate the catastrophic drainage of lakes as discussed above, gradual subsidence of the terrain surrounding the thaw lake, can lead to its gradual drainage on longer timescales than considered here. It is further likely that using a model setup with a more complex meso-scale landscape topology, could result in more rapid drainage.

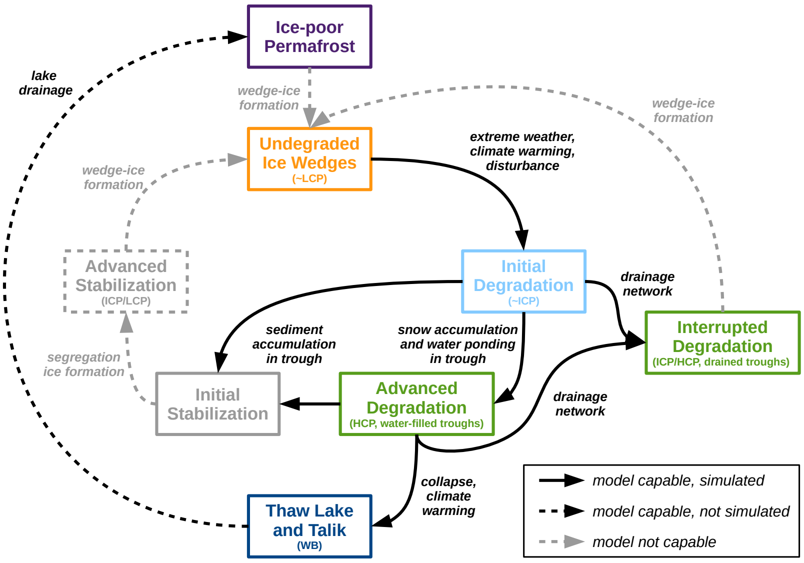
Ice-poor Permafrost
lake drainage
wedge-ice formation
wedge-ice formation
Undegraded Ice Wedges (~LCP)
extreme weather, climate warming, disturbance
wedge-ice formation
Advanced Stabilization (ICP/LCP)
Initial Degradation (~ICP)
drainage network
Interrupted Degradation (ICP/HCP, drained troughs)
sediment accumulation in trough
snow accumulation and water ponding in trough
segregation ice formation
Initial Stabilization
Advanced Degradation (HCP, water-filled troughs)
drainage network
collapse, climate warming
Thaw Lake and Talik (WB)
model capable, simulated
model capable, not simulated
model not capable

Figure 6. Schematic depiction of pathways of ice-rich permafrost landscape evolution as simulated within the presented model framework. The “inner” cycle reflects the cyclic evolution of ice wedges as described by Kanevskiy et al. (2017). The outer cycle involving the thaw lake stage reflects the thaw lake cylce as hypothesized by Billings and Peterson (1980). Formation of excess ice is lacking in the model such that the full cycles cannot be simulated. Adapted from Jorgenson et al. (2015) and Nitzbon et al. (2019).

As indicated in Fig. 6, several processes are not represented in our model, such that it cannot capture the full cycles of ice-rich permafrost evolution. In order to represent the initial stabilization of ice wedges more realistically, further ecological processes like vegetation succession and organic matter formation would need to be represented Jorgenson et al. (2015); Kanevskiy et al. (2017). However, lateral sediment transport into the troughs captures this stage to a certain extent. The advanced stabilization of ice wedges, involves the formation of ice-rich layers consisting of segregation ice above the massive ice wedge. The process of ice-segregation would require a more sophisticated subsurface hydrology scheme, representing the migration of liquid pore water towards the freezing front, as well as vertical displacement of sediment resulting from frost heave (O’Neill et al., 2019). Finally, and probably most importantly, the formation of wedge ice is not yet represented in the model, which is, however, necessary to from the initial stage of undegraded ice wedges from various other evolutionary stages (Fig. 6). In contrast to the formation of segregation ice, wedge-ice formation involves both vertical and horizontal processes, which presupposes the formation of frost cracks due to mechanical stress, which in turn is controlled by climatic conditions at the ground surface and at the top of permafrost (Lachenbruch, 1962).

5 Conclusions

In the present study, we employed a multi-scale hierarchical tiling approach in the CryoGrid 3 numerical model to assess the response of ice-rich permafrost landscapes in northeast Siberia to a warming climate. Specifically, we explored the sensitivity of the model simulations to different representations of micro- and meso-scale heterogeneities and lateral fluxes. From the results of this study, we draw the following conclusions:

1. Representing meso-scale heterogeneity and lateral fluxes allows to represent a wider range of permafrost degradation pathways under a warming climate, including, e.g., the large-scale drainage initiated by ice-wedge degradation or the dynamic formation and drainage of thaw lakes.

2. Representing micro-scale heterogeneity and lateral fluxes associated with ice-wedge polygons affects the timing and the rate of permafrost thaw, as well as the hydrological response to climate warming. In particular, the drainage network that evolves when ice wedges melt, favors large-scale drainage of the landscape and can impede new thaw lake formation.

3. Incorporating subgrid-scale heterogneities and lateral fluxes using a multi-scale tiling approach allows to constrain uncertainties in the response of ice-rich permafrost landscapes to a warming climate. The response of permafrost is more gradual in simulations representing subgrid-scale processes compared to abrupt changes projected by simple one-dimensional representations. Micro-scale lateral sediment transport is an example for a stabilizing process in ice-wedge terrain, which moderates rapid thaw processes.

4. Irrespective of uncertainties associated with future climate forcing, robust projections of the response of permafrost to climate change require solid knowledge on the distribution of (excess) ground ice on different scales, as well as information on topographic conditions (i.e., slope, connectivity, topology of drainage systems, etc.) which govern the meso-scale hydrology.

In summary, our work provides further constraints on projections of future permafrost degradation and landscape evolution in ice-rich lowland tundra of northeast Siberia, and contributes to the development of realistic and computationally efficient representations of the permafrost region in land surface schemes of ESMs.

6 Outlook

The presented modeling framework allows to reflect a multitude of transient degradation pathways and feedback processes in ice-rich permafrost landscapes and can thus contribute to an improved understanding of permafrost evolution in response to changing climatic conditions. In order to evaluate and validate the process representations in the model further, a next step would be to apply the model to different sites across the permafrost region, provided the necessary field data to set up and evaluate the simulations. Depending on site-specific or regional circumstances, the model would need to be extended by further parameterizations. For example, Zweigel et al. (2020) introduced an improved snow scheme into the CryoGrid model, in order to capture more complex snow dynamics at a high-Arctic permafrost site on Svalbard. Such case studies employing field data for validation will contribute to build confidence in permafrost models' projections in general, and in the CryoGrid framework in particular.

Besides such site-specific case studies, our model provides the opportunity to assess the response of (ice-rich) permafrost on regional to pan-Arctic scales. Given the sensitivity of permafrost thaw dynamics to subgrid-scale heterogeneity and lateral fluxes, we suggest that a combination of tiling concepts as presented in this study, and statistical methods such as model ensembles could provide more robust and realistic projections. Facilitating further abstraction of real-world landscapes in numerical models, methods from graph theory (i.e., network theory) could be explored as a potential technique to represent lateral processes such water transport across spatial scales (e.g., Zuecco et al. (2019)). The tiling setups depicted in Fig. 2 correspond to simple graph topologies.

Finally, remotely-sensed data that provide information on topographic and hydrological characteristics, such as the distance to a downstream drainage point, the upstream catchment area, or the slope, are an opportunity to inform and improve numerical model assessments. In addition, such data can be used to evaluate model performance under recent climatic conditions. For example, various recent studies addressed the mapping of ice-wedge polygon geomorphology based on high-resolution DEMs (e.g., Kartoziia (2019)), and machine-learning techniques are being developed to map ice-wedge polygons in increasingly large areas of hundreds of square kilometers (Abolt et al., 2019; Zhang et al., 2018; Abolt and Young, 2020; Zhang et al., 2020). In the future, time series of such high-resolution elevation data of ice-rich terrain, would allow better evaluation and improvement of numerical models like CryoGrid 3 that simulated elevation changes due to melting of excess ice (e.g., Wagner et al. (2018)). It is thus desirable, that high-resolution elevation models would become a key observable of long-term permafrost monitoring efforts, similar to the systematic monitoring of ground temperatures and active layer depths.

Code availability. The model code used and settings used for the simulations is available from https://github.com/CryoGrid/CryoGrid3/tree/xice_mpi_polygon_landscape. It will be permanently deposited upon acceptance of the manuscript. The code is published under the GNU General Public License v3.0.

Appendix A: Calculation of lateral surface and subsurface water fluxes

Lateral water fluxes (q_α $[\mathrm{m\,s^{-1}}]$) to a tile α from hydrologically connected tiles $\beta \in \mathcal{N}(\alpha)$ were calculated as the sum of surface and subsurface contributions:

$$q_\alpha = q_\alpha^{\text{surf}} + q_\alpha^{\text{subs}} \tag{A1}$$

Following Darcy's law, both surface and subsurface fluxes were assumed to be proportional to a gradient in the hydraulic heads (h), but assuming different saturated hydraulic conductivities ($K^{\text{surf/subs}}$) and contact heights ($H^{\text{surf/subs}}$):

$$q_\alpha^{\text{surf}} = \frac{1}{A_\alpha} \sum_{\beta \in \mathcal{N}(\alpha)} K_{\alpha\beta}^{\text{surf}} \frac{h_\beta - h_\alpha}{D_{\alpha\beta}} H_{\alpha\beta}^{\text{surf}} L_{\alpha\beta} \tag{A2}$$

$$q_\alpha^{\text{subs}} = \frac{1}{A_\alpha} \sum_{\beta \in \mathcal{N}(\alpha)} K_{\alpha\beta}^{\text{subs}} \frac{h_\beta - h_\alpha}{D_{\alpha\beta}} H_{\alpha\beta}^{\text{subs}} L_{\alpha\beta} \tag{A3}$$

where D is the distance between the tiles and L the contact length which have been introduced in Section 2.4.3. The hydraulic head of each tile was identified with the water table elevation (w), or the frost table elevation (f) if no water table was present $(h = \max(w, f))$. The contact heights for the surface and subsurface fluxes were obtained as follows:

$$H_{\alpha\beta}^{\text{surf}} = \max(0, h^{\max} - \max(s^{\max}, f^{\max})) \tag{A4}$$

$$H_{\alpha\beta}^{\text{subs}} = \max(0, \min(h^{\max} - f^{\max}, s^{\max} - f^{\max})) \tag{A5}$$

where $h^{\max} = \max(h_\alpha, h_\beta)$ is the maximum hydraulic head, $s^{\max} = \max(s_\alpha, s_\beta)$ is the maximum soil surface elevation, and $f^{\max} = \max(f_\alpha, f_\beta)$ is the maximum frost table elevation of the two involved tiles. As described in Nitzbon et al. (2019), lateral water fluxes were only applied, when both tiles were snow-free and the uppermost soil grid cell unfrozen.

Author contributions. J.N. designed the study, conducted the numerical simulations, analyzed the results, and led the manuscript preparations. L.M and T.S.v.D. contributed to the model development. M.L., S.W. and J.B. co-designed the study. All authors interpreted the simulation results and contributed to the manuscript preparation.

Competing interests. The authors declare that they have no conflict of interests.

Acknowledgements. The authors gratefully acknowledge the Climate Geography Group at the Humboldt-Universität zu Berlin for providing resources on their high-performance-computer system. This work was supported by a grant of the Research Council of Norway (project PERMANOR, grant no. 255331). J.N. was supported by the Geo.X Research Network. M.L. was supported by a BMBF grant (project PermaRisk, grant no. 01LN1709A). S.W. acknowledges funding through Nunataryuk (EU grant agreement no. 773421).

References

Aas, K. S., Martin, L., Nitzbon, J., Langer, M., Boike, J., Lee, H., Berntsen, T. K., and Westermann, S.: Thaw processes in ice-rich permafrost landscapes represented with laterally coupled tiles in a land surface model, The Cryosphere, 13, 591–609, https://doi.org/10.5194/tc-13-591-2019, 2019.

Abolt, C. J. and Young, M. H.: High-resolution mapping of spatial heterogeneity in ice wedge polygon geomorphology near Prudhoe Bay, Alaska, Scientific Data, 7, 1–7, https://doi.org/10.1038/s41597-020-0423-9, 2020.

Abolt, C. J., Young, M. H., Atchley, A. L., and Harp, D. R.: Microtopographic control on the ground thermal regime in ice wedge polygons, The Cryosphere, 12, 1957–1968, https://doi.org/10.5194/tc-12-1957-2018, 2018.

Abolt, C. J., Young, M. H., Atchley, A. L., and Wilson, C. J.: Brief communication: Rapid machine-learning-based extraction and measurement of ice wedge polygons in high-resolution digital elevation models, The Cryosphere, 13, 237–245, https://doi.org/https://doi.org/10.5194/tc-13-237-2019, 2019.

Abolt, C. J., Young, M. H., Atchley, A. L., Harp, D. R., and Coon, E. T.: Feedbacks Between Surface Deformation and Permafrost Degradation in Ice Wedge Polygons, Arctic Coastal Plain, Alaska, Journal of Geophysical Research: Earth Surface, 125, e2019JF005 349, https://doi.org/10.1029/2019JF005349, 2020.

AMAP: Snow, Water, Ice and Permafrost in the Arctic (SWIPA) 2017, Arctic Monitoring and Assessment Programme, Oslo, Norway, oCLC: 1038467657, 2017.

Andresen, C. G., Lawrence, D. M., Wilson, C. J., McGuire, A. D., Koven, C., Schaefer, K., Jafarov, E., Peng, S., Chen, X., Gouttevin, I., Burke, E., Chadburn, S., Ji, D., Chen, G., Hayes, D., and Zhang, W.: Soil moisture and hydrology projections of the permafrost region – a model intercomparison, The Cryosphere, 14, 445–459, https://doi.org/https://doi.org/10.5194/tc-14-445-2020, 2020.

Billings, W. D. and Peterson, K. M.: Vegetational Change and Ice-Wedge Polygons through the Thaw-Lake Cycle in Arctic Alaska, Arctic and Alpine Research, 12, 413–432, https://doi.org/10.1080/00040851.1980.12004204, 1980.

Biskaborn, B. K., Smith, S. L., Noetzli, J., Matthes, H., Vieira, G., Streletskiy, D. A., Schoeneich, P., Romanovsky, V. E., Lewkowicz, A. G., Abramov, A., Allard, M., Boike, J., Cable, W. L., Christiansen, H. H., Delaloye, R., Diekmann, B., Drozdov, D., Etzelmüller, B., Grosse, G., Guglielmin, M., Ingeman-Nielsen, T., Isaksen, K., Ishikawa, M., Johansson, M., Johannsson, H., Joo, A., Kaverin, D., Kholodov, A., Konstantinov, P., Kröger, T., Lambiel, C., Lanckman, J.-P., Luo, D., Malkova, G., Meiklejohn, I., Moskalenko, N., Oliva, M., Phillips, M., Ramos, M., Sannel, A. B. K., Sergeev, D., Seybold, C., Skryabin, P., Vasiliev, A., Wu, Q., Yoshikawa, K., Zheleznyak, M., and Lantuit, H.: Permafrost is warming at a global scale, Nature Communications, 10, 264, https://doi.org/10.1038/s41467-018-08240-4, 2019.

Boike, J., Wille, C., and Abnizova, A.: Climatology and summer energy and water balance of polygonal tundra in the Lena River Delta, Siberia, Journal of Geophysical Research, 113, https://doi.org/10.1029/2007JG000540, 2008.

Boike, J., Kattenstroth, B., Abramova, K., Bornemann, N., Chetverova, A., Fedorova, I., Fröb, K., Grigoriev, M., Grüber, M., Kutzbach, L., Langer, M., Minke, M., Muster, S., Piel, K., Pfeiffer, E.-M., Stoof, G., Westermann, S., Wischnewski, K., Wille, C., and Hubberten, H.-W.: Baseline characteristics of climate, permafrost and land cover from a new permafrost observatory in the Lena River Delta, Siberia (1998–2011), Biogeosciences, 10, 2105–2128, https://doi.org/10.5194/bg-10-2105-2013, 2013.

Boike, J., Nitzbon, J., Anders, K., Grigoriev, M., Bolshiyanov, D., Langer, M., Lange, S., Bornemann, N., Morgenstern, A., Schreiber, P., Wille, C., Chadburn, S., Gouttevin, I., Burke, E., and Kutzbach, L.: A 16-year record (2002–2017) of permafrost, active-layer, and meteorological conditions at the Samoylov Island Arctic permafrost research site, Lena River delta, northern Siberia: an opportunity to validate remote-sensing data and land surface, snow, and permafrost models, Earth System Science Data, 11, 261–299, https://doi.org/10.5194/essd-11-261-2019, 2019.

Farquharson, L. M., Romanovsky, V. E., Cable, W. L., Walker, D. A., Kokelj, S. V., and Nicolsky, D.: Climate Change Drives Widespread and Rapid Thermokarst Development in Very Cold Permafrost in the Canadian High Arctic, Geophysical Research Letters, 46, 6681–6689, https://doi.org/10.1029/2019GL082187, 2019.

Fortier, D., Allard, M., and Shur, Y.: Observation of rapid drainage system development by thermal erosion of ice wedges on Bylot Island, Canadian Arctic Archipelago, Permafrost and Periglacial Processes, 18, 229–243, https://doi.org/10.1002/ppp.595, 2007.

Godin, E., Fortier, D., and Coulombe, S.: Effects of thermo-erosion gullying on hydrologic flow networks, discharge and soil loss, Environmental Research Letters, 9, 105 010, https://doi.org/10.1088/1748-9326/9/10/105010, 2014.

Gouttevin, I., Langer, M., Löwe, H., Boike, J., Proksch, M., and Schneebeli, M.: Observation and modelling of snow at a polygonal tundra permafrost site: spatial variability and thermal implications, The Cryosphere, 12, 3693–3717, https://doi.org/https://doi.org/10.5194/tc-12-3693-2018, 2018.

Grosse, G., Jones, B., and Arp, C.: 8.21 Thermokarst Lakes, Drainage, and Drained Basins, in: Treatise on Geomorphology, edited by Shroder, J. F., pp. 325–353, Academic Press, San Diego, https://doi.org/10.1016/B978-0-12-374739-6.00216-5, 2013.

Hjort, J., Karjalainen, O., Aalto, J., Westermann, S., Romanovsky, V. E., Nelson, F. E., Etzelmüller, B., and Luoto, M.: Degrading permafrost puts Arctic infrastructure at risk by mid-century, Nature Communications, 9, https://doi.org/10.1038/s41467-018-07557-4, 2018.

Jafarov, E. E., Coon, E. T., Harp, D. R., Wilson, C. J., Painter, S. L., Atchley, A. L., and Romanovsky, V. E.: Modeling the role of preferential snow accumulation in through talik development and hillslope groundwater flow in a transitional permafrost landscape, Environmental Research Letters, 13, 105 006, https://doi.org/10.1088/1748-9326/aadd30, 2018.

Jones, B. M., Grosse, G., Arp, C. D., Jones, M. C., Anthony, K. M. W., and Romanovsky, V. E.: Modern thermokarst lake dynamics in the continuous permafrost zone, northern Seward Peninsula, Alaska, Journal of Geophysical Research: Biogeosciences, 116, https://doi.org/10.1029/2011JG001666, 2011.

Jorgenson, M. T., Shur, Y. L., and Pullman, E. R.: Abrupt increase in permafrost degradation in Arctic Alaska, Geophysical Research Letters, 33, https://doi.org/10.1029/2005GL024960, 2006.

Jorgenson, M. T., Kanevskiy, M., Shur, Y., Moskalenko, N., Brown, D. R. N., Wickland, K., Striegl, R., and Koch, J.: Role of ground ice dynamics and ecological feedbacks in recent ice wedge degradation and stabilization, Journal of Geophysical Research: Earth Surface, 120, 2280–2297, https://doi.org/10.1002/2015JF003602, 2015.

Kanevskiy, M., Shur, Y., Jorgenson, T., Brown, D. R., Moskalenko, N., Brown, J., Walker, D. A., Raynolds, M. K., and Buchhorn, M.: Degradation and stabilization of ice wedges: Implications for assessing risk of thermokarst in northern Alaska, Geomorphology, 297, 20–42, https://doi.org/10.1016/j.geomorph.2017.09.001, 2017.

Kartoziia, A.: Assessment of the Ice Wedge Polygon Current State by Means of UAV Imagery Analysis (Samoylov Island, the Lena Delta), Remote Sensing, 11, 1627, https://doi.org/10.3390/rs11131627, 2019.

Kessler, M. A., Plug, L. J., and Anthony, K. M. W.: Simulating the decadal- to millennial-scale dynamics of morphology and sequestered carbon mobilization of two thermokarst lakes in NW Alaska, Journal of Geophysical Research: Biogeosciences, 117, G00M06, https://doi.org/10.1029/2011JG001796, 2012.

Knoblauch, C., Beer, C., Liebner, S., Grigoriev, M. N., and Pfeiffer, E.-M.: Methane production as key to the greenhouse gas budget of thawing permafrost, Nature Climate Change, 8, 309–312, https://doi.org/10.1038/s41558-018-0095-z, 2018.

Kokelj, S. V. and Jorgenson, M. T.: Advances in Thermokarst Research, Permafrost and Periglacial Processes, 24, 108–119, https://doi.org/10.1002/ppp.1779, 2013.

Lachenbruch, A. H.: Mechanics of Thermal Contraction Cracks and Ice-Wedge Polygons in Permafrost, in: Geological Society of America Special Papers, vol. 70, pp. 1–66, Geological Society of America, https://doi.org/10.1130/SPE70-p1, 1962.

Langer, M., Westermann, S., Muster, S., Piel, K., and Boike, J.: The surface energy balance of a polygonal tundra site in northern Siberia - Part 2: Winter, The Cryosphere, 5, 509–524, https://doi.org/10.5194/tc-5-509-2011, 2011a.

Langer, M., Westermann, S., Muster, S., Piel, K., and Boike, J.: The surface energy balance of a polygonal tundra site in northern Siberia - Part 1: Spring to fall, The Cryosphere, 5, 151–171, https://doi.org/10.5194/tc-5-151-2011, 2011b.

Langer, M., Westermann, S., Boike, J., Kirillin, G., Grosse, G., Peng, S., and Krinner, G.: Rapid degradation of permafrost underneath waterbodies in tundra landscapes—Toward a representation of thermokarst in land surface models, Journal of Geophysical Research: Earth Surface, 121, 2446–2470, https://doi.org/10.1002/2016JF003956, 2016.

Lara, M. J., McGuire, A. D., Euskirchen, E. S., Tweedie, C. E., Hinkel, K. M., Skurikhin, A. N., Romanovsky, V. E., Grosse, G., Bolton, W. R., and Genet, H.: Polygonal tundra geomorphological change in response to warming alters future CO2 and CH4 flux on the Barrow Peninsula, Global Change Biology, 21, 1634–1651, https://doi.org/10.1111/gcb.12757, 2015.

Lawrence, D. M., Slater, A. G., and Swenson, S. C.: Simulation of Present-Day and Future Permafrost and Seasonally Frozen Ground Conditions in CCSM4, Journal of Climate, 25, 2207–2225, https://doi.org/10.1175/JCLI-D-11-00334.1, 2012.

Lee, H., Swenson, S. C., Slater, A. G., and Lawrence, D. M.: Effects of excess ground ice on projections of permafrost in a warming climate, Environmental Research Letters, 9, 124 006, https://doi.org/10.1088/1748-9326/9/12/124006, 2014.

Liljedahl, A. K., Boike, J., Daanen, R. P., Fedorov, A. N., Frost, G. V., Grosse, G., Hinzman, L. D., Iijma, Y., Jorgenson, J. C., Matveyeva, N., Necsoiu, M., Raynolds, M. K., Romanovsky, V. E., Schulla, J., Tape, K. D., Walker, D. A., Wilson, C. J., Yabuki, H., and Zona, D.: Pan-Arctic ice-wedge degradation in warming permafrost and its influence on tundra hydrology, Nature Geoscience, 9, 312–318, https://doi.org/10.1038/ngeo2674, 2016.

Martin, L. C. P., Nitzbon, J., Aas, K. S., Etzelmüller, B., Kristiansen, H., and Westermann, S.: Stability Conditions of Peat Plateaus and Palsas in Northern Norway, Journal of Geophysical Research: Earth Surface, https://doi.org/10.1029/2018JF004945, 2019.

Muster, S., Langer, M., Heim, B., Westermann, S., and Boike, J.: Subpixel heterogeneity of ice-wedge polygonal tundra: a multi-scale analysis of land cover and evapotranspiration in the Lena River Delta, Siberia, Tellus B: Chemical and Physical Meteorology, 64, 17 301, https://doi.org/10.3402/tellusb.v64i0.17301, 2012.

Nitzbon, J., Langer, M., Westermann, S., Martin, L., Aas, K. S., and Boike, J.: Pathways of ice-wedge degradation in polygonal tundra under different hydrological conditions, The Cryosphere, 13, 1089–1123, https://doi.org/10.5194/tc-13-1089-2019, 2019.

Nitzbon, J., Westermann, S., Langer, M., Martin, L. C. P., Strauss, J., Laboor, S., and Boike, J.: Fast response of cold ice-rich permafrost in northeast Siberia to a warming climate, Nature Communications, 11, 2201, https://doi.org/10.1038/s41467-020-15725-8, 2020.

O'Neill, H. B., Wolfe, S. A., and Duchesne, C.: New ground ice maps for Canada using a paleogeographic modelling approach, The Cryosphere, 13, 753–773, https://doi.org/https://doi.org/10.5194/tc-13-753-2019, 2019.

Painter, S. L., Coon, E. T., Atchley, A. L., Berndt, M., Garimella, R., Moulton, J. D., Svyatskiy, D., and Wilson, C. J.: Integrated surface/subsurface permafrost thermal hydrology: Model formulation and proof-of-concept simulations, Water Resources Research, 52, 6062–6077, https://doi.org/10.1002/2015WR018427, 2016.

Rowland, J. C., Jones, C. E., Altmann, G., Bryan, R., Crosby, B. T., Hinzman, L. D., Kane, D. L., Lawrence, D. M., Mancino, A., Marsh, P., McNamara, J. P., Romanvosky, V. E., Toniolo, H., Travis, B. J., Trochim, E., Wilson, C. J., and Geernaert, G. L.:

Arctic Landscapes in Transition: Responses to Thawing Permafrost, Eos, Transactions American Geophysical Union, 91, 229–230, https://doi.org/10.1029/2010EO260001, 2010.

Rowland, J. C., Travis, B. J., and Wilson, C. J.: The role of advective heat transport in talik development beneath lakes and ponds in discontinuous permafrost, Geophysical Research Letters, 38, https://doi.org/10.1029/2011GL048497, 2011.

Schneider von Deimling, T., Grosse, G., Strauss, J., Schirrmeister, L., Morgenstern, A., Schaphoff, S., Meinshausen, M., and Boike, J.: Observation-based modelling of permafrost carbon fluxes with accounting for deep carbon deposits and thermokarst activity, Biogeosciences, 12, 3469–3488, https://doi.org/10.5194/bg-12-3469-2015, 2015.

Schuur, E. A. and Mack, M. C.: Ecological Response to Permafrost Thaw and Consequences for Local and Global Ecosystem Services, Annual Review of Ecology, Evolution, and Systematics, 49, 279–301, https://doi.org/10.1146/annurev-ecolsys-121415-032349, 2018.

Schuur, E. A. G., McGuire, A. D., Schädel, C., Grosse, G., Harden, J. W., Hayes, D. J., Hugelius, G., Koven, C. D., Kuhry, P., Lawrence, D. M., Natali, S. M., Olefeldt, D., Romanovsky, V. E., Schaefer, K., Turetsky, M. R., Treat, C. C., and Vonk, J. E.: Climate change and the permafrost carbon feedback, Nature, 520, 171–179, https://doi.org/10.1038/nature14338, 2015.

Schwamborn, G., Rachold, V., and Grigoriev, M. N.: Late Quaternary sedimentation history of the Lena Delta, Quaternary International, 89, 119–134, https://doi.org/10.1016/S1040-6182(01)00084-2, 2002.

Schädel, C., Bader, M. K.-F., Schuur, E. A. G., Biasi, C., Bracho, R., Čapek, P., De Baets, S., Diáková, K., Ernakovich, J., Estop-Aragones, C., Graham, D. E., Hartley, I. P., Iversen, C. M., Kane, E., Knoblauch, C., Lupascu, M., Martikainen, P. J., Natali, S. M., Norby, R. J., O'Donnell, J. A., Chowdhury, T. R., Šantrůčková, H., Shaver, G., Sloan, V. L., Treat, C. C., Turetsky, M. R., Waldrop, M. P., and Wickland, K. P.: Potential carbon emissions dominated by carbon dioxide from thawed permafrost soils, Nature Climate Change, 6, 950–953, https://doi.org/10.1038/nclimate3054, 2016.

Slater, A. G. and Lawrence, D. M.: Diagnosing Present and Future Permafrost from Climate Models, Journal of Climate, 26, 5608–5623, https://doi.org/10.1175/JCLI-D-12-00341.1, 2013.

Teufel, B. and Sushama, L.: Abrupt changes across the Arctic permafrost region endanger northern development, Nature Climate Change, 9, 858–862, https://doi.org/10.1038/s41558-019-0614-6, 2019.

Turetsky, M. R., Abbott, B. W., Jones, M. C., Walter Anthony, K., Olefeldt, D., Schuur, E. A. G., Koven, C., McGuire, A. D., Grosse, G., Kuhry, P., Hugelius, G., Lawrence, D. M., Gibson, C., and Sannel, A. B. K.: Permafrost collapse is accelerating carbon release, Nature, 569, 32–34, https://doi.org/10.1038/d41586-019-01313-4, 2019.

Turetsky, M. R., Abbott, B. W., Jones, M. C., Anthony, K. W., Olefeldt, D., Schuur, E. A. G., Grosse, G., Kuhry, P., Hugelius, G., Koven, C., Lawrence, D. M., Gibson, C., Sannel, A. B. K., and McGuire, A. D.: Carbon release through abrupt permafrost thaw, Nature Geoscience, 13, 138–143, https://doi.org/10.1038/s41561-019-0526-0, 2020.

Vincent, W. F., Lemay, M., and Allard, M.: Arctic permafrost landscapes in transition: towards an integrated Earth system approach, Arctic Science, 3, 39–64, https://doi.org/10.1139/as-2016-0027, 2017.

Wagner, A. M., Lindsey, N. J., Dou, S., Gelvin, A., Saari, S., Williams, C., Ekblaw, I., Ulrich, C., Borglin, S., Morales, A., and Ajo-Franklin, J.: Permafrost Degradation and Subsidence Observations during a Controlled Warming Experiment, Scientific Reports, 8, 1–9, https://doi.org/10.1038/s41598-018-29292-y, 2018.

Walter Anthony, K., Deimling, T. S. v., Nitze, I., Frolking, S., Emond, A., Daanen, R., Anthony, P., Lindgren, P., Jones, B., and Grosse, G.: 21st-century modeled permafrost carbon emissions accelerated by abrupt thaw beneath lakes, Nature Communications, 9, 3262, https://doi.org/10.1038/s41467-018-05738-9, 2018.

Westermann, S., Langer, M., Boike, J., Heikenfeld, M., Peter, M., Etzelmüller, B., and Krinner, G.: Simulating the thermal regime and thaw processes of ice-rich permafrost ground with the land-surface model CryoGrid 3, Geosci. Model Dev., 9, 523–546, https://doi.org/10.5194/gmd-9-523-2016, 2016.

Zhang, W., Witharana, C., Liljedahl, A., Kanevskiy, M., Zhang, W., Witharana, C., Liljedahl, A. K., and Kanevskiy, M.: Deep Convolutional Neural Networks for Automated Characterization of Arctic Ice-Wedge Polygons in Very High Spatial Resolution Aerial Imagery, Remote Sensing, 10, 1487, https://doi.org/10.3390/rs10091487, 2018.

Zhang, W., Liljedahl, A. K., Kanevskiy, M., Epstein, H. E., Jones, B. M., Jorgenson, M. T., and Kent, K.: Transferability of the Deep Learning Mask R-CNN Model for Automated Mapping of Ice-Wedge Polygons in High-Resolution Satellite and UAV Images, Remote Sensing, 12, 1085, https://doi.org/10.3390/rs12071085, 2020.

Zuecco, G., Rinderer, M., Penna, D., Borga, M., and van Meerveld, H. J.: Quantification of subsurface hydrologic connectivity in four headwater catchments using graph theory, Science of The Total Environment, 646, 1265–1280, https://doi.org/10.1016/j.scitotenv.2018.07.269, 2019.

Zweigel, R., Westermann, S., Nitzbon, J., Langer, M., Boike, J., Etzelmüller, B., and Vikhamar Schuler, T.: Simulating snow redistribution and its effect on the ground thermal regime at a high-Arctic site on Svalbard, Journal of Geophysical Research: Earth Surface, in review, 2020.

Bibliography

Aas, K. S., L. Martin, J. Nitzbon, M. Langer, J. Boike, H. Lee, T. K. Berntsen, and S. Westermann (2019): 'Thaw processes in ice-rich permafrost landscapes represented with laterally coupled tiles in a land surface model'. *The Cryosphere*, vol. 13(2): pp. 591–609. doi: `10.5194/tc-13-591-2019` (cit. on p. 38).

Aas, K. S., K. Gisnås, S. Westermann, and T. K. Berntsen (2017): 'A Tiling Approach to Represent Subgrid Snow Variability in Coupled Land Surface–Atmosphere Models'. *Journal of Hydrometeorology*, vol. 18(1): pp. 49–63. doi: `10.1175/JHM-D-16-0026.1` (cit. on p. 23).

Abolt, C. J., M. H. Young, A. L. Atchley, and D. R. Harp (2018): 'Microtopographic control on the ground thermal regime in ice wedge polygons'. *The Cryosphere*, vol. 12(6): pp. 1957–1968. doi: `10.5194/tc-12-1957-2018` (cit. on p. 10).

Abolt, C. J. and M. H. Young (2020a): 'High-resolution mapping of spatial heterogeneity in ice wedge polygon geomorphology near Prudhoe Bay, Alaska'. *Scientific Data*, vol. 7: p. 87. doi: `10.1038/s41597-020-0423-9`.

Abolt, C. J., M. H. Young, A. L. Atchley, D. R. Harp, and E. T. Coon (2020b): 'Feedbacks Between Surface Deformation and Permafrost Degradation in Ice Wedge Polygons, Arctic Coastal Plain, Alaska'. *Journal of Geophysical Research: Earth Surface*, vol. 125(3): e2019JF005349. doi: `10.1029/2019JF005349`.

Abolt, C. J., M. H. Young, A. L. Atchley, and C. J. Wilson (2019): 'Brief communication: Rapid machine-learning-based extraction and measurement of ice wedge polygons in high-resolution digital elevation models'. *The Cryosphere*, vol. 13(1): pp. 237–245. doi: `10.5194/tc-13-237-2019`.

Abolt, C. J., M. H. Young, and T. G. Caldwell (2017): 'Numerical Modelling of Ice-Wedge Polygon Geomorphic Transition'. *Permafrost and Periglacial Processes*, vol. 28(1): pp. 347–355. doi: `10.1002/ppp.1909`.

AMAP (2017): *Snow, Water, Ice and Permafrost in the Arctic (SWIPA) 2017*. OCLC: 1038467657. Oslo, Norway: Arctic Monitoring and Assessment Programme (cit. on p. 10).

Andresen, C. G. et al. (2020): 'Soil moisture and hydrology projections of the permafrost region – a model intercomparison'. *The Cryosphere*, vol. 14(2): pp. 445–459. doi: `10.5194/tc-14-445-2020` (cit. on p. 9).

Avissar, R. and R. A. Pielke (1989): 'A Parameterization of Heterogeneous Land Surfaces for Atmospheric Numerical Models and Its Impact on Regional Meteorology'. *Monthly Weather*

Review, vol. 117(10): pp. 2113–2136. DOI: `10.1175/1520-0493(1989)117<2113:APOHLS>2.0.CO;2` (cit. on p. 23).

Best, M. J. et al. (2011): 'The Joint UK Land Environment Simulator (JULES), model description – Part 1: Energy and water fluxes'. *Geoscientific Model Development*, vol. 4(3): pp. 677–699. DOI: `10.5194/gmd-4-677-2011` (cit. on p. 9).

Billings, W. D. and K. M. Peterson (1980): 'Vegetational Change and Ice-Wedge Polygons through the Thaw-Lake Cycle in Arctic Alaska'. *Arctic and Alpine Research*, vol. 12(4): pp. 413–432. DOI: `10.1080/00040851.1980.12004204` (cit. on p. 18).

Bisht, G., W. J. Riley, H. M. Wainwright, B. Dafflon, F. Yuan, and V. E. Romanovsky (2018): 'Impacts of microtopographic snow redistribution and lateral subsurface processes on hydrologic and thermal states in an Arctic polygonal ground ecosystem: a case study using ELM-3D v1.0'. *Geoscientific Model Development*, vol. 11(1): pp. 61–76. DOI: `10.5194/gmd-11-61-2018`.

Biskaborn, B. K. et al. (2019): 'Permafrost is warming at a global scale'. *Nature Communications*, vol. 10: p. 264. DOI: `10.1038/s41467-018-08240-4` (cit. on pp. 4, 22).

Boike, J., C. Georgi, G. Kirilin, S. Muster, K. Abramova, I. Fedorova, A. Chetverova, M. Grigoriev, N. Bornemann, and M. Langer (2015): 'Thermal processes of thermokarst lakes in the continuous permafrost zone of northern Siberia – observations and modeling (Lena River Delta, Siberia)'. *Biogeosciences*, vol. 12(20): pp. 5941–5965. DOI: `https://doi.org/10.5194/bg-12-5941-2015` (cit. on p. 22).

Boike, J., J. Nitzbon, K. Anders, M. Grigoriev, D. Bolshiyanov, M. Langer, S. Lange, N. Bornemann, A. Morgenstern, P. Schreiber, C. Wille, S. Chadburn, I. Gouttevin, E. Burke, and L. Kutzbach (2019): 'A 16-year record (2002–2017) of permafrost, active-layer, and meteorological conditions at the Samoylov Island Arctic permafrost research site, Lena River delta, northern Siberia: an opportunity to validate remote-sensing data and land surface, snow, and permafrost models'. *Earth System Science Data*, vol. 11(1): pp. 261–299. DOI: `10.5194/essd-11-261-2019` (cit. on p. 22).

Boike, J., C. Wille, and A. Abnizova (2008): 'Climatology and summer energy and water balance of polygonal tundra in the Lena River Delta, Siberia'. *Journal of Geophysical Research*, vol. 113: G03025. DOI: `10.1029/2007JG000540`.

Boike, J. et al. (2013): 'Baseline characteristics of climate, permafrost and land cover from a new permafrost observatory in the Lena River Delta, Siberia (1998–2011)'. *Biogeosciences*, vol. 10(3): pp. 2105–2128. DOI: `10.5194/bg-10-2105-2013` (cit. on p. 22).

Britton, M. (1957): *Vegetation of the Arctic Tundra*. Oregon State University Press (cit. on p. 18).

Brown, J., O. J. Ferrians Jr., J. A. Heginbottom, and E. S. Melnikov (1997): *Circum-Arctic map of permafrost and ground-ice conditions*. DOI: `10.3133/cp45` (cit. on p. 20).

Burke, E. J., I. P. Hartley, and C. D. Jones (2012): 'Uncertainties in the global temperature change caused by carbon release from permafrost thawing'. *The Cryosphere*, vol. 6(5): pp. 1063–1076. DOI: `10.5194/tc-6-1063-2012`.

BURN, C. R. (1997): 'Cryostratigraphy, paleogeography, and climate change during the early Holocene warm interval, western Arctic coast, Canada'. *Canadian Journal of Earth Sciences*, vol. 34(7): pp. 912–925. DOI: 10.1139/e17-076.

CHADBURN, S. E., E. J. BURKE, R. L. H. ESSERY, J. BOIKE, M. LANGER, M. HEIKENFELD, P. M. COX, and P. FRIEDLINGSTEIN (2015): 'Impact of model developments on present and future simulations of permafrost in a global land-surface model'. *The Cryosphere*, vol. 9(4): pp. 1505–1521. DOI: 10.5194/tc-9-1505-2015 (cit. on p. 9).

CHRISTIANSEN, H. H., N. MATSUOKA, and T. WATANABE (2016): 'Progress in Understanding the Dynamics, Internal Structure and Palaeoenvironmental Potential of Ice Wedges and Sand Wedges'. *Permafrost and Periglacial Processes*, vol. 27(4): pp. 365–376. DOI: 10.1002/ppp.1920 (cit. on p. 16).

CIAIS, P., C. SABINE, G. BALA, L. BOPP, V. BROVKIN, J. CANADELL, A. CHHABRA, R. DEFRIES, J. GALLOWAY, M. HEIMANN, et al. (2014): 'Carbon and other biogeochemical cycles'. *Climate change 2013: the physical science basis. Contribution of Working Group I to the Fifth Assessment Report of the Intergovernmental Panel on Climate Change*: pp. 465–570 (cit. on p. 4).

CLARK, D. B., L. M. MERCADO, S. SITCH, C. D. JONES, N. GEDNEY, M. J. BEST, M. PRYOR, G. G. ROONEY, R. L. H. ESSERY, E. BLYTH, O. BOUCHER, R. J. HARDING, C. HUNTINGFORD, and P. M. COX (2011): 'The Joint UK Land Environment Simulator (JULES), model description – Part 2: Carbon fluxes and vegetation dynamics'. *Geoscientific Model Development*, vol. 4(3): pp. 701–722. DOI: 10.5194/gmd-4-701-2011 (cit. on p. 9).

COSENZA, P., R. GUERIN, and A. TABBAGH (2003): 'Relationship between thermal conductivity and water content of soils using numerical modelling'. *European Journal of Soil Science*, vol. 54(3): pp. 581–588. DOI: 10.1046/j.1365-2389.2003.00539.x (cit. on p. 27).

COULTHARD, T. J. (2001): 'Landscape evolution models: a software review'. *Hydrological Processes*, vol. 15(1): pp. 165–173. DOI: 10.1002/hyp.426.

CRATE, S., M. ULRICH, J. O. HABECK, A. R. DESYATKIN, R. V. DESYATKIN, A. N. FEDOROV, T. HIYAMA, Y. IIJIMA, S. KSENOFONTOV, C. MÉSZÁROS, and H. TAKAKURA (2017): 'Permafrost livelihoods: A transdisciplinary review and analysis of thermokarst-based systems of indigenous land use'. *Anthropocene*, vol. 18: pp. 89–104. DOI: 10.1016/j.ancene.2017.06.001 (cit. on p. 4).

CRESTO ALEINA, F., V. BROVKIN, S. MUSTER, J. BOIKE, L. KUTZBACH, T. SACHS, and S. ZUYEV (2013): 'A stochastic model for the polygonal tundra based on Poisson–Voronoi diagrams'. *Earth Syst. Dynam.* Vol. 4(2): pp. 187–198. DOI: 10.5194/esd-4-187-2013.

DALL'AMICO, M., S. ENDRIZZI, S. GRUBER, and R. RIGON (2011): 'A robust and energy-conserving model of freezing variably-saturated soil'. *The Cryosphere*, vol. 5(2): pp. 469–484. DOI: 10.5194/tc-5-469-2011 (cit. on p. 26).

EKICI, A., C. BEER, S. HAGEMANN, J. BOIKE, M. LANGER, and C. HAUCK (2014): 'Simulating high-latitude permafrost regions by the JSBACH terrestrial ecosystem model'. *Geosci. Model Dev.* Vol. 7(2): pp. 631–647. DOI: 10.5194/gmd-7-631-2014 (cit. on p. 9).

EKICI, A., S. CHADBURN, N. CHAUDHARY, L. H. HAJDU, A. MARMY, S. PENG, J. BOIKE, E. BURKE, A. D. FRIEND, C. HAUCK, G. KRINNER, M. LANGER, P. A. MILLER, and C. BEER (2015): 'Site-level model intercomparison of high latitude and high altitude soil thermal dynamics in tundra and barren landscapes'. *The Cryosphere*, vol. 9(4): pp. 1343–1361. DOI: `10.5194/tc-9-1343-2015` (cit. on p. 9).

ELBERLING, B., A. MICHELSEN, C. SCHÄDEL, E. A. G. SCHUUR, H. H. CHRISTIANSEN, L. BERG, M. P. TAMSTORF, and C. SIGSGAARD (2013): 'Long-term CO2 production following permafrost thaw'. *Nature Climate Change*, vol. 3(10): pp. 890–894. DOI: `10.1038/nclimate1955`.

ENDRIZZI, S., S. GRUBER, M. DALL'AMICO, and R. RIGON (2014): 'GEOtop 2.0: simulating the combined energy and water balance at and below the land surface accounting for soil freezing, snow cover and terrain effects'. *Geoscientific Model Development*, vol. 7(6): pp. 2831–2857. DOI: `10.5194/gmd-7-2831-2014` (cit. on p. 10).

ESSERY, R. L. H., M. J. BEST, R. A. BETTS, P. M. COX, and C. M. TAYLOR (2003): 'Explicit Representation of Subgrid Heterogeneity in a GCM Land Surface Scheme'. *Journal of Hydrometeorology*, vol. 4(3): pp. 530–543. DOI: `10.1175/1525-7541(2003)004<0530:EROSHI>2.0.CO;2` (cit. on p. 23).

EVERDINGEN, R. O. van (1998): *Glossary of Permafrost and Related Ground-Ice Terms*. Inernational Permafrost Association (cit. on pp. 4, 13, 16).

FARQUHARSON, L. M., V. E. ROMANOVSKY, W. L. CABLE, D. A. WALKER, S. V. KOKELJ, and D. NICOLSKY (2019): 'Climate Change Drives Widespread and Rapid Thermokarst Development in Very Cold Permafrost in the Canadian High Arctic'. *Geophysical Research Letters*, vol. 46(12): pp. 6681–6689. DOI: `10.1029/2019GL082187` (cit. on p. 4).

FEDOROV, A. N. et al. (2018): 'Permafrost-Landscape Map of the Republic of Sakha (Yakutia) on a Scale 1:1,500,000'. *Geosciences*, vol. 8(12): p. 465. DOI: `10.3390/geosciences8120465`.

FERRANTI, J. de (2014): *Digital Elevation Data*. URL: `http://viewfinderpanoramas.org/dem3.html` (visited on 08/28/2019).

FISHER, R. A. and C. D. KOVEN (2020): 'Perspectives on the Future of Land Surface Models and the Challenges of Representing Complex Terrestrial Systems'. *Journal of Advances in Modeling Earth Systems*, vol. 12(4): e2018MS001453. DOI: `10.1029/2018MS001453` (cit. on p. 23).

FORTIER, D. and M. ALLARD (2004): 'Late Holocene syngenetic ice-wedge polygons development, Bylot Island, Canadian Arctic Archipelago'. *Canadian Journal of Earth Sciences*, vol. 41(8): pp. 997–1012. DOI: `10.1139/e04-031`.

FORTIER, D., M. ALLARD, and Y. SHUR (2007): 'Observation of rapid drainage system development by thermal erosion of ice wedges on Bylot Island, Canadian Arctic Archipelago'. *Permafrost and Periglacial Processes*, vol. 18(3): pp. 229–243. DOI: `10.1002/ppp.595` (cit. on p. 18).

FRASER, R., S. KOKELJ, T. LANTZ, M. MCFARLANE-WINCHESTER, I. OLTHOF, D. LACELLE, R. H. FRASER, S. V. KOKELJ, T. C. LANTZ, M. MCFARLANE-WINCHESTER, I. OLTHOF, and D. LACELLE (2018): 'Climate Sensitivity of High Arctic Permafrost Terrain Demonstrated by Widespread Ice-Wedge Thermokarst on Banks Island'. *Remote Sensing*, vol. 10(6): p. 954. DOI: `10.3390/rs10060954`.

FRENCH, H. M. (2007): *The Periglacial Environment*. Third Edition. West Sussex, England: John Wiley & Sons Ltd,. DOI: `10.1002/9781118684931` (cit. on pp. 16, 17).

GENUCHTEN, M. T. v. van (1980): ‘A Closed-form Equation for Predicting the Hydraulic Conductivity of Unsaturated Soils’. *Soil Science Society of America Journal*, vol. 44(5): pp. 892–898. DOI: `10.2136/sssaj1980.03615995004400050002x` (cit. on p. 26).

GILBERT, G. L., S. CABLE, C. THIEL, H. H. CHRISTIANSEN, and B. ELBERLING (2017): ‘Cryostratigraphy, sedimentology, and the late Quaternary evolution of the Zackenberg River delta, northeast Greenland’. *The Cryosphere*, vol. 11(3): pp. 1265–1282. DOI: `10.5194/tc-11-1265-2017`.

GILBERT, G. L., M. KANEVSKIY, and J. B. MURTON (2016): ‘Recent Advances (2008–2015) in the Study of Ground Ice and Cryostratigraphy’. *Permafrost and Periglacial Processes*, vol. 27(4): pp. 377–389. DOI: `10.1002/ppp.1912` (cit. on p. 16).

GILG, O., K. M. KOVACS, J. AARS, J. FORT, G. GAUTHIER, D. GREMILLET, R. A. IMS, H. MELTOFTE, J. MOREAU, E. POST, N. M. SCHMIDT, G. YANNIC, and L. BOLLACHE (2012): ‘Climate change and the ecology and evolution of Arctic vertebrates’. *Annals of the New York Academy of Sciences* (The Year in Ecology and Conservation Biology), vol. 1249: pp. 166–190. DOI: `10.1111/j.1749-6632.2011.06412.x` (cit. on p. 4).

GIORGI, F. and R. AVISSAR (1997): ‘Representation of heterogeneity effects in Earth system modeling: Experience from land surface modeling’. *Reviews of Geophysics*, vol. 35(4): pp. 413–437. DOI: `10.1029/97RG01754` (cit. on p. 23).

GÖCKEDE, M., F. KITTLER, M. J. KWON, I. BURJACK, M. HEIMANN, O. KOLLE, N. ZIMOV, and S. ZIMOV (2017): ‘Shifted energy fluxes, increased Bowen ratios, and reduced thaw depths linked with drainage-induced changes in permafrost ecosystem structure’. *The Cryosphere*, vol. 11(6): pp. 2975–2996. DOI: `10.5194/tc-11-2975-2017`.

GODIN, E., D. FORTIER, and S. COULOMBE (2014): ‘Effects of thermo-erosion gullying on hydrologic flow networks, discharge and soil loss’. *Environmental Research Letters*, vol. 9(10): p. 105010. DOI: `10.1088/1748-9326/9/10/105010`.

GOUTTEVIN, I., M. LANGER, H. LÖWE, J. BOIKE, M. PROKSCH, and M. SCHNEEBELI (2018): ‘Observation and modelling of snow at a polygonal tundra permafrost site: spatial variability and thermal implications’. *The Cryosphere*, vol. 12(11): pp. 3693–3717. DOI: `10.5194/tc-12-3693-2018` (cit. on p. 22).

GRANT, R. F., Z. A. MEKONNEN, W. J. RILEY, B. ARORA, and M. S. TORN (2017a): ‘Mathematical Modelling of Arctic Polygonal Tundra with Ecosys: 2. Microtopography Determines How CO2 and CH4 Exchange Responds to Changes in Temperature and Precipitation’. *Journal of Geophysical Research: Biogeosciences*, vol. 122(12): pp. 3174–3187. DOI: `10.1002/2017JG004037`.

GRANT, R. F., Z. A. MEKONNEN, W. J. RILEY, H. M. WAINWRIGHT, D. GRAHAM, and M. S. TORN (2017b): ‘Mathematical Modelling of Arctic Polygonal Tundra with Ecosys: 1. Microtopography Determines How Active Layer Depths Respond to Changes in Temperature and Precipitation’. *Journal of Geophysical Research: Biogeosciences*, vol. 122(12): pp. 3161–3173. DOI: `10.1002/2017JG004035`.

GRENIER, C. et al. (2018): ‘Groundwater flow and heat transport for systems undergoing freeze-thaw: Intercomparison of numerical simulators for 2D test cases’. *Advances in Water Resources*, vol. 114: pp. 196–218. DOI: `10.1016/j.advwatres.2018.02.001` (cit. on p. 10).

GROSSE, G., B. JONES, and C. ARP (2013): '8.21 Thermokarst Lakes, Drainage, and Drained Basins'. *Treatise on Geomorphology*. Ed. by SHRODER, J. F. San Diego: Academic Press: pp. 325–353. DOI: 10.1016/B978-0-12-374739-6.00216-5 (cit. on pp. 18, 19).

GROSSE, G., L. SCHIRRMEISTER, C. SIEGERT, V. V. KUNITSKY, E. A. SLAGODA, A. A. ANDREEV, and A. Y. DEREVIAGYN (2007): 'Geological and geomorphological evolution of a sedimentary periglacial landscape in Northeast Siberia during the Late Quaternary'. *Geomorphology*, vol. 86(1): pp. 25–51. DOI: 10.1016/j.geomorph.2006.08.005.

GÜNTHER, F., P. P. OVERDUIN, A. V. SANDAKOV, G. GROSSE, and M. N. GRIGORIEV (2013): 'Short- and long-term thermo-erosion of ice-rich permafrost coasts in the Laptev Sea region'. *Biogeosciences*, vol. 10(6): pp. 4297–4318. DOI: 10.5194/bg-10-4297-2013.

HAMMOND, G. E., P. C. LICHTNER, and R. T. MILLS (2014): 'Evaluating the performance of parallel subsurface simulators: An illustrative example with PFLOTRAN'. *Water Resources Research*, vol. 50(1): pp. 208–228. DOI: 10.1002/2012WR013483 (cit. on p. 10).

HEIMANN, M. and M. REICHSTEIN (2008): 'Terrestrial ecosystem carbon dynamics and climate feedbacks'. *Nature*, vol. 451(7176): pp. 289–292. DOI: 10.1038/nature06591 (cit. on p. 5).

HELBIG, M., J. BOIKE, M. LANGER, P. SCHREIBER, B. R. K. RUNKLE, and L. KUTZBACH (2013): 'Spatial and seasonal variability of polygonal tundra water balance: Lena River Delta, northern Siberia (Russia)'. *Hydrogeology Journal*, vol. 21(1): pp. 133–147. DOI: 10.1007/s10040-012-0933-4 (cit. on p. 22).

HINZMAN, L. D. et al. (2005): 'Evidence and Implications of Recent Climate Change in Northern Alaska and Other Arctic Regions'. *Climatic Change*, vol. 72(3): pp. 251–298. DOI: 10.1007/s10584-005-5352-2 (cit. on p. 4).

HJORT, J., O. KARJALAINEN, J. AALTO, S. WESTERMANN, V. E. ROMANOVSKY, F. E. NELSON, B. ETZELMÜLLER, and M. LUOTO (2018): 'Degrading permafrost puts Arctic infrastructure at risk by mid-century'. *Nature Communications*, vol. 9: p. 5147. DOI: 10.1038/s41467-018-07557-4 (cit. on p. 4).

HUGELIUS, G. et al. (2014): 'Estimated stocks of circumpolar permafrost carbon with quantified uncertainty ranges and identified data gaps'. *Biogeosciences*, vol. 11(23): pp. 6573–6593. DOI: 10.5194/bg-11-6573-2014 (cit. on p. 4).

IRRGANG, A. M., H. LANTUIT, R. R. GORDON, A. PISKOR, and G. K. MANSON (2019): 'Impacts of past and future coastal changes on the Yukon coast — threats for cultural sites, infrastructure, and travel routes'. *Arctic Science*, vol. 5(2): pp. 107–126. DOI: 10.1139/as-2017-0041 (cit. on p. 4).

JAFAROV, E. E., E. T. COON, D. R. HARP, C. J. WILSON, S. L. PAINTER, A. L. ATCHLEY, and V. E. ROMANOVSKY (2018): 'Modeling the role of preferential snow accumulation in through talik development and hillslope groundwater flow in a transitional permafrost landscape'. *Environmental Research Letters*, vol. 13(10): p. 105006. DOI: 10.1088/1748-9326/aadd30 (cit. on p. 10).

JAN, A., E. T. COON, S. L. PAINTER, R. GARIMELLA, and J. D. MOULTON (2018): 'An intermediate-scale model for thermal hydrology in low-relief permafrost-affected landscapes'. *Computational Geosciences*, vol. 22(1): pp. 163–177. DOI: 10.1007/s10596-017-9679-3.

Jones, B. M., G. Grosse, C. D. Arp, M. C. Jones, K. M. W. Anthony, and V. E. Romanovsky (2011): ‘Modern thermokarst lake dynamics in the continuous permafrost zone, northern Seward Peninsula, Alaska’. *Journal of Geophysical Research: Biogeosciences* (G00M03), vol. 116. doi: `10.1029/2011JG001666`.

Jones, B. M., G. Grosse, C. D. Arp, E. Miller, L. Liu, D. J. Hayes, and C. F. Larsen (2015): ‘Recent Arctic tundra fire initiates widespread thermokarst development’. *Scientific Reports*, vol. 5: p. 15865. doi: `10.1038/srep15865`.

Jorgenson, M. T., M. Kanevskiy, Y. Shur, N. Moskalenko, D. R. N. Brown, K. Wickland, R. Striegl, and J. Koch (2015): ‘Role of ground ice dynamics and ecological feedbacks in recent ice wedge degradation and stabilization’. *Journal of Geophysical Research: Earth Surface*, vol. 120(11): pp. 2280–2297. doi: `10.1002/2015JF003602`.

Jorgenson, M. T., Y. L. Shur, and E. R. Pullman (2006): ‘Abrupt increase in permafrost degradation in Arctic Alaska’. *Geophysical Research Letters*, vol. 33(2): p. L02503. doi: `10.1029/2005GL024960` (cit. on pp. 4, 18).

Kanevskiy, M., T. Jorgenson, Y. Shur, J. A. O’Donnell, J. W. Harden, Q. Zhuang, and D. Fortier (2014): ‘Cryostratigraphy and Permafrost Evolution in the Lacustrine Lowlands of West-Central Alaska’. *Permafrost and Periglacial Processes*, vol. 25(1): pp. 14–34. doi: `10.1002/ppp.1800`.

Kanevskiy, M., Y. Shur, T. Jorgenson, D. R. Brown, N. Moskalenko, J. Brown, D. A. Walker, M. K. Raynolds, and M. Buchhorn (2017): ‘Degradation and stabilization of ice wedges: Implications for assessing risk of thermokarst in northern Alaska’. *Geomorphology*, vol. 297: pp. 20–42. doi: `10.1016/j.geomorph.2017.09.001` (cit. on p. 18).

Kartoziia, A. (2019): ‘Assessment of the Ice Wedge Polygon Current State by Means of UAV Imagery Analysis (Samoylov Island, the Lena Delta)’. *Remote Sensing*, vol. 11(13): p. 1627. doi: `10.3390/rs11131627`.

Kessler, M. A., L. J. Plug, and K. M. W. Anthony (2012): ‘Simulating the decadal- to millennial-scale dynamics of morphology and sequestered carbon mobilization of two thermokarst lakes in NW Alaska’. *Journal of Geophysical Research: Biogeosciences*, vol. 117: G00M06. doi: `10.1029/2011JG001796` (cit. on p. 19).

Khvorostyanov, D. V., P. Ciais, G. Krinner, and S. A. Zimov (2008): ‘Vulnerability of east Siberia’s frozen carbon stores to future warming’. *Geophysical Research Letters*, vol. 35(10): p. L10703. doi: `10.1029/2008GL033639`.

Kleinen, T. and V. Brovkin (2018): ‘Pathway-dependent fate of permafrost region carbon’. *Environmental Research Letters*, vol. 13(9): p. 094001. doi: `10.1088/1748-9326/aad824`.

Knoblauch, C., C. Beer, S. Liebner, M. N. Grigoriev, and E.-M. Pfeiffer (2018): ‘Methane production as key to the greenhouse gas budget of thawing permafrost’. *Nature Climate Change*, vol. 8(4): pp. 309–312. doi: `10.1038/s41558-018-0095-z`.

Kokelj, S. V. and M. T. Jorgenson (2013): ‘Advances in Thermokarst Research’. *Permafrost and Periglacial Processes*, vol. 24(2): pp. 108–119. doi: `10.1002/ppp.1779` (cit. on pp. 6, 17, 18).

KOKELJ, S. V., T. C. LANTZ, S. A. WOLFE, J. C. KANIGAN, P. D. MORSE, R. COUTTS, N. MOLINA-GIRALDO, and C. R. BURN (2014): 'Distribution and activity of ice wedges across the forest-tundra transition, western Arctic Canada'. *Journal of Geophysical Research: Earth Surface*, vol. 119(9): pp. 2032–2047. DOI: 10.1002/2014JF003085.

KOSTER, R. D. and M. J. SUAREZ (1992): 'Modeling the land surface boundary in climate models as a composite of independent vegetation stands'. *Journal of Geophysical Research: Atmospheres* (D3), vol. 97: pp. 2697–2715. DOI: 10.1029/91JD01696 (cit. on p. 23).

KOVEN, C. D., B. RINGEVAL, P. FRIEDLINGSTEIN, P. CIAIS, P. CADULE, D. KHVOROSTYANOV, G. KRINNER, and C. TARNOCAI (2011): 'Permafrost carbon-climate feedbacks accelerate global warming'. *Proceedings of the National Academy of Sciences*, vol. 108(36): pp. 14769–14774. DOI: 10.1073/pnas.1103910108.

KOVEN, C. D., D. M. LAWRENCE, and W. J. RILEY (2015): 'Permafrost carbon–climate feedback is sensitive to deep soil carbon decomposability but not deep soil nitrogen dynamics'. *Proceedings of the National Academy of Sciences*, vol. 112(12): pp. 3752–3757. DOI: 10.1073/pnas.1415123112.

KOVEN, C. D., W. J. RILEY, and A. STERN (2013): 'Analysis of Permafrost Thermal Dynamics and Response to Climate Change in the CMIP5 Earth System Models'. *Journal of Climate*, vol. 26(6): pp. 1877–1900. DOI: 10.1175/JCLI-D-12-00228.1 (cit. on pp. 3, 6).

KRINNER, G., N. VIOVY, N. D. NOBLET-DUCOUDRÉ, J. OGÉE, J. POLCHER, P. FRIEDLINGSTEIN, P. CIAIS, S. SITCH, and I. C. PRENTICE (2005): 'A dynamic global vegetation model for studies of the coupled atmosphere-biosphere system'. *Global Biogeochemical Cycles*, vol. 19(1). DOI: 10.1029/2003GB002199 (cit. on p. 9).

KUDRYAVTSEV, V. A., L. S. GARAGULYA, K. A. KONDRAT YEVA, and V. G. MELAMED (1977): *Fundamentals of Frost Forecasting in Geological Engineering Investigations*. Hanover NH: Cold Regions Research and Engineering Lab (cit. on p. 8).

KUMAR, J., N. COLLIER, G. BISHT, R. T. MILLS, P. E. THORNTON, C. M. IVERSEN, and V. ROMANOVSKY (2016): 'Modeling the spatiotemporal variability in subsurface thermal regimes across a low-relief polygonal tundra landscape'. *The Cryosphere*, vol. 10(5): pp. 2241–2274. DOI: 10.5194/tc-10-2241-2016 (cit. on p. 10).

KURYLYK, B. L., M. HAYASHI, W. L. QUINTON, J. M. MCKENZIE, and C. I. VOSS (2016): 'Influence of vertical and lateral heat transfer on permafrost thaw, peatland landscape transition, and groundwater flow'. *Water Resources Research*, vol. 52(2): pp. 1286–1305. DOI: 10.1002/2015WR018057 (cit. on p. 10).

LACHENBRUCH, A. H. (1962): 'Mechanics of Thermal Contraction Cracks and Ice-Wedge Polygons in Permafrost'. *Geological Society of America Special Papers*. Vol. 70. Geological Society of America: pp. 1–66. DOI: 10.1130/SPE70-p1 (cit. on pp. 15, 16).

LANGER, M., S. WESTERMANN, J. BOIKE, G. KIRILLIN, G. GROSSE, S. PENG, and G. KRINNER (2016): 'Rapid degradation of permafrost underneath waterbodies in tundra landscapes—Toward a representation of thermokarst in land surface models'. *Journal of Geophysical Research: Earth Surface*, vol. 121(12): pp. 2446–2470. DOI: 10.1002/2016JF003956 (cit. on pp. 11, 19, 23, 24, 29).

Langer, M., S. Westermann, S. Muster, K. Piel, and J. Boike (2011a): 'The surface energy balance of a polygonal tundra site in northern Siberia - Part 1: Spring to fall'. *The Cryosphere*, vol. 5(1): pp. 151–171. doi: `10.5194/tc-5-151-2011` (cit. on p. 22).

Langer, M., S. Westermann, S. Muster, K. Piel, and J. Boike (2011b): 'The surface energy balance of a polygonal tundra site in northern Siberia - Part 2: Winter'. *The Cryosphere*, vol. 5(2): pp. 509–524. doi: `10.5194/tc-5-509-2011` (cit. on p. 22).

Lara, M. J., A. D. McGuire, E. S. Euskirchen, C. E. Tweedie, K. M. Hinkel, A. N. Skurikhin, V. E. Romanovsky, G. Grosse, W. R. Bolton, and H. Genet (2015): 'Polygonal tundra geomorphological change in response to warming alters future CO2 and CH4 flux on the Barrow Peninsula'. *Global Change Biology*, vol. 21(4): pp. 1634–1651. doi: `10.1111/gcb.12757` (cit. on p. 18).

Lawrence, D. M., A. G. Slater, and S. C. Swenson (2012): 'Simulation of Present-Day and Future Permafrost and Seasonally Frozen Ground Conditions in CCSM4'. *Journal of Climate*, vol. 25(7): pp. 2207–2225. doi: `10.1175/JCLI-D-11-00334.1`.

Lawrence, D. M. et al. (2019): 'The Community Land Model Version 5: Description of New Features, Benchmarking, and Impact of Forcing Uncertainty'. *Journal of Advances in Modeling Earth Systems*, vol. 11(12): pp. 4245–4287. doi: `10.1029/2018MS001583` (cit. on p. 8).

Lee, H., S. C. Swenson, A. G. Slater, and D. M. Lawrence (2014): 'Effects of excess ground ice on projections of permafrost in a warming climate'. *Environmental Research Letters*, vol. 9(12): p. 124006. doi: `10.1088/1748-9326/9/12/124006` (cit. on pp. 10, 29).

Leffingwell, E. d. K. (1915): 'Ground-Ice Wedges: The Dominant Form of Ground-Ice on the North Coast of Alaska'. *The Journal of Geology*, vol. 23(7): pp. 635–654. doi: `10.1086/622281` (cit. on p. 16).

Lenton, T. M. (2012): 'Arctic Climate Tipping Points'. *AMBIO*, vol. 41(1): pp. 10–22. doi: `10.1007/s13280-011-0221-x`.

Liljedahl, A. K. et al. (2016): 'Pan-Arctic ice-wedge degradation in warming permafrost and its influence on tundra hydrology'. *Nature Geoscience*, vol. 9(4): pp. 312–318. doi: `10.1038/ngeo2674` (cit. on pp. 4, 17, 18).

Lunardini, V. J. (1978): 'Theory of n-factors and correlation of data'. *Proceedings of the Third International Conference on Permafrost*. National Research Council of Canada Ottawa: pp. 40–46 (cit. on p. 8).

Luo, Y. (2007): 'Terrestrial Carbon–Cycle Feedback to Climate Warming'. *Annual Review of Ecology, Evolution, and Systematics*, vol. 38(1): pp. 683–712. doi: `10.1146/annurev.ecolsys.38.091206.095808` (cit. on p. 5).

MacKay, J. R. (2000): 'Thermally induced movements in ice-wedge polygons, western arctic coast: a long-term study'. *Géographie physique et Quaternaire*, vol. 54(1): p. 41. doi: `10.7202/004846ar`.

Martin, L. C. P., J. Nitzbon, K. S. Aas, B. Etzelmüller, H. Kristiansen, and S. Westermann (2019): 'Stability Conditions of Peat Plateaus and Palsas in Northern Norway'. *Journal of Geophysical Research: Earth Surface*, vol. 124: pp. 705–719. doi: `10.1029/2018JF004945` (cit. on p. 38).

MASSON, V. et al. (2013): 'The SURFEXv7.2 land and ocean surface platform for coupled or offline simulation of earth surface variables and fluxes'. *Geoscientific Model Development*, vol. 6(4): pp. 929–960. DOI: `10.5194/gmd-6-929-2013` (cit. on p. 9).

MCGUIRE, A. D. et al. (2016): 'Variability in the sensitivity among model simulations of permafrost and carbon dynamics in the permafrost region between 1960 and 2009'. *Global Biogeochemical Cycles*, vol. 30(7): pp. 1015–1037. DOI: `10.1002/2016GB005405` (cit. on p. 9).

MONIN, A. S. and A. M. OBUKHOV (1954): 'Basic laws of turbulent mixing in the surface layer of the atmosphere'. *Tr. Akad. Nauk SSSR Geophiz. Inst.* Vol. 24(151): pp. 163–187 (cit. on p. 28).

MORGENSTERN, A., G. GROSSE, F. GÜNTHER, I. FEDOROVA, and L. SCHIRRMEISTER (2011): 'Spatial analyses of thermokarst lakes and basins in Yedoma landscapes of the Lena Delta'. *The Cryosphere*, vol. 5(4): pp. 849–867. DOI: `10.5194/tc-5-849-2011`.

MORGENSTERN, A., M. ULRICH, F. GÜNTHER, S. ROESSLER, I. FEDOROVA, N. RUDAYA, S. WETTERICH, J. BOIKE, and L. SCHIRRMEISTER (2013): 'Evolution of thermokarst in East Siberian ice-rich permafrost: A case study'. *Geomorphology*, vol. 201: pp. 363–379. DOI: `10.1016/j.geomorph.2013.07.011` (cit. on p. 19).

MUSTER, S., M. LANGER, B. HEIM, S. WESTERMANN, and J. BOIKE (2012a): 'Subpixel heterogeneity of ice-wedge polygonal tundra: a multi-scale analysis of land cover and evapotranspiration in the Lena River Delta, Siberia'. *Tellus B: Chemical and Physical Meteorology*, vol. 64(1): p. 17301. DOI: `10.3402/tellusb.v64i0.17301` (cit. on pp. 19, 22).

MUSTER, S., M. LANGER, B. HEIM, S. WESTERMANN, and J. BOIKE (2012b): 'Land cover classification of Samoylov Island and Landsat subpixel water cover of Lena River Delta, Siberia, with links to ESRI grid files'. *PANGAEA*, vol. DOI: `10.1594/PANGAEA.786927` (cit. on p. 7).

MUSTER, S., W. J. RILEY, K. ROTH, M. LANGER, F. CRESTO ALEINA, C. D. KOVEN, S. LANGE, A. BARTSCH, G. GROSSE, C. J. WILSON, B. M. JONES, and J. BOIKE (2019): 'Size Distributions of Arctic Waterbodies Reveal Consistent Relations in Their Statistical Moments in Space and Time'. *Frontiers in Earth Science*, vol. 7. DOI: `10.3389/feart.2019.00005` (cit. on p. 18).

NATALI, S. M. et al. (2019): 'Large loss of CO 2 in winter observed across the northern permafrost region'. *Nature Climate Change*, vol. 9(11): pp. 852–857. DOI: `10.1038/s41558-019-0592-8` (cit. on p. 4).

NAUTA, A. L., M. M. P. D. HEIJMANS, D. BLOK, J. LIMPENS, B. ELBERLING, A. GALLAGHER, B. LI, R. E. PETROV, T. C. MAXIMOV, J. van HUISSTEDEN, and F. BERENDSE (2015): 'Permafrost collapse after shrub removal shifts tundra ecosystem to a methane source'. *Nature Climate Change*, vol. 5(1): pp. 67–70. DOI: `10.1038/nclimate2446`.

NELSON, F. E., O. A. ANISIMOV, and N. I. SHIKLOMANOV (2002): 'Climate Change and Hazard Zonation in the Circum-Arctic Permafrost Regions'. *Natural Hazards*, vol. 26(3): pp. 203–225. DOI: `10.1023/A:1015612918401` (cit. on p. 4).

Nitzbon, J., M. Langer, S. Westermann, L. Martin, K. S. Aas, and J. Boike (2019): 'Pathways of ice-wedge degradation in polygonal tundra under different hydrological conditions'. *The Cryosphere*, vol. 13(4): pp. 1089–1123. doi: `10.5194/tc-13-1089-2019`.

Nitze, I., G. Grosse, B. M. Jones, V. E. Romanovsky, and J. Boike (2018): 'Remote sensing quantifies widespread abundance of permafrost region disturbances across the Arctic and Subarctic'. *Nature Communications*, vol. 9: p. 5423. doi: `10.1038/s41467-018-07663-3`.

Niu, G.-Y., Z.-L. Yang, K. E. Mitchell, F. Chen, M. B. Ek, M. Barlage, A. Kumar, K. Manning, D. Niyogi, E. Rosero, M. Tewari, and Y. Xia (2011): 'The community Noah land surface model with multiparameterization options (Noah-MP): 1. Model description and evaluation with local-scale measurements'. *Journal of Geophysical Research: Atmospheres*, vol. 116: p. D12109. doi: `10.1029/2010JD015139` (cit. on p. 9).

Obu, J., S. Westermann, A. Kääb, and A. Bartsch (2018): 'Ground Temperature Map, 2000-2016, Northern Hemisphere Permafrost'. *PANGAEA*, vol. doi: `10.1594/PANGAEA.888600`.

Obu, J. et al. (2019): 'Northern Hemisphere permafrost map based on TTOP modelling for 2000–2016 at 1 km2 scale'. *Earth-Science Reviews*, vol. 193: pp. 299–316. doi: `10.1016/j.earscirev.2019.04.023` (cit. on pp. 4, 5, 8, 19).

Olefeldt, D., S. Goswami, G. Grosse, D. Hayes, G. Hugelius, P. Kuhry, A. D. McGuire, V. E. Romanovsky, A. B. K. Sannel, E. a. G. Schuur, and M. R. Turetsky (2016): 'Circumpolar distribution and carbon storage of thermokarst landscapes'. *Nature Communications*, vol. 7: p. 13043. doi: `10.1038/ncomms13043` (cit. on p. 10).

O'Neill, H. B., S. A. Wolfe, and C. Duchesne (2019): 'New ground ice maps for Canada using a paleogeographic modelling approach'. *The Cryosphere*, vol. 13(3): pp. 753–773. doi: `10.5194/tc-13-753-2019`.

Painter, S. L., J. D. Moulton, and C. J. Wilson (2013): 'Modeling challenges for predicting hydrologic response to degrading permafrost'. *Hydrogeology Journal*, vol. 21(1): pp. 221–224. doi: `10.1007/s10040-012-0917-4`.

Painter, S. L., E. T. Coon, A. L. Atchley, M. Berndt, R. Garimella, J. D. Moulton, D. Svyatskiy, and C. J. Wilson (2016): 'Integrated surface/subsurface permafrost thermal hydrology: Model formulation and proof-of-concept simulations'. *Water Resources Research*, vol. 52(8): pp. 6062–6077. doi: `10.1002/2015WR018427` (cit. on p. 10).

Plaza, C., E. Pegoraro, R. Bracho, G. Celis, K. G. Crummer, J. A. Hutchings, C. E. Hicks Pries, M. Mauritz, S. M. Natali, V. G. Salmon, C. Schädel, E. E. Webb, and E. A. G. Schuur (2019): 'Direct observation of permafrost degradation and rapid soil carbon loss in tundra'. *Nature Geoscience*, vol. 12(8): pp. 627–631. doi: `10.1038/s41561-019-0387-6`.

Plug, L. J. and J. J. West (2009): 'Thaw lake expansion in a two-dimensional coupled model of heat transfer, thaw subsidence, and mass movement'. *Journal of Geophysical Research: Earth Surface*, vol. 114: F01002. doi: `10.1029/2006JF000740` (cit. on p. 19).

Pörtner, H.-O., D. C. Roberts, V. Masson-Delmotte, P. Zhai, M. Tignor, E. Poloczanska, K. Mintenbeck, A. Alegría, M. Nicolai, A. Okem, J. Petzold, B. Rama, and N. M. Weyer, eds. (2019): *IPCC Special Report on the Ocean and Cryosphere in a Changing Climate*. In press. IPCC.

Richards, L. A. (1931): ‘Capillary conduction of liquids through porous mediums’. *Physics*, vol. 1(5): pp. 318–333. doi: `10.1063/1.1745010` (cit. on p. 29).

Richardson, L. F. (1922): *Weather prediction by numerical process*. In collab. with University of California Libraries. Cambridge, The University press. 262 pp. (cit. on p. 29).

Riseborough, D. W. (2002): ‘The mean annual temperature at the top of permafrost, the TTOP model, and the effect of unfrozen water’. *Permafrost and Periglacial Processes*, vol. 13(2): pp. 137–143. doi: `10.1002/ppp.418` (cit. on p. 8).

Riseborough, D. W., N. Shiklomanov, B. Etzelmüller, S. Gruber, and S. Marchenko (2008): ‘Recent advances in permafrost modelling’. *Permafrost and Periglacial Processes*, vol. 19(2): pp. 137–156. doi: `10.1002/ppp.615` (cit. on p. 8).

Rizzoli, P., M. Martone, C. Gonzalez, C. Wecklich, D. Borla Tridon, B. Bräutigam, M. Bachmann, D. Schulze, T. Fritz, M. Huber, B. Wessel, G. Krieger, M. Zink, and A. Moreira (2017): ‘Generation and performance assessment of the global TanDEM-X digital elevation model’. *ISPRS Journal of Photogrammetry and Remote Sensing*, vol. 132: pp. 119–139. doi: `10.1016/j.isprsjprs.2017.08.008`.

Roering, J. J., J. W. Kirchner, and W. E. Dietrich (2001): ‘Hillslope evolution by nonlinear, slope-dependent transport: Steady state morphology and equilibrium adjustment timescales’. *Journal of Geophysical Research: Solid Earth* (B8), vol. 106: pp. 16499–16513. doi: `10.1029/2001JB000323`.

Rowland, J. C., B. J. Travis, and C. J. Wilson (2011): ‘The role of advective heat transport in talik development beneath lakes and ponds in discontinuous permafrost’. *Geophysical Research Letters*, vol. 38(17). doi: `10.1029/2011GL048497`.

Rowland, J. C. et al. (2010): ‘Arctic Landscapes in Transition: Responses to Thawing Permafrost’. *Eos, Transactions American Geophysical Union*, vol. 91(26): pp. 229–230. doi: `10.1029/2010EO260001` (cit. on p. 4).

Rowland, J. C. and E. T. Coon (2015): ‘From documentation to prediction: raising the bar for thermokarst research’. *Hydrogeology Journal*, vol. 24(3): pp. 645–648. doi: `10.1007/s10040-015-1331-5` (cit. on p. 10).

Schädel, C. et al. (2016): ‘Potential carbon emissions dominated by carbon dioxide from thawed permafrost soils’. *Nature Climate Change*, vol. 6(10): pp. 950–953. doi: `10.1038/nclimate3054`.

Schaphoff, S., U. Heyder, S. Ostberg, D. Gerten, J. Heinke, and W. Lucht (2013): ‘Contribution of permafrost soils to the global carbon budget’. *Environmental Research Letters*, vol. 8(1): p. 014026. doi: `10.1088/1748-9326/8/1/014026`.

Schirrmeister, L., D. Froese, V. Tumskoy, G. Grosse, and S. Wetterich (2013): ‘PERMAFROST AND PERIGLACIAL FEATURES | Yedoma: Late Pleistocene Ice-Rich Syngenetic Permafrost of Beringia’. *Encyclopedia of Quaternary Science*. Elsevier: pp. 542–552. doi: `10.1016/B978-0-444-53643-3.00106-0` (cit. on pp. 19, 20).

Schirrmeister, L., G. Grosse, V. Kunitsky, D. Magens, H. Meyer, A. Dereviagin, T. Kuznetsova, A. Andreev, O. Babiy, F. Kienast, M. Grigoriev, P. Pier Overduin, and F. Preusser (2008):

'Periglacial landscape evolution and environmental changes of Arctic lowland areas for the last 60 000 years (western Laptev Sea coast, Cape Mamontov Klyk)'. *Polar Research*, vol. 27(2): pp. 249–272. DOI: 10.1111/j.1751-8369.2008.00067.x (cit. on p. 19).

SCHIRRMEISTER, L., G. GROSSE, S. WETTERICH, P. P. OVERDUIN, J. STRAUSS, E. A. G. SCHUUR, and H.-W. HUBBERTEN (2011): 'Fossil organic matter characteristics in permafrost deposits of the northeast Siberian Arctic'. *Journal of Geophysical Research: Biogeosciences* (G00M02), vol. 116. DOI: 10.1029/2011JG001647.

SCHNEIDER VON DEIMLING, T., G. GROSSE, J. STRAUSS, L. SCHIRRMEISTER, A. MORGENSTERN, S. SCHAPHOFF, M. MEINSHAUSEN, and J. BOIKE (2015): 'Observation-based modelling of permafrost carbon fluxes with accounting for deep carbon deposits and thermokarst activity'. *Biogeosciences*, vol. 12(11): pp. 3469–3488. DOI: 10.5194/bg-12-3469-2015.

SCHUUR, E. A. G. and M. C. MACK (2018): 'Ecological Response to Permafrost Thaw and Consequences for Local and Global Ecosystem Services'. *Annual Review of Ecology, Evolution, and Systematics*, vol. 49(1): pp. 279–301. DOI: 10.1146/annurev-ecolsys-121415-032349 (cit. on p. 4).

SCHUUR, E. A. G. et al. (2015): 'Climate change and the permafrost carbon feedback'. *Nature*, vol. 520: pp. 171–179. DOI: 10.1038/nature14338 (cit. on pp. 4, 6, 10).

SCHWAMBORN, G., V. RACHOLD, and M. N. GRIGORIEV (2002): 'Late Quaternary sedimentation history of the Lena Delta'. *Quaternary International*, vol. 89(1): pp. 119–134. DOI: 10.1016/S1040-6182(01)00084-2 (cit. on pp. 20, 22).

SHUR, Y. L. and M. T. JORGENSON (2007): 'Patterns of permafrost formation and degradation in relation to climate and ecosystems'. *Permafrost and Periglacial Processes*, vol. 18(1): pp. 7–19. DOI: 10.1002/ppp.582 (cit. on pp. 4, 8, 18).

SJÖBERG, Y., E. COON, A. B. K. SANNEL, R. PANNETIER, D. HARP, A. FRAMPTON, S. L. PAINTER, and S. W. LYON (2016): 'Thermal effects of groundwater flow through subarctic fens: A case study based on field observations and numerical modeling'. *Water Resources Research*, vol. 52(3): pp. 1591–1606. DOI: 10.1002/2015WR017571 (cit. on p. 10).

SLATER, A. G. and D. M. LAWRENCE (2013): 'Diagnosing Present and Future Permafrost from Climate Models'. *Journal of Climate*, vol. 26(15): pp. 5608–5623. DOI: 10.1175/JCLI-D-12-00341.1.

SMITH, M. W. and D. W. RISEBOROUGH (1996): 'Permafrost monitoring and detection of climate change'. *Permafrost and Periglacial Processes*, vol. 7(4): pp. 301–309. DOI: 10.1002/(SICI)1099-1530(199610)7:4<301::AID-PPP231>3.0.CO;2-R (cit. on p. 8).

STEFAN, J. (1891): 'Ueber die Theorie der Eisbildung, insbesondere über die Eisbildung im Polarmeere'. *Annalen der Physik*, vol. 278(2): pp. 269–286. DOI: 10.1002/andp.18912780206 (cit. on p. 8).

STOCKER, T. F., D. QIN, G.-K. PLATTNER, M. TIGNOR, S. K. ALLEN, J. BOSCHUNG, A. NAUELS, Y. XIA, V. BEX, P. M. MIDGLEY, et al. (2013): 'Climate change 2013: The physical science basis'. *Contribution of working group I to the fifth assessment report of the intergovernmental panel on climate change*, vol. (cit. on p. 3).

STRAUSS, J., L. SCHIRRMEISTER, G. GROSSE, D. FORTIER, G. HUGELIUS, C. KNOBLAUCH, V. ROMANOVSKY, C. SCHÄDEL, T. SCHNEIDER VON DEIMLING, E. A. G. SCHUUR, D. SHMELEV, M. ULRICH, and A. VEREMEEVA (2017): 'Deep Yedoma permafrost: A synthesis of depositional characteristics and carbon vulnerability'. *Earth-Science Reviews*, vol. 172: pp. 75–86. DOI: `10.1016/j.earscirev.2017.07.007` (cit. on p. 19).

STRAUSS, J., L. SCHIRRMEISTER, G. GROSSE, S. WETTERICH, M. ULRICH, U. HERZSCHUH, and H.-W. HUBBERTEN (2013): 'The deep permafrost carbon pool of the Yedoma region in Siberia and Alaska'. *Geophysical Research Letters*, vol. 40(23): pp. 6165–6170. DOI: `10.1002/2013GL058088`.

STRAUSS, J. et al. (2016): 'Database of Ice-Rich Yedoma Permafrost (IRYP)'. *PANGAEA*, vol. DOI: `10.1594/pangaea.861733`.

TANSKI, G., D. WAGNER, C. KNOBLAUCH, M. FRITZ, T. SACHS, and H. LANTUIT (2019): 'Rapid CO2 Release From Eroding Permafrost in Seawater'. *Geophysical Research Letters*, vol. 46(20): pp. 11244–11252. DOI: `10.1029/2019GL084303`.

TESI, T., F. MUSCHITIELLO, R. H. SMITTENBERG, M. JAKOBSSON, J. E. VONK, P. HILL, A. ANDERSSON, N. KIRCHNER, R. NOORMETS, O. DUDAREV, I. SEMILETOV, and Ö. GUSTAFSSON (2016): 'Massive remobilization of permafrost carbon during post-glacial warming'. *Nature Communications*, vol. 7: p. 13653. DOI: `10.1038/ncomms13653` (cit. on p. 5).

TEUFEL, B. and L. SUSHAMA (2019): 'Abrupt changes across the Arctic permafrost region endanger northern development'. *Nature Climate Change*, vol. 9(11): pp. 858–862. DOI: `10.1038/s41558-019-0614-6`.

TURETSKY, M. R., B. W. ABBOTT, M. C. JONES, K. W. ANTHONY, D. OLEFELDT, E. A. G. SCHUUR, G. GROSSE, P. KUHRY, G. HUGELIUS, C. KOVEN, D. M. LAWRENCE, C. GIBSON, A. B. K. SANNEL, and A. D. MCGUIRE (2020): 'Carbon release through abrupt permafrost thaw'. *Nature Geoscience*, vol. 13(2): pp. 138–143. DOI: `10.1038/s41561-019-0526-0`.

TURETSKY, M. R., B. W. ABBOTT, M. C. JONES, K. WALTER ANTHONY, D. OLEFELDT, E. A. G. SCHUUR, C. KOVEN, A. D. MCGUIRE, G. GROSSE, P. KUHRY, G. HUGELIUS, D. M. LAWRENCE, C. GIBSON, and A. B. K. SANNEL (2019): 'Permafrost collapse is accelerating carbon release'. *Nature*, vol. 569: pp. 32–34. DOI: `10.1038/d41586-019-01313-4` (cit. on pp. 4, 6, 10).

ULRICH, M., G. GROSSE, J. STRAUSS, and L. SCHIRRMEISTER (2014): 'Quantifying Wedge-Ice Volumes in Yedoma and Thermokarst Basin Deposits'. *Permafrost and Periglacial Processes*, vol. 25(3): pp. 151–161. DOI: `10.1002/ppp.1810` (cit. on p. 19).

VINCENT, W. F., M. LEMAY, and M. ALLARD (2017): 'Arctic permafrost landscapes in transition: towards an integrated Earth system approach'. *Arctic Science*, vol. 3(2): pp. 39–64. DOI: `10.1139/as-2016-0027` (cit. on p. 4).

VOSS, C. I. (1984): 'SUTRA, A finite-element simulation model for saturated-unsaturated fluid-density-dependent ground-water flow with energy transport or chemically-reactive single-species solute transport'. *U.S. Geological Survey Water-Resources Investigations Report*, vol. 84-4369: p. 409 (cit. on p. 9).

WAGNER, A. M., N. J. LINDSEY, S. DOU, A. GELVIN, S. SAARI, C. WILLIAMS, I. EKBLAW, C. ULRICH, S. BORGLIN, A. MORALES, and J. AJO-FRANKLIN (2018): 'Permafrost Degradation and Subsidence

Observations during a Controlled Warming Experiment'. *Scientific Reports*, vol. 8(1): pp. 1–9. DOI: 10.1038/s41598-018-29292-y.

WALDER, J. and B. HALLET (1985): 'A theoretical model of the fracture of rock during freezing'. *GSA Bulletin*, vol. 96(3): pp. 336–346. DOI: 10.1130/0016-7606(1985)96<336:ATMOTF>2.0.CO;2 (cit. on p. 16).

WALTER ANTHONY, K., T. S. V. DEIMLING, I. NITZE, S. FROLKING, A. EMOND, R. DAANEN, P. ANTHONY, P. LINDGREN, B. JONES, and G. GROSSE (2018): '21st-century modeled permafrost carbon emissions accelerated by abrupt thaw beneath lakes'. *Nature Communications*, vol. 9: p. 3262. DOI: 10.1038/s41467-018-05738-9.

WALTER, K. M., M. E. EDWARDS, G. GROSSE, S. A. ZIMOV, and F. S. CHAPIN (2007): 'Thermokarst Lakes as a Source of Atmospheric CH4 During the Last Deglaciation'. *Science*, vol. 318(5850): pp. 633–636. DOI: 10.1126/science.1142924 (cit. on p. 5).

WALTER, K. M., S. A. ZIMOV, J. P. CHANTON, D. VERBYLA, and F. S. CHAPIN (2006): 'Methane bubbling from Siberian thaw lakes as a positive feedback to climate warming'. *Nature*, vol. 443: pp. 71–75. DOI: 10.1038/nature05040 (cit. on p. 5).

WALVOORD, M. A. and B. L. KURYLYK (2016): 'Hydrologic Impacts of Thawing Permafrost—A Review'. *Vadose Zone Journal*, vol. 15(6): 1–20 vzj2016.01.0010. DOI: 10.2136/vzj2016.01.0010 (cit. on p. 18).

WESTERMANN, S., M. LANGER, J. BOIKE, M. HEIKENFELD, M. PETER, B. ETZELMÜLLER, and G. KRINNER (2016): 'Simulating the thermal regime and thaw processes of ice-rich permafrost ground with the land-surface model CryoGrid 3'. *Geosci. Model Dev.* Vol. 9(2): pp. 523–546. DOI: 10.5194/gmd-9-523-2016 (cit. on pp. 10, 11, 19, 24, 28, 29).

WESTERMANN, S., T. V. SCHULER, K. GISNÅS, and B. ETZELMÜLLER (2013): 'Transient thermal modeling of permafrost conditions in Southern Norway'. *The Cryosphere*, vol. 7(2): pp. 719–739. DOI: 10.5194/tc-7-719-2013 (cit. on p. 26).

WESTERMANN, S., M. PETER, M. LANGER, G. SCHWAMBORN, L. SCHIRRMEISTER, B. ETZELMÜLLER, and J. BOIKE (2017): 'Transient modeling of the ground thermal conditions using satellite data in the Lena River delta, Siberia'. *The Cryosphere*, vol. 11(3): pp. 1441–1463. DOI: 10.5194/tc-11-1441-2017.

WOLTER, J., H. LANTUIT, M. FRITZ, M. MACIAS-FAURIA, I. MYERS-SMITH, and U. HERZSCHUH (2016): 'Vegetation composition and shrub extent on the Yukon coast, Canada, are strongly linked to ice-wedge polygon degradation'. *Polar Research*, vol. 35(1): p. 27489. DOI: 10.3402/polar.v35.27489.

WRONA, F. J., M. JOHANSSON, J. M. CULP, A. JENKINS, J. MÅRD, I. H. MYERS-SMITH, T. D. PROWSE, W. F. VINCENT, and P. A. WOOKEY (2016): 'Transitions in Arctic ecosystems: Ecological implications of a changing hydrological regime'. *Journal of Geophysical Research: Biogeosciences*, vol. 121(3): pp. 650–674. DOI: 10.1002/2015JG003133 (cit. on p. 4).

YEN, Y.-C. (1981): *Review of thermal properties of snow, ice, and sea ice*. Vol. 81. 10. US Army, Corps of Engineers, Cold Regions Research and Engineering Laboratory (cit. on p. 28).

YERSHOV, E. D. (1998): *General Geocryology*. Cambridge University Press (cit. on p. 15).

YERSHOV, E. D., K. A. KONDRAT'YEVA, V. F. LOGINOV, and I. K. SYCHEV (1999): *Geocryological map of Russia and neighbouring republics* (cit. on p. 19).

Zhang, W., A. K. Liljedahl, M. Kanevskiy, H. E. Epstein, B. M. Jones, M. T. Jorgenson, and K. Kent (2020): ‘Transferability of the Deep Learning Mask R-CNN Model for Automated Mapping of Ice-Wedge Polygons in High-Resolution Satellite and UAV Images’. *Remote Sensing*, vol. 12(7): p. 1085. doi: `10.3390/rs12071085`.

Zhang, W., C. Witharana, A. Liljedahl, M. Kanevskiy, W. Zhang, C. Witharana, A. K. Liljedahl, and M. Kanevskiy (2018): ‘Deep Convolutional Neural Networks for Automated Characterization of Arctic Ice-Wedge Polygons in Very High Spatial Resolution Aerial Imagery’. *Remote Sensing*, vol. 10(9): p. 1487. doi: `10.3390/rs10091487`.

Zhang, Y., S. K. Carey, W. L. Quinton, J. R. Janowicz, J. W. Pomeroy, and G. N. Flerchinger (2010): ‘Comparison of algorithms and parameterisations for infiltration into organic-covered permafrost soils’. *Hydrology and Earth System Sciences*, vol. 14(5): pp. 729–750. doi: `10.5194/hess-14-729-2010`.

Zubrzycki, S., L. Kutzbach, G. Grosse, A. Desyatkin, and E.-M. Pfeiffer (2013): ‘Organic carbon and total nitrogen stocks in soils of the Lena River Delta’. *Biogeosciences*, vol. 10(6): pp. 3507–3524. doi: `10.5194/bg-10-3507-2013`.

Zuecco, G., M. Rinderer, D. Penna, M. Borga, and H. J. van Meerveld (2019): ‘Quantification of subsurface hydrologic connectivity in four headwater catchments using graph theory’. *Science of The Total Environment*, vol. 646: pp. 1265–1280. doi: `10.1016/j.scitotenv.2018.07.269`.

Zweigel, R., S. Westermann, J. Nitzbon, M. Langer, J. Boike, B. Etzelmüller, and T. Vikhamar Schuler (2020): ‘Simulating snow redistribution and its effect on the ground thermal regime at a high-Arctic site on Svalbard’. *Journal of Geophysical Research: Earth Surface*, vol. in review (cit. on p. 38).

Publications

Articles related to this dissertation published in peer-reviewed journals

1. Nitzbon, J., S. Westermann, M. Langer, L. C. P. Martin, J. Strauss, S. Laboor, and J. Boike (2020): 'Fast response of cold ice-rich permafrost in northeast Siberia to a warming climate'. *Nature Communications*, vol. 11: p. 2201. doi: `10.1038/s41467-020-15725-8`.
2. Nitzbon, J., M. Langer, S. Westermann, L. Martin, K. S. Aas, and J. Boike (2019): 'Pathways of ice-wedge degradation in polygonal tundra under different hydrological conditions'. *The Cryosphere*, vol. 13(4): pp. 1089–1123. doi: `10.5194/tc-13-1089-2019`.
3. Aas, K. S., L. Martin, J. Nitzbon, M. Langer, J. Boike, H. Lee, T. K. Berntsen, and S. Westermann (2019): 'Thaw processes in ice-rich permafrost landscapes represented with laterally coupled tiles in a land surface model'. *The Cryosphere*, vol. 13(2): pp. 591–609. doi: `10.5194/tc-13-591-2019`.
4. Martin, L. C. P., J. Nitzbon, K. S. Aas, B. Etzelmüller, H. Kristiansen, and S. Westermann (2019): 'Stability Conditions of Peat Plateaus and Palsas in Northern Norway'. *Journal of Geophysical Research: Earth Surface*, vol. 124: pp. 705–719. doi: `10.1029/2018JF004945`.
5. Boike, J., J. Nitzbon, K. Anders, M. Grigoriev, D. Bolshiyanov, M. Langer, S. Lange, N. Bornemann, A. Morgenstern, P. Schreiber, C. Wille, S. Chadburn, I. Gouttevin, E. Burke, and L. Kutzbach (2019): 'A 16-year record (2002–2017) of permafrost, active-layer, and meteorological conditions at the Samoylov Island Arctic permafrost research site, Lena River delta, northern Siberia: an opportunity to validate remote-sensing data and land surface, snow, and permafrost models'. *Earth System Science Data*, vol. 11(1): pp. 261–299. doi: `10.5194/essd-11-261-2019`.

Articles related to this dissertation submitted to peer-reviewed journals

1. Nitzbon, J., M. Langer, L. C. P. Martin, S. Westermann, T. Schneider von Deimling, and J. Boike (2020): 'Effects of multi-scale heterogeneity on the simulated evolution of ice-rich permafrost lowlands under a warming climate'. *The Cryosphere*, vol. submitted.

2. Zweigel, R., S. Westermann, J. Nitzbon, M. Langer, J. Boike, B. Etzelmüller, and T. Vikhamar Schuler (2020): 'Simulating snow redistribution and its effect on the ground thermal regime at a high-Arctic site on Svalbard'. *Journal of Geophysical Research: Earth Surface*, vol. in review.

Software code developed within the context of this dissertation

1. Nitzbon, J., M. Langer, S. Westermann, and L. C. P. Martin (2019): *CryoGrid/CryoGrid3: CryoGrid 3 set-up for ice-wedge polygons*. doi: `10.5281/zenodo.2601973`.
2. Nitzbon, J., M. Langer, S. Westermann, and L. C. P. Martin (2020): *CryoGrid/CryoGrid3: CryoGrid 3 set-up for ice-rich permafrost*. doi: `10.5281/zenodo.3648266`.

Articles not related to this dissertation published in peer-reviewed journals

1. Nitzbon, J., J. Heitzig, and U. Parlitz (2017a): 'Sustainability, collapse and oscillations in a simple World-Earth model'. *Environmental Research Letters*, vol. 12(7): p. 074020. doi: `10.1088/1748-9326/aa7581`.
2. Nitzbon, J., P. Schultz, J. Heitzig, J. Kurths, and F. Hellmann (2017b): 'Deciphering the imprint of topology on nonlinear dynamical network stability'. *New Journal of Physics*, vol. 19(3): p. 033029. doi: `10.1088/1367-2630/aa6321`.

A Supplementary Information for Article 2

Supplementary Information for

FAST RESPONSE OF COLD ICE-RICH PERMAFROST IN NORTHEAST SIBERIA TO A WARMING CLIMATE

by JAN NITZBON et al.

Supplementary Methods 1

Calculation of the NESAL carbon stocks. We used total organic carbon (TOC) data from a total of 984 soil samples from the study region as input for the statistical bootstrapping approach by Strauss et al.[1] in order to derive representative soil organic carbon pools for the different landscape types considered in the simulations (drained lake basins (LB), Holocene deposits(HD), Yedoma deposits (YD)). Scaling the organic carbon pools with the areas of the respective landscape types (see Table 1 in Methods), resulted in estimated pools of 24.7 GtC for LB, 63.0 GtC for HD, and 13.0 GtC for YD, giving a total NESAL carbon pool of 100.7 GtC. Note that these pools include both active layer and permafrost deposits. For illustration, the total carbon pool was converted to an atmospheric CO_2 concentration using the conversion factor of 0.471 by Battle[2] and an airborne fraction of 0.5.

Supplementary Methods 2

Details on the numerical model. The numerical model of ice-wedge terrain we used for our study was based on the model setup by Nitzbon et al.[3,4] While we adapted most of the model setup used in that study, we extended and modified the model, in order to represent more processes and to be applicable to further landscape types. The changes compared to the model version of Nitzbon et al.[3] are detailed in the subsequent sections. Those process implementations and parameter values which are not discussed in the subsequent sections were adopted as described by Nitzbon et al.[3] The model code and the settings to reproduce the numerical simulations of the present study are available from `https://doi.org/10.5281/zenodo.3648266`.

Implementation of lateral sediment transport. The calculation of lateral sediment fluxes was adapted from Roering et al.[5] and Plug and West[6], who proposed a law for the effective hillslope sediment transport (q^{sed}) as a combination of diffusive (q^{diff}) and advective (q^{adv}) processes. The diffusive part of the sediment transport is increasing linearly with the slope. In our tile-based model the slope between two adjacent tiles is obtained from the difference in soil surface elevations (a) and the lateral distance between the tiles (D). The diffusive sediment flux (in m^2 s^{-1}) between two tiles i and j is thus given as follows (see blue curve in Supplementary Figure 11):

$$q^{\text{diff}}_{i \leftarrow j} = K_{\text{eff}} \, \frac{a_j - a_i}{D_{ij}} \tag{1}$$

where K_{eff} (m^2 s^{-1}) is a sediment transport coefficient detailed below. The advective part of the sediment transport is negligible for small slope angles, but diverges when a critical slope α_{crit} is approached. It can be expresses in terms of the slope angle $\alpha = \arctan\left(\frac{a_j - a_i}{D_{ij}}\right)$ as follows (see red curve in Supplementary Figure 11):

$$q^{\text{adv}}_{i \leftarrow j} = K_{\text{eff}} \frac{a_j - a_i}{D_{ij}} \frac{\alpha^2}{\alpha^2_{\text{crit}} - \alpha^2} \tag{2}$$

The total sediment flux is obtained by summing up the diffusive and advective contributions (see yellow curve in Supplementary Figure 11):

$$
\begin{aligned}
q^{\text{sed}}_{i\leftarrow j} &= q^{\text{diff}}_{i\leftarrow j} + q^{\text{adv}}_{i\leftarrow j} && (3)\\
&= K_{\text{eff}} \frac{a_j - a_i}{D_{ij}} \frac{\alpha^2_{\text{crit}}}{\alpha^2_{\text{crit}} - \alpha^2} && (4)\\
&= K_{\text{eff}} \frac{a_j - a_i}{D_{ij}} \frac{1}{1 - \left(\frac{\alpha}{\alpha_{\text{crit}}}\right)^2} && (5)
\end{aligned}
$$

The volumetric sediment flux between two tiles (in $\text{m}^3\,\text{s}^{-1}$) is obtained by multiplying the fluxes q with the contact length of the interface between the two involved tiles (L_{ij}). The sediment deposition rate (in $\text{m}\,\text{s}^{-1}$) of tile i is obtained by dividing the actual flux by the area of the tile (A_i).

The effective sediment transport coefficient (K_{eff}, also referred to as “hillslope diffusivity”, in $\text{m}^2\,\text{s}^{-1}$) is calculated as the reciprocal sum of the land (subaerial) and water (subaqueous) part of the vertical interface between the soil surface altitudes of the involved tiles (see Supplementary Figure 12 for an illustration). In the illustration and the equations below, a refers to the soil surface altitude, and s refers to the surface altitude including water bodies above the the soil level. K_{eff} is calculated as follows:

$$
\begin{aligned}
K_{\text{eff}} &= \frac{\varphi_{\text{tot}}}{\frac{\varphi_{\text{water}}}{K_{\text{water}}} + \frac{\varphi_{\text{land}}}{K_{\text{land}}}} \qquad \text{, where:} && (6)\\
\varphi_{\text{tot}} &= |a_i - a_j| \ , && (7)\\
\varphi_{\text{land}} &= \max\left[0, \max\left(a_i, a_j\right) - \min\left(s_i, s_j\right)\right] \ , && (8)\\
\varphi_{\text{water}} &= \max\left[0, \min\left(\varphi_{\text{tot}}, \min\left(s_i, s_j\right) - \min\left(a_i, a_j\right)\right)\right] \ . && (9)
\end{aligned}
$$

For our simulations we used $K_{\text{land}} = 3 \times 10^{-10}\,\text{m}^2\,\text{s}^{-1}$ and $K_{\text{water}} = 3 \times 10^{-8}\,\text{m}^2\,\text{s}^{-1}$.

According to Plug and West[6] the value of the critical slope angle (α_{crit}) differs for frozen and unfrozen sediment. For unfrozen conditions we adopted the proposed value of $\alpha_{\text{crit}} = 45°$ by Plug and West[6]. For frozen ground conditions the authors suggested a value of $\alpha_{\text{crit}} = 90°$, leading to substantially reduced sediment transport during freezing conditions. For simplicity, we set lateral sediment transport to zero during freezing conditions. An overview of the parameter values used for the lateral sediment transport is provided in Table 2.

In CryoGrid 3, the lateral sediment fluxes are calculated at each lateral transport time step (Δt_{lat}) which was set to 3600 s in our simulations. The sediment flux was further differentiated into mineral and organic contributions, according to the mineral and organic fractions in the uppermost grid cell of the more elevated tile. The lateral sediment transport scheme thus conserves the total sediment amount as well as the amounts of minerals and organics.

We assumed a dynamic equilibrium between the diffusive hillslope transport and the heaving of the ground surface due to aggradation of ground ice. Hence we did not explicitly apply the diffusive sediment fluxes, but only considered the advective fluxes. These advective fluxes correspond to rapid mass movement (“mass-wasting” or “slumping”) which is observable in permafrost environments at steep unfrozen slopes.

Note that our model does not take into account periglacial processes like forst-cracking, ground ice accumulation, and frost-creep, which control periglacial landscape evolution on timescales of thousands to millions of years[7,8]. On timescales tens to hundreds of years, other processes such as ground subsidence and slumping are dominating the surface geomorphology in ice- and organic-rich soils, particularly under warming climatic conditions.

Hydrological boundary conditions. In our simulations the hydrological conditions were controlled via a hypothetical external “water reservoir” at a fixed altitude a_{res}. While Nitzbon et al.[3] used a reservoir which allows fluxes in both directions, i.e. from the troughs into the reservoir and vice versa, for the present study we excluded fluxes from the reservoir into the troughs.

The reservoir hydraulic conductivity (K_{res}) factors in the distance (D_{res}) and contact length (L_{res}) to the reservoir. Assuming that the modelled system is surrounded by a circular reservoir at distance D_{res} gives a contact length of $L_{\text{res}} = 2\pi D_{\text{res}}$, such that the distance cancels out:

$$K_{\text{res}} = K \frac{L_{\text{res}}}{D_{\text{res}}} = 2\pi K \tag{10}$$

where $K = 1 \cdot 10^{-5}\,\text{m}\,\text{s}^{-1}$ is the same subsurface hydraulic conductivity which is used for the lateral water fluxes between two tiles.

Snow redistribution. Snow was redistributed among the different tiles (polygon centres, polygon rims, and troughs), assuming a preferential accumulation of snow in topographic depressions. The maximum height of the snow pack was limited to $h^{\text{max}} = 0.4\,\text{m}$ relative to the tile with the highest topographic elevation (including soil and water surfaces).

The snow redistribution scheme differed slightly from the implementation used by Nitzbon et al.[3] We scaled the incoming solid precipitation based on the differences in the surface altitudes (including snow cover) of the tiles, similarly to the scheme employed by Aas et al.[9] As long as the snow height of a tile is below a threshold height which reflects the snow catch effect of the vegetation ($h^{\text{catch}} = 0.1\,\text{m}$), the respective tile receives the full solid precipitation input from the forcing data. The snow input of low-lying tiles is scaled up, if there are higher-elevated tiles whose snow cover exceeds the threshold height. The higher-elevated tiles whose snow height exceeds the threshold height do not receive snow input until the lower-lying tiles' snow heights are equal. The scaling approach takes into account the different areas of the tiles such that the total amount of incoming solid precipitation is conserved.

Surface topology of ice-wedge polygons. The lateral transport schemes for heat, snow, water, and sediment require topological relations between the different tiles (polygon centres, polygon rims, and troughs). For the total area of one polygonal structure we assumed the same value as Nitzbon et al.[3] ($A_{\text{tot}} = 140\,\text{m}^2$), which is based on mapping of polygonal tundra at a well-studied site within the study area[10]. The areas of each tile are calculated using their areal fractions (γ) for which we also used the same values as Nitzbon et al.[3] (see Table 1):

$$A_{\mathrm{C}} = \gamma_{\mathrm{C}} A_{\mathrm{tot}} \tag{11}$$

$$A_{\mathrm{R}} = \gamma_{\mathrm{R}} A_{\mathrm{tot}} \tag{12}$$

$$A_{\mathrm{T}} = \gamma_{\mathrm{T}} A_{\mathrm{tot}} \tag{13}$$

In order to derive further topological relations between the tiles, we assumed a nested circular geometry in which the polygon centres are embedded into circularly shaped rims and troughs (see Supplementary Figure 10 for an illustration). The (outer) radii of the respective circular structures are obtained as follows:

$$r_{\mathrm{C}} = \sqrt{\frac{A_{\mathrm{C}}}{\pi}} \tag{14}$$

$$r_{\mathrm{R}} = \sqrt{\frac{A_{\mathrm{C}} + A_{\mathrm{R}}}{\pi}} \tag{15}$$

$$r_{\mathrm{T}} = \sqrt{\frac{A_{\mathrm{C}} + A_{\mathrm{R}} + A_{\mathrm{T}}}{\pi}} \tag{16}$$

The radii can be used to calculate the lateral distances between the centre and rim tiles (D_{CR}), and between the rim and the trough tiles (D_{RT}) as follows:

$$D_{\mathrm{CR}} = \frac{1}{2}(r_{\mathrm{C}} + r_{\mathrm{R}}) \tag{17}$$

$$D_{\mathrm{RT}} = r_{\mathrm{T}} - \frac{r_{\mathrm{R}}}{2} - \frac{r_{\mathrm{C}}}{2} \tag{18}$$

The contact lengths between the center and rim tiles (L_{CR}), and between the rim and trough tiles (L_{RT}) are the perimeters of the respective circular structures:

$$L_{\mathrm{CR}} = 2\pi r_{\mathrm{C}} \tag{19}$$

$$L_{\mathrm{RT}} = 2\pi r_{\mathrm{R}} \tag{20}$$

The values of all topological parameters described above are provided in Table 1.

Subsurface stratigraphies of ice-wedge polygons. While we partitioned ice-wedge terrain based on the surface microtopography of polygonal tundra into three tiles (centers, rims, troughs), the deeper subsurface of ice-wedge terrain is essentially partitioned into two units, namely pure wedge ice ("wed"), and ice-rich sediment between the ice wedges ("sed")[1]. In an idealized polygonal tundra landscape the polygon centers are underlain by ice-rich sediment while there is pure wedge ice below the troughs (down to the maximum depth of the ice wedges). The rims of the polygons are underlain partly by sediment and partly by wedge ice, depending on the lateral dimensions of the ice wedges (Supplementary Figure 10). We assumed the volumetric ground ice content to be $\theta_{\mathrm{i}}^{\mathrm{wed}} = 0.95$ for pure wedge ice, and $\theta_{\mathrm{i}}^{\mathrm{sed}} = 0.65$ for ice-rich sediment, following Strauss et al.[1] The volumetric ground ice contents of the three tiles (C,R,T) were composed of these values follows (see 10):

$$\theta_{\mathrm{i,C}} = \theta_{\mathrm{i}}^{\mathrm{sed}} \tag{21}$$

$$\theta_{\mathrm{i,R}} = \frac{1}{\gamma_{\mathrm{R}}}\left((\gamma_{\mathrm{sed}} - \gamma_{\mathrm{C}})\theta_{\mathrm{i}}^{\mathrm{sed}} + (\gamma_{\mathrm{wed}} - \gamma_{\mathrm{T}})\theta_{\mathrm{i}}^{\mathrm{wed}}\right) \tag{22}$$

$$\theta_{\mathrm{i,T}} = \theta_{\mathrm{i}}^{\mathrm{wedge}} \tag{23}$$

where γ_{sed} is the overall fraction of ice-rich sediment. $\gamma_{\mathrm{wed}} = 1 - \gamma_{\mathrm{sed}}$ is the overall fraction of wedge ice in the subsurface. It corresponds to the wedge-ice volumes provided in Table 1 for the different landscape types (LB, HD, YD). Soil layers for which the ice content (θ_{i}) exceeded the "natural" porosity ($\phi_{\mathrm{nat}} = 0.55$) were considered by the model to contain excess ice. The thickness of the ice-rich deposits (i.e. the depth of the ice wedges) was based on published estimates on ice-wedge dimensions from the study area[1,11] and field experience. We assumed best-guess depths for the NESAL of 4.0 m for LB, 10.0 m for HD, and 20.0 m for YD (see Tables 1).

The organic an mineral fractions were based on soil samples from the study region as described in the Mehtods section of the main text. An overview of the soil stratigraphies, including the organic, mineral, and ice contents as well as soil textures is provided in Tables 3 to 5.

Supplementary Methods 3

Reference runs. We conducted reference runs to reflect the response of the subsurface to warming climatic conditions in a model setup which is comparable to the design of land surface schemes of ESMs. For this we used CryoGrid 3 with a one-dimensional representation of the subsurface, i.e. without multiple tiles among which lateral fluxes occur. Moreover, the soil stratigraphy did not contain any excess ice (see Table 6). All surface water was considered as runoff and thus removed from the system. All other processes (heat conduction, snow scheme, hydrology scheme), parameter values, and the forcing data were identical to the model runs with a tiled setup. The simulation period included a 50-year spin-up (10/1949–12/1999) and a 100-year comparison period (01/2000–12/2099). We conducted one run under the RCP4.5 scenario, and one run under the RCP8.5 scenario.

The maximum thaw depth (11-year running mean) and the hydrological regime of unfrozen ground are display in Supplementary Figure 6. Under both warming scenarios the maximum thaw depth increased significantly within the simulation period. However, permafrost remained stable beyond 2100, as no permanently unfrozen layer (talik) formed in the simulations. This is in agreement with projections from land surface models for the same region[12–15]. Overall, permafrost degradation (i.e., lowering of the permafrost table) was significantly smaller in the reference runs compared to the runs with a tiled setup, since the latter took into account the melting of excess ground ice as well as feedback processes through lateral fluxes of heat, water, snow, and sediment.

Supplementary Methods 4

Simulations for an ambitious mitigation scenario (RCP2.6). We conducted additional simulations for the ambitious mitigation scenario RCP2.6. Supplementary Figure 7 shows the results in terms of accumulated ground subsidence, maximum thaw depth, and subsurface hydrological conditions, in analogy to Figure 3 of the main text.

Except for YD under water-logged conditions there is no subsidence due to melting of excess ground ice. The maximum thaw depths as well as the subsurface hydrological conditions remain stable throughout the simulation period. Under water-logged conditions YD show an accumulated mean subsidence of about 0.4 m, associated with the formation of a shallow surface water body (Supplementary Figure 7 f). This is, however, small compared to the thaw lake depth of about 2 m under RCP4.5 and about 4 m under RCP8.5 by the end of the simulation period (Figure 3 i,l).

In summary, under the RCP2.6 warming scenario ice-rich permafrost in the NESAL is projected to remain largely stable. Ice-wedge melt and surface water body formation could, however occur in very ice-rich Yedoma deposits. It should further be noted, that the process of ice-wedge growth and thus ground-ice accumulation could play a more important role for permafrost stability under RCP2.6 compared to RCP4.5 and RCP8.5. However, it is not taken into account by the model used for this study, and is likely to be negligible on the time scales of interest.

Supplementary Notes 1

Terminology and definitions. The terminology in our article largely follows the definitions in the "Cryosphere Glossary" of the the National Snow and Ice Data Center[16] and Kokelj and Jorgenson[17]:

Ground ice: a general term referring to all types of ice contained in freezing and frozen ground.[16]

Massive ice: a comprehensive term used to describe large masses of ground ice, including ice wedges, pingo ice, buried ice and large ice lenses.[16]

Wedge ice: ice occurring in an ice wedge.[16]

Excess ice: the volume of ice in the ground which exceeds the total pore volume that the ground would have under natural unfrozen conditions.[16]

Ice-rich permafrost: permafrost containing excess ice.[16]

Thermokarst (process): refers to the suite of processes by which characteristic landforms result from the thawing of ice-rich permafrost or melting of massive ground ice.[17]

Thermokarst landforms: Landforms emerging form thermokarst activity. In continuous permafrost these comprise, e.g., thermokarst lakes (or thaw lakes), drained lake basins ("alas"), thermokarst mounds ("baidzharakhs"), thermokarst troughs, high-centred polygons, thermo-erosional gullies, retrogressive thaw slumps, and active-layer detachments. These landforms co-occur or interact with each other, giving rise to other landforms (e.g. drainage of a thermokarst lake through incision of a thermo-erosional gully).

Thermokarst-inducing processes (numerical models): We introduce this term to refer to the structures and processes which are needed for representing the initiation and evolution of thermokarst and associated feedbacks in numerical permafrost models. These comprise, but are not limited to

- representation of excess ground ice and ground subsidence upon thawing of ice-rich permafrost (e.g., refs. [18,19])
- ponding of surface water and related thermal processes (e.g., refs. [19–21])
- spatially heterogeneous distribution of (excess) ground ice (e.g., refs. [3,9,20])
- micro- (meters to tens of meters) and meso-scale lateral fluxes of heat, water, snow (e.g., refs. [3,9,20–22])
- micro-scale lateral fluxes of sediment (slumping) (e.g., this study)

Thermokarst-inducing processes can cause permafrost thaw dynamics which are fundamentally different from the gradual top-down thawing of permafrost in ice-poor terrain.

Supplementary Notes 2

Dominant types of excess ground ice and associated degradation pathways. Our study specifically addresses permafrost degradation pathways which occur in ice-rich permafrost landscapes that are underlain by massive ice wedges, since these constitute the dominant type of excess ground ice in the lowlands of northeast Siberia (NESAL) [23,24]. Other types of massive ground ice such as buried glacier ice, buried lake ice, or buried snowpacks are not common in the study area [23]. Past landscape evolution throughout the Holocene has preconditioned the northeast Siberian lowlands with different cryostratigraphies, characterized by different depths and sizes of ice wedges (Supplementary Figure 1). Our modelling approach thus focuses on the representation of ice-wedge degradation at the micro-scale (individual polygon scale), taking into account different abundances of wedge ice in the subsurface. At the meso-scale (or landscape-scale) the degradation of ice wedges can lead to the emergence of larger-scale thaw features such as thaw lakes or thermo-erosional valleys. While our model setup does not explicitly represent the spatio-temporal dynamics of these features (e.g. shoreline erosion or drainage of thaw lakes), the thaw processes involved at the micro-scale are reflected by performing simulations under contrasting hydrological conditions (water-logged versus well-drained).

By restricting our analysis to lowlands, we a priori exclude certain thermokarst features that are characteristic to hillslopes, such as landslides or active layer detachments[17]. We further do not address degradation pathways of ice-rich permafrost which are very localized (e.g., retrogressive thaw slumps) or linear (e.g., coastal erosion). For example, Nitze et al.[25] estimated that between 1999 and 2014 a total area of $1.08\,\mathrm{km}^2$ was be affected by 140 retrogressive thaw slumps within a transect of about $43000\,\mathrm{km}^2$ which intersects with a large part of our study area. Even if thaw slumps would become more abundant in a warming climate, the total area directly affected would still be small compared to our estimated areas of ice-wedge terrain. Similarly, Günther et al.[26] estimated recent erosion rates of ice-rich coastline along the Laptev sea (about $1400\,\mathrm{km}$) to be in the order of $5\,\mathrm{m\,yr}^{-1}$. Assuming a more pessimistic value of $10\,\mathrm{m\,yr}^{-1}$ over a 100 year time-frame, would yield a total affected area of $1400\,\mathrm{km}^2$. Hence, the total areas and carbon pools affected by these mass-wasting lateral erosion processes are small compared to the vast areas underlain by ice wedges which would be affected by spacious ice-wedge degradation (about $493000\,\mathrm{km}^2$). Overall, we are thus confident that our model approach captures the dominant pathways of permafrost degradation in the study region.

Supplementary Notes 3

Relations between cryostratigraphy, subsidence, permafrost thaw, and thawed organic carbon. Our simulations shed light on the interrelations between cryostratigraphy, ground subsidence, permafrost thaw, and the amount of thawed organic carbon in a warming climate. As indicated in main Figure 3 j, the amount of thawed permafrost (ΔP) is composed of the accumulated ground subsidence (ΔS) and the increase in thaw depth (ΔD_{AL}):

$$\Delta P = \Delta S + \Delta D_{\mathrm{AL}} \tag{24}$$

Moreover, there is an idealized linear relation between permafrost thaw (ΔP) and ground subsidence (ΔS) when assuming that thawing ice-rich soil layers (immediately) settle with a (constant) natural porosity (ϕ_{nat}), and that the excess ice ($\theta_{\mathrm{i}} - \phi_{\mathrm{nat}}$) is removed from the soil column. Under these assumptions the following relation holds for ΔP:

$$\Delta P = \Delta S \, \frac{1 - \phi_{\mathrm{nat}}}{\theta_{\mathrm{i}} - \phi_{\mathrm{nat}}} \tag{25}$$

Equating the right hand sides of equations (24) and (25), and solving for ΔD_{AL} gives:

$$\Delta D_{\mathrm{AL}} = \Delta S \, \frac{1 - \theta_{\mathrm{i}}}{\theta_{\mathrm{i}} - \phi_{\mathrm{nat}}} \tag{26}$$

Similarly, ΔP can be expressed in terms of ΔD_{AL}:

$$\Delta P = \Delta D_{\mathrm{AL}} \, \frac{1 - \phi_{\mathrm{nat}}}{1 - \theta_{\mathrm{i}}} \tag{27}$$

Supplementary Figure 8 a shows the simulated and idealized relations between ΔD_{AL} and ΔS over the entire simulation period for the three different landscape types (i.e., cryostratigraphies) and the two hydrological conditions (water-logged, well-drained) considered in this study. As the above-mentioned assumptions underlie the excess ice scheme of CryoGrid 3, the simulated trajectories follow the idealized dependencies fairly well. As expected, ΔS increases with the mean excess ice content (θ_{i}) of the landscape type. Also ΔD_{AL} by the end of the simulation period increases with θ_{i}, reflecting that for the RCP8.5 scenario the permafrost is not in equilibrium with the warmer climate. Overall, ΔP by the end of the simulation period shows a strong dependence on the cryostratigraphy.

However, as the volumetric organic contents (θ_o) vary among the sediments of the different landscape types, the relation between the additional organic carbon subject to thawed conditions (ΔC) does not show the same dependence on ΔS as ΔD_AL (Supplementary Figure 8 b). Interestingly, the value of ΔC by the end of the simulation period shows little dependence on the landscape type, indicating that different organic contents between the landscapes counterbalance different increases in thaw depth.

Overall, these considerations highlight the importance of quantifying both the ground ice content (θ_i) and the natural porosity (ϕ_nat) in order to establish reliable relations between permafrost thaw, subsidence, thawed organic carbon, and the cryostratigraphy.

Supplementary Notes 4

Sensitivity analysis. To analyze the sensitivity of the results against parameter variations, we conducted four additional sets of simulations, in which single parameter values were changed from their default values. For each varied parameter, we conducted simulations for the Holocene Deposits (HD) stratigraphy, under constrasting hydrological conditions (water-logged versus well-drained) and two warming scenarios (RCP4.5 and RCP8.5). The results of these simulations in terms of accumulated ground subsidence and increae in thaw depth are shown in Supplementary Figure 13. Note that additional sensitivity analyses were carried out in a preceding study[3].

The strongest deviations from the default runs were found when reducing the snow density to $\rho_{\text{snow}} = 200\,\text{kg}\,\text{m}^{-3}$. The onset of ice-wedge degradation was shifted to the middle of the twenty-first century under well-drained and to the 2020s under water-logged conditions. Under RCP4.5 ice-wedge stabilization occured only under well-drained conditions, and a thaw lake formed under water-logged conditions, reaching a depth of about $2.5\,\text{m}$ by 2100. Under RCP8.5 subsidence rates compared to the default setting were substantially higher under well-drained conditions, and of similar magnitude (but temporally shifted) under water-logged conditions. These findings highlight the crucial role of snow characteristics for the stability of permafrost.

When reducing the sediment transport coefficients by a factor of three to $K_{\text{land}} = 1{\cdot}10^{-10}\,\text{m}\,\text{s}^{-1}$ and $K_{\text{water}} = 1 \cdot 10^{-8}\,\text{m}\,\text{s}^{-1}$, respectively, the results in terms of subsidence and maximum thaw depth did not change significantly, suggesting that the lateral sediment transport scheme is robust against such variations. However, if the transport coefficients were reduced by orders of magnitude, ice-wedges would not stabilize and the results would become unphysical. Conversely, increasing the transport coefficients to very high rates, would lead to fast flattening of the terrain, standing in contrast to observations.

Reducing the field capacity to $\theta_{\text{fc}} = 0.4$, has almost no effect on simulated subsidence rates and thaw depths. Only under RCP4.5 and water-logged conditions (Supplementary Figure 13 c) ice-wedge degradation was delayed by about two decades relative to the default run. The fractions of saturated and unsaturated conditions prevailing in thawed ground were not substantially affected by the change in field capacity (not shown).

By reducing the natural porosity to $\phi_{\text{nat}} = 0.45$ [1] the fraction of ice which is treated as excess ice is increased by 0.1. Consequently, the simulated subsidence rates and thaw depths for the HD stratigraphy, are similar to the corresponding results for Yedoma Deposits (YD) and default parameters ($\phi_{\text{nat}} = 0.55$; see Figure 3 c,f,i,l). However, this underlines the importance of constraining both the absolute ice content (θ_{i}) and the natural porosity of the ice-bearing sediments (ϕ_{nat}) in order to make quantitative predictions of ice-rich permafrost thaw.

In summary, the results were found to be robust against variations in parameters related to the hydrology scheme (θ_{fc}) and the lateral sediment transport scheme (K_{land}, K_{water}). While the results were affected by changes to the snow properties (ρ_{snow}) and the excess ice (ϕ_{nat}), our default choice for these parameters can be considered conservative.

---

[1] The field capacity was simultaneously reduced to $\theta_{\text{fc}} = 0.4$ to fulfill the constraint $\theta_{\text{fc}} < \phi_{\text{nat}}$.

Supplementary Figures

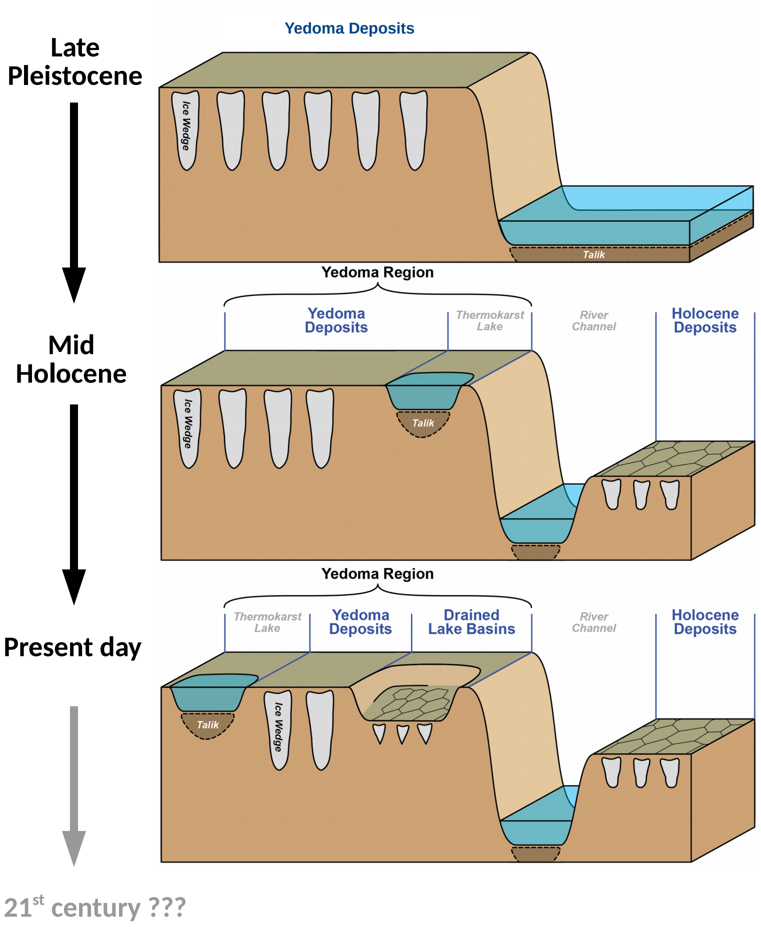
Late Pleistocene
Yedoma Deposits
Ice Wedge
Talik
Yedoma Region
Mid Holocene
Yedoma Deposits
Thermokarst Lake
River Channel
Holocene Deposits
Ice Wedge
Talik
Yedoma Region
Present day
Thermokarst Lake
Yedoma Deposits
Drained Lake Basins
River Channel
Holocene Deposits
Talik
Ice Wedge
21st century ???

Supplementary Figure 1: Schematic evolution of ice-rich permafrost landscapes in the NESAL during the Holocene. Ice- and organic-rich Yedoma deposits which accumulated during the last glacial period started to degrade through thermokarst and thermoerosion processes under the warmer climate of the Holocene. Meanwhile the climate within the NESAL was cold enough such that ground ice accumulated in newly formed Holocene deposits, leading to the growth of so-called syngenetic ice wedges. Occasional drainage of thermokarst lakes led to permafrost aggradation in drained lake basins and the growth of so-called epigenetic ice wedges (conical shape). Depending on the evolution during the Holocene, different types of ice wedges underlie the NESAL at present. The distribution of ground ice preconditions the landscapes for different pathways of permafrost thaw in the future, for which a warming climate is projected.

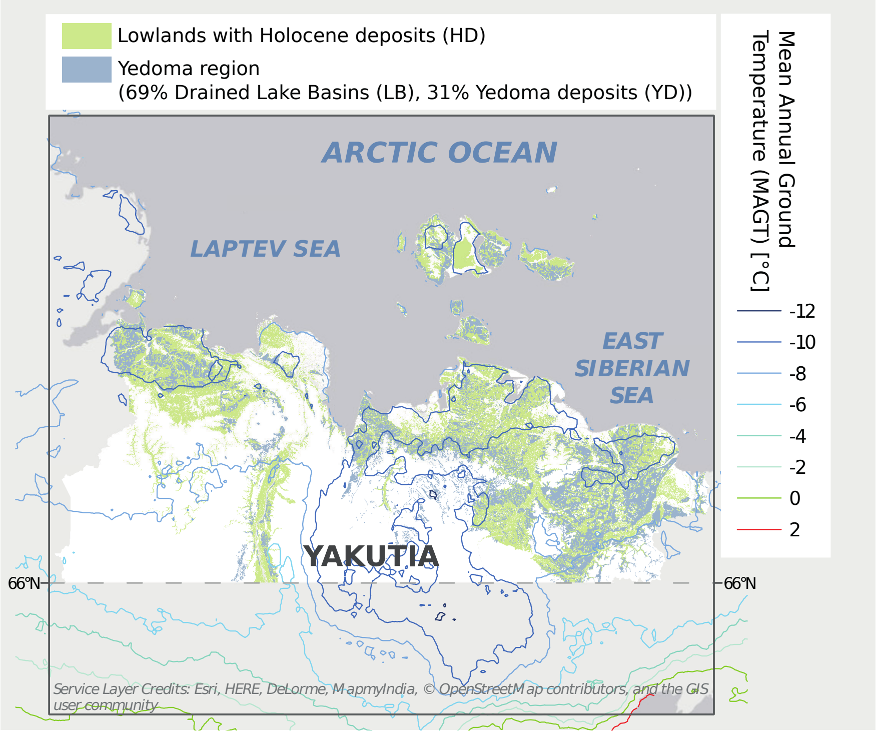
Lowlands with Holocene deposits (HD)
Yedoma region
(69% Drained Lake Basins (LB), 31% Yedoma deposits (YD))
ARCTIC OCEAN
LAPTEV SEA
EAST SIBERIAN SEA
YAKUTIA
66°N
66°N
Mean Annual Ground Temperature (MAGT) [°C]
-12
-10
-8
-6
-4
-2
0
2
Service Layer Credits: Esri, HERE, DeLorme, MapmyIndia, © OpenStreetMap contributors, and the GIS user community

Supplementary Figure 2: Map of the northeast Siberian Arctic (white region). Lowlands belonging to the Yedoma region (undegraded Yedoma deposits (YD) and drained thermokarst lake basins (LB) are indicated in pale blue. Lowlands outside the Yedoma region with younger Holocene deposits (HD) are indicated in pale green. The majority of the lowlands has present-day mean annual ground temperatures ranging between −8 and −12°C. The Yedoma region was mapped by Strauss et al.[27]. Ground temperature data are taken from Obu et al.[28]

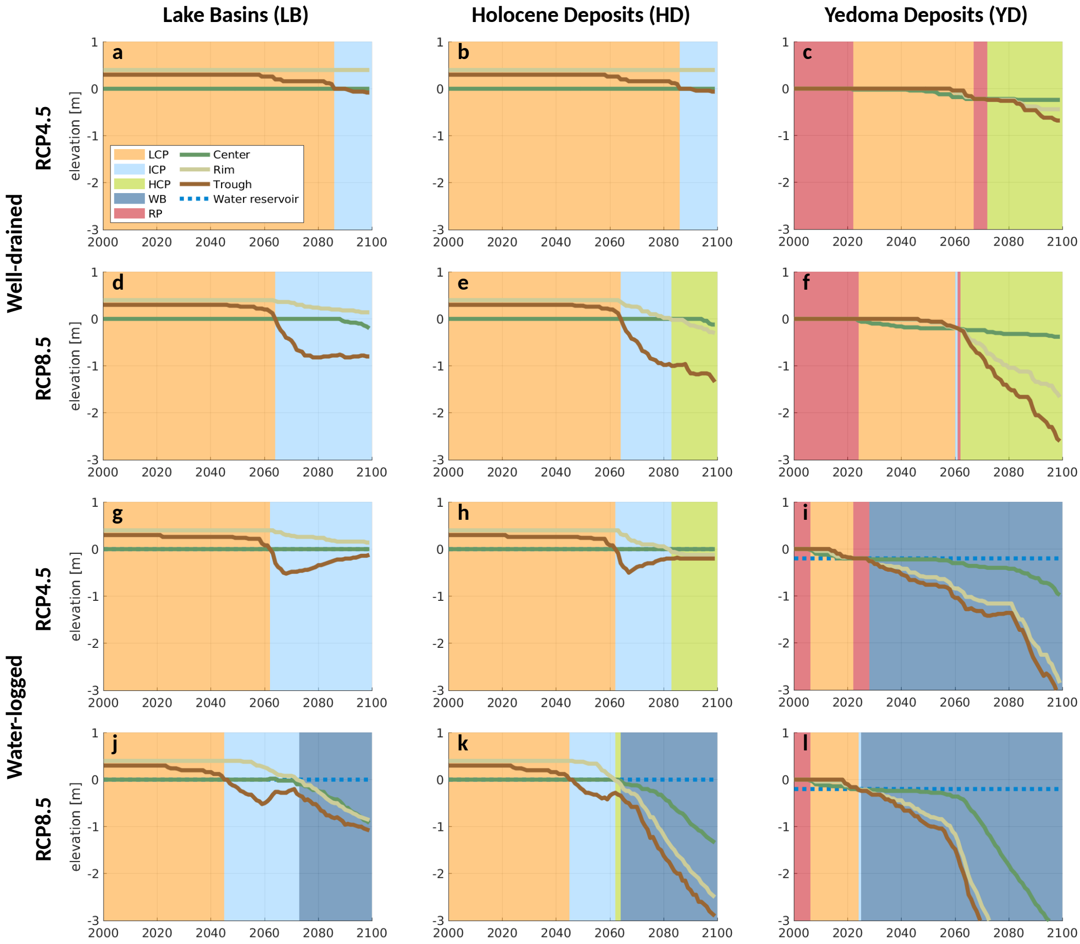

Supplementary Figure 3: Simulated evolution of the microtopography for all runs under RCP4.5 and RCP8.5. Bold lines show the soil surface altitudes of the three tiles (centres, rims, troughs), and background colours indicate the corresponding microtopographic states according to Eqn. (2) to (6).

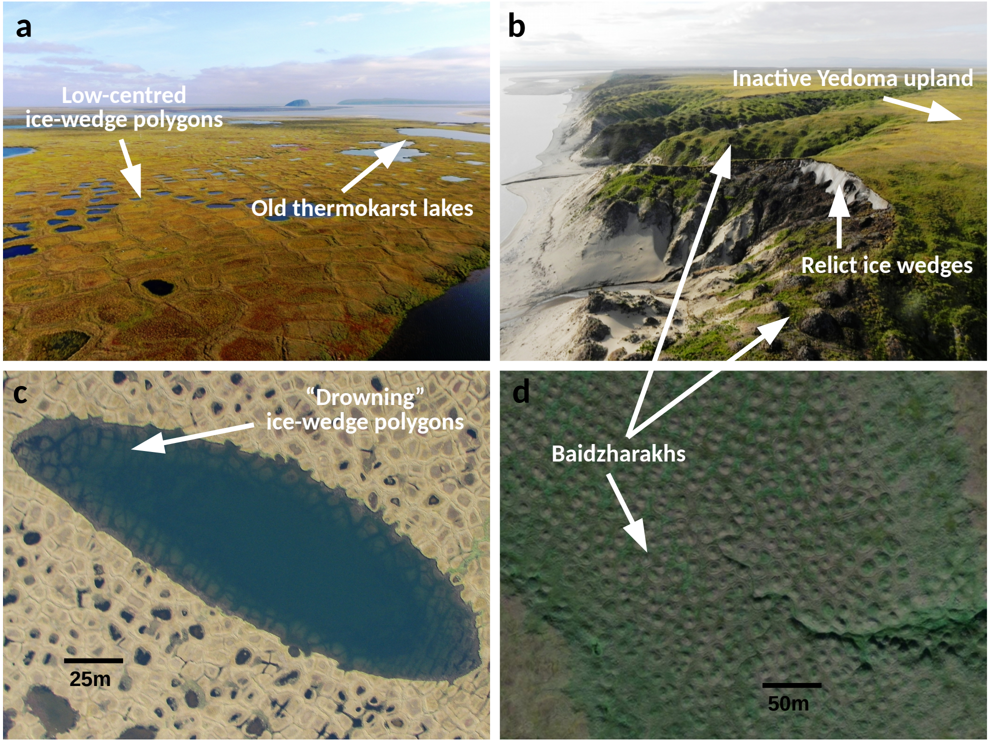
a
Low-centred ice-wedge polygons
Old thermokarst lakes
b
Inactive Yedoma upland
Relict ice wedges
Baidzharakhs
c
"Drowning" ice-wedge polygons
25m
d
50m

Supplementary Figure 4: Photographies of thaw features in the study region. The photographies show typical landforms and degradation features of ice-rich permafrost landscapes, corresponding to simulated states using our numerical model.

a: Ice-wedge polygons with a low-centred microtopography in the central Lena River delta (Samoylov Island). Small thermokarst lakes in the background are indicative of thermokarst activity in the past.

b: Yedoma deposits in the central Lena River delta (Kurungnakh Island). The undegraded uplands on the right have a flat surface topography while conical mounds termed "Baidzharakhs" are visible in the center. These form through melting of relict ice wedges at the exposure.

c: Thermokarst lakes on Samoylov Island. The high-centred microtopography of the ice-wedge polygons is preserved at the bottom of the water bodies.

d: "Baidzharakhs" at the bottom of a drained lake basin on Kurungnakh Island.

Image credits: a,b: Sebastian Zubrzycki (distributed via imaggeo.egu.eu under a CC BY-NC-SA 3.0 license). c: The authors. d: Esri, DigitalGlobe, GeoEye, Earthstar Geographics, CNES/Airbus DS, USDA, USGS, AeroGRID, IGN, and the GIS User Community.

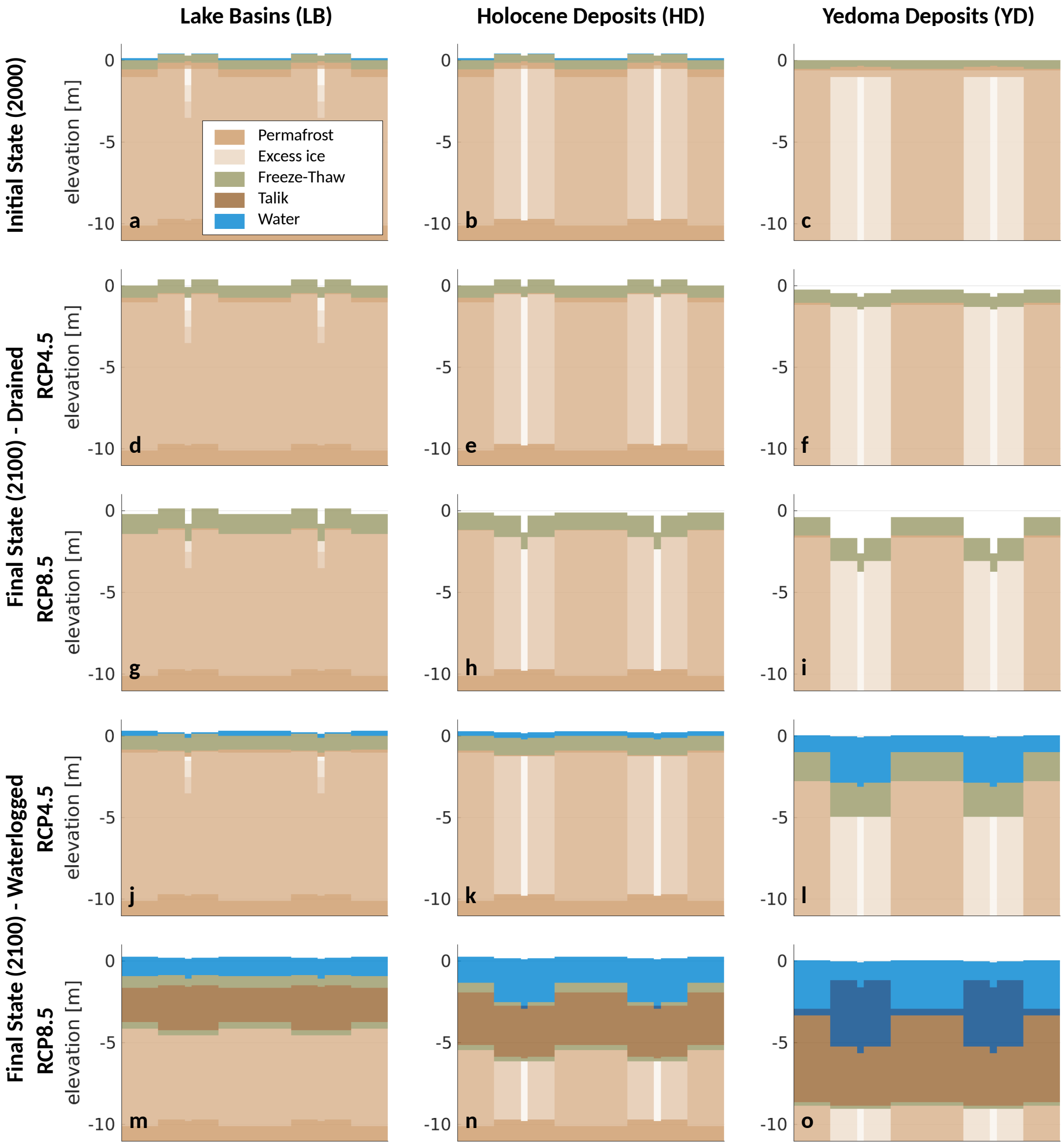

Supplementary Figure 5: Initial (2000) and final (2100) states of the landscape for all runs under RCP4.5 and RCP8.5. Layers containing excess ice are shown with a white overlay.

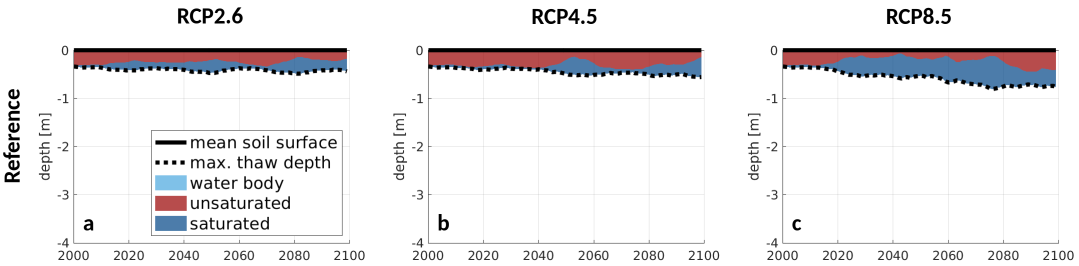

Supplementary Figure 6: Permafrost thaw in the reference runs. Dashed lines show the 11-year running mean of the maximum annual thaw depth for the reference runs without excess ground ice. As there is no ground subsidence (solid lines), permafrost degradation occurs only through active-layer deepening. Coloured areas indicate the fractions of unsaturated (red) and saturated (dark blue) conditions prevailing in the thawed ground throughout each year.

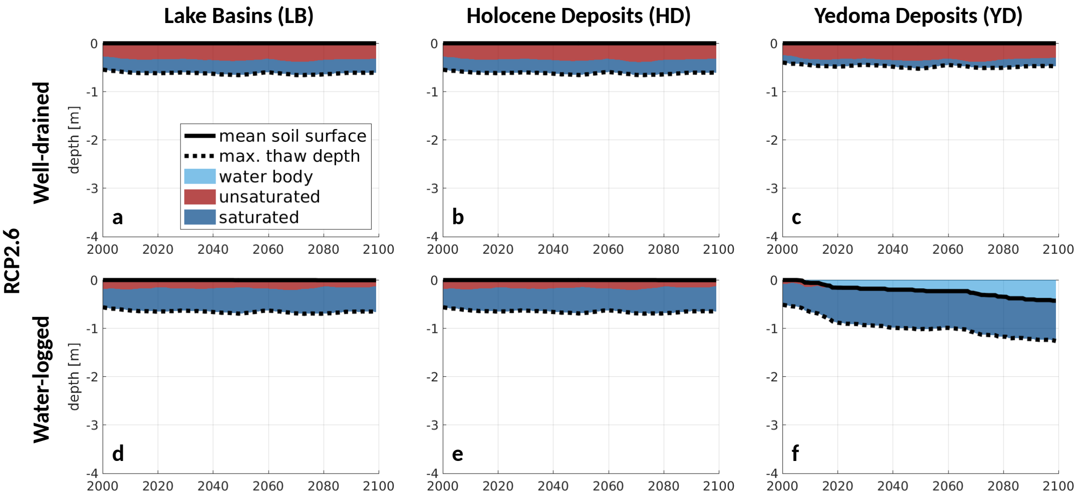

Supplementary Figure 7: Permafrost thaw in the RCP2.6 runs. Solid lines show the mean ground subsidence and dashed lines the 11-year running mean of the (area-weighted) maximum annual thaw depth for all runs under RCP2.6 warming scenario. Coloured areas indicate the fractions of unsaturated (red) and saturated (dark blue) conditions prevailing in the thawed ground throughout each year.

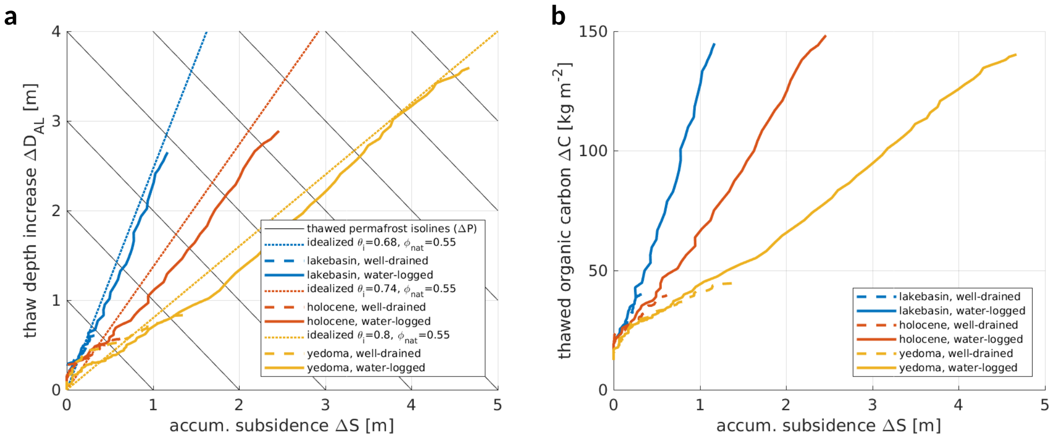

Supplementary Figure 8: Relations between the accumulated ground subsidence (ΔS) and the increase in maximum thaw depth (ΔD_{AL}, a), and the additional thawed organic carbon (ΔC, b). All displayed trajectories are for the RCP8.5 warming scenario.

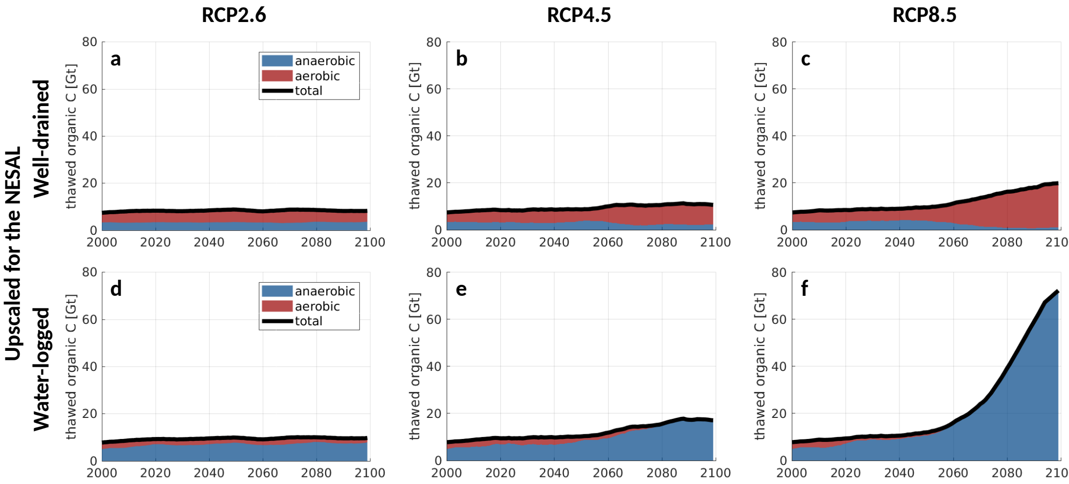

Supplementary Figure 9: Total amounts of thawed organic carbon from all landscape types within the NESAL for all combinations of hydrological conditions and warming scenarios. Coloured areas indicate the fractions of unsaturated (red) and saturated (dark blue) conditions to which thawed organic matter was exposed throughout each year.

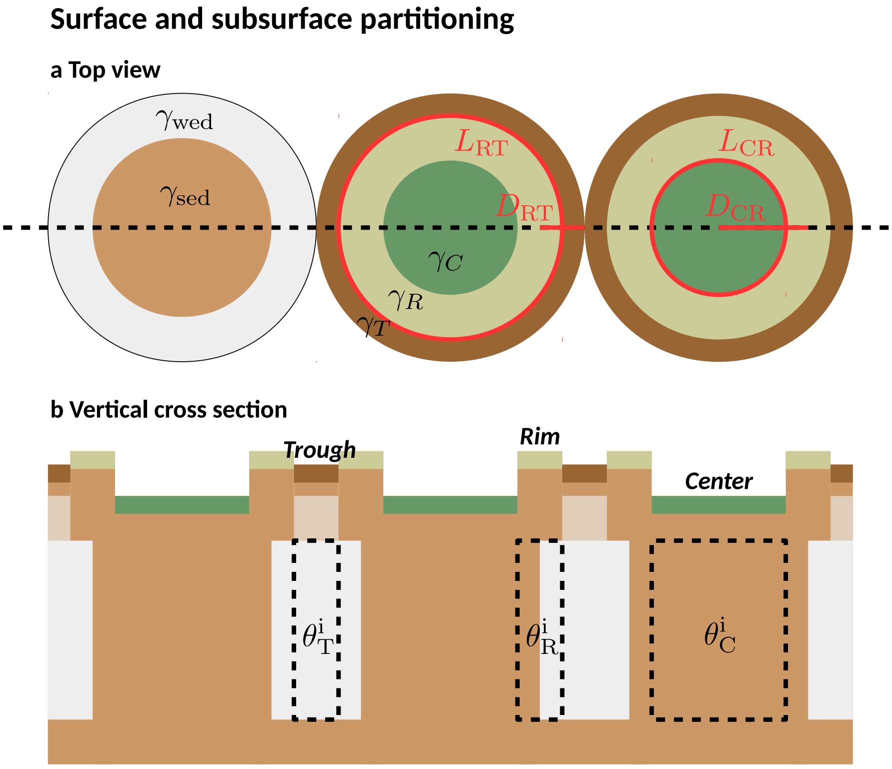
Surface and subsurface partitioning
a Top view
γ_{wed}
γ_{sed}
L_{RT}
D_{RT}
γ_C
γ_R
γ_T
L_{CR}
D_{CR}
b Vertical cross section
Trough
Rim
Center
$\theta^{\text{i}}_{\text{T}}$
$\theta^{\text{i}}_{\text{R}}$
$\theta^{\text{i}}_{\text{C}}$

Supplementary Figure 10: Schematics of the partitioning of the surface according to microtopography and the subsurface according to ground ice distribution. The surface microtopography is divided into three tiles: polygon centers, polygon rims, and troughs. The subsurface is divided into wedge ice (“wed”) and ice-rich sediment (“sed”). See text for definitions.

a: Topological relations between these tiles are derived under the assumption of nested circular shapes (a). The lateral distances (D) and contact lengths (L) are between the adjacent tiles are indicated in red.

b: While the subsurface of polygon centers is assumed to consist of ice-rich sediment, and the subsurface of troughs is assumed to consist of pure wedge ice, the subsurface of polygon rims is a mixture of the two, with the fractions γ_{wed} and γ_{sed} depending on the landscape type (LB, HD, YD).

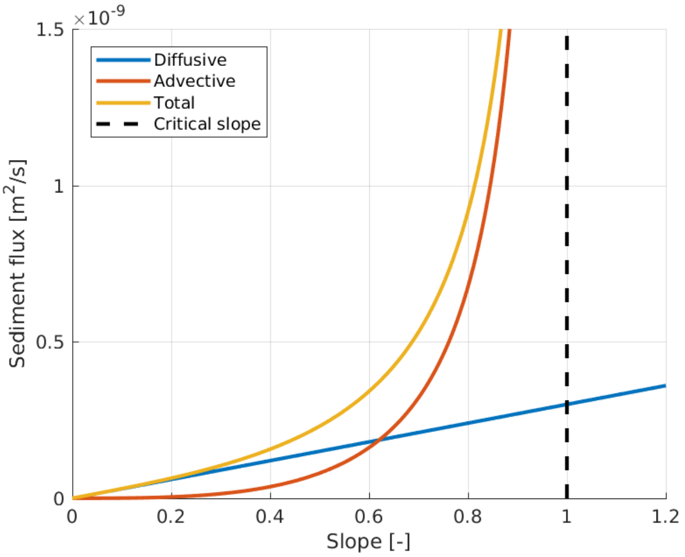

Supplementary Figure 11: Lateral sediment transport rates in dependence of slope. Diffusive, advective, and total lateral sediment flux rates between two tiles, according to equations (1), (2), and (5).

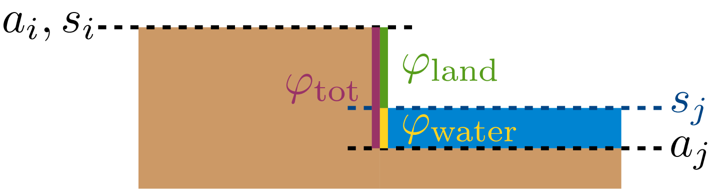
a_i, s_i
φ_{tot}
φ_{land}
s_j
φ_{water}
a_j

Supplementary Figure 12: Illustration of the lateral sediment transport coefficient. K_{eff} is composed of an subaerial and subaqueous parts.

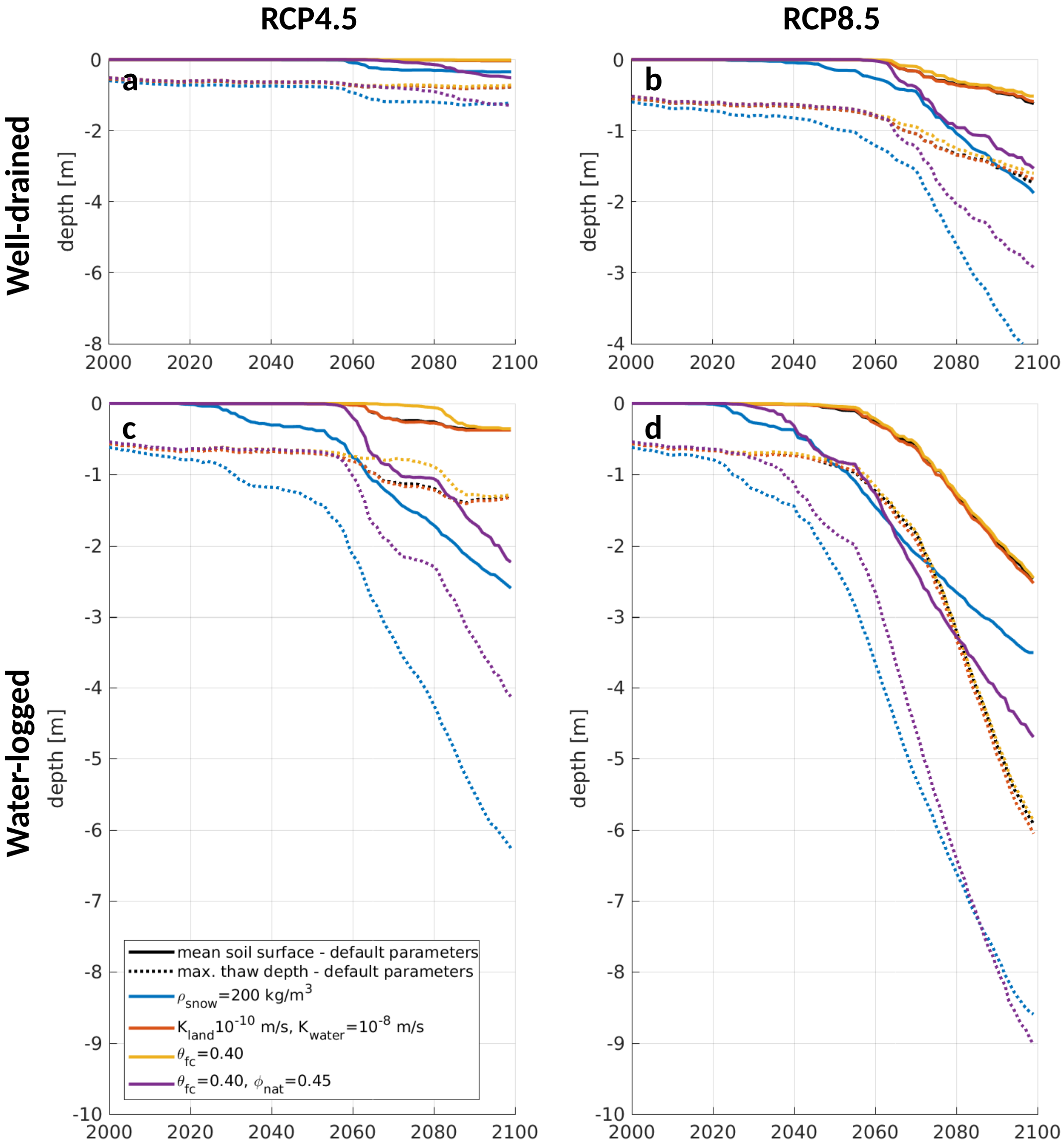

Supplementary Figure 13: Results of the sensitivity analysis. Each panel displays the accumulated ground subsidence and maximum thaw depth (11-year running mean) for simulations in which single parameters deviated from the default values. All results were obtained for the Holocene Deposits (HD) stratigraphy. See Supplementary Methods for a discussion.

Supplementary Tables

Supplementary Table 1: Parameter values reflecting the topology of ice-wedge polygons. Values for r, D, and L are rounded to one decimal place.

Parameter	Symbol	Unit	Tiles (α, $\alpha\beta$)				
			C	CR	R	RT	T
areal fraction	γ_α	-	0.3	-	0.6	-	0.1
area	A_α	m^2	42	-	84	-	14
outer radius	r_α	m	3.7	-	6.3	-	6.7
distance	$D_{\alpha\beta}$	m	-	5.0	-	1.7	-
contact length	$L_{\alpha\beta}$	m	-	23.0	-	39.8	-

Supplementary Table 2: Parameters of the lateral sediment transport scheme used for our simulations.

Parameter	Symbol	Unit	Value
Subaerial transport coefficient	K_{land}	$m^2\,s^{-1}$	3×10^{-10}
Subaqueous transport coefficient	K_{water}	$m^2\,s^{-1}$	3×10^{-8}
Critical slope angle	α_{crit}	°	45
Lateral transport time step	Δt_{lat}	s	3600

Supplementary Table 3: Overview of the soil stratigraphies used for polygon centres, rims, and troughs of drained lake basins (LB). Excess ice layers are shown in bold. Depths are relative to the initial altitude (a) of the respective tile.

Depth [m]	Mineral θ_m	Organic θ_o	Nat. por. ϕ_nat	Soil type	Water θ_w^0	Comment
Lake Basins (LB)						
Center ($a_\text{C} = 0.0\,\text{m}$)						
0-0.1	0	0.15	0.85	sand	0.85	Vegetation layer
0.1-0.2	0.10	0.15	0.75	sand	0.75	Organic layer
0.2-1.0	0.25	0.10	0.65	silt	0.65	Mineral layer
1.0-10.0	**0.20**	**0.15**	**0.55**	**sand**	**0.65**	Ice-rich deposits
10.0–20.0	0.35	0.10	0.55	sand	0.55	Younger taberit deposits
20.0–40.0	0.50	0.05	0.45	sand	0.45	Older taberit deposits
>40.0	0.90	0	0.10	sand	0.10	Bedrock
Rim ($a_\text{R} = 0.4\,\text{m}$)						
0.0-0.1	0.10	0.15	0.75	sand	0.75	Organic layer
0.1-0.9	0.25	0.10	0.65	silt	0.65	Mineral layer
0.9-10.0	**0.20**	**0.15**	**0.55**	**sand**	**0.65**	Ice-rich deposits
10.0–20.0	0.35	0.10	0.55	sand	0.55	Younger taberit deposits
20.0–40.0	0.50	0.05	0.45	sand	0.45	Older taberit deposits
>40.0	0.90	0	0.10	sand	0.10	Bedrock
Trough ($a_\text{T} = 0.3\,\text{m}$)						
0-0.1	0	0.15	0.85	sand	0.85	Vegetation layer
0.1-0.2	0.10	0.15	0.75	sand	0.75	Organic layer
0.2-0.6	0.25	0.10	0.65	silt	0.65	Mineral layer
0.6-0.8	**0.20**	**0.15**	**0.55**	**sand**	**0.65**	Intermediate layer
0.8-1.8	**0.05**	**0**	**0.55**	**sand**	**0.95**	Ice wedge
1.8-2.8	**0.10**	**0.05**	**0.55**	**sand**	**0.85**	Ice wedge and ice-rich deposits
2.8-3.8	**0.15**	**0.10**	**0.55**	**sand**	**0.75**	Ice wedge and ice-rich deposits
3.8-10.0	**0.20**	**0.15**	**0.55**	**sand**	**0.65**	Ice-rich deposits
10.0–20.0	0.35	0.10	0.55	sand	0.55	Younger taberit deposits
20.0–40.0	0.50	0.05	0.45	sand	0.45	Older taberit deposits
>40.0	0.90	0	0.10	sand	0.10	Bedrock

Supplementary Table 4: Overview of the soil stratigraphies used for polygon centres, rims, and troughs of Holocene deposits (HD). Excess ice layers are shown in bold. Depths are relative to the initial altitude (a) of the respective tile.

Depth [m]	Mineral θ_m	Organic θ_o	Nat. por. ϕ_nat	Soil type	Water θ_w^0	Comment
Holocene Deposits (HD)						
Center ($a_\mathrm{C} = 0.0\,\mathrm{m}$)						
0-0.1	0	0.15	0.85	sand	0.85	Vegetation layer
0.1-0.2	0.10	0.15	0.75	sand	0.75	Organic layer
0.2-1.0	0.25	0.10	0.65	silt	0.65	Mineral layer
1.0-10.0	**0.20**	**0.15**	**0.55**	**sand**	**0.65**	Ice-rich deposits
10.0–30.0	0.50	0.05	0.45	sand	0.45	Older taberit deposits
>30.0	0.90	0	0.10	sand	0.10	Bedrock
Rim ($a_\mathrm{R} = 0.4\,\mathrm{m}$)						
0.0-0.1	0.10	0.15	0.75	sand	0.75	Organic layer
0.1-0.9	0.25	0.10	0.65	silt	0.65	Mineral layer
0.9-10.0	**0.15**	**0.10**	**0.55**	**sand**	**0.75**	Ice wedge and ice-rich deposits
10.0–30.0	0.50	0.05	0.45	sand	0.45	Older taberit deposits
>30.0	0.90	0	0.10	sand	0.10	Bedrock
Trough ($a_\mathrm{T} = 0.3\,\mathrm{m}$)						
0-0.1	0	0.15	0.85	sand	0.85	Vegetation layer
0.1-0.2	0.10	0.15	0.75	sand	0.75	Organic layer
0.2-0.6	0.25	0.10	0.65	silt	0.65	Mineral layer
0.6-0.8	**0.20**	**0.15**	**0.55**	**sand**	**0.65**	Intermediate layer
0.8-10.0	**0.05**	**0**	**0.55**	**sand**	**0.95**	Ice wedge
10.0–30.0	0.50	0.05	0.45	sand	0.45	Older taberit deposits
>30.0	0.90	0	0.10	sand	0.10	Bedrock

Supplementary Table 5: Overview of the soil stratigraphies used for polygon centres, rims, and troughs of Yedoma deposits (YD). Excess ice layers are shown in bold. Depths are relative to the initial altitude (a) of the respective tile.

Depth [m]	Mineral θ_m	Organic θ_o	Nat. por. ϕ_nat	Soil type	Water θ_w^0	Comment
Yedoma Deposits (YD)						
Center ($a_\mathrm{C} = 0.0\,\mathrm{m}$)						
0-0.1	0	0.15	0.85	sand	0.85	Vegetation layer
0.1-0.2	0.10	0.15	0.75	sand	0.75	Organic layer
0.2-0.6	0.25	0.10	0.65	silt	0.65	Mineral layer
0.6-20.0	**0.25**	**0.10**	**0.55**	**sand**	**0.65**	Ice-rich deposits
20.0–30.0	0.35	0.10	0.55	sand	0.55	Younger taberit deposits
30.0–50.0	0.50	0.05	0.45	sand	0.45	Older taberit deposits
>50.0	0.90	0	0.10	sand	0.10	Bedrock
Rim ($a_\mathrm{R} = 0.0\,\mathrm{m}$)						
0-0.1	0	0.15	0.85	sand	0.85	Vegetation layer
0.1-0.2	0.10	0.15	0.75	sand	0.75	Organic layer
0.2-0.6	0.25	0.10	0.65	silt	0.65	Mineral layer
0.6-1.0	**0.25**	**0.10**	**0.55**	**sand**	**0.65**	Intermediate layer
1.0-20.0	**0.10**	**0.05**	**0.55**	**sand**	**0.85**	Ice wedge and ice-rich deposits
20.0–30.0	0.35	0.10	0.55	sand	0.55	Younger taberit deposits
30.0–50.0	0.50	0.05	0.45	sand	0.45	Older taberit deposits
>50.0	0.90	0	0.10	sand	0.10	Bedrock
Trough ($a_\mathrm{T} = 0.0\,\mathrm{m}$)						
0-0.1	0	0.15	0.85	sand	0.85	Vegetation layer
0.1-0.2	0.10	0.15	0.75	sand	0.75	Organic layer
0.2-0.6	0.25	0.10	0.65	silt	0.65	Mineral layer
0.6-1.0	**0.25**	**0.10**	**0.55**	**sand**	**0.65**	Intermediate layer
1.0-20.0	**0.05**	**0**	**0.55**	**sand**	**0.95**	Ice wedge
20.0–30.0	0.35	0.10	0.55	sand	0.55	Younger taberit deposits
30.0–50.0	0.50	0.05	0.45	sand	0.45	Older taberit deposits
>50.0	0.90	0	0.10	sand	0.10	Bedrock

Supplementary Table 6: Overview of the soil stratigraphies used for the reference runs. Note that there are no excess ice layers. Depths are relative to the soil surface.

Depth [m]	Mineral θ_m	Organic θ_o	Nat. por. ϕ_nat	Soil type	Water θ_w^0	Comment
Reference run						
0-0.1	0	0.15	0.85	sand	0.85	Vegetation layer
0.1-0.2	0.10	0.15	0.75	sand	0.75	Organic layer
0.2-20.0	0.25	0.10	0.65	silt	0.65	Mineral layer
20.0–30.0	0.35	0.10	0.55	sand	0.55	Younger taberit deposits
30.0–50.0	0.50	0.05	0.45	sand	0.45	Older taberit deposits
>50.0	0.90	0	0.10	sand	0.10	Bedrock

Supplementary References

1. Strauss, J. *et al.* The deep permafrost carbon pool of the Yedoma region in Siberia and Alaska. *Geophysical Research Letters* **40**, 6165–6170 (2013).
2. Battle, M. Global Carbon Sinks and Their Variability Inferred from Atmospheric O2 and 13c. *Science* **287**, 2467–2470 (2000).
3. Nitzbon, J. *et al.* Pathways of ice-wedge degradation in polygonal tundra under different hydrological conditions. *The Cryosphere* **13**, 1089–1123 (2019).
4. Nitzbon, J., Langer, M., Westermann, S. & Martin, L. CryoGrid/CryoGrid3: CryoGrid 3 set-up for ice-wedge polygons (2019).
5. Roering, J. J., Kirchner, J. W. & Dietrich, W. E. Hillslope evolution by nonlinear, slope-dependent transport: Steady state morphology and equilibrium adjustment timescales. *Journal of Geophysical Research: Solid Earth* **106**, 16499–16513 (2001).
6. Plug, L. J. & West, J. J. Thaw lake expansion in a two-dimensional coupled model of heat transfer, thaw subsidence, and mass movement. *Journal of Geophysical Research: Earth Surface* **114** (2009).
7. Egholm, D. L., Andersen, J. L., Knudsen, M. F., Jansen, J. D. & Nielsen, S. B. The periglacial engine of mountain erosion &ndash; Part 2: Modelling large-scale landscape evolution. *Earth Surface Dynamics* **3**, 463–482 (2015).
8. Andersen, J. L., Egholm, D. L., Knudsen, M. F., Jansen, J. D. & Nielsen, S. B. The periglacial engine of mountain erosion &ndash; Part 1: Rates of frost cracking and frost creep. *Earth Surface Dynamics* **3**, 447–462 (2015).
9. Aas, K. S. *et al.* Thaw processes in ice-rich permafrost landscapes represented with laterally coupled tiles in a land surface model. *The Cryosphere* **13**, 591–609 (2019).

10. Muster, S., Langer, M., Heim, B., Westermann, S. & Boike, J. Subpixel heterogeneity of ice-wedge polygonal tundra: a multi-scale analysis of land cover and evapotranspiration in the Lena River Delta, Siberia. *Tellus B: Chemical and Physical Meteorology* **64**, 17301 (2012).
11. Ulrich, M., Grosse, G., Strauss, J. & Schirrmeister, L. Quantifying Wedge-Ice Volumes in Yedoma and Thermokarst Basin Deposits. *Permafrost and Periglacial Processes* **25**, 151–161 (2014).
12. Koven, C. D. *et al.* Permafrost carbon-climate feedbacks accelerate global warming. *Proceedings of the National Academy of Sciences* **108**, 14769–14774 (2011).
13. Lawrence, D. M., Slater, A. G. & Swenson, S. C. Simulation of Present-Day and Future Permafrost and Seasonally Frozen Ground Conditions in CCSM4. *Journal of Climate* **25**, 2207–2225 (2012).
14. Slater, A. G. & Lawrence, D. M. Diagnosing Present and Future Permafrost from Climate Models. *Journal of Climate* **26**, 5608–5623 (2013).
15. Koven, C. D., Lawrence, D. M. & Riley, W. J. Permafrost carbon–climate feedback is sensitive to deep soil carbon decomposability but not deep soil nitrogen dynamics. *Proceedings of the National Academy of Sciences* **112**, 3752–3757 (2015).
16. NSIDC. Cryosphere Glossary, frozen ground or permafrost (2020). Https://nsidc.org/cryosphere/glossary-terms/frozen-ground-or-permafrost.
17. Kokelj, S. V. & Jorgenson, M. T. Advances in Thermokarst Research. *Permafrost and Periglacial Processes* **24**, 108–119 (2013).
18. Lee, H., Swenson, S. C., Slater, A. G. & Lawrence, D. M. Effects of excess ground ice on projections of permafrost in a warming climate. *Environmental Research Letters* **9**, 124006 (2014).
19. Westermann, S. *et al.* Simulating the thermal regime and thaw processes of ice-rich permafrost ground with the land-surface model CryoGrid 3. *Geosci. Model Dev.* **9**, 523–546 (2016).

20. Langer, M. *et al.* Rapid degradation of permafrost underneath waterbodies in tundra landscapes—Toward a representation of thermokarst in land surface models. *Journal of Geophysical Research: Earth Surface* **121**, 2446–2470 (2016).

21. Painter, S. L. *et al.* Integrated surface/subsurface permafrost thermal hydrology: Model formulation and proof-of-concept simulations. *Water Resources Research* **52**, 6062–6077 (2016).

22. Abolt, C. J., Young, M. H., Atchley, A. L. & Harp, D. R. Microtopographic control on the ground thermal regime in ice wedge polygons. *The Cryosphere* **12**, 1957–1968 (2018).

23. Schirrmeister, L. *et al.* Periglacial landscape evolution and environmental changes of Arctic lowland areas for the last 60 000 years (western Laptev Sea coast, Cape Mamontov Klyk). *Polar Research* **27**, 249–272 (2008).

24. Fedorov, A. N. *et al.* Permafrost-Landscape Map of the Republic of Sakha (Yakutia) on a Scale 1:1,500,000. *Geosciences* **8**, 465 (2018).

25. Nitze, I., Grosse, G., Jones, B. M., Romanovsky, V. E. & Boike, J. Remote sensing quantifies widespread abundance of permafrost region disturbances across the Arctic and Subarctic. *Nature Communications* **9**, 5423 (2018).

26. Günther, F., Overduin, P. P., Sandakov, A. V., Grosse, G. & Grigoriev, M. N. Short- and long-term thermo-erosion of ice-rich permafrost coasts in the Laptev Sea region. *Biogeosciences* **10**, 4297–4318 (2013).

27. Strauss, J. *et al.* Database of Ice-Rich Yedoma Permafrost (IRYP). *PANGAEA* https://doi.org/10.1594/pangaea.861733 (2016).

28. Obu, J., Westermann, S., Kääb, A. & Bartsch, A. Ground Temperature Map, 2000-2016, Northern Hemisphere Permafrost. *PANGAEA* (2018). Type: Dataset, DOI: 10.1594/PANGAEA.888600.